Forschungsbericht 2025-30

Advancement of SAR Imaging Techniques for the Observation of Terrestrial and Planetary Snow and Ice

Andreas Benedikter

Deutsches Zentrum für Luft- und Raumfahrt
Institut für Hochfrequenztechnik und Radarsysteme
Oberpfaffenhofen

DLR Deutsches Zentrum für Luft- und Raumfahrt

Forschungsbericht 2025-30

Advancement of SAR Imaging Techniques for the Observation of Terrestrial and Planetary Snow and Ice

Andreas Benedikter

Deutsches Zentrum für Luft- und Raumfahrt
Institut für Hochfrequenztechnik und Radarsysteme
Oberpfaffenhofen

162 Seiten
114 Bilder
14 Tabellen
139 Literaturstellen

Deutsches Zentrum
DLR für Luft- und Raumfahrt

Herausgeber:

Deutsches Zentrum
für Luft- und Raumfahrt e. V.
Wissenschaftliche Information
Linder Höhe
D-51147 Köln

ISSN 1434-8454
ISRN DLR-FB-2025-30
Erscheinungsjahr 2025
DOI: 10.57676/bwj8-jd91

SAR, SAR interferometry, snow, ice, icy moons, Enceladus, planetary mission concepts, SAR autofocus, radar signal processing, orbits

Andreas BENEDIKTER
German Aerospace Center (DLR), Microwaves and Radar Institute, Oberpfaffenhofen

Advancement of SAR Imaging Techniques for the Observation of Terrestrial and Planetary Snow and Ice

Doctoral Thesis, Friedrich-Alexander-Universität Erlangen-Nürnberg (FAU)

Radar remote sensing is an essential tool for observing Earth's cryosphere and has revolutionized our understanding of the state and dynamics of glaciers, ice sheets, and snow covers in the context of a changing climate. Beyond terrestrial snow and ice, radar imaging is a crucial technology for future exploration missions to the so-called icy moons of the giant planets, of which Saturn's moon Enceladus has recently been identified as the key target for investigating habitability on other worlds. Especially synthetic aperture radar (SAR) imaging has been extensively used for monitoring snow covers as well as the extent and dynamics of glaciers and ice sheets. Besides basic SAR imagery, SAR interferometry (InSAR) and tomography (TomoSAR) provide unparalleled measurement capabilities for the observation of Earth's cryosphere. Although modern radar remote sensing techniques like InSAR and TomoSAR are considered standard in Earth Observation (EO), they have not yet been adopted for the exploration of icy moons due to increased system complexity and strong orbit perturbations. However, these techniques have been recently identified as key developments for future exploration missions to Saturn's moon Enceladus. Upcoming Earth Observation (EO) SAR missions will acquire SAR, InSAR and TomoSAR data incorporating advanced capabilities, by: i) operating at lower frequencies (e.g., in the P- and L-band), resulting in considerable signal penetration into snow and ice covers, ii) providing very high spatial resolution, and/or iii) acquire as a satellite constellation to provide multi-aspect observations. The radar signal penetration capability at lower frequencies allows to image structures and processes within or underneath the snow and ice cover. Besides these opportunities, the penetration of the signals results in position ambiguities of imaged features, as well as biases and distortions in InSAR and TomoSAR products. An additional dimension of information in SAR observations of snow and ice that has not received much attention in the past is the propagation effect on the SAR signals when penetrating in the snow and ice volumes. The aim of this thesis is to improve SAR, InSAR and TomoSAR imaging techniques for snow and ice observation in the frame of future EO and planetary missions by developing novel approaches for exploiting and compensating SAR signal propagation effects, as well as enabling InSAR and TomoSAR for the exploration of icy moons. This thesis presents several novel concepts grouped into four research objectives. First, it describes the information content in single SAR images regarding snow and ice volume properties and introduces new single-image retrieval approaches that can be applied independently of polarimetric, interferometric, or tomographic information. These single-image approaches are highly relevant in scenarios where interferometric or tomographic information is unavailable (e.g., in planetary exploration missions), as well as for calibrating interferometric and tomographic products over ice sheets and glaciers. The remaining research objectives focus on advancing SAR interferometric and tomographic techniques for snow and ice observation. The second objective assesses the feasibility and potential of using repeat-pass InSAR and TomoSAR for exploring icy moons, particularly within the context of an Enceladus mission scenario. Despite the strong orbit perturbations around Enceladus, highly stable repeat-pass orbits are designed to meet the stringent conditions for InSAR and TomoSAR. This assessment is adopted in a mission proposal currently being developed at the Jet Propulsion Laboratory (JPL), targeting repeat-pass InSAR observations of Enceladus for deformation and topography mapping. The third objective addresses the significance of commonly ignored propagation effects in elevation measurements of ice sheets and glaciers using InSAR. These propagation effects result in considerable geolocation errors of meters to tens of meters beyond the well-known penetration bias. Several adapted processing approaches are developed to accommodate the propagation effects in terms of range and phase offsets, representing an important step toward a robust penetration bias calibration in InSAR elevation products. The final objective tackles the limitations of current differential InSAR (D-InSAR) techniques for retrieving snow parameters. A novel explanation of temporal decorrelation over snow-covered areas is provided, linking snow density changes to the decorrelation of SAR signals caused by changes in the wavenumber within the snow volume. Additionally, methods to mitigate the 2-π phase ambiguity of the interferometric measurement are developed by exploiting multiple D-InSAR acquisitions with different squint angles, which can also serve as a direct measurement of snow density. The upcoming Harmony mission by the European Space Agency (ESA) is a suitable candidate to implement these developed concepts due to its large squint diversity among the satellite constellation. This thesis demonstrates the significant potential of synergistically developing terrestrial and planetary radar remote sensing. It advances the state-of-the-art of SAR imaging techniques for observing glaciers, ice sheets, and snow covers, as well as for exploring icy moons.

SAR, SAR Interferometrie, Schnee, Eis, Eismonde, Enceladus, Planetare Missionskonzepte, SAR Autofokus, Radar Signalverarbeitung, Orbits

(Published in English)

Andreas BENEDIKTER
DLR, Institut für Hochfrequenztechnik und Radarsysteme, Oberpfaffenhofen

Weiterentwicklung von SAR Bildgebungstechniken zur Beobachtung von Terrestrischen und Planetaren Schnee- und Eisvorkommen
Dissertation, Friedrich-Alexander-Universität Erlangen-Nürnberg (FAU)

Die Radarfernerkundung ist ein unverzichtbares Werkzeug zur Beobachtung der Kryosphäre der Erde und hat unser Verständnis des Zustands und der Dynamik von Gletschern, Eisschilden und Schneevorkommen im Kontext des Klimawandels grundlegend verändert. Neben der Beobachtung terrestrischer Schnee- und Eisvorkommen ist die Radarbildgebung eine Schlüsseltechnologie für zukünftige Explorationsmissionen zu den sogenannten Eismonden der Gasriesen, wobei der Saturnmond Enceladus kürzlich als Hauptziel für die Erforschung von extraterrestrischen Welten identifiziert wurde, die potenziell die notwendigen Bedingungen für die Entwicklung von Leben aufweisen. Besonders die Synthetische Apertur Radar (SAR) Technik wird intensiv zur Beobachtung von Schneevorkommen sowie der Ausdehnung und Dynamik von Gletschern und Eisschilden genutzt. Neben der klassischen SAR-Bildgebung bieten SAR-Interferometrie (InSAR) und Tomografie (TomoSAR) einzigartige Messmöglichkeiten zur Beobachtung der Kryosphäre der Erde. Obwohl InSAR und TomoSAR in der Erdbeobachtung mittlerweile Standard sind, werden sie aufgrund der erhöhten Systemkomplexität und der limitierten Navigationsgenauigkeit bei planetaren Missionen bisher nicht für die Erkundung von Eismonden eingesetzt. Allerdings wurden diese Techniken kürzlich als entscheidende Messmethoden für zukünftige Missionen zum Saturnmond Enceladus identifiziert. Kommende SAR-Missionen zur Erdbeobachtung werden SAR-, InSAR- und TomoSAR-Daten in neuartigen Konfigurationen erfassen, wobei sie: i) Signale in niedrigeren Frequenzen (z. B. im P- und L-Band) nutzen, was eine erhebliche Eindringung in Schnee und Eis ermöglicht, ii) eine sehr hohe räumliche Auflösung bieten und/oder iii) als Satellitenkonstellation operieren, um Mehrfachbeobachtungen aus verschiedenen Blickwinkeln zu ermöglichen. Die Eindringfähigkeit bei niedrigeren Frequenzen erlaubt es, Strukturen und Prozesse innerhalb oder unter der Schnee- und Eisdecke abzubilden, kann jedoch auch zu Positionsungenauigkeiten der abgebildeten Strukturen sowie zu Verzerrungen und Verschiebungen in InSAR- und TomoSAR-Produkten führen. Ein bisher wenig beachteter Aspekt bei der SAR-Bildgebung von Schnee und Eis ist der Einfluss von Signalausbreitungseffekten, wenn die Radarsignale in die Schnee- und Eisvolumina eindringen. Ziel dieser Dissertation ist es, SAR-, InSAR- und TomoSAR-Bildgebungstechniken zur Beobachtung von Schnee und Eis im Rahmen zukünftiger Erdbeobachtungs- und Planetenmissionen zu verbessern. Dies wird durch die Entwicklung neuer Ansätze zur Nutzung und Kompensation von SAR-Signalausbreitungseffekten sowie durch die Anwendung von InSAR und TomoSAR für die Erforschung von Eismonden erreicht. Diese Arbeit stellt mehrere neuartige Konzepte vor, die in vier Forschungsziele unterteilt sind. Zunächst wird der Informationsgehalt in einzelnen SAR-Bildern in Bezug auf Eis- und Schneeparameter beschrieben und neue Ansätze zur Informationsgewinnung aus Einzelbildern entwickelt, die unabhängig von polarimetrischen, interferometrischen oder tomografischen Aufnahmen angewendet werden können. Diese Einzelbildansätze sind besonders in Szenarien relevant, in denen interferometrische oder tomografische Daten nicht verfügbar sind (z. B. bei Planetenmissionen), sowie zur Kalibrierung interferometrischer und tomografischer Produkte über Eisschilden und Gletschern. Die weiteren Forschungsziele sind fokussiert auf die Fortentwicklung interferometrischer und tomografischer SAR-Techniken zur Beobachtung von Schnee und Eis. Das zweite Ziel untersucht die Realisierbarkeit und das Potenzial von repeat-pass InSAR- und TomoSAR-Konzepten zur Erforschung von Eismonden, insbesondere im Kontext einer Enceladus Mission. Trotz der starken Bahnstörungen um Enceladus können stabile repeat-pass Orbits identifiziert werden, die die herausfordernden Bedingungen für InSAR und TomoSAR erfüllen. Die entwickelten Orbitkonzepte fließen in einen Missionsvorschlag ein, der derzeit am Jet Propulsion Laboratory (JPL) entwickelt wird und auf repeat-pass InSAR-Beobachtungen von Enceladus zur Deformations- und Topografiekartierung abzielt. Das dritte Ziel adressiert die Bedeutung von Ausbreitungseffekten bei der Höhenmessung von Eisschilden und Gletschern mittels InSAR. Diese Effekte können zu erheblichen Geolokalisierungsfehlern von einigen Metern führen, zusätzlich zu dem allgemein bekannten Bias-Effekt durch die Eindringung in das Volumen. Es werden mehrere angepasste Verarbeitungsansätze entwickelt, um die Ausbreitungseffekte hinsichtlich Signalverzögerung und Phasenversatz zu berücksichtigen, was einen wichtigen Schritt zur robusten Kalibrierung der Signaleindringung in InSAR-Höhenmessungen darstellt. Das letzte Ziel befasst sich mit den Einschränkungen differenzieller InSAR-Techniken (D-InSAR) zur Messung von Schneeparametern. Eine neuartige Erklärung der temporalen Dekorrelation über schneebedeckten Gebieten wird vorgestellt, die Veränderungen der Schneedichte mit der Dekorrelation der SAR-Signale in Verbindung bringt, die durch Änderungen der Wellenzahl im Schneevolumen verursacht wird. Darüber hinaus werden Methoden zur Kompensation der 2-π-Phasenmehrdeutigkeit bei interferometrischen Messungen entwickelt, indem mehrere D-InSAR-Aufnahmen mit unterschiedlichen Schielwinkeln genutzt werden. Diese Methode kann auch als direkte Messung der Schneedichte dienen. Die bevorstehende Harmony Mission der Europäischen Weltraumorganisation (ESA) ist ein geeigneter Kandidat für die Implementierung dieser Konzepte, da sie eine große Schielwinkeldifferenz innerhalb der Satellitenkonstellation aufweist. Diese Dissertation zeigt das erhebliche Potenzial einer gemeinsamen Entwicklung der terrestrischen und planetaren Radarfernerkundung und bringt den Stand der Technik in der SAR-Bildgebung zur Beobachtung von Gletschern, Eisschilden und Schneevorkommen sowie zur Erforschung von Eismonden entscheidend voran.

Advancement of SAR Imaging Techniques for the Observation of Terrestrial and Planetary Snow and Ice

Weiterentwicklung von SAR Bildgebungstechniken zur Beobachtung von Terrestrischen und Planetaren Schnee- und Eisvorkommen

Der Technischen Fakultät der
Universität Erlangen-Nürnberg

zur Erlangung des Grades

Doktor-Ingenieur (Dr.-Ing.)

vorgelegt von

Andreas Benedikter

aus München

Als Dissertation genehmigt von
der Technischen Fakultät
der Friedrich-Alexander Universität Erlangen-Nürnberg

Tag der mündlichen Prüfung:	12. 02. 2025
Gutachter:	Prof. Dr.-Ing. Gerhard Krieger
	Prof. Dr. Matthias Braun

To my family.

Acknowledgements

This thesis is the result of more than five years of research activity at the Microwaves and Radar Institute of DLR and the Institute of Microwaves and Photonics of the Friedrich-Alexander Universität Erlangen-Nürnberg. It has been a journey shaped by the contributions and support of many great individuals.

First and foremost, I extend my deepest gratitude to Prof. Dr. Gerhard Krieger and Dr. Marc Rodriguez-Cassola, who provided me with the opportunity to pursue a PhD on a fascinating topic within an environment of exceptional expertise. After completing my master's thesis at DLR, it was Gerhard who encouraged and convinced me to continue with a PhD in collaboration with the Friedrich-Alexander Universität Erlangen-Nürnberg and DLR. His extensive experience in the field of SAR has been instrumental in shaping this work over the past five years. I am especially grateful for his guidance as my Doktorvater, and for his encouragement, which always steered me in the right direction. The trust he placed in me, both in research and in various projects, was something very special and helped me develop confidence in my own abilities. I am equally thankful to Marc for his unwavering supervision and guidance, both scientifically and personally. I appreciate the freedom I was given to explore and develop my own ideas, contribute to projects, and advance my research career. Marc, you guided my growth as a researcher and supported me in finding my pathway within the SAR community. I would also like to express my sincere thanks to Prof. Dr. Martin Vossiek and Prof. Dr. Alberto Moreira for the opportunity to work within such interdisciplinary research environments at leading institutes for radar and SAR. Alberto, your interest in my research and our valuable discussions over the years have been greatly appreciated. Additionally, I am thankful to Prof. Dr. Matthias Braun for agreeing to serve as a co-examiner for my work and for his keen interest in my research. A significant portion of my work revolved around the Enceladus Explorer Initiative, where I had the pleasure of working closely with Michael Stelzig. A heartfelt thank you to Michael for the great collaboration over the years, the exciting and successful teamwork during field campaigns, and the memorable times during conferences and skiing trips. Special thanks go to Dr. Pau Prats-Iraola, who provided significant support for my research activities related to the Harmony mission and was always available for insightful discussions. I also wish to thank my colleagues and friends at the institute – Jalal, Nicola, Luca, Maron, Felipe, Eduardo, Dominik, Mai, Georg, Kristina, Andrea, Daniel, and many others. Your expertise

was invaluable, and you contributed to a fun and stimulating atmosphere.

Lastly, my deepest gratitude goes to my family, especially my parents, for their unwavering support throughout this journey. Thank you for everything.

Munich, September 2024

Andreas Benedikter

Abstract

Radar remote sensing is an essential tool for observing Earth's cryosphere and has revolutionized our understanding of the state and dynamics of glaciers, ice sheets, and snow covers in the context of a changing climate. Beyond terrestrial snow and ice, radar imaging is a crucial technology for future exploration missions to the so-called icy moons of the giant planets, of which Saturn's moon Enceladus has recently been identified as the key target for investigating habitability on other worlds. Especially synthetic aperture radar (SAR) imaging has been extensively used for monitoring snow covers as well as the extent and dynamics of glaciers and ice sheets. Besides basic SAR imagery, SAR interferometry (InSAR) and tomography (TomoSAR) provide unparalleled measurement capabilities for the observation of Earth's cryosphere. Although modern radar remote sensing techniques like InSAR and TomoSAR are considered standard in Earth Observation (EO), they have not yet been adopted for the exploration of icy moons due to increased system complexity and strong orbit perturbations. However, these techniques have been recently identified as key developments for future exploration missions to Saturn's moon Enceladus. Upcoming Earth Observation (EO) SAR missions will acquire SAR, InSAR and TomoSAR data incorporating advanced capabilities, by: i) operating at lower frequencies (e.g., in the P- and L-band), resulting in considerable signal penetration into snow and ice covers, ii) providing very high spatial resolution, and/or iii) acquire as a satellite constellation to provide multi-aspect observations. The radar signal penetration capability at lower frequencies allows to image structures and processes within or underneath the snow and ice cover. Besides these opportunities, the penetration of the signals results in position ambiguities of imaged features, as well as biases and distortions in InSAR and TomoSAR products. An additional dimension of information in SAR observations of snow and ice that has not received much attention in the past is the propagation effect on the SAR signals when penetrating in the snow and ice volumes.

The aim of this thesis is to improve SAR, InSAR and TomoSAR imaging techniques for snow and ice observation in the frame of future EO and planetary missions by developing novel approaches for exploiting and compensating SAR signal propagation effects, as well as enabling InSAR and TomoSAR for the exploration of icy moons.

This thesis presents several novel concepts grouped into four research objectives. First, it

describes the information content in single SAR images regarding snow and ice volume properties and introduces new single-image retrieval approaches that can be applied independently of polarimetric, interferometric, or tomographic information. These single-image approaches are highly relevant in scenarios where interferometric or tomographic information is unavailable (e.g., in planetary exploration missions), as well as for calibrating interferometric and tomographic products over ice sheets and glaciers.

The remaining research objectives focus on advancing SAR interferometric and tomographic techniques for snow and ice observation. The second objective assesses the feasibility and potential of using repeat-pass InSAR and TomoSAR for exploring icy moons, particularly within the context of an Enceladus mission scenario. Despite the strong orbit perturbations around Enceladus, highly stable repeat-pass orbits are designed to meet the stringent conditions for InSAR and TomoSAR. This assessment is adopted in a mission proposal currently being developed at the Jet Propulsion Laboratory (JPL), targeting repeat-pass InSAR observations of Enceladus for deformation and topography mapping.

The third objective addresses the significance of commonly ignored propagation effects in elevation measurements of ice sheets and glaciers using InSAR. These propagation effects result in considerable geolocation errors of meters to tens of meters beyond the well-known penetration bias. Several adapted processing approaches are developed to accommodate the propagation effects in terms of range and phase offsets, representing an important step toward a robust penetration bias calibration in InSAR elevation products.

The final objective tackles the limitations of current differential InSAR (D-InSAR) techniques for retrieving snow parameters. A novel explanation of temporal decorrelation over snow-covered areas is provided, linking snow density changes to the decorrelation of SAR signals caused by changes in the wavenumber within the snow volume. Additionally, methods to mitigate the 2π phase ambiguity of the interferometric measurement are developed by exploiting multiple D-InSAR acquisitions with different squint angles, which can also serve as a direct measurement of snow density. The upcoming Harmony mission by the European Space Agency (ESA) is a suitable candidate to implement these developed concepts due to its large squint diversity among the satellite constellation.

This thesis demonstrates the significant potential of synergistically developing terrestrial and planetary radar remote sensing. It advances the state-of-the-art of SAR imaging techniques for observing glaciers, ice sheets, and snow covers, as well as for exploring icy moons.

Kurzzusammenfassung

Die Radarfernerkundung ist ein unverzichtbares Werkzeug zur Beobachtung der Kryosphäre der Erde und hat unser Verständnis des Zustands und der Dynamik von Gletschern, Eisschilden und Schneevorkommen im Kontext des Klimawandels grundlegend verändert. Neben der Beobachtung terrestrischer Schnee- und Eisvorkommen ist die Radarbildgebung eine Schlüsseltechnologie für zukünftige Explorationsmissionen zu den sogenannten Eismonden der Gasriesen, wobei der Saturnmond Enceladus kürzlich als Hauptziel für die Erforschung von extraterrestrischen Welten identifiziert wurde, die potenziell die notwendigen Bedingungen für die Entwicklung von Leben aufweisen. Besonders die Synthetische Apertur Radar (SAR) Technik wird intensiv zur Beobachtung von Schneevorkommen sowie der Ausdehnung und Dynamik von Gletschern und Eisschilden genutzt. Neben der klassischen SAR-Bildgebung bieten SAR-Interferometrie (InSAR) und Tomografie (TomoSAR) einzigartige Messmöglichkeiten zur Beobachtung der Kryosphäre der Erde. Obwohl InSAR und TomoSAR in der Erdbeobachtung mittlerweile Standard sind, werden sie aufgrund der erhöhten Systemkomplexität und der limitierten Navigationsgenauigkeit bei planetaren Missionen bisher nicht für die Erkundung von Eismonden eingesetzt. Allerdings wurden diese Techniken kürzlich als entscheidende Messmethoden für zukünftige Missionen zum Saturnmond Enceladus identifiziert. Kommende SAR-Missionen zur Erdbeobachtung werden SAR-, InSAR- und TomoSAR-Daten in neuartigen Konfigurationen erfassen, wobei sie: i) Signale in niedrigeren Frequenzen (z. B. im P- und L-Band) nutzen, was eine erhebliche Eindringung in Schnee und Eis ermöglicht, ii) eine sehr hohe räumliche Auflösung bieten und/oder iii) als Satellitenkonstellation operieren, um Mehrfachbeobachtungen aus verschiedenen Blickwinkeln zu ermöglichen. Die Eindringfähigkeit bei niedrigeren Frequenzen erlaubt es, Strukturen und Prozesse innerhalb oder unter der Schnee- und Eisdecke abzubilden, kann jedoch auch zu Positionsungenauigkeiten der abgebildeten Strukturen sowie zu Verzerrungen und Verschiebungen in InSAR- und TomoSAR-Produkten führen. Ein bisher wenig beachteter Aspekt bei der SAR-Bildgebung von Schnee und Eis ist der Einfluss von Signalausbreitungseffekten, wenn die Radarsignale in die Schnee- und Eisvolumina eindringen.

Ziel dieser Dissertation ist es, SAR-, InSAR- und TomoSAR-Bildgebungstechniken zur Beobachtung von Schnee und Eis im Rahmen zukünftiger Erdbeobachtungs- und

Planetenmissionen zu verbessern. Dies wird durch die Entwicklung neuer Ansätze zur Nutzung und Kompensation von SAR-Signalausbreitungseffekten sowie durch die Anwendung von InSAR und TomoSAR für die Erforschung von Eismonden erreicht.

Diese Arbeit stellt mehrere neuartige Konzepte vor, die in vier Forschungsziele unterteilt sind. Zunächst wird der Informationsgehalt in einzelnen SAR-Bildern in Bezug auf Eis- und Schneeparameter beschrieben und neue Ansätze zur Informationsgewinnung aus Einzelbildern entwickelt, die unabhängig von polarimetrischen, interferometrischen oder tomografischen Aufnahmen angewendet werden können. Diese Einzelbildansätze sind besonders in Szenarien relevant, in denen interferometrische oder tomografische Daten nicht verfügbar sind (z. B. bei Planetenmissionen), sowie zur Kalibrierung interferometrischer und tomografischer Produkte über Eisschilden und Gletschern.

Die weiteren Forschungsziele sind fokussiert auf die Fortentwicklung interferometrischer und tomografischer SAR-Techniken zur Beobachtung von Schnee und Eis. Das zweite Ziel untersucht die Realisierbarkeit und das Potenzial von repeat-pass InSAR- und TomoSAR-Konzepten zur Erforschung von Eismonden, insbesondere im Kontext einer Enceladus Mission. Trotz der starken Bahnstörungen um Enceladus können stabile repeat-pass Orbits identifiziert werden, die die herausfordernden Bedingungen für InSAR und TomoSAR erfüllen. Die entwickelten Orbitkonzepte fließen in einen Missionsvorschlag ein, der derzeit am Jet Propulsion Laboratory (JPL) entwickelt wird und auf repeat-pass InSAR-Beobachtungen von Enceladus zur Deformations- und Topografiekartierung abzielt.

Das dritte Ziel adressiert die Bedeutung von Ausbreitungseffekten bei der Höhenmessung von Eisschilden und Gletschern mittels InSAR. Diese Effekte können zu erheblichen Geolokalisierungsfehlern von einigen Metern führen, zusätzlich zu dem allgemein bekannten Bias-Effekt durch die Eindringung in das Volumen. Es werden mehrere angepasste Verarbeitungsansätze entwickelt, um die Ausbreitungseffekte hinsichtlich Signalverzögerung und Phasenversatz zu berücksichtigen, was einen wichtigen Schritt zur robusten Kalibrierung der Signaleindringung in InSAR-Höhenmessungen darstellt.

Das letzte Ziel befasst sich mit den Einschränkungen differenzieller InSAR-Techniken (D-InSAR) zur Messung von Schneeparametern. Eine neuartige Erklärung der temporalen Dekorrelation über schneebedeckten Gebieten wird vorgestellt, die Veränderungen der Schneedichte mit der Dekorrelation der SAR-Signale in Verbindung bringt, die durch Änderungen der Wellenzahl im Schneevolumen verursacht wird. Darüber hinaus werden Methoden zur Kompensation der 2π-Phasenmehrdeutigkeit bei interferometrischen Messungen entwickelt, indem mehrere D-InSAR-Aufnahmen mit unterschiedlichen Schielwinkeln genutzt werden. Diese Methode kann auch als direkte Messung der Schneedichte dienen. Die bevorstehende Harmony Mission der Europäischen Weltraumorganisation (ESA) ist ein geeigneter Kandidat

für die Implementierung dieser Konzepte, da sie eine große Schielwinkeldifferenz innerhalb der Satellitenkonstellation aufweist.

Diese Dissertation zeigt das erhebliche Potenzial einer gemeinsamen Entwicklung der terrestrischen und planetaren Radarfernerkundung und bringt den Stand der Technik in der SAR-Bildgebung zur Beobachtung von Gletschern, Eisschilden und Schneevorkommen sowie zur Erforschung von Eismonden entscheidend voran.

Contents

1 Introduction

Radar remote sensing offers unparalleled advantages for the observation and exploration of Earth's cryosphere and ice-covered planetary bodies, providing critical data that enhance our understanding of these environments. The benefits of radar compared to other sensor modalities mainly stem from its capability to: i) sense almost-independent of solar illumination and atmospheric conditions, ii) provide high spatial resolution and large coverage, iii) image structures and processes within or underneath the snow and ice cover due to its penetration capability, and iv) measure deformations, movements, and topography not only at high accuracy, but also fine resolution and wide coverage.

A major milestone in the development of radar remote sensing was the conception of the synthetic aperture radar (SAR) principle by Carl A. Wiley [1]. SAR provides metric or sub-metric resolution imaging independent of the range distance and sensing frequency. The launch of the first civilian SAR satellite, Seasat, in 1978 [2] by the National Aeronautics and Space Administration (NASA) ushered in an era of success of spaceborne SAR remote sensing. This success was marked by multiple SAR satellite launches in the 1990s and 2000s, with a rapid increase in recent years. Currently, more than 50 civilian SAR satellites are operational, deployed by both space agencies and the commercial sector. The application spectrum of SAR has been broadened by the development of new techniques that exploit multiple SAR images acquired in different polarizations (SAR polarimetry), at slightly different incident angles (SAR interferometry and SAR tomography), and/or at different times (differential SAR interferometry) [3–8]. Some prominent examples of currently active SAR sensors for Earth observation are: TerraSAR-X and TanDEM-X (X band) by the German Aerospace Center (DLR) and Airbus [9, 10], Sentinel-1 (C band) by the European Space Agency (ESA) [11], and ALOS-2 (L band) by the Japan Aerospace Exploration Agency (JAXA) [12]. The application of SAR for planetary exploration was pioneered by the SAR instruments of the Venera 15 and 16 probes (Soviet Union) and the Magellan mission (NASA) to image the surface of Venus through its dense atmosphere [13, 14]. Another notable application of SAR in planetary exploration was the imaging of Saturn's moon Titan and other icy moons of Saturn by the RADAR instrument of the Cassini Mission (NASA) [15].

1.1 Motivation

The first publications presenting SAR imagery over glaciers were introduced in works such as [16–18], utilizing data from both airborne systems and Seasat. These early images demonstrated the potential of SAR for identifying surface and subsurface features, including flowlines and crevasses, and for classifying glacier zones or facies characterized by varying radar backscatter. Since then, spaceborne SAR measurements from nearly all civilian SAR sensors across different frequency bands have been extensively used for snow cover mapping, classification, and characterization [19–23]. They have also been instrumental in monitoring the extent, composition, and dynamics (i.e., temporal change) of glaciers and ice sheets [24–28]. Figure 1.1 shows a SAR image acquired by TerraSAR-X over the Drygalski glacier in Antarctica, highlighting the capability of SAR to reveal high resolution characteristics of glaciers and ice sheets. The development of SAR interferometry and SAR tomography significantly broadened the application spectrum in the context of snow and ice observation. Classical applications are: glacier flow measurements using differential SAR interferometry (D-InSAR) and speckle tracking, snow water equivalent (SWE) retrieval using D-InSAR, glacier mass balance estimation using InSAR elevation measurements, and 3-D imaging of ice sheets and glaciers using SAR tomography. Figure 1.2 shows an example of elevation change measurements over the Northern Patagonian Ice Field using TanDEM-X data.

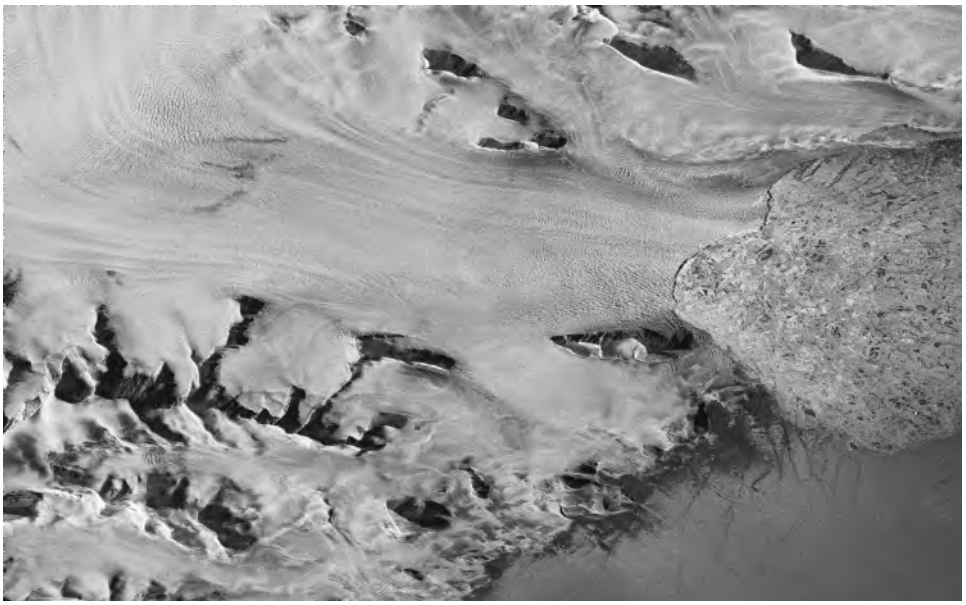

Figure 1.1: TerraSAR-X image acquired over the Drygalski Glacier on the Antarctic Peninsula [29].

One distinctive characteristic of SAR signals when imaging snow and ice covers is their ability to penetrate into the volume. Depending on the sensing frequency and the properties of the snow and ice, the signals can penetrate to depths ranging from centimeters to hundreds of meters. This capability allows for imaging structures and processes within or beneath

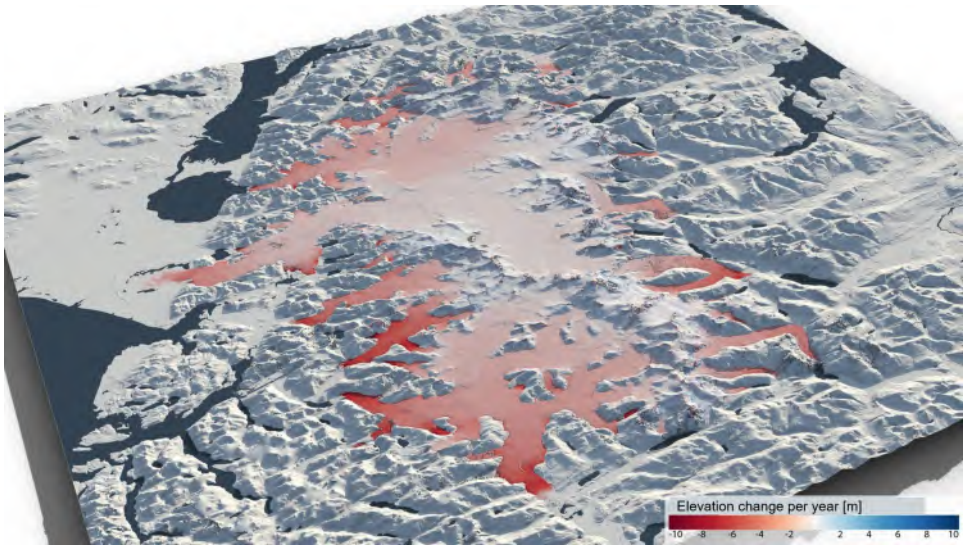

Figure 1.2: Rate of elevation change over the Northern Patagonian Ice Field between 2000 and 2012, derived from TanDEM-X data [30].

the snow and ice cover, as well as inferring dielectric properties (and related parameters) of the penetrated volume. However, the penetration also introduces challenges, such as position ambiguities of imaged features, and biases and distortions in SAR interferometric and tomographic products [31–35]. A specific example is the so-called penetration bias in interferometric surface elevation measurements over ice sheets and glaciers [31, 32]. A consequence of the penetration that has so far only been given attention in few research works is the effect of the dielectric properties of snow and ice on the SAR signal propagation characteristics, leading in a first consequence to a signal delay and redirection of the individual radar echoes, and may result in a second consequence in shifts and defocusing of SAR image features, as well as additional biases, distortions, and decorrelation in SAR interferometric and tomographic products.

Beyond terrestrial snow and ice, during the Galileo and Cassini-Huygens missions by NASA and ESA, the icy moons of Jupiter and Saturn were identified as key targets for future planetary exploration missions. Especially Saturn's icy moon Enceladus is in the spotlight of the planetary science community and was recently selected as the prime target for the first large class mission within ESA's Voyage 2050 program [36]. Enceladus, with a diameter of just about 500 km, is a geologically active and differentiated body, likely consisting of a porous rocky core and an ice shell separated by a global subsurface saltwater ocean [37]. The discovery of plumes ejecting gas and ice particles through cracks in the ice crust of the south polar region, along with the presence of complex organic molecules within the plume ejecta [38–40], has brought Enceladus to the forefront for exploratory missions aimed at investigating habitability on other worlds [41–45]. SAR instruments are expected to be a key enabling technology for the exploration of icy moons, especially Enceladus [36]. The day-and-night capability of SAR can

provide high-resolution imagery of the polar regions that experience winter darkness for periods of up to 15 years along the 30-year revolution period of the Saturn system around the Sun. Furthermore, as demonstrated over decades for terrestrial ice sheets, SAR can provide unique information on the structural and compositional properties of the ice crust of Enceladus to infer past and present states of geophysical properties, tectonics, activity, and habitability [36]. Figure 1.3 shows two images acquired by the SAR instrument of the Cassini mission of Titan [in panel a)] and Enceladus [in panel b)]. The dark features revealed in the SAR imagery of Titan are expected to be lakes of liquid methane [46] on the icy surface of Titan. The imaged swath at Enceladus (overlaid on an optical image) covers a region close to the south pole and is the only SAR acquisition at Enceladus, highlighting the complementary information that SAR provides with respect to optical imagery. Although SAR interferometry and tomography are standard technologies for observing terrestrial snow and ice, they have not yet been used for planetary exploration (apart from a few Earth-based observations), due to the increased system and navigation complexity compared to Earth observation satellites. Triggered by the strong interest in Enceladus as a future exploration target, orbital repeat-pass differential InSAR has been identified as a key enabling technology for constraining the geophysical state and the state of habitability of Enceladus through accurate deformation and topography measurements [47]. The limited navigation capability for a spacecraft orbiting Enceladus has been identified as the most critical aspect that may prevent the feasibility of repeat-pass interferometric imaging [47].

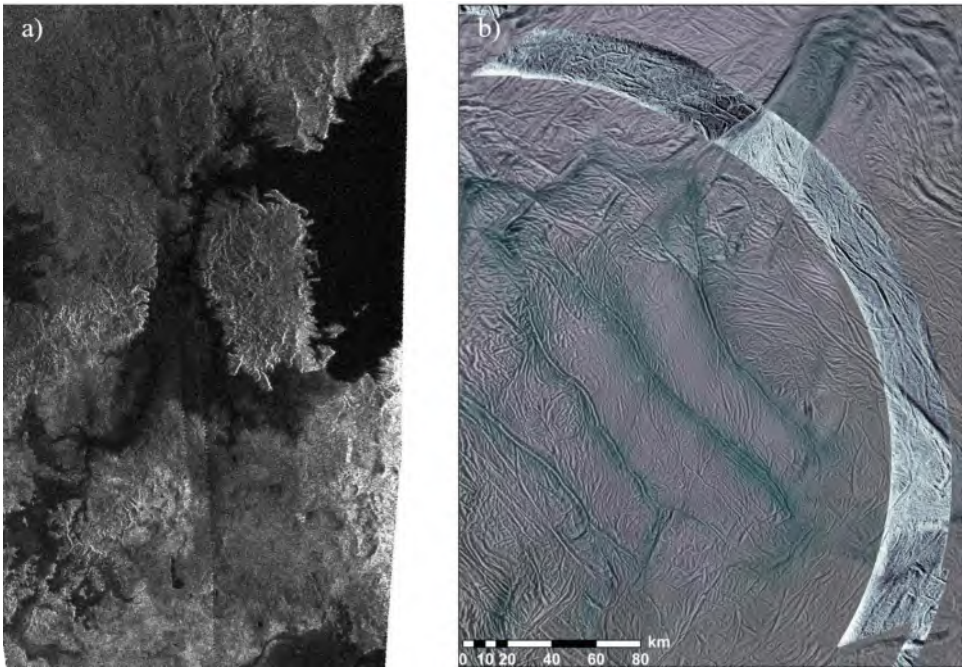

Figure 1.3: SAR imagery acquired during the Cassini mission of Saturn's icy moons (a) Titan and (b) Enceladus [48, 49].

1.2 Research Objectives and Scope of the Thesis

This thesis aims to advance SAR imaging techniques for the observation of terrestrial snow and ice, as well as for the exploration of icy moons, with a specific focus on Enceladus mission scenarios. The advancements address two primary problem statements. First, the thesis provides a detailed description of signal propagation effects in snow and ice on SAR measurements and develops methods to compensate for and exploit these effects in applications based on different SAR techniques, including simple SAR imagery, single-pass and differential SAR interferometry, as well as SAR tomography. Second, it assesses the feasibility and potential of modern radar remote sensing techniques, in particular, SAR interferometry and tomography, for future Enceladus missions. The developments presented in this thesis are motivated by the stringent boundary conditions of an Enceladus mission scenario, such as low instrument complexity and limited navigation capability. Additionally, they address the need to improve state-of-the-art SAR techniques for future terrestrial missions, demonstrating the significant potential of a synergistic development of terrestrial and planetary radar remote sensing.

This cumulative thesis is based on the publications [Pub1], [Pub2], [Pub3], [Pub4], [Pub5], [Pub6], and [Pub7] and addresses the following four research objectives, progressing from simple SAR imaging to advanced interferometric and tomographic techniques:

RO_1 *Modeling and exploiting SAR propagation effects in snow and ice for volumetric information retrieval from single SAR acquisitions.*

RO_2 *Enabling orbital repeat-pass SAR interferometric and tomographic imaging of Enceladus: feasibility and potential.*

RO_3 *Compensating and exploiting propagation effects for accurate single-pass InSAR elevation measurements of ice sheets and glaciers.*

RO_4 *Modeling and exploiting propagation effects in differential InSAR for snow parameter retrieval.*

Figure 1.4 shows the interconnection between the research objectives and the publications of the thesis.

1.3 Organization of the Thesis

The cumulative thesis is organized as follows. In Chapter 1, the motivation and problem statements, the research objectives, and the author's contributions to the included publications are described.

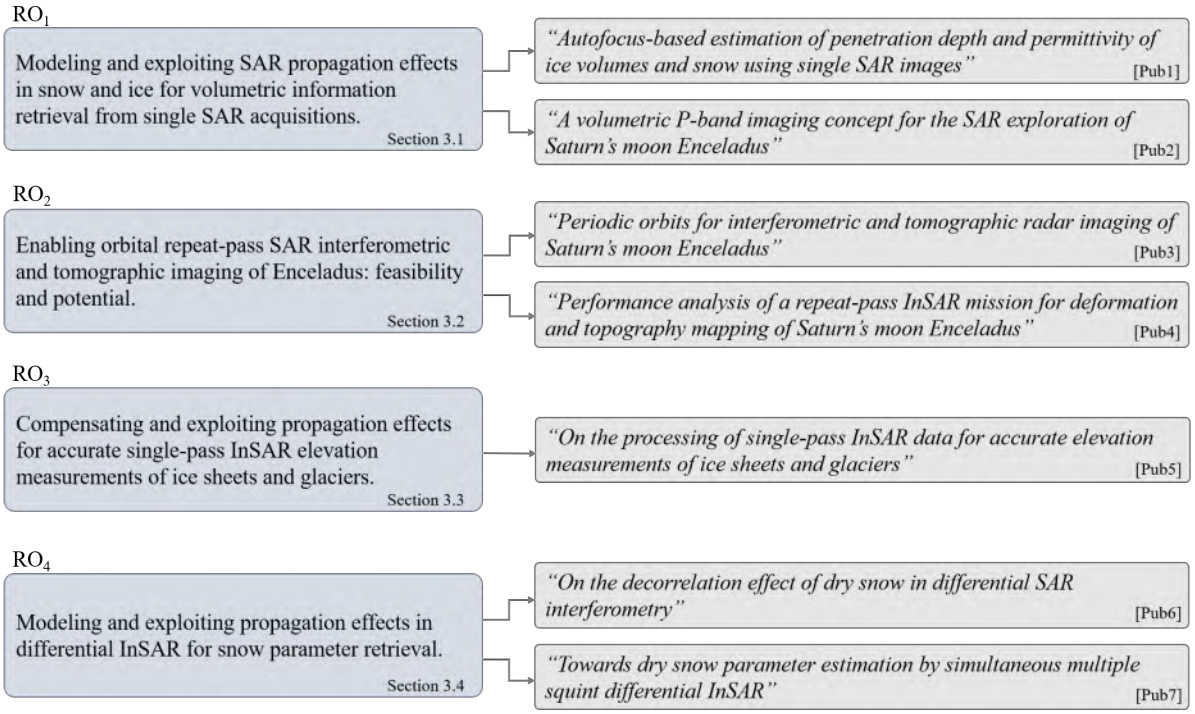

Figure 1.4: Flow chart capturing the four research objectives of the thesis and the interconnections to the publications that form the cumulative thesis.

Chapter 2 provides theoretical background beyond the discussions in the publications, relevant for a better understanding of the findings in this thesis. An overview of relevant principles of SAR techniques as well as signal propagation effects in snow and ice is given, followed by a discussion of the state-of-the-art of SAR for terrestrial and planetary snow and ice observation.

Chapter 3 presents the contributions of this thesis to the advancement of SAR for terrestrial and planetary snow and ice observation, addressing the four research objectives discussed in Section 1.2 and listed in Figure 1.4. The chapter summarizes the findings of the publications, provides further information and results, relates them to a broader context, and proposes prospects for future research. The chapter's sections are aligned with the four research objectives.

Chapter 4 summarizes the conclusions of this thesis.

1.4 Publications in the Frame of the Cumulative Thesis

The publications [Pub1] to [Pub7] form the basis of this cumulative thesis and have been developed in lead authorship by the author of this thesis. The publications are attached as Annex at the end of the thesis. In the following, the author's contribution to each of the publications is listed, based on the classification of the CRediT-System (Contributor Roles Taxonomy):

- The publication [Pub1], *"Autofocus-based estimation of penetration depth and permittivity of ice volumes and snow using single SAR images"*, originated in collaboration with the DLR colleagues listed in the paper, where most parts of the publication's content have been developed and composed by the author of this thesis. The following contributions to [Pub1] have been performed by the author of this thesis: conceptualization, methodology, software, validation, formal analysis, investigation, data curation, visualization, writing – original draft, and writing – review & editing. The subsequent contributions originated in collaboration with the co-authors: software, writing – review & editing.

- The publication [Pub2], *"A volumetric P-band imaging concept for the SAR exploration of Saturn's moon Enceladus"*, originated in collaboration with the DLR colleague listed in the paper, where most parts of the publication's content have been developed and composed by the author of this thesis. The following contributions to [Pub2] have been performed by the author of this thesis: conceptualization, methodology, software, validation, formal analysis, investigation, visualization, writing – original draft, and writing – review & editing. The subsequent contributions originated in collaboration with the co-author: writing – review & editing.

- The publication [Pub3], *"Periodic orbits for interferometric and tomographic radar imaging of Saturn's moon Enceladus"*, originated in collaboration with the DLR colleagues listed in the paper, where most parts of the publication's content have been developed and composed by the author of this thesis. The following contributions to [Pub3] have been performed by the author of this thesis: conceptualization, methodology, software, validation, formal analysis, investigation, visualization, writing – original draft, and writing – review & editing. The subsequent contributions originated in collaboration with the co-authors: conceptualization, software, writing – review & editing.

- The publication [Pub4], *"Performance analysis of a repeat-pass InSAR mission for deformation and topography mapping of Saturn's moon Enceladus"*, originated in collaboration with the colleagues from NASA JPL and DLR, listed in the paper, where large parts of the publication's content have been developed and composed by the author of this thesis. The following contributions to [Pub4] have been performed by the author of this thesis: conceptualization, methodology, software, validation, formal analysis, investigation, visualization, writing – original draft, and writing – review & editing. The subsequent contributions originated in collaboration with the co-authors: conceptualization, methodology, software, writing – review & editing.

- The publication [Pub5], *"On the processing of single-pass InSAR data for accurate el-*

evation measurements of ice sheets and glaciers", originated in collaboration with the DLR colleagues listed in the paper, where most parts of the publication's content have been developed and composed by the author of this thesis. The following contributions to [Pub5] have been performed by the author of this thesis: conceptualization, methodology, software, validation, formal analysis, investigation, visualization, writing – original draft, and writing – review & editing. The subsequent contributions originated in collaboration with the co-authors: software, writing – review & editing.

- The publication [Pub6], *"On the decorrelation effect of dry snow in differential SAR interferometry"*, originated in collaboration with the DLR colleagues listed in the paper, where most parts of the publication's content have been developed and composed by the author of this thesis. The following contributions to [Pub6] have been performed by the author of this thesis: conceptualization, methodology, software, validation, formal analysis, investigation, data curation, visualization, writing – original draft, and writing – review & editing. The subsequent contributions originated in collaboration with the co-authors: writing – review & editing.

- The publication [Pub7], *"Towards dry snow parameter estimation by simultaneous multiple squint differential InSAR"*, originated in collaboration with the DLR colleagues listed in the paper, where most parts of the publication's content have been developed and composed by the author of this thesis. The following contributions to [Pub7] have been performed by the author of this thesis: conceptualization, methodology, software, validation, formal analysis, investigation, data curation, visualization, writing – original draft, and writing – review & editing. The subsequent contributions originated in collaboration with the co-authors: writing – review & editing.

2 Background

This chapter aims to give an introduction into *Synthetic Aperture Radar (SAR)* techniques for the monitoring of snow- and ice-covered regions in Earth Observation and planetary exploration, providing relevant background beyond the discussions in the publications of this cumulative thesis. Section 2.1 gives a brief overview of the technical background of SAR used for snow and ice monitoring, focused on aspects needed for a better understanding and interpretation of the results presented in this thesis, namely basic SAR principles, SAR interferometry, and SAR tomography. Ample references are provided for a more in-depth introduction of each topic. Section 2.2 explains propagation and scattering effects of radar signals in snow and ice volumes that are relevant for the techniques developed in the frame of this thesis. Section 2.3 summarizes the state-of-the-art of SAR applications for snow and ice monitoring, individually for Earth Observation and planetary exploration.

2.1 SAR Techniques for Snow and Ice Observation

SAR is an active microwave imaging system which measures the two-dimensional complex reflectivity of a scene [50]. Since the SAR principle was first suggested in the 1950s by Carl Wiley [1], many airborne and spaceborne SAR systems have been used operationally. SAR data have the advantage of a large coverage, potentially short revisit time, and day and night imaging capability at almost all weather conditions [3], an important requirement for the monitoring of terrestrial glaciers, ice sheets and snow covers experiencing polar night and cloud cover for much of the year, as well as the polar regions of icy moons that experience long times of winter darkness, e.g., roughly 15 years for Saturn's moon Enceladus. Spatial resolutions on the order of few meters make SAR imagery suitable not only for the rather homogeneous interior of ice sheets, but also for outlet and alpine glaciers that are typically characterized by more complex structural and topographic properties. Radar signals in commonly used frequency bands (e.g., from P to X band) significantly penetrate into optical non-transparent natural media such as snow, firn, and ice, providing sensitivity of the SAR acquisition to both, backscatter from the surface and also scattering structures within the volume. This provides the opportunity for large scale characterization of the subsurface of terrestrial and planetary snow and ice volumes.

2.1.1 SAR Principle

The basic principle of SAR is a side-looking radar, most commonly operating on an airborne or spaceborne platform, that transmits electromagnetic pulses [50]. The transmitted signals are backscattered at the illuminated area on the ground and received as echoes by the radar sensor. The backscatter characteristics mainly depend on geometric (i.e., roughness, size, orientation) and dielectric properties of the scatterers on the surface and subsurface [51]. The radar samples the returning echoes coherently, i.e., it retains both amplitude and phase, and stores them for further processing. The 2-D imaging capability is achieved by determining the across-track (range) position of the received signals from their travel time, and the along-track (azimuth) position by their Doppler frequency, where the spatial resolution is established by exploiting the signal bandwidth in the range direction, and the Doppler bandwidth in the azimuth direction [50].

2.1.1.1 SAR Geometry

Figure 2.1 shows the simplified SAR acquisition geometry for a conventional monostatic system. The platform moves with a velocity v at an altitude H and the antenna looks slant-wise towards the ground, illuminating a swath that is limited by the antenna footprint, generally defined as the half power antenna beamwidth at the surface. The two coordinates of the SAR image are the azimuth dimension along the radar track and the slant range dimension along the line-of-sight. Projecting the slant range dimension onto ground results in the ground range dimension. The outstanding feature of SAR is to obtain a fine azimuth resolution by synthesizing a long aperture via a coherent integration of many recorded echoes along the radar track. The synthetic aperture formation process is commonly performed on ground on the recorded data and is referred to as SAR image formation. The length of the synthetic aperture is limited by the time in which the antenna footprint illuminates the same point on ground and can be approximated (assuming the simplified geometry in Figure 2.1) as

$$L_{\mathrm{s}} \approx \frac{\lambda \cdot r_0}{L_{\mathrm{a}}}, \tag{2.1}$$

where λ is the carrier wavelength, r_0 the distance of closest approach to the point on ground, and L_{a} the length of the radar antenna in azimuth direction.

2.1.1.2 SAR Signal Characteristics

For SAR imaging, commonly, linear frequency-modulated (LFM) waveforms, also known as chirps, are used. A chirp pulse is characterized by a constant amplitude and a quadratic phase

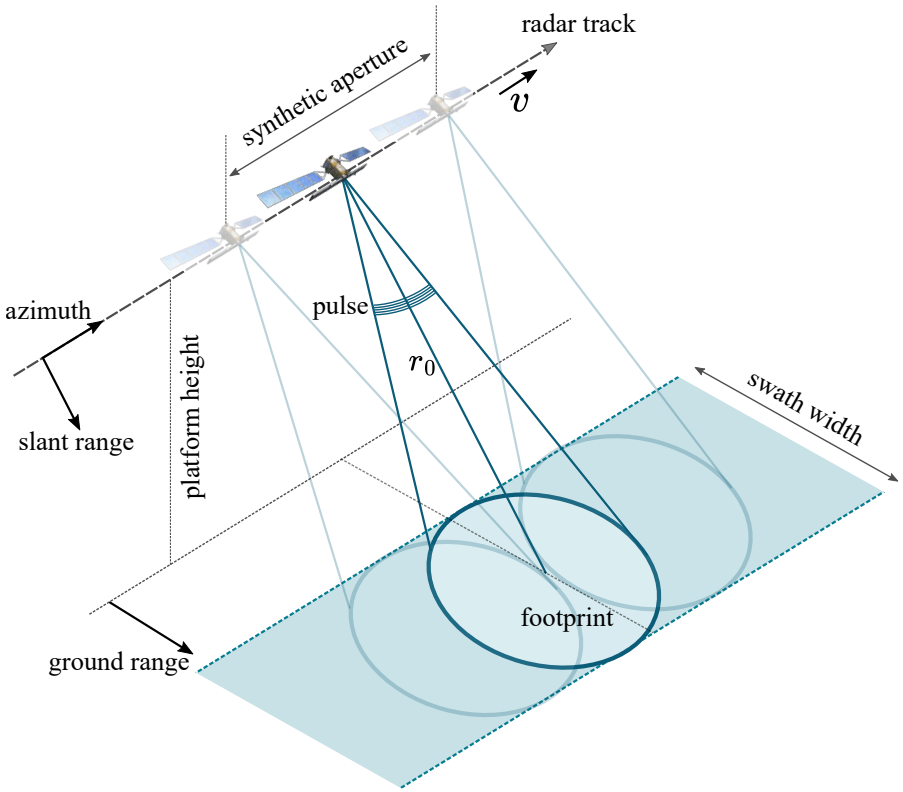

Figure 2.1: Simplified SAR acquisition geometry, where r_0 stands for the shortest approach distance and v for the platform velocity.

variation (i.e., a linear frequency variation) and has the form

$$s(t) = \text{rect}\left(\frac{t}{\tau_\text{p}}\right) \cdot \exp\left(\text{j} \cdot \pi \cdot \frac{B}{\tau_\text{p}} \cdot t^2\right), \tag{2.2}$$

where t is the time variable, $\text{rect}(t)$ represents the rectangle function and describes the pulse envelope, τ_p is the pulse duration, B describes the chirp bandwidth, and j the imaginary unit. For transmission, the signal $s(t)$ is mixed with a carrier of angular frequency ω_c, resulting in the transmission signal

$$s_\text{tx}(t) = \text{rect}\left(\frac{t}{\tau_\text{p}}\right) \cdot \exp\left(\text{j} \cdot \omega_\text{c} \cdot t + \text{j} \cdot \pi \cdot k_\text{r} \cdot t^2\right), \tag{2.3}$$

where $k_\text{r} = \frac{B}{\tau_\text{p}}$ is the chirp rate. The transmitted pulse travels until it reaches a target at distance r, where it is scattered and its echo travels back to the radar. After coherent demodulation in the receiver, the echo signal is a time delayed, phase-shifted, and attenuated version of the

transmission signal $s(t)$ with an additive white Gaussian noise (AWGN), $n(t)$:

$$s_{\mathrm{rx}}(t) = A \cdot \mathrm{rect}\left(\frac{t-\tau}{\tau_{\mathrm{p}}}\right) \cdot \exp\left[\mathrm{j} \cdot \pi \cdot k_{\mathrm{r}} \cdot (t-\tau)^2\right] \cdot \exp\left(-\mathrm{j} \cdot 2 \cdot \pi \cdot f \cdot \tau\right) + n(t), \quad (2.4)$$

where τ is the 2-way travel time to the target, f is the carrier frequency, and A accounts for the antenna gain as well as for the attenuation that is dominated by the geometrical spread of the electromagnetic wave, but is also modulated by the properties of the target and by propagation losses through the atmosphere and through semi-transparent media like snow, firn, or ice. In order to describe the variation of the received signal from a target while the platform is moving along the radar track, the travel time τ is replaced by a varying travel time $\tau(t_{\mathrm{a}})$, where t_{a} represents the azimuth time scale of the moving platform. The two-dimensional receive signal from a target can be written as

$$s_{\mathrm{rx}}(t, t_{\mathrm{a}}) = A \cdot w^2\left(t_{\mathrm{a}}\right) \cdot \mathrm{rect}\left[\frac{t-\tau(t_{\mathrm{a}})}{\tau_{\mathrm{p}}}\right] \cdot \exp\left[\mathrm{j} \cdot \pi \cdot k_{\mathrm{r}} \cdot (t-\tau(t_{\mathrm{a}}))^2\right] \cdot \exp\left[-\mathrm{j} \cdot 2 \cdot \pi \cdot f \cdot \tau(t_{\mathrm{a}})\right] + n(t, t_{\mathrm{a}}), \quad (2.5)$$

where $w\left(t_{\mathrm{a}}\right)$ represents the normalized amplitude antenna pattern on ground. The first exponential in (2.5) describes the range chirp, whereas the second exponential describes the azimuth phase variation that is exploited to obtain a fine azimuth resolution.

The azimuth phase is characterized by the travel time $\tau(t_{\mathrm{a}})$, which is proportional to the varying range between the radar and the target, commonly referred to as range history. Carl A. Wiley noticed for the first time that the range variation along azimuth introduces a Doppler frequency shift which is related to the instantaneous squint angle, ψ, with which the target is illuminated by the radar [1]. In other words, for each platform position of the radar within the synthetic aperture, a target on ground is observed with a different Doppler frequency that can be written as

$$f_{\mathrm{D}}(t_{\mathrm{a}}) = \frac{2 \cdot v \cdot \sin\left[\psi(t_{\mathrm{a}})\right]}{\lambda}, \quad (2.6)$$

with v being the effective velocity between sensor and target. For non-squinted acquisitions (i.e., the antenna is looking perpendicular to the radar track) of a stationary scene, the azimuth phase can be approximated by a quadratic function of the form

$$\Phi(t_{\mathrm{a}}) \approx \tau_0 \cdot f \cdot 2 \cdot \pi + f_{\mathrm{R}} \cdot \pi \cdot t_{\mathrm{a}}^2, \quad (2.7)$$

where τ_0 is the travel time corresponding to the closest approach distance and f_{R} is the Doppler rate. From a target's perspective, in analogy to the chirp rate, the Doppler rate describes the

changing rate of the Doppler frequency under which it is observed and is given by [50]

$$f_{\mathrm{R}} = \frac{4 \cdot v^2}{\lambda \cdot c \cdot \tau_0}, \tag{2.8}$$

where c is the speed of light.

Over the extent of the synthetic aperture, the radar samples a Doppler spectrum, where the largest and smallest frequencies correspond to the platform positions at the start and end of the synthetic aperture, respectively. Hence, the SAR signal is a 2-D band-limited signal. In range direction limited by the chirp bandwidth and in azimuth direction limited by the Doppler bandwidth.

2.1.1.3 SAR Image Formation

The recorded echos (corresponding to the individual pulse events) are stored side-by-side in a two-dimensional matrix, called the raw data matrix. The coordinates are the pulse travel time t (corresponding to the slant range position) and the azimuth time t_{a}. For each azimuth position, the received echoes of all targets in the antenna beam add up and give the raw data matrix a noise-like appearance.

A processing step is needed to obtain a focused SAR image with its distinctive high resolution. The so-called SAR image formation consists of a two-dimensional matched filter operation in range and azimuth direction, which maximizes the signal-to-noise ratio (SNR). The matched filter corresponds to the complex conjugate of the impulse response function of the SAR system, which is equivalent to the point target signal model in (2.5). In the context of an imaging system, the enhancement of SNR can be interpreted as the compression of signal energy into a smaller spatial extent, i.e., a small resolution cell. For efficiency reasons, the image formation is commonly implemented in the frequency domain. In the frequency domain, the image formation can be understood as the removal of the systematic phase modulation in range and azimuth directions.

The data after the range matched filter operation are usually referred to as range-compressed data. The attainable slant range resolution δr is proportional to the reciprocal of the chirp bandwidth:

$$\delta r = \frac{c}{2 \cdot B}, \tag{2.9}$$

The ground range resolution results from the ground projection of δr and is given by

$$\delta r_{\mathrm{g}} = \frac{\delta r}{\sin \theta_{\mathrm{i}}}, \tag{2.10}$$

where θ_{i} is the local incident angle, i.e., the angle between the radar line-of-sight and the normal vector of the surface. It is important to note that δr_{g} varies across the swath and with the topography.

The azimuth matched filtering (i.e., the azimuth compression) coherently integrates the echoes received along the synthetic aperture, similar to a phased array. Therefore, by means of signal processing, a very sharp equivalent azimuth beam is synthesized which leads to the high azimuth resolution. Since the range to a target on ground is varying along the synthetic aperture, the range compressed data of the target spread over multiple range bins in the raw data matrix, a phenomenon known as range cell migration (RCM) [50]. Several algorithms have been proposed to efficiently accommodate the RCM, among which the most common ones are based on the range-Doppler, the chirp scaling, or the ω-k algorithms [52]. In analogy to the range resolution, the azimuth resolution is proportional to the reciprocal of the Doppler bandwidth, B_{D}, and scales with the effective velocity between the platform and the ground target:

$$\delta x = \frac{v}{B_{\mathrm{D}}}. \tag{2.11}$$

Assuming the simplified acquisition geometry shown in Figure 2.1 with a linear horizontal radar track and assuming that the processed Doppler band is limited by the half-power beam width of the antenna, B_{D} can be approximated as

$$B_{\mathrm{D}} \approx \frac{2 \cdot v}{L_{\mathrm{a}}}. \tag{2.12}$$

Hence, the attainable azimuth resolution is approximately half the antenna length:

$$\delta x \approx \frac{L_{\mathrm{a}}}{2}. \tag{2.13}$$

2.1.1.4 SAR Image Properties

SAR images are 2-D complex data with the dimensions azimuth and range. Each image pixel contains amplitude and phase information, including a deterministic component and a random component. The deterministic component of the amplitude is related to the strength of the radar backscatter in the corresponding scene area and the phase is related to the closest approach distance between the radar and the corresponding target position on ground. The random component results from the presence of many scattering elements within the SAR resolution cell, contributing with slightly different ranges to the sensor, i.e., different phases. The formation of a single pixel can be understood as the summation of randomly oriented phasors, leading to constructive and destructive interferences. The phenomenon is called speckle and

gives the SAR image a noisy appearance. The intensity of a SAR image over a homogeneous scene follows an exponential distribution and the amplitude follows a Rayleigh distribution. Speckle can be reduced by averaging over multiple resolution cells, at the cost of reduced spatial resolution. Figure 2.2 shows a SAR image example acquired over the K-transect in Greenland by DLR's airborne SAR sensor F-SAR in C band, where the characteristic speckle appearance in SAR images is visible, especially in the homogeneous areas of the scene, as highlighted in the zoomed-in patch.

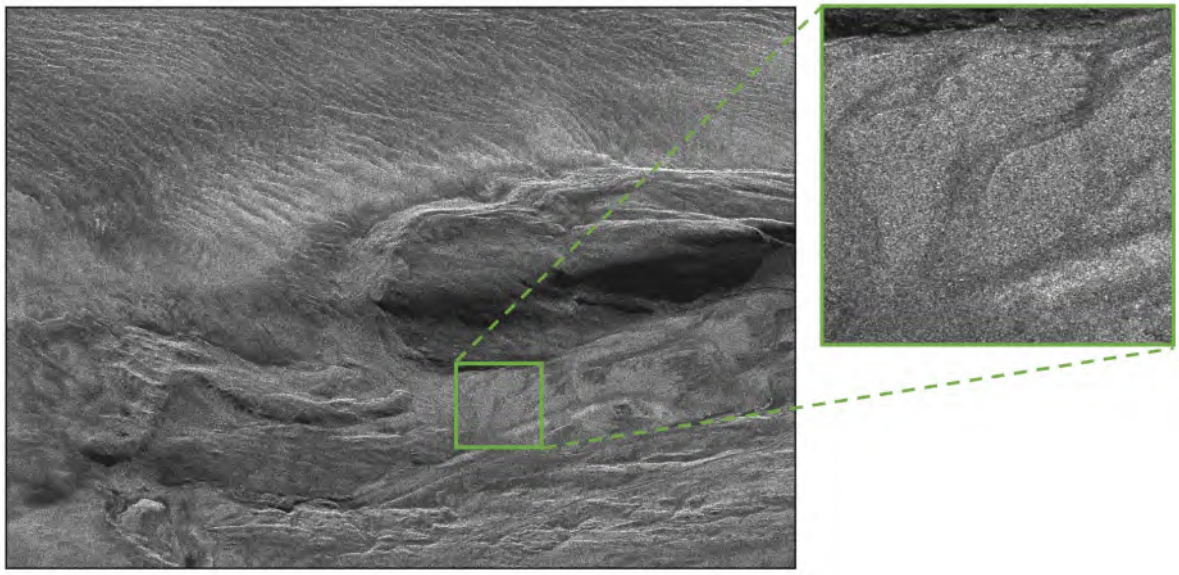

Figure 2.2: SAR image example acquired over the K-transect in Greenland by DLR's airborne SAR sensor F-SAR in C band, showing the border between the ice sheet and rocky terrain. Speckle is clearly visible in homogeneous areas of the scene, as highlighted in the zoomed-in patch.

A simple model of the signal in a single image pixel can be written as

$$i\left[t, t_{\mathrm{a}}\right] = A \cdot \exp\left[\mathrm{j} \cdot \left(\varphi_r + \varphi_{\mathrm{scatter}}\right)\right] = A \cdot \exp\left[\mathrm{j} \cdot \left(\frac{4 \cdot \pi}{\lambda} \cdot r_0 + \varphi_{\mathrm{scatter}}\right)\right], \tag{2.14}$$

where t and t_{a} indicate the range time and azimuth time coordinates, respectively, A is the amplitude, φ_r is the deterministic phase component corresponding to the target distance r_0, and $\varphi_{\mathrm{scatter}}$ is the random phase component introduced by the multi-element scattering process. Because of the random component, the phase of a single SAR image is generally not useful. SAR interferometry, described in Section 2.1.2, overcomes this difficulty by controlling the SAR acquisition environment adequately to achieve (and then cancel) the same random phase components in two images.

2.1.2 SAR Interferometry

SAR interferometry (InSAR) makes use of the phase information of the SAR images. If two SAR images are acquired from only slightly mutually displaced radar tracks, the scattering phase component, φ_{scatter}, in (2.14) of each pixel is similar among the images and can be canceled by forming the phase difference, leaving an interferometric phase, $\Delta\varphi$, that is proportional to the change of the signal's propagation path length, Δr:

$$\Delta\varphi = \frac{4 \cdot \pi}{\lambda} \cdot \Delta r, \tag{2.15}$$

where Δr can result from a displacement of the imaged scene between the two acquisitions, different acquisition geometries, and different propagation delays caused by changing dielectric properties (Δr has to be considered as optical length). The general InSAR geometry is illustrated in Figure 2.3. It is important to note that Δr also introduces a mutual shift between the images that has to be compensated in a coregistration step before computing the interferometric phase. The phase sensitivity allows SAR interferometry to perform differential range measurements with an accuracy of a fraction of the wavelength. However, if the magnitude of the range change reaches or exceeds the wavelength, the interferometric measurement will become ambiguous since the phase will periodically revisit the entire (0; 2π) phase interval. This phenomenon is referred to as phase wrapping, and procedures for retrieving the absolute phase are necessary, known as phase unwrapping techniques. SAR interferometric techniques that are used for snow and ice observation can be grouped in differential interferometry and across-track interferometry.

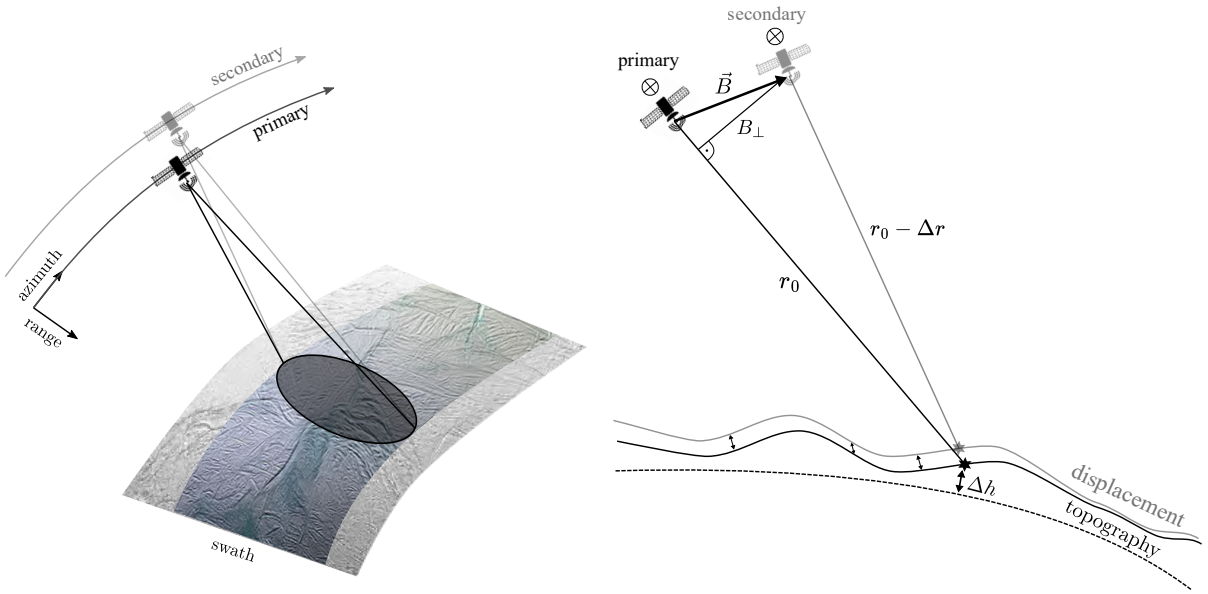

Figure 2.3: Illustration of the SAR interferometry imaging geometry. Adapted from [Pub3].

2.1.2.1 Differential Interferometry

Differential interferometry entails repeated measurements of the phase of signals scattered from a scene. Two or more SAR images are acquired at different times and by comparing the phases of the two SAR images, any displacement of scatterers between them is identified as a phase change and can be quantified. Assuming that the two SAR images are acquired from identical radar tracks and no other phenomena significantly affect the phase, $\Delta r_{\mathrm{disp.}}$ can be computed from the interferometric phase as

$$\Delta r_{\mathrm{disp.}} = \frac{\lambda}{4 \cdot \pi} \cdot \Delta\varphi. \tag{2.16}$$

Note that the measurement is only sensitive to the displacement along the radar's line of sight. Furthermore, in practice, there are several other factors that affect the interferometric phase. Usually it is not feasible to exactly repeat the same radar track using airborne and spaceborne platforms, introducing systematic phase signatures related to the topography of the imaged scene. The topographic phase signatures can be compensated by using an accurate digital elevation model (DEM). Also, the signals usually do not propagate through a vacuum but through the atmosphere, which can impose a phase delay due to tropospheric or ionospheric effects. Additional phase delays may originate from propagation into snow, ice, or soil. In order to successfully retrieve the true displacement using differential interferometry, one needs to properly account for these aspects. While complicating the displacement measurement, the sensitivity to the topography and the dielectric properties of the propagation medium (atmosphere, snow, ice, soil, ...) potentially allow for the measurement of those observables.

2.1.2.2 Across-Track Interferometry

Across-track interferometry uses SAR images acquired by spatially separated receive units. The images can be acquired in a single-pass configuration by two or more spatially separated receiving antennas on one platform or on multiple platforms flying in a close formation. Otherwise, a repeat-pass configuration is possible with a single receive unit and temporally separated tracks. The spatial distance between the sensor positions is called baseline. In a single-pass configuration, the contributions to the interferometric measurements are mainly the topography of the scene and the vertical distribution of the scatterers within one resolution cell. The phase to height conversion, which depends on the acquisition geometry, is described by the vertical interferometric wavenumber

$$\Delta k_z = \frac{4 \cdot \pi}{\lambda} \cdot \frac{\Delta\theta_{\mathrm{i}}}{\sin\theta_{\mathrm{i}}} = \frac{4 \cdot \pi}{\lambda} \cdot \frac{B_{\perp}}{r_0 \cdot \sin\theta_{\mathrm{i}}}, \tag{2.17}$$

where θ_i is the incident angle, $\Delta\theta_\mathrm{i}$ the incident angle difference between the acquisitions, r_0 the target distance, and $B_\perp$ the perpendicular projection of the baseline between the two sensors onto the radar line-of-sight. The sensitivity to the topography increases for larger interferometric baselines. Related to the vertical wavenumber is also the height of ambiguity (HoA), which describes the height of the 2π-interval of the interferometric phase

$$\mathrm{HoA} = \frac{2 \cdot \pi}{\Delta k_z}. \tag{2.18}$$

State-of-the-art SAR interferometers, like TanDEM-X, provide topography measurements with metric or even sub-metric accuracy at a spatial resolution of several meters.

2.1.2.3 Interferometric Coherence

InSAR methods rely on measuring the phase difference between two (or more) SAR images. In order to successfully perform interferometric measurements, the two data sets need to have a sufficient degree of coherence, i.e., their phase information needs to be correlated to a certain extent so that the relevant phase term can be identified and extracted. Interferometric coherence is a measure of the complex correlation of the two signals. The complex coherence can be estimated by [53]

$$\gamma = \frac{\langle i_\mathrm{p} \cdot i_\mathrm{s}^* \rangle}{\sqrt{\langle i_\mathrm{p} \cdot i_\mathrm{p}^* \rangle \cdot \langle i_\mathrm{s} \cdot i_\mathrm{s}^* \rangle}}, \tag{2.19}$$

where i_p and i_s are the SAR images of the primary and secondary acquisitions, respectively, $*$ indicates complex conjugation, and $\langle \cdot \rangle$ represents the spatial average, estimated using a moving window over the images. The coherence estimate is also a 2-D complex image, mapping the local similarity between the two SAR images. Its absolute value, $|\gamma|$, varies for each pixel between 0 (no coherence) and 1 (full coherence). The phase of the measured coherence is an intensity-weighted average phase offset between all pixels within the averaging window, and thus the phase of the interferometric coherence between two images is an estimate of the phase difference between the two images.

A low value of coherence magnitude indicates a large influence of noise or other decorrelation phenomena. The observed coherence can be described as a product of several decorrelation sources:

$$\gamma = \gamma_\mathrm{SNR} \cdot \gamma_\mathrm{temp} \cdot \gamma_\mathrm{geo} \cdot \gamma_\mathrm{vol} \cdot \gamma_\mathrm{proc}, \tag{2.20}$$

where:

- γ_{SNR} describes the decorrelation due to noise and depends on the SAR system sensitivity as well as on the backscatter of the scene. It typically only leads to low coherence values for areas with very low backscatter (e.g., water bodies),

- γ_{temp} is the temporal decorrelation caused by changes of the scattering process (i.e., a change of the elementary scattering center distribution) or propagation delay between the acquisitions. This can have a significant influence on InSAR products of ice sheets, glaciers, and snow covers, for instance caused by melting processes, wind transport, and compaction,

- γ_{geo} summarizes the range and azimuth spectral decorrelation, resulting from the baseline separation between the acquisitions and non-parallel radar tracks, respectively. The slightly different acquisition geometries introduce differences in the scattering-inherent phase contribution within a pixel [see equation (2.14)] between the acquisitions, leading to decorrelation. From a signal processing perspective, the band-limited radar signals from the two acquisitions map different portions of the observed ground scattering spectrum if acquired with different geometries. Only for identical geometries the spectra overlap completely. γ_{geo} can be mitigated by filtering the non-overlapping portions of the spectrum, at the cost of a reduced spatial resolution. The baseline separation resulting in complete decorrelation is referred to as critical baseline and is a function of the signal bandwidth as well as the acquisition geometry,

- γ_{vol}, the volumetric coherence, follows a similar rational as the range spectral decorrelation, but captures the contribution by vertically separated scatterers within a volume. It depends on the vertical distribution of the scatterers in the volume as well as the baseline separation. γ_{vol} can be used as a measure for the vertical scattering distribution, if all other decorrelation sources can be calibrated,

- γ_{proc} combines several minor decorrelation sources, e.g., coregistration errors or quantization noise. For state-of-the-art SAR interferometers, these contributions are usually negligible compared to the ones described above.

The main coherence contributions of interest in this thesis are the temporal, geometric and volume decorrelation, since they carry relevant information on the characteristics of the imaged ice and snow volumes as well as their temporal changes and drive the required acquisition geometries.

2.1.3 SAR Tomography

Extending the concept of across-track interferometry by multiple passes allows the formation of a synthetic antenna aperture in the elevation direction, perpendicular to the radar line-of-sight. Besides the 2-D capability of traditional SAR, the backscatter distribution of the scene can be resolved in the vertical direction. Combined with the penetration capability of the radar waves into semi-transparent natural media (e.g., snow, firn, ice, vegetation, sand, soil), this approach, which is commonly referred to as SAR tomography (TomoSAR), enables direct 3-D imaging of a volume. TomoSAR has been successfully applied for the imaging and characterization of e.g., forests, ice sheets, glaciers, and urban areas.

2.2 Propagation Effects in Snow and Ice

The SAR imaging techniques developed in the frame of this thesis aim on compensating or exploiting propagation effects particular to radar wave propagation in snow and ice volumes, and therefore, providing improved or even novel observation capabilities. This section provides a brief background on basic wave propagation concepts relevant for a better understanding of the developed techniques.

2.2.1 Basics of Electromagnetic Wave Propagation in Snow and Ice

Only a brief outline of electromagnetic wave propagation, sufficient for the understanding of the following concepts, is given here. Detailed reviews can be found in, e.g., [54] or [55]. The fundamental relation describing the shape and propagation of an electromagnetic wave is the so-called wave equation or Helmholtz equation. It can be written in terms of the electrical field $\vec{E}$ as [55]

$$\nabla^2 \vec{E} = \mu \cdot \varepsilon \cdot \frac{\delta^2 \vec{E}}{\delta t^2}, \tag{2.21}$$

where $\nabla^2 = \Delta$ denotes the Laplace operator. The permittivity ε and permeability μ are properties of the propagation medium. For now, a linear, homogeneous, and isotropic medium is assumed, such that ε and μ can be treated as scalars.

One particular solution to the wave equation in (2.21) can be derived in form of a monochromatic (i.e. single-frequency), time-harmonic wave [55], which can be written as

$$\vec{E}(\vec{r}, t) = \mathrm{Re}\left\{\vec{E}_0 \cdot \exp\left(-\mathrm{j}\vec{k} \cdot \vec{r}\right) \cdot \exp\left(\mathrm{j}\omega t\right)\right\} = \mathrm{Re}\left\{\vec{E}(\vec{r}) \cdot \exp\left(\mathrm{j}\omega t\right)\right\}. \tag{2.22}$$

A detailed derivation is given in [55]. In (2.22), $\vec{E}_0$ is the constant and complex amplitude

vector of the electrical field, ω stands for the angular frequency of the wave, $\vec{r}$ is a position vector of an observed point in space, and $\vec{k}$ represents the complex propagation vector. The wave function in (2.22) is characterized by wave fronts of constant phase,

$$\omega t - \vec{k} \cdot \vec{r} = \text{const.}, \tag{2.23}$$

where at any time, the front coincides with a plane orthogonal to $\vec{k}$, with $\vec{k} \cdot \vec{r} = \text{const.}$ Such waves are called plane waves. Due to the simplicity and as in the far-field of an antenna wave fronts are approximated adequately by a plane, the plane wave solution is commonly used for describing propagation phenomena. The propagation vector is defined as $\vec{k} = k_\text{c}\hat{k}$, where $\hat{k}$ is a unit vector describing the direction of propagation. The so called propagation constant k_c is defined as

$$k_\text{c} = \omega\sqrt{\mu\varepsilon_\text{c}}, \tag{2.24}$$

with ε_c being the complex permittivity given by

$$\varepsilon_\text{c} = \varepsilon - \text{j}\frac{\sigma}{\omega}, \tag{2.25}$$

where σ describes the conductivity of the medium. It is insightful to write the real and imaginary part of ε_c as ε' and ε'':

$$\varepsilon_\text{c} = \varepsilon' - \text{j}\varepsilon''. \tag{2.26}$$

Furthermore, the permittivity and permeability are typically expressed in terms of their values in vacuum and are then referred to as relative permittivity and relative permeability:

$$\varepsilon_\text{r} = \frac{\varepsilon_\text{c}}{\varepsilon_0} = \varepsilon'_\text{r} - \text{j}\varepsilon''_\text{r}, \tag{2.27}$$

$$\mu_\text{r} = \frac{\mu}{\mu_0}, \tag{2.28}$$

where ε_0 and μ_0 represent the values in vacuum. For most natural materials in the microwave region the assumption $\mu_\text{r} \approx 1$ is valid [54]. It is possible to rewrite the complex electrical field $\vec{E}(\vec{r})$ described in (2.22) in terms of a real and imaginary part of its exponential:

$$\vec{E}(\vec{r}) = \vec{E}_0 \cdot \exp\left[-(\alpha + \text{j}\beta)\,\hat{k} \cdot \vec{r}\right], \tag{2.29}$$

where α is the attenuation constant describing the absorption in the medium and β is the phase constant describing the change in phase along the travel path. Therefore, β is related to

the velocity of the wave. Since the absorption has only a secondary effect on the developed techniques in this thesis, we focus here on the phase constant (i.e., the propagation constant), β. Starting from (2.24) and (2.26), β is found to be

$$\beta = k_0 \left\{ \frac{\varepsilon'_{\mathrm{r}}}{2} \left[\left(1 + \left(\frac{\varepsilon''}{\varepsilon'} \right)^2 \right)^{\frac{1}{2}} + 1 \right] \right\}^{\frac{1}{2}}, \tag{2.30}$$

where k_0 is the so-called wavenumber in vacuum and is defined as

$$k_0 = \omega \sqrt{\mu_0 \varepsilon_0} = \frac{2\pi}{\lambda_0}. \tag{2.31}$$

For a low-loss medium with $\left(\frac{\varepsilon''}{\varepsilon'}\right)^2 \ll 1$, which is appropriate for dry snow and ice [54], the phase constant can be approximated as

$$\beta \approx k_0 \sqrt{\varepsilon'_{\mathrm{r}}}. \tag{2.32}$$

The propagation velocity of the wave is given by

$$c = \frac{\omega}{\beta}, \tag{2.33}$$

which leads to the following expression for a low-loss medium:

$$c = \frac{1}{\sqrt{\mu_0 \varepsilon_0 \varepsilon'_{\mathrm{r}}}} = \frac{c_0}{\sqrt{\varepsilon'_{\mathrm{r}}}} = \frac{c_0}{n}, \tag{2.34}$$

where c_0 is the speed of light in vacuum and n is the refractive index of the medium.

2.2.2 Propagation Effects at Dielectric Boundaries

A standard approximation made in SAR observations of snow covers, ice sheets, and glaciers is to treat the propagation volume as a layered dielectric medium, where each layer is characterized by its dielectric permittivity (i.e., refractive index). A representative example is illustrated in Figure 2.4, comprising an air, or vacuum layer with a relative permittivity of $\varepsilon'_{\mathrm{r}} \approx 1$ and a snow, or ice layer underneath with $\varepsilon'_{\mathrm{r}} > 1$. When a plane wave impinges on the glacial interface, it splits into two waves, a reflected one propagating back in the first medium, and a refracted one transmitting into the second medium. Thereby, the waves experience a change in propagation direction, propagation velocity, and intensity. Figure 2.4 shows only the incoming and refracted wave.

It is insightful to describe the wave propagation in form of the wavenumber vector, $\vec{k}$, (i.e.,

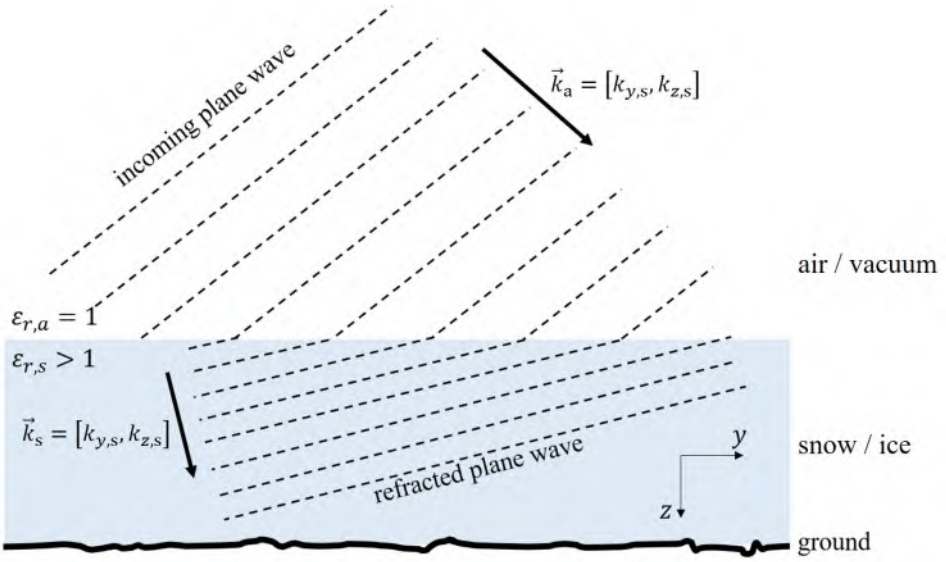

Figure 2.4: Illustration of a plane wave propagating into a snow or ice volume. Adapted from [Pub6].

in the so-called wavenumber domain) in a decomposed form with a horizontal component, k_y, parallel to the interface and a vertical component, k_z, perpendicular to the interface. Following (2.31), the wavenumbers in air can be written as

$$k_{y,\mathrm{a}} = \frac{2 \cdot \pi}{\lambda_0} \sin \theta_\mathrm{i}, \tag{2.35}$$

$$k_{z,\mathrm{a}} = \frac{2 \cdot \pi}{\lambda_0} \cos \theta_\mathrm{i}, \tag{2.36}$$

where θ_i is the incident angle. At the interface, the horizontal boundary conditions have to be satisfied [55], i.e.,

$$k_{y,\mathrm{a}} = k_{y,\mathrm{s}}, \tag{2.37}$$

where the indices a and s represent air and the glacial volume, respectively. The vertical wave number in the volume, $k_{z,\mathrm{s}}$, can be derived via the wave equation in (2.23), which takes the following form when accounting for the low-loss approximations outlined above:

$$k_{y,\mathrm{s}}^2 + k_{z,\mathrm{s}}^2 = \omega^2 \cdot \varepsilon_{\mathrm{r,s}} \cdot \varepsilon_0 \cdot \mu_0, . \tag{2.38}$$

From (2.37), (2.38), and (2.35) the vertical wavenumber in the glacial volume can be derived as:

$$\begin{aligned} k_{z,\mathrm{s}} &= \sqrt{\omega^2 \cdot \varepsilon_{\mathrm{r,s}} \cdot \varepsilon_0 \cdot \mu_0 - k_{y,\mathrm{a}}^2} \\ &= \frac{2 \cdot \pi}{\lambda_0} \cdot \sqrt{\varepsilon_{\mathrm{r,s}} - \sin^2(\theta_\mathrm{i})}. \end{aligned} \tag{2.39}$$

To summarize, the horizontal wavenumber stays constant when propagating into the volume, whereas the vertical wavenumber is a function of the permittivity.

The stretch of the vertical wavenumber results in a direction change of the wave, i.e., the refraction effect. The direction change is commonly described by Snell's law of refraction [55]:

$$\frac{\sin\theta_\mathrm{i}}{\sin\theta_\mathrm{r}} = \frac{\sqrt{\varepsilon_\mathrm{r,s}}}{\sqrt{\varepsilon_\mathrm{r,a}}}, \tag{2.40}$$

where θ_r is the refraction angle with respect to the oppositely directed surface normal vector. Snell's law is a direct consequence of the wavenumber description above.

2.2.3 Propagation in Complex Dielectric Media

A description of the signal propagation in dielectric media with a more complex distribution (e.g., caused by density variations within the snow or ice volume) can be provided by the Eikonal equation [55]:

$$(\nabla T)^2 = \frac{n^2(x,y,z)}{c_0}, \tag{2.41}$$

where ∇ symbolizes the gradient, $T(x,y,z)$ is the travel time of the phase fronts, and $n(x,y,z)$ is the refractive index distribution within the propagation medium. The Eikonal equation is a high-frequency approximation to the wave equation in (2.21), describing the wave as propagating wave fronts of constant runtime. It allows a description of large-scale propagation effects in a heterogeneous dielectric medium, while not accounting for scattering effects. An interpretation of the Eikonal equation is given by Fermat's principle of least time, stating that an electromagnetic wave follows the travel path for which it takes the least time between two points in a dielectric medium, i.e., it tends to bend towards low refractive index areas that are characterized by a faster propagation velocity. Note that Snell's law is a direct consequence of Fermat's principle. Figure 2.5 shows the simulation of a propagating wave front through a complex refractive index distribution, where the range of refractive index values, n, is representative for snow and ice environments. The simulation is performed by a numerical solution of the Eikonal equation. Note the distinctive bending effect of the refractive index variation on the wave fronts. The Eikonal equation has been used to model the propagation through portions of the Enceladus ice crust in [Pub2] and [56].

2.2.4 Permittivity of Dry Snow, Firn and Ice

As discussed above, the real part of the dielectric permittivity of a medium (equivalently described by its refractive index) determines the propagation characteristics within the medium.

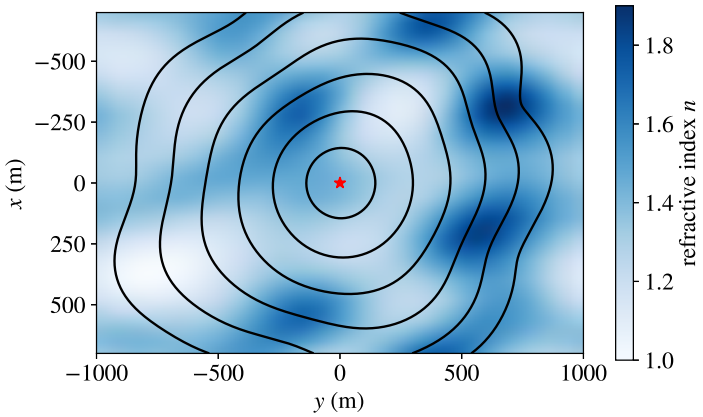

Figure 2.5: Simulation of the propagating wave fronts from a point source (red star) through a complex refractive index distribution. The range of refractive index values, n, is representative for snow and ice environments.

The imaginary part drives the dielectric absorption and plays a secondary role for the developed techniques and is not further discussed here. For the sake of simplicity, the term permittivity is from here on used as synonym for the real part of the relative permittivity. Comprehensive reviews on dielectric properties of snow and ice are provided, e.g., in [57–60].

Dry snow and firn can be described as a mixture of ice and air. The permittivity of both have a negligible frequency dependence between 10 MHz and 100 GHz. Within this range, the permittivity can be assumed to be solely dependent on the snow/firn density, ρ, and can be approximated as [61]

$$\varepsilon_{\mathrm{r}}(\rho) = \begin{cases} 1 + a \cdot \rho + b \cdot \rho^3 & \rho \leq 0.4\,\mathrm{g\,cm^{-3}} \\ \left[\left(1 - \frac{\rho}{\rho_{\mathrm{ice}}}\right) \cdot \varepsilon_{\mathrm{r,h}}^{\frac{1}{3}} + \frac{\rho}{\rho_{\mathrm{ice}}} \cdot \varepsilon_{\mathrm{r,ice}}^{\frac{1}{3}}\right]^3 & \rho > 0.4\,\mathrm{g\,cm^{-3}}, \end{cases} \tag{2.42}$$

where ρ is assumed to have the unit $\mathrm{g\,cm^{-3}}$ and the constants are given by $a = 1.5995\,\mathrm{cm^3\,g^{-1}}$, $b = 1.861\,\mathrm{cm^9 g^{-3}}$, $\rho_{\mathrm{ice}} = 0.917\,\mathrm{g\,cm^{-3}}$, $\varepsilon_{\mathrm{r,h}} = 1.005$, and $\varepsilon_{\mathrm{r,ice}} = 3.179$. Figure 2.6 shows the permittivity over the whole range of possible density values, from fresh snow to solid ice. Table 2.1 indicates the density value range for typical characteristics of snow, firn and, ice, ranging from roughly $0.05\,\mathrm{g\,cm^{-3}}$ for freshly fallen snow to $0.917\,\mathrm{g\,cm^{-3}}$ of solid ice.

2.3 State-of-the-Art of SAR for Terrestrial and Planetary Snow and Ice Observation

SAR has been used for the exploration and monitoring of the Earth's and other planetary bodies' cryosphere for several decades. Radar imaging provides year-round, day-and-night, as

Density [$\mathrm{g\,cm^{-3}}$]	Characteristic
0.05 - 0.15	new snow (uncompacted)
0.15 - 0.3	settled snow on ground, self-compacted over several days
0.3 - 0.5	settled snow at the end of the winter season or heavily wind-compacted snow
0.5 - 0.83	firn, naturally compacted and aged over at least one year. A form of ice still containing air channels
0.83 - 0.917	ice with air bubbles
0.917	solid ice

Table 2.1: Typical snow, firn, and ice densities.

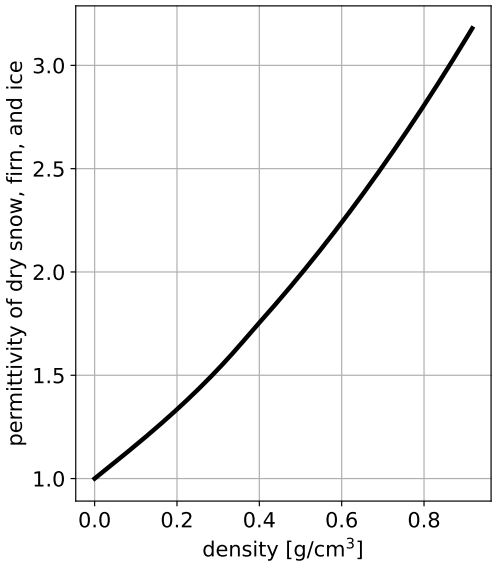

Figure 2.6: Permittivity of dry snow, firn, and ice for different density values.

well as atmosphere-independent monitoring capabilities. This is especially useful for polar latitude areas which experience polar night. Particularly in the context of icy moons exploration, the day-and-night capability can provide access to regions of interest that experience winter darkness over the course of a whole mission life time. Figure 2.7 shows the sunlight-illuminated latitudes at Enceladus during years 2040 to 2065, a time frame in which a mission is likely to arrive at Enceladus that is launched in the 2030s or 2040s. Large portions of the most-interesting polar regions are in winter darkness over the course of almost 15 years (i.e., the Saturnian polar winter period). Hence, beyond the scientific applications for icy moon exploration, SAR can be considered as a mission-enabling imaging technology used for mapping and reconnaissance, in the context of, e.g., lander missions [36].

The greatest focus of SAR for terrestrial cryospheric applications to date has been on the use of the measured single-polarization SAR backscatter of glaciers, ice sheets, and snow covers. As introduced in Section 1.1, spaceborne single-polarization SAR backscatter measurements from almost all civilian SAR sensors at different frequency bands have been widely used for snow cover mapping, classification and characterization [19–23] as well as monitoring the extent, composition, and dynamics (i.e., temporal change) of glaciers and ice sheets [24–28].

2.3.1 Opportunities and Challenges from SAR Signal Penetration

As discussed in Subsection 2.2, when the radar echo impinges on the snow or ice surface, part of the signal energy is scattered or reflected, whereas the other part penetrates into the volume.

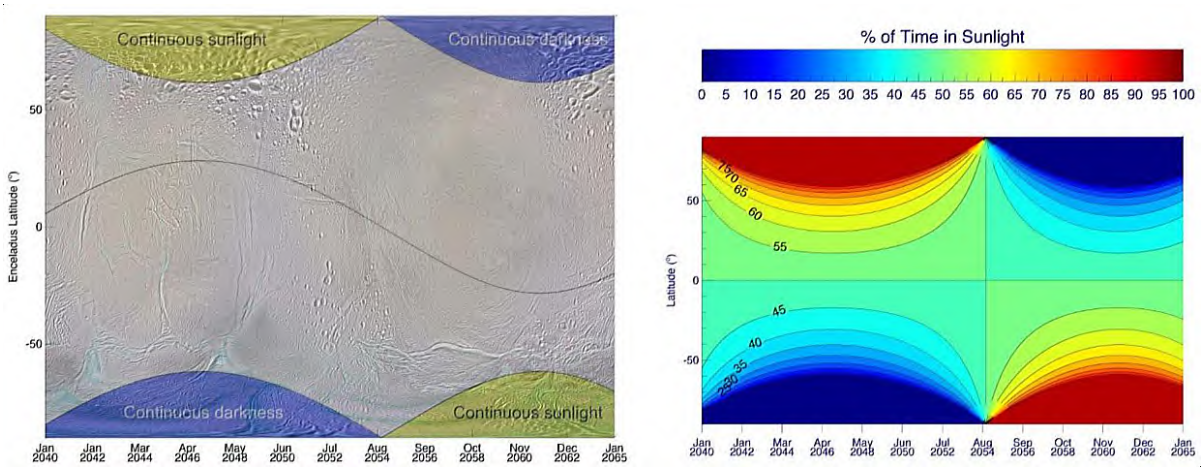

Figure 2.7: (Left) illuminated latitudes at Enceladus during years 2040 - 2065. The dark line indicates the sub-solar latitude. (Right) Percentage of daylight time for different latitudes at Enceladus over the same time period. Illustration adapted from [36].

The amount of signal energy penetrating into the volume depends on the interface roughness, dielectric properties, and the sensing frequency, where lower frequencies tend to experience less surface scattering. Within the volume, the echoes experience dielectric absorption and scattering losses, that are summarized by the so-called power extinction. The penetration capability is usually described by the two-way penetration length l that is twice the distance over which the power decreases by a factor e. The penetration length is commonly translated into a penetration depth

$$d_{\text{pen.}} = l \cdot \cos(\theta_{\text{r}}), \tag{2.43}$$

where θ_{r} is the refraction angle [see Snell's law in (2.40)]. $d_{\text{pen.}}$ is an indicator of the maximum depth within a medium that contributes to the backscatter. The penetration depth in solid ice increases with decreasing frequency, temperature, and impurity of the ice. Figure 2.8 shows the modeled penetration length in solid ice for different frequencies within the spectrum commonly used for SAR and for 3 different temperatures. The model is based on the work of *Hufford* [62]. Frequencies below $1\,\text{GHz}$ allow penetration beyond $100\,\text{m}$, whereas frequencies beyond $20\,\text{GHz}$ penetrate less than $1\,\text{m}$. For snow and firn (i.e., a conglomerate of ice crystals packed in air), the penetration depth additionally depends on the snow density and the ice crystal size. For low frequencies, this commonly results in an increased penetration (e.g., down to several hundreds of meters below $1\,\text{GHz}$). For frequencies beyond $10\,\text{GHz}$, the penetration decreases significantly compared to the solid ice case, because scattering losses are starting to dominate the power extinction, resulting in common penetration depth values, e.g., in Ka band ($35\,\text{GHz}$), of only several centimeters.

The different penetration characteristics in different frequency bands allow for specific applications, since they provide sensitivity to different portions of the ice and snow volumes.

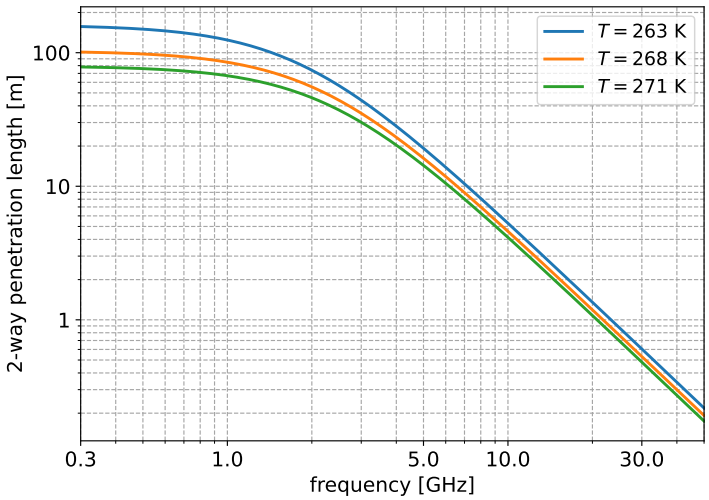

Figure 2.8: Two-way penetration length in solid ice for different frequencies and temperatures, T.

Table 2.2 depicts the two-way penetration depth (solid ice case) for exemplary SAR sensors in common frequency bands with comments on classical cryospheric applications in the specific frequency band. An incident angle of $25°$ and an ice temperature of $263\,\mathrm{K}$ are assumed for the representative penetration depth value.

The intrinsic challenge in SAR imaging of ice sheets and glaciers is the ambiguity in the position of the scattering structures within the volume. An example of the complex backscatter distribution within an ice sheet is illustrated in Figure 2.9, where different features may contribute to the return signal in a single resolution cell which, in elevation direction, is only bounded by the antenna beam width. Those features can reach from the surface to the bedrock underneath the ice, and their backscatter accumulates into one 2-D SAR resolution cell. The vertical position ambiguity leads to several challenges (additionally addressed below). In standard SAR imagery, the ambiguity significantly complicates the geophysical interpretation of imaged features, since a discrimination between surface and subsurface returns is not directly possible. The elevation ambiguity may be tackled by applying SAR polarimetric, interferometric, or tomographic techniques, but also there, the penetration into the volume introduces biases and geolocation errors.

2.3.2 Exploiting SAR Polarimetric Information

A major step beyond single-polarization SAR backscatter measurements was the use of SAR polarimetry (PolSAR) over glaciers, ice sheets, and snow covers. Polarimetric techniques have not been the focus of the work conducted within the frame of this thesis and are therefore only briefly addressed here.

For glaciers and ice sheets, several studies (e.g., [17, 63, 64]) revealed particular polarimet-

Frequency & example sensors	Penetration depth	Common applications
P band (435 MHz), Biomass (ESA)	146 m	Subsurface imaging and characterization of ice sheets via SAR interferometry and tomography
L band (1.25 GHz), NISAR (NASA / ISRO)	106 m	Same applications as in P band for ice sheets and glaciers; snow parameter estimation via SAR polarimetry and interferometry
C band (5.405 GHz), Sentinel-1 and Harmony (ESA)	16.1 m	Glacier velocity measurements via offset tracking or differential InSAR; elevation and elevation change measurements of ice sheets via interferometry; snow cover monitoring and snow parameter estimation via SAR imagery, polarimetry and interferometry
X band (9.65 GHz), TerraSAR-X / TanDEM-X (DLR / Airbus)	5.4 m	Same applications as in C band but less penetration (snow parameter estimation via interferometry is significantly limited)
Ka band (35 GHz), UAVSAR-Ka (NASA airborne sensor)	0.4 m	Elevation and elevation change measurements of ice sheets, glaciers, and snow covers

Table 2.2: Common SAR sensor operating frequencies, connected penetration depth in pure ice at 263 K, and classical cryospheric applications.

ric properties of different glacier zones from volume scattering in the subsurface, resulting in strong cross-polarized backscatter. Based on these studies, the first polarimetric models described the main scattering contributions from the scattering structures of the Greenland ice sheet. Advancements in polarimetric modeling, combining rough surface and volume scattering, as well as the introduction of anisotropy effects, allowed further interpretation of PolSAR measurements of ice sheets, such as glacier zone classification and firn thickness estimation [65,66]. However, PolSAR measurements contain no direct information about the vertical scatterer distribution in the subsurface of glaciers and ice sheets.

For snow observation, PolSAR methods provide insights into the snow composition (driving the scattering mechanisms) and its anisotropy (resulting in a polarization-dependent propagation velocity), potentially allowing estimates of the snow height, density, and snow water equivalent [67–70], as well as classification into snow types (e.g., wet snow, freshly fallen snow, and settled snow) [19,71,72].

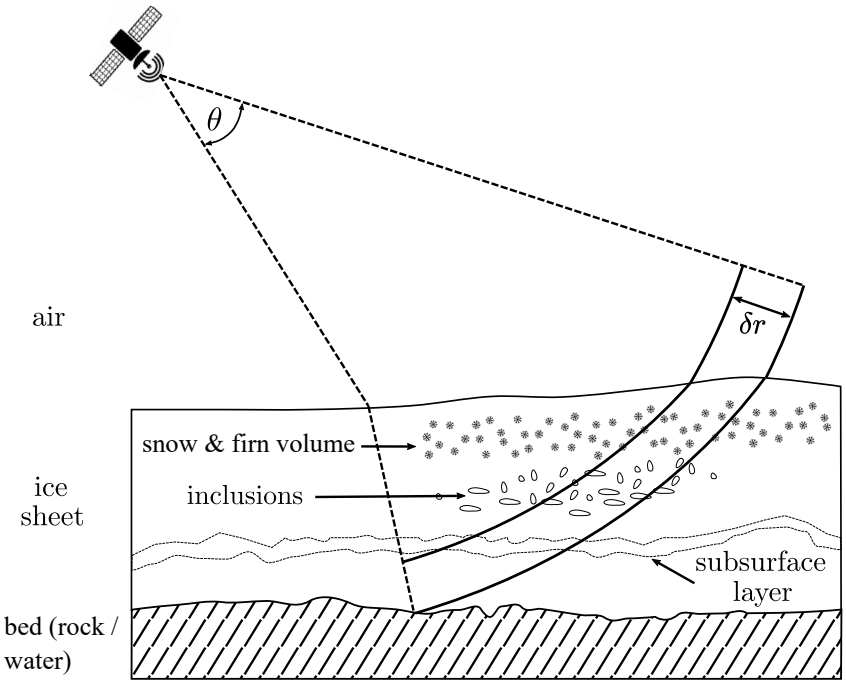

Figure 2.9: Illustration of the potentially complex backscatter scenario of an ice sheet. Scattering sources from various depths may contribute in the SAR resolution cell, indicated by the range resolution δr and bounded by the antenna beamwidth in elevation direction, θ.

2.3.3 SAR Interferometry for Snow and Ice Observation

2.3.3.1 Across-Track InSAR for Elevation and Elevation Change Measurements

Across-track InSAR provides a direct measure of the vertical location of the scattering phase center. Digital elevation models (DEMs) generated with across-track InSAR in a single-pass configuration are a main source for mapping the surface elevation and topographic changes over ice sheets and glaciers [73–78]. Another application of across-track InSAR is to study the subsurface structure and composition of ice sheets by exploiting the dependence of the interferometric phase and coherence on the vertical backscatter distribution [31–34] which has been used for the classification and characterization of glacier zones in ice sheets [79] and of snow [80–82].

The main challenge in InSAR DEM generation over glaciers and ice sheets is the penetration of radar signals into snow, firn, and ice at commonly used frequency bands, e.g., from P to X band. This results in an elevation bias of the backscatter phase center compared to the surface elevation, typically described in the literature as penetration bias [31, 32, 73, 79, 83–87]. Putting it in simple words, the DEM generated from InSAR data does not replicate the surface, but is biased downward. Extensive work has been invested in developing techniques for estimating the penetration bias and subsequently calibrating the InSAR DEM for retrieving the surface elevation. The most common approaches rely on estimating the penetration from

the InSAR coherence, combined with a modeling of the vertical backscatter distribution within the glacial volume [31–34, 79, 87]. Those approaches perform well over homogeneous parts of ice sheets (e.g., in the central parts of Greenland), but are likely to be significantly biased over heterogeneous glacial volumes such as glaciers, since commonly no *a priori* knowledge of the vertical backscatter distribution is available.

2.3.3.2 Differential InSAR

Differential InSAR (D-InSAR) allows to measure displacements or signal delays between two acquisitions with an accuracy of a fraction of the wavelength. A standard application of D-InSAR is the measurement of ice sheet and glacier deformation and flow [88–94], directly exploiting the high-accuracy differential range measurements provided by D-InSAR. The D-InSAR phase measurement is only sensitive to the displacement or flow component in the direction of the radar line-of-sight (i.e., the range direction). Along-track displacements can be measured by offset-tracking using small image patches, exploiting the coherent speckle and image contrast among the D-InSAR pairs [91]. Phase measurements sensitive to along-track displacements can be obtained by exploiting squinted acquisitions, as planned for ESA's upcoming Harmony mission [95].

Over the last years, large research focus has been put on D-InSAR methods aiming on the retrieval of the snow water equivalent (SWE), i.e., the amount of water stored in the snow cover. SWE is one of the key observables in Earth Observation. In contrast to operationally used passive microwave and gamma radiation remote sensing sensors, D-InSAR potentially allows to measure SWE for dry snow with a large coverage, a spatial resolution in the order of tens of meters, and a millimeter accuracy [96–101]. The concept relies on the transparency of dry snow at microwave frequencies and the higher dielectric permittivity of snow, compared to air, introducing a signal delay that replicates in the D-InSAR phase. The D-InSAR phase is sensitive to a SWE change, $\Delta\mathrm{SWE}$. D-InSAR SWE retrieval has been demonstrated over 20 years ago by *Guneriussen et al.* [96], but is so far not applied operationally, mainly because:

- low temporal coherence areas limit the accuracy of the phase measurement and complicate the phase-unwrapping process,
- if the phase delay introduced by the propagation through snow surpasses 2π, the D-InSAR phase carries an unknown offset, resulting only in a relative $\Delta\mathrm{SWE}$ estimate,
- D-InSAR SWE retrieval is only applicable under dry snow conditions, where the signals can penetrate the snow cover.

Besides, conventional D-InSAR does not provide a direct measurement of the snow permittivity and density, which are important parameters for the phase-to-SWE inversion as well as for

snow modeling approaches.

2.3.4 SAR Tomography for 3-D Imaging of Glaciers and Ice Sheets

Multi-baseline coherent data are exploited in SAR tomography for direct 3-D imaging of the subsurface of ice sheets and glaciers. In recent studies, SAR tomography has been demonstrated to be capable of imaging subsurface features in snow [102,103], lake and fjord ice [104], glaciers [35, 105], and ice sheets [33, 106, 107]. The 3-D resolving capability is used to constrain the structure and composition of the glacial volumes. SAR tomography of ice sheets and glaciers has been performed so far only from airborne platforms. With the upcoming ESA mission Biomass [108], spaceborne SAR tomography of the Earth's ice masses will be performed for the first time. Compared to SAR tomographic imaging of forests or urban scenes (other classical applications of tomography), the permittivity of snow, fir, and ice leads to significant biases and distortions of the imaged volumes [35, 105]. Corrections are commonly performed based on external estimates of the permittivity. The development of approaches for data-based estimation of the permittivity is of high relevance for the calibration and accurate processing of SAR tomograms of glacial volumes, especially when considering future missions like Biomass.

2.3.5 SAR for the Exploration of Planetary Ice

Beyond Earth-based observations of planetary bodies using radar telescopes, radar exploration of ice volumes on planetary bodies has been focused on radar sounder instruments (i.e., nadir-looking sensors, sensitive to specular scattering of interfaces) at relative low frequencies (HF and VHF bands), pioneered by the observation of the polar ice caps on Mars by the MARSIS [109] and SHARAD [110] instruments. SAR observations of planetary bodies were pioneered by the mapping of the surface of Venus through its optical dense atmosphere by the Venera 15, Venera 16, and Magellan mission that mapped $98\,\%$ of the surface [111]. The first and to-date only SAR observations of icy moons have been conducted by NASA's Cassini mission, focused on mapping Saturn's moon Titan through its dense atmosphere, revealing liquid methane lakes in the north polar region [46] and a complex and young surface with a variety of geologic features, suggesting cryo-volcanic constructs, flows and channels [112, 113]. Cassini also acquired a single SAR swath over the southern hemisphere of Enceladus, showing different terrain characteristics, from smooth terrain resulting from the resurfacing by the plumes to strongly tectonically ruptured terrain [114]. One of the major findings (backed by Earth-based radar observation) was the high backscatter of the Enceladus surface with backscatter values beyond 0 dB, reaching up to 6 dB, both measured in Ku band by Cassini and in S band by the Arecibo telescope [114–116]. High backscatter values (i.e., a high radar albedo) are also

observed at other icy moons, but not reaching the values of Enceladus, making Enceladus the radar-brightest body in the solar system. Different explanations have been proposed for the anomalous backscatter. The most prominent one is the coherent backscatter effect, resulting from efficient multiple scattering within the ice volume [117], also observable in dry firn areas on Earth [118]. Future high-resolution radar observations of Enceladus are expected to play a major role for understanding the backscatter enhancing effect and constrain the anomalous ice composition of Enceladus, leading to the extreme backscatter.

SAR interferometric and tomographic spaceborne radar exploration have not been used for planetary exploration yet, due to the increased system complexity. The VERITAS mission [119] to Venus will conduct for the first time (beyond Earth-based observations) SAR interferometric measurements of a planetary body, performing topography measurements using a single-pass SAR interferometer (VISAR) mounted on the VERITAS spacecraft. Triggered by the strong interest in Enceladus as a future exploration target (see Section 1.1), orbital repeat-pass differential InSAR has been identified as a key enabling technology for constraining the geological state and the state of habitability of Enceladus by accurate deformation and topography measurements [47].

3 Advancement of SAR Techniques for Terrestrial and Planetary Snow and Ice Observation

This chapter outlines the contributions of this cumulative thesis to the advancement of SAR techniques for terrestrial and planetary snow and ice observation. The key contributions and findings of the publications [Pub1] to [Pub7] are summarized and contextualized within a broader scope of application scenarios and future research. The sections are aligned with the four research objectives that are introduced in Section 1.2 and shown in Figure 1.4. The interrelation of the research objectives is highlighted within each section.

In Section 3.1 (research objective RO_1), the information content in single SAR images on snow and ice volume properties is described and novel retrieval approaches are presented that are of high relevance in scenarios in which no interferometric or tomographic information is available (e.g., relevant in the frame of planetary exploration missions), as well as for the calibration of interferometric and tomographic products over ice sheets and glaciers. The other sections and the corresponding research objectives are targeted towards the advancement of SAR interferometric and tomographic techniques for snow and ice observation. Section 3.2 (research objective RO_2) assesses the feasibility and potential of using modern radar remote sensing in the form of repeat-pass SAR interferometry and tomography, beyond Earth Observation, for the exploration of icy moons, in particular, in the context of an Enceladus mission scenario. Section 3.3 (research objective RO_3) describes the relevance of commonly ignored propagation effects in elevation measurements of ice sheets and glaciers using SAR interferometry and outlines adapted processing approaches to accurately accommodate the SAR signal penetration. Section 3.4 (research objective RO_4) describes the effect of propagation phenomena on snow parameter retrieval using differential SAR interferometry and presents novel retrieval approaches that can be applied in future missions like ESA's Harmony mission [95] that acquire with multiple squint angles.

3.1 Exploiting Propagation Effects for Volumetric Information Retrieval from Single SAR Acquisitions

When radar signals penetrate into snow and ice, they experience an additional delay due to the higher permittivity of the glacial volume. The delay is a function of the penetration depth (more precisely, the vertical position of the backscatter phase center), the permittivity of the volume, and the acquisition geometry. Additionally, the delay of the radar echoes varies systematically along the synthetic aperture. In other words, it is a function of the Doppler frequency (i.e., the instantaneous squint angle), introducing a residual azimuth phase signature on the SAR signals. The functional dependence to the Doppler frequency provides an additional dimension of information contained within the SAR signals that can be exploited to retrieve the glacial volume properties (vertical position and permittivity). This provides access to the volume properties from single SAR images, without exploiting polarimetric, interferometric, or tomographic information.

This source of information has been for the first time described and exploited in [Pub1] and [Pub2]. This section provides a broader context to [Pub1] and [Pub2]. After outlining the general problem statement and relevance of single SAR image approaches for volume parameter retrieval, the key contributions of [Pub1, Pub2] are presented. Additionally, an overview and discussion on potential extensions of the developed concepts and application scenarios in the frame of current and future SAR missions is provided.

3.1.1 Problem Statement and Relevance

The capability of extracting volumetric information of snow and ice covers from single SAR images is of high relevance for both missions relying on simple SAR imagery as well as SAR interferometric or even tomographic missions.

3.1.1.1 Relevance for Simple SAR Imagery

An important geophysical distinction of SAR image features in the assessment of ice sheets and glaciers is their characterization as surface or volume structures and furthermore, their exact position within the ice. As already outlined in Section 2.3.1, SAR imagery does not provide information on the vertical position of the imaged features within the volume, even if the surface topography is known, because the SAR acquisition can be understood as a projection of the 3-D backscatter distribution into a 2-D image (see also Figure 2.9). As introduced above, the elevation ambiguity may be resolved by applying SAR interferometric or tomographic techniques. However, their spaceborne implementation exhibits a significantly higher complexity than missions relying on simple SAR imagery, since multiple satellites in a single-pass

interferometry configuration, or precise repeat-passes are required. Especially when considering planetary missions, in particular to icy moons in the outer solar system (e.g., Enceladus), the implementation of interferometric techniques may fail due to exceeding cost, complexity, data volume, and accommodation of multiple sensors in terms of resources and operation requirements, as well as the limited accuracy in navigation and orbit determination. Also, the development trend in Earth Observation towards constellations of simple SAR satellites can profit from applications based on single SAR acquisitions.

3.1.1.2 Relevance for Interferometry and Tomography

SAR interferometry (InSAR) and tomography (TomoSAR) provide direct access to the vertical position of the scattering features within the glacial volume, or can even resolve them. However, even those sophisticated techniques are biased due to an unknown surface topography and/or inaccurate estimates of the permittivity.

In a scenario where no accurate information on the surface topography is available (likely a probable scenario over glaciers and ice sheets that experience elevation changes), InSAR in an across-track constellation only provides the elevation position of the backscatter phase center, but it does not give direct access to the depth of the phase center. This leads to the so-called penetration bias in InSAR surface elevation measurements of ice sheets and glaciers (see also Section 2.3.3.1). Common approaches for estimating the penetration bias, e.g., based on the InSAR coherence, are likely to fail over heterogeneous parts of ice sheets and over glaciers (see also the description in Section 2.3.3.1). The approaches developed in [Pub1, Pub2], based on single SAR images, can be used as complementary estimates, especially in heterogeneous parts of ice sheets and on glaciers.

Even in a scenario where the surface topography is known, or when considering TomoSAR that allows a direct imaging of the vertical position of the scattering features, the lack of accurate knowledge on the permittivity of the volume introduces significant biases in the InSAR height estimates and biases and distortions in the tomographic products. Figure 3.1 shows the height errors in InSAR and TomoSAR products, if not accounting for the permittivity in the processing. Two cases are shown: i) a snow and firn volume with a mean permittivity of 1.8, and ii) solid ice with a permittivity of 3.15. Significant errors are to be expected for representative depths of the backscatter phase center (or imaged features within the TomoSAR products). The single image approaches in [Pub1, Pub2] can be used to calibrate the estimate of the permittivity of the penetrated volume. Besides the relevance for providing calibrated InSAR and TomoSAR products, the permittivity is a direct measure of the density of the volume, which is an import glaciological parameter.

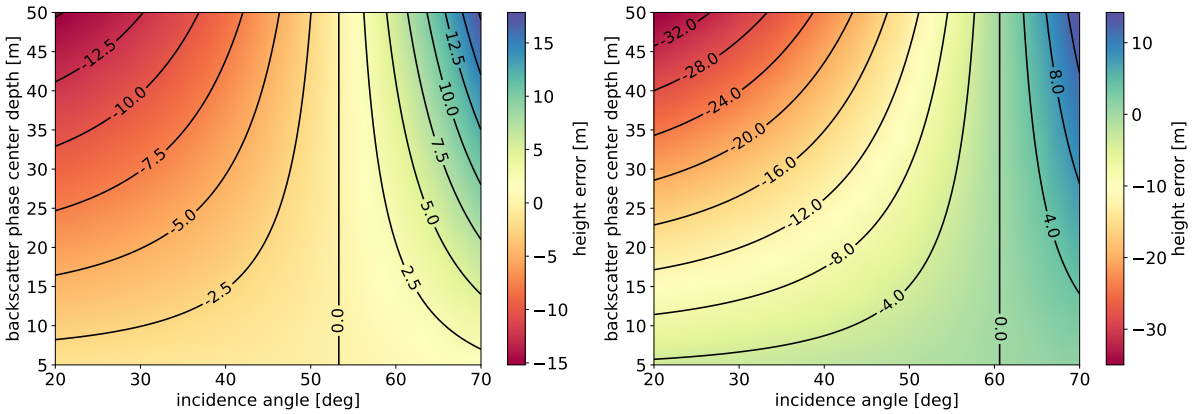

Figure 3.1: Interferometric or tomographic height estimation error, if not accounting for the permittivity of the glacial volume in the processing. Values for different backscatter phase center depths and incidence angles are shown for (left) a mean permittivity of 1.8 (corresponding to a snow and firn volume) and (right) a mean permittivity of 3.15 (corresponding to solid ice).

3.1.2 Key Contributions

The publications [Pub1] and [Pub2] describe for the first time the information contained in the SAR azimuth signals on the depth of the scattering structures within the snow, firn, and ice and on the permittivity of the penetrated volume. Furthermore, dedicated retrieval approaches are presented. In the following, the key contributions of [Pub1, Pub2] to the advancement of SAR techniques for snow and ice observation are listed:

- The effect of the radar signal penetration into snow, firn, and ice on the SAR azimuth signal and the SAR impulse response has been assessed and described for the first time.
- A phase error model has been developed that allows an inversion of the penetration depth into the volume (i.e., the depth of the dominantly scattering structures) and the permittivity of the penetrated volume.
- A SAR autofocus-based retrieval algorithm has been developed that allows the estimation of the penetration and permittivity on single SAR images over snow covers, glaciers, and ice sheets without the need of prominent scatterers within the scene. The autofocus is based on the shift measurement between two images generated from two disjoint portions of the sampled Doppler spectrum.
- The retrieval approach has been successfully tested on P-band airborne SAR images collected over the K-transect of the Greenland ice sheet and validated using SAR tomographic products of the same scene.
- It has been shown for the first time that the sensitivity of the SAR acquisition to the permittivity of the snow/ice volume can be exploited to obtain a vertical resolution effect

of targets and structures within ice sheets and glaciers, when using very-high resolution systems. This can be considered as a single-image tomography.

- The single-image tomography has been shown to be suitable as a volumetric imaging approach for an Enceladus mission scenario, because the special orbit geometries potentially allow for very-high-resolution acquisitions, allowing 3-D imaging of subsurface structures without the need for forming SAR tomographic acquisitions (requiring multiple satellites or precise repeat orbits).

3.1.3 Application Scenarios

The proposed approaches are expected to provide valuable information in current and future SAR missions. In [Pub1, Pub2], the assessments are limited to SAR systems with a high azimuth resolution that sample a broad angular range (in azimuth), providing sensitivity to the penetration into the glacial volume. Giving a clear statement on the required sensitivity (i.e., achievable accuracy) is complicated by the fact that the autofocus approach in [Pub1] is largely dependent on the contrast in the imaged scenes, a quantity that is difficult to model. Tests and simulations indicated that angular extents of the SAR surveys (in azimuth) of at least few degrees are necessary. Beyond high-resolution airborne sensors, a few spaceborne SAR systems implement spotlight modes, capable of scanning a wide angular extent. For example, Terra-SAR-X and TanDEM-X in staring spotlight mode can acquire with an azimuth resolution of $20\,\mathrm{cm}$ by electronically steering the antenna beam to acquire over 4.4° azimuth angle [120]. Especially in the New Space sector, a trend for very-high-resolution SAR systems has started, e.g., ICEYE offers so-called dwell modes capable of producing an azimuth resolution $< 10\,\mathrm{cm}$ by mechanically rolling the spacecraft to illuminate a target over up to 90° azimuth angle [121]. Such systems would be well suited for applying the proposed single-image approaches.

The intrinsic drawback of very-high-resolution systems is the limited swath width of only several kilometers at sub-metric azimuth resolution. The single-image approach in [Pub1] can be adapted to a system acquiring simultaneously two images with different squint angles and thereby sampling two disjoint portions of the Doppler band. Such scenario may be realized in two manners, i) by a single platform generating two antenna beams pointing with different squints, similar to the experimental bidirectional (BiDi) SAR imaging mode of TerraSAR-X [123], or ii) by two or more satellites flying in a constellation and acquiring simultaneously over the same scene with different squint angles. The two scenarios are illustrated in Figure 3.2. The latter case corresponds to the operational concept of ESA's 10th Earth Explorer Harmony [95], consisting of two receive-only companions to Sentinel-1, acquiring with $\approx \pm 25^\circ$ squint, depending on the range distance. Such systems can cover wide swaths since they only sample portions of the Doppler spectrum and would be well suited for applying the single-

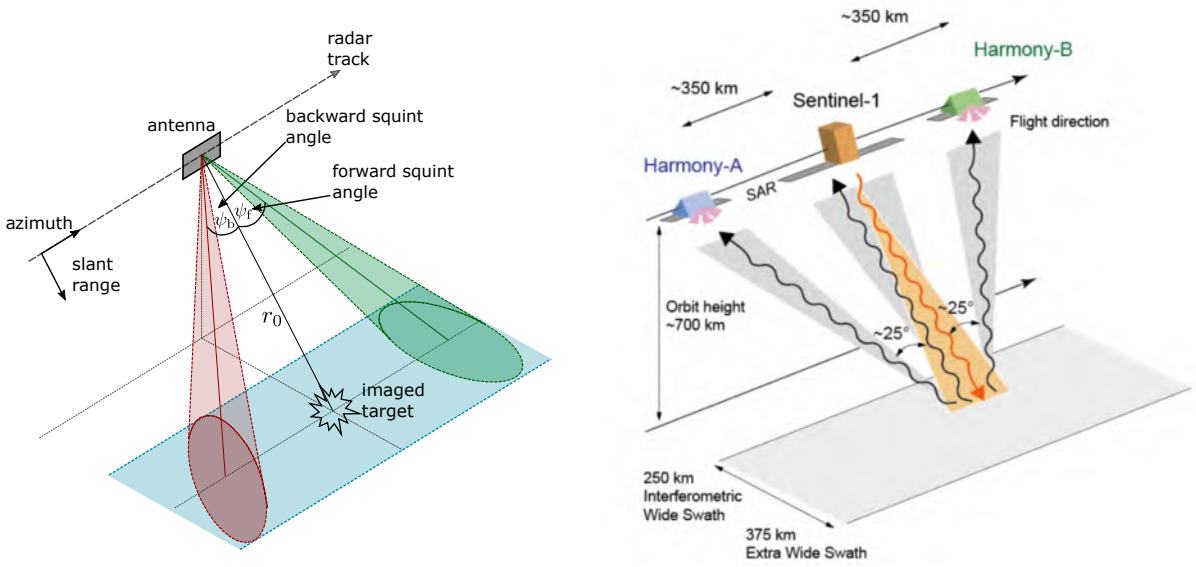

Figure 3.2: Concepts for implementing multiple simultaneous acquisitions with different squint angles, (left) using a single platform capable of generating two antenna beams looking forward and backward and (right), the case of the Harmony mission, implementing two receive-only companion satellites to Sentinel-1 acquiring the same scene with squint angles of roughly $25°$, $0°$, and $-25°$ (adapted from [122]).

image approaches by performing the measurement as in [Pub1] between the images acquired with different squints.

For the Harmony mission that is partly focused on performing single-pass InSAR elevation and elevation change measurements of land ice for mass balance estimates, the proposed approaches may provide information on the penetration into the snow, firn, and ice. This information can be used complementary to standard approaches based on the InSAR coherence to calibrate the penetration bias in the elevation measurement. An initial assessment for the Harmony case is provided in [124].

The applications described in Section 3.1.1 and in [Pub1, Pub2] are focused on estimating the penetration into ice sheets and glaciers (or estimating the depth of imaged features) and the permittivity of the penetrated volume. When considering dry snow covers, where radar signals in the P , L , or C bands are expected to penetrate the whole vertical extent of the snow cover, the single-image approach may be used to estimate the snow depth and, related to it, the snow water equivalent (SWE). The SWE is one of the key observables in Earth Observation. In contrast to differential InSAR approaches for SWE retrieval, the single-image approach is sensitive to the total SWE of the snow cover and not the SWE change. Figure 3.3 shows the simulation of a target located below a $2\,\mathrm{m}$ snow cover with a density of $0.2\,\mathrm{g\,cm^{-3}}$ that is imaged simultaneously with a squint of $20°$ (red) and $-20°$ (green), an acquisition scenario as illustrated in Figure 3.2 (left). Note the clear shift between the point target responses. The shift

can be measured and directly linked to the snow depth and the SWE. In a realistic scenario, the shift between image features has to be measured (based on the image contrast) with similar approaches as described in [Pub1]. The concept has been awarded a patent [125].

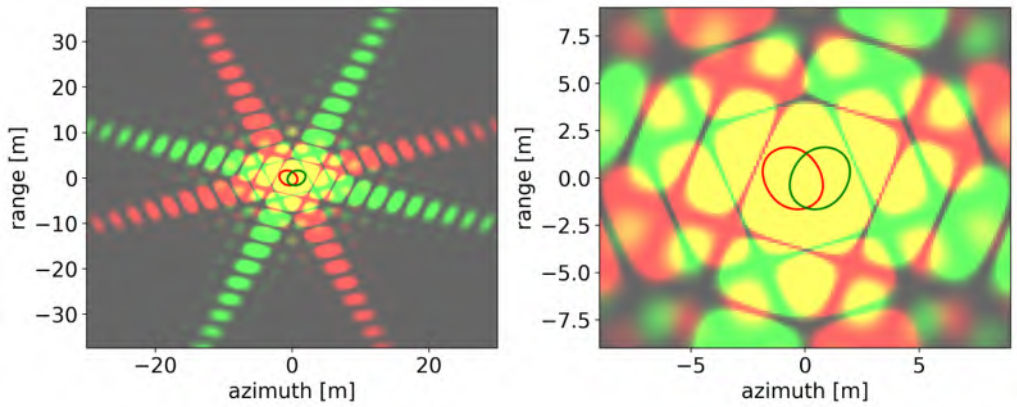

Figure 3.3: Simulation of a target located below a $2\,\mathrm{m}$ snow cover with a density of $0.2\,\mathrm{g\,cm^{-3}}$ that is imaged simultaneously with a squint of $20°$ (red) and $-20°$ (green), showing (left) a larger scene extent and (right) a small section around the target position. The solid contours indicate the $-3\,\mathrm{dB}$ power level.

3.2 Enabling Orbital Repeat-Pass InSAR and TomoSAR for Saturn's Moon Enceladus

Over the last decades, InSAR for deformation measurement and topographic mapping has revolutionized our understanding of many geophysical processes on Earth. For planetary bodies such as Enceladus, opportunities to measure geodetic state and change have been few. Geodesy at Enceladus has been limited to low-order shape parameters (e.g. spherical harmonics) based on Voyager and Cassini fly-by gravity measurements, or static topography and libration estimates from optical imagery [126]. In recent years, the relevance for measuring high-resolution surface deformation and topography at Enceladus using InSAR has been stated [47, 127] and concepts are beginning to be formulated, e.g., in [45, 128] and in [Pub3, Pub4]. Beyond InSAR, TomoSAR has been proven capable in many airborne experiments to provide valuable information on the subsurface structure and composition of glaciers and ice sheets and may be of high relevance for directly imaging the poorly understood subsurface characteristics of the Enceladus ice crust.

In [Pub3], it has been demonstrated for the first time that modern geodesy in form of repeat-pass SAR interferometry and tomography at Enceladus is expected to be feasible, despite the strongly perturbed orbit dynamic. Based on the findings in [Pub3], among other studies, a new mission concept is currently being developed at the Jet Propulsion Laboratory (JPL) of NASA.

The concept aims at using (besides other modalities) repeat-pass InSAR for deformation and topography mapping to understand Enceladus' past and present structural, dynamical, and kinematical properties and constrain its state of habitability. In [Pub4], an initial assessment on performance and processing approaches for the proposed mission concept has been conducted.

This section provides a broader context to [Pub3] and [Pub4]. First, the general problem statement for InSAR and TomoSAR at Enceladus is discussed. After outlining the key contributions of [Pub3] and [Pub4], an outlook is presented.

3.2.1 Problem Statement

Implementing InSAR and TomoSAR in a repeat-pass manner at Enceladus is favorable compared to a single-pass approach because of the tight restrictions in terms of mass and allocated space, intrinsic to planetary missions. Compared to Earth, Enceladus has several distinctive characteristics that favor the use of repeat-pass InSAR and TomoSAR. These include an almost-absent atmosphere, negligible temporal decorrelation effects in most areas, high backscatter (above 0 dB were measured in Ku- and S-band), and short orbital repeat cycles of approximately 30 hours.

The strongly perturbed orbit dynamic at Enceladus has been identified as the main limiting factor for repeat-pass InSAR at Enceladus [47]. The key orbit requirements can be summarized as:

- **Baseline Requirement:** The reference and repeat orbit trajectory, viewed in an Enceladus co-rotating coordinate system (i.e., body-fixed frame), must be almost parallel and the baseline between the orbital tracks, projected on a line perpendicular to the radar line-of-sight, must be significantly less than the critical baseline to avoid a complete decorrelation of the acquisitions (see Section 2.1.2.3). The critical baseline is a function of the wavelength, signal bandwidth, distance to the scene and incidence angle on the scene, with higher values of these quantities resulting in longer critical baselines. For typical Enceladus orbit heights of $100\,\mathrm{km}$ to $300\,\mathrm{km}$, the critical baseline takes values between tens of meters (Ka-band frequencies) and few kilometers (P-band frequencies).

- **Inclination Requirement:** To provide coverage of the prominent south polar region at Enceladus (see Section 1.1) with incidence angles suitable for InSAR and TomoSAR (i.e., 25° to 60°), the orbit is required to have sufficient inclination. For typical Enceladus orbit heights, inclinations toward 60° are required.

- **Stability Requirement:** The orbit is required to exhibit a natural stability to minimize the necessary propellant and complexity for orbit maintenance. The stability requirement for InSAR and TomoSAR is much more stringent than commonly adapted in orbit design

around small bodies. The orbit needs to be stable within an imaginary tube around a reference trajectory, where the size of the tube is related to the critical baseline.

For the TomoSAR case, the baseline requirement translates into a sampling requirement, where the maximum baseline is constrained by the necessity of a sufficiently dense sampling of the synthetic antenna aperture in elevation to avoid ambiguities.

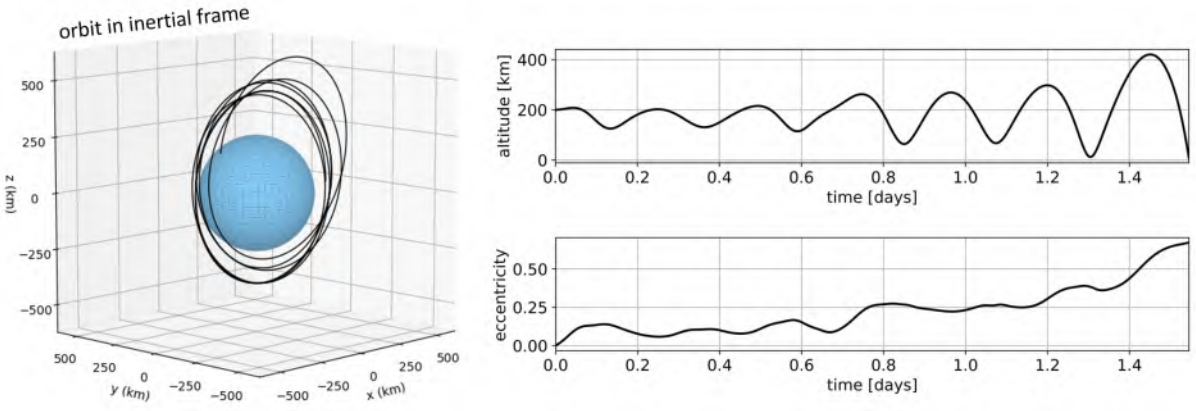

Figure 3.4: Example of an Enceladus orbit propagated from initial conditions corresponding to a $200\,\mathrm{km}$ altitude circular Kepler orbit with an inclination of $90°$. The orbiter impacts the Enceladus surface after approximately 1.5 days.

Even if considered standard in Earth Observation, harmonizing these requirements for an Enceladus orbiter is challenging, due to the strong third-body perturbation of Saturn, resulting from the small mass of Enceladus and its proximity to Saturn. The third-body perturbation leads to extreme instabilities for high-inclined orbits, with life times (the orbiter impacts into Enceladus) of polar orbits of few days. Figure 3.4 shows an example of an Enceladus orbit propagated from initial conditions corresponding to a $200\,\mathrm{km}$ altitude circular Kepler orbit with an inclination of $90°$. The propagation is performed including perturbations by Saturn, the 5 closest Saturnian moons, Jupiter, and the non-spherical gravity contribution from Enceladus and Saturn. The orbit gets continuously more eccentric, until it impacts the Enceladus surface after 1.5 days. The orbit design goal for an InSAR or TomoSAR application at Enceladus is to find orbits with maximized inclination that provide the desired repeat-pass stability. Orbit solutions with maximized inclination (up to $60°$) that have been proposed in the literature have been found to not provide the desired repeat-pass characteristic and stability when analyzing them in a realistic n-body ephemeris propagation.

3.2.2 Key Contributions

The publication [Pub3] shows for the first time that suitable orbits for repeat-pass InSAR and TomoSAR at Enceladus can be found, contradicting the general assumption of previous years.

Feasibility assessments are provided in [Pub3] and an analysis for a mission concept in development at JPL is shown in [Pub4]. In the following, the key contributions of [Pub3, Pub4] to the advancement of SAR techniques for the exploration of icy moons are summarized:

- The orbital requirements for InSAR and TomoSAR at Enceladus have been derived.
- A search approach for periodic orbits (i.e., repeat-pass orbits) in a high fidelity ephemeris model has been developed and successfully applied to the Enceladus case.
- A family of high-inclined (up to $61°$) orbits with a natural stability of years has been identified. These orbits fulfill the above-mentioned requirements for InSAR and TomoSAR in terms of small baselines, maximized inclination, and long-term stability.
- The robustness of the designed orbits against various perturbations and uncertainties (in terms of gravity field knowledge and navigation) has been shown.
- The suitability of the designed orbits for repeat-pass InSAR and TomoSAR in terms of repeat periods and baseline availability has been demonstrated. In addition to SAR applications, the long-term stability and high inclination of the orbits promotes them as general science orbits and as a communication relay for a potential lander mission.
- In [Pub4], the performance of a dedicated InSAR mission scenario (in development at JPL) that is based on the designed orbits has been assessed and processing approaches have been validated, indicating the general feasibility of the mission concept.

3.2.3 Outlook

The assessments in [Pub3, Pub4] provide the first step toward enabling modern remote sensing in form of repeat-pass InSAR and TomoSAR for the exploration of Enceladus. Among the icy moons of Saturn and Jupiter, Enceladus is expected to exert the most challenging orbit dynamic, due to the small ratio of the gravitational force by the moon and by the central planet. Hence, it is to be expected that repeat-pass concepts are realizable also at other icy moons, or in general at natural satellites of planets with a comparable gravity ratio.

Beyond the challenges imposed by the orbit dynamic and navigation accuracy, also the sheer distance to Earth leads to a significantly increased system an mission complexity for realizing an InSAR mission. The distance (between 9 and 11 astronomical units) drastically reduces the down-link capacity. This requires to perform the SAR and InSAR processing on board the spacecraft down to a multi-looked interferogram level to reduce the data volume. The large distance to the Sun significantly complicates the power generation, with $1\,\%$ of the solar flux arriving at Enceladus compared to Earth. This either requires large solar arrays (toward

$100\,\mathrm{m}^2$), or the use of radioisotope thermoelectric generators (RTG), as used, e.g., for the Cassini mission.

One particular aspect that has to be studied in detail in the future is the very particular backscatter characteristic of Enceladus (see Section 2.3.5). The high backscatter values beyond $0\,\mathrm{dB}$, reported based on measurements by Cassini (in the Ku band) [114, 115] and Earth-based measurements with the Arecibo radar telescope (in the S band) [129], suggest a highly efficient multiple scattering from the subsurface volume across large portions of the microwave spectrum. The high backscatter is helpful for reducing the required power-aperture product of the radar to achieve a particular SNR and to allow large incidence angles. However, the hint toward efficient volume scattering may imply a significant InSAR performance impact by volume decorrelation (see Section 2.1.2). Volume decorrelation increases with an increasing depth of the volume that contributes to the backscatter. The degree to which the backscatter at Enceladus is concentrated near the surface or spread deeply through the depths of the ice crust is not known. Models suggest that it could be either [117]. The Cassini SAR images of Enceladus (see right panel of Figure 1.3) show clear layover and shadow features typical of scattering from sloped surfaces due to the side-looking geometry of a SAR. Based on this, one may argue that the dominant scattering cannot be too defuse within the volume. SAR imagery from Earth of ice sheets that allow deep radar penetration (e.g., the dry snow zone in Greenland) exhibit a diffuse, unfocused appearance. Further modeling efforts and experiments for constraining the structural properties of the Enceladus ice crust and its effect on the backscatter and volume decorrelation are fundamental for converging toward a specific InSAR system and operational concept.

Beyond InSAR and TomoSAR, the single-image approaches proposed in [Pub1, Pub2] (see Section 3.1) are expected to provide valuable information for a SAR mission at Enceladus. Especially in cases where the baselines are too large for performing robust InSAR or TomoSAR, the single-image approaches are still capable of providing information on the depth of the imaged features, or even a vertical resolving capability. Additionally, the potential for calibrating the penetration and permittivity for InSAR and TomoSAR products is of high relevance for providing reliable tomographic imagery as well as unbiased estimates of deformation processes and topography.

3.3 Compensation of Propagation Effects for InSAR Elevation Measurements of Ice Sheets and Glaciers

Digital elevation models (DEMs) produced using single-pass InSAR in an across-track configuration are essential for mapping surface elevation and monitoring topographic changes of

ice sheets and glaciers. The considerable penetration of radar signals into snow, firn, and ice at commonly used frequency bands (e.g., P to X band) leads to an elevation bias of the backscatter phase center relative to the actual surface. This phenomenon, often referred to as penetration bias in the literature, means that the DEM generated from InSAR data does not accurately represent the surface but is instead biased downward. Several model-based inversion strategies have been developed to estimate the penetration bias from the interferometric coherence, the backscatter, or both. Additionally, the single-image approach in [Pub1] can potentially be used for estimating the penetration when using high-resolution systems or systems acquiring with multiple squints.

In [Pub5], it is shown that beyond the above-mentioned penetration bias, significant additional vertical and horizontal offsets occur in conventionally processed InSAR DEMs over ice and snow due to uncompensated propagation effects within the volume that are commonly not considered. Adapted processing approaches, capable of correctly accommodating the penetration bias are proposed in [Pub5]. This section summarizes the problem statement and key findings of [Pub5] and gives an outlook toward a robust correction of the penetration bias in InSAR elevation products.

3.3.1 Problem Statement

Across-track InSAR is sensitive to the elevation position of the backscatter phase center within the glacial volume. However, there is a systematic bias between the physical phase center position and the position retrieved with conventionally processed InSAR data that has so far been neglected in InSAR-based elevation measurements over ice sheets and glaciers. Figure 3.5 illustrates the scenario. The systematic bias stems from the higher permittivity of the glacial volume compared to the one of air, resulting in first consequence in a reduced signal propagation velocity and refraction at the surface interface and in second consequence in range delays and a stretch of the interferometric vertical wave number. This leads to vertical and horizontal geolocation errors, beyond the well-known penetration bias, in the InSAR DEM generation. In Figure 3.5, the penetration bias is symbolized by Δh and the bias from the uncompensated propagation effects by Δh_2.

If solely correcting the penetration bias, Δh, (e.g., estimated via coherence-based approaches [31, 32], or the single-image approach [Pub1]) for retrieving the surface elevation, residual geolocation errors from the propagation effects are to be expected. For accurate elevation measurements, the penetration bias has to be accounted for in the InSAR processing to calibrate the interferometric phase and the range distance.

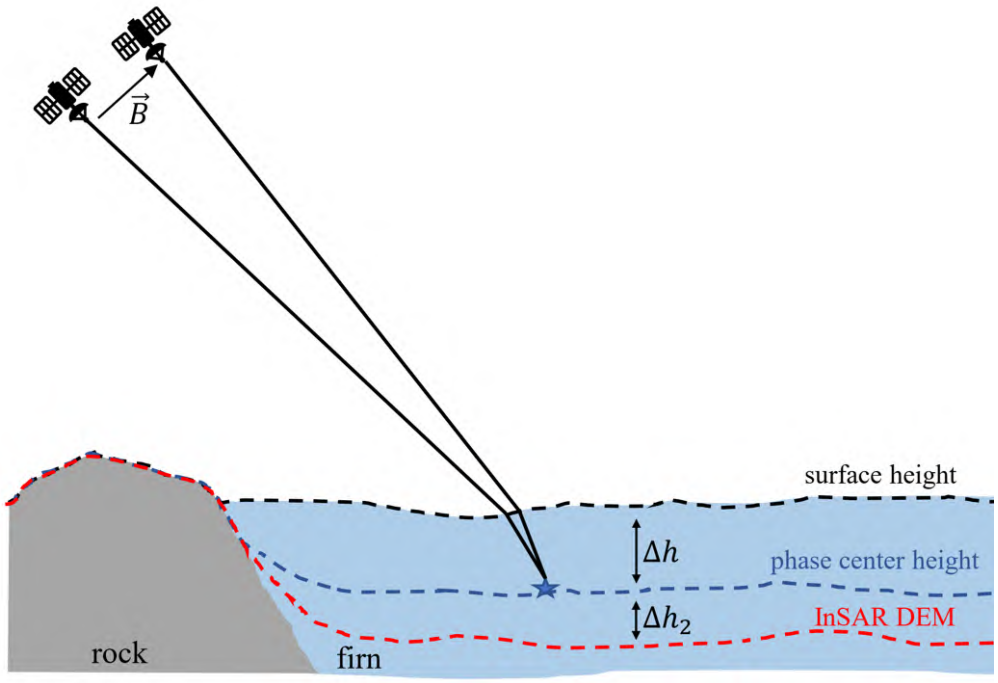

Figure 3.5: Schematic of the InSAR elevation retrieval problem statement, illustrating the systematic difference between the physical phase center height (connected to the well-known penetration bias, Δh) and the elevation of the DEM retrieved with conventionally processed InSAR. The nomenclature, Δh and Δh_2, corresponds to the one in [Pub5].

3.3.2 Key Contributions

The publication [Pub5] provides adapted InSAR processing approaches to accommodate the propagation into the glacial volume to correctly retrieve the surface elevation or phase center elevation. The key contributions are listed below:

- The impact of propagation effects on InSAR DEMs over ice sheets and glaciers has been assessed and quantified, showing considerable geolocation errors of meters to few tens of meters beyond the well-known penetration bias.

- Multiple adapted processing approaches have been proposed, capable of accommodating the propagation effects in terms of range and phase offsets with sufficient accuracy. The developed approaches are simple to integrate in existing InSAR processors.

- The developed approaches have been validated on simulated InSAR acquisitions of the upcoming Harmony mission by ESA using the Harmony End-To-End Performance Simulator (HEEPS), showing good performance compared to the state-of-the-art penetration bias correction.

3.3.3 Outlook

The publication [Pub5] describes how to accurately accommodate the signal penetration in the InSAR processing, providing an important step toward a robust penetration bias calibration in InSAR elevation products. Still, the accurate estimation of the penetration bias (i.e., the depth of the backscatter phase center) based on the InSAR data faces limitations. Especially in heterogeneous parts of glaciers and ice sheets, where coherence-based approaches [31, 32] tend to be systematically biased because the backscatter distribution model assumptions do not replicate the reality.

In such cases, the single-image approaches in [Pub1] are expected to perform rather well, since they rely on the contrast of the imaged scenery. For ESA's Harmony mission, that is partly focused on providing InSAR elevation products over land ice, the single-image approaches can potentially exploit the large squint diversity (beyond $20°$) between the Harmony satellites and Sentinel-1. The Harmony satellites are flying in an across-track formation $350\,\mathrm{km}$ behind Sentinel-1. A first assessment for the Harmony case is provided in [124].

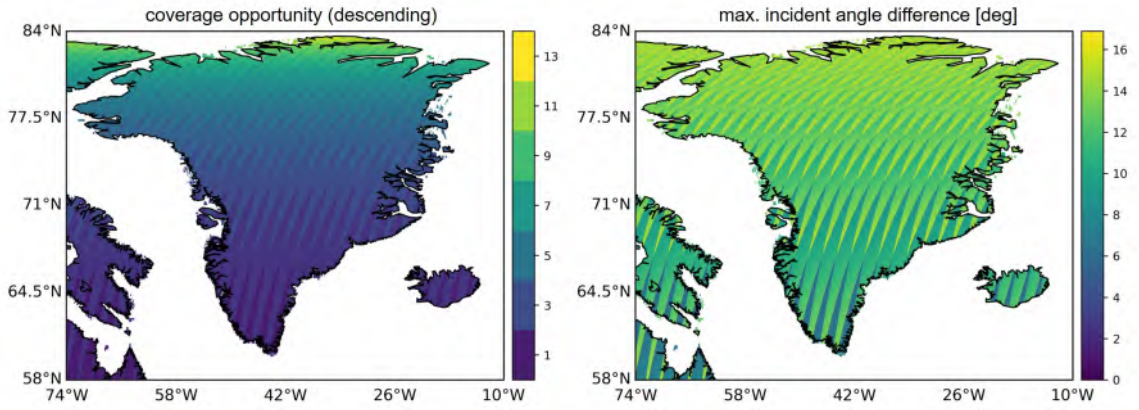

Figure 3.6: Coverage opportunity of Sentinel-1 (corresponds to the Harmony mission) over Greenland, showing (left) the number of coverage opportunities from different orbit passes within the 12-day repeat cycle and (right) the maximum incident angle difference. Only descending passes are shown.

Beyond, the assessments in [Pub5] indicate that there is a significant incident angle dependence of the geolocation error (see the Figures 4 and 5 in [Pub5]) that can be exploited for estimating the penetration bias. This would require two InSAR acquisitions of the same scene with different incident angles that are closely spaced in time to assure that no relevant changes of the ice sheet or glacier occurred. Especially at higher latitudes, such acquisitions could be generated from different orbit passes. As an example, Figure 3.6 (left panel) shows the Sentinel-1 coverage opportunity over Greenland within the 12-day repeat period (the Harmony satellites acquire the same swath as Sentinel-1), where values greater than 1 indicate the access from different orbits, i.e., with different incident angles. The nominal swath of Sentinel-1 in interferometric wide-swath (IW) mode and descending orbits are assumed. The

maximum incident angle difference for the specific points on ground is illustrated in the right panel, showing the potential of acquiring the same scene with significantly different viewing geometries. A dedicated assessment of such concept is suggest for future research.

3.4 Exploitation of Propagation Effects for Differential InSAR Observations of Snow

The potential of differential InSAR (D-InSAR) for dry snow parameter retrieval, especially the snow water equivalent (SWE), has been first identified by *Guneriussen et al.* [96]. D-InSAR potentially provides SWE change measurements at millimeter accuracy, high spatial resolution, and wide coverage. The concept directly exploits the signal delay caused by the snow cover and relies on the transparency of dry snow at microwave frequencies and a strong sensitivity of the D-InSAR phase to a change in snow height or snow density between the repeat acquisitions of a D-InSAR pair. The D-InSAR snow parameter retrieval is usually complicated or even hindered by low temporal coherence and ambiguous measurements caused by the 2π ambiguity of the interferometric phase. Several explanations for the decorrelation effect over snow covered scenes have been already proposed as well as approaches for recovering the absolute SWE change in scenarios where the snow accumulation results in a 2π phase ambiguity.

The publications [Pub6] and [Pub7] provide further steps toward a robust D-InSAR-based snow parameter estimation. In [Pub6], an explanation for the temporal decorrelation effect of dry snow covers is presented, relating slight changes of the snow density to the decorrelation of the SAR signals. [Pub7] proposes novel D-InSAR techniques for unambiguous SWE change measurements and a direct estimation of the snow density by exploiting simultaneous D-InSAR acquisitions with different squint angles.

3.4.1 Problem Statement

D-InSAR SWE monitoring is so far not used operationally due to several limiting factors, the two main ones being:

- **Low temporal coherence areas:** Snow covered areas show strong temporal decorrelation effects. The low coherence reduces the accuracy of the phase measurement and can significantly complicate the phase-unwrapping process, which is essential for assessing spatial snow height dynamics in typical snow packs. The decorrelation can reach a point where no robust SWE retrieval is possible.

- 2π **phase ambiguity:** To estimate the absolute phase, a reference point with known SWE change is required within the scene. This is because the D-InSAR phase may have

an unknown offset if the phase delay caused by the propagation through snow exceeds 2π.

3.4.1.1 Dry Snow Decorrelation Effect

Temporal decorrelation is the main limiting factor in D-InSAR SWE retrieval. The common explanation of the decorrelation effect is a change in the underlying scattering center distribution due to melting/refreezing, snow accumulation, or redistribution of underlying vegetation. In scenarios with wet snow or snow that has undergone melt and refreeze cycles, a change in scatterer distribution is likely to be the dominant decorrelation source. In dry snow conditions and at sufficiently low frequencies (e.g., in the C or L band), the backscatter contribution from the snow volume can be expected to be much less than the backscatter from the underlying ground (e.g., rock, soil, ice, vegetation). Hence, the explanation of decorrelation due to changes in scatterer distribution seems counter-intuitive, because: i) no melting and refreezing is to be expected, ii) dry snow accumulation should not significantly affect the backscatter, and iii) the ground scatterer distribution (e.g., vegetation) should remain relatively stable compared to the snow-free case. Still, strong decorrelation is commonly observed in snow-covered areas at low temperatures. An interpretation of the decorrelation effect of a dry snow cover is given in [97], describing that the decorrelation may result from a change in the sub-pixel scale snow height distribution. Significant sub-pixel snow height changes are, however, only expected from strong wind-induced snow drifts.

A novel explanation of the dry snow decorrelation effect is provided in [Pub6], relating decorrelation to a slight change of the bulk snow density (i.e., the permittivity), caused by a change of the wavenumber in the snow volume (see Section 2.2.2). The density change may result from a settling of the snow, metamorphism, and wind effects. The publication [Pub6] has been awarded the first prize of the Student Paper Competition of the IEEE International Geoscience and Remote Sensing Symposium 2023 Conference held in Pasadena, CA, USA.

3.4.1.2 Phase Ambiguity

An unknown bulk offset in the D-InSAR SWE change measurement occurs, if the snow height change leads to a D-InSAR phase beyond 2π. This is especially critical at C band or higher frequencies, where already snow height changes of several centimeters result in phase shifts beyond 2π. At lower frequencies this effect is less critical, but still problematic for moderate to high snow accumulation scenarios, e.g., in mountainous areas. The bulk offset does not allow an unambiguous SWE change measurement. Several approaches for recovering the phase ambiguity have been suggested, exploiting the sensitivity of the D-InSAR snow measurement to the frequency (delta-k approaches) [98], the topography [130], or the polarization [131].

Novel approaches for the unambiguous and robust D-InSAR SWE change measurement are presented in [Pub7]. The approaches are based on the differential sensitivity of simultaneous D-InSAR acquisitions with different squint angles. The line-of-sight diversity between two or more interferograms acquired using different squint angles creates a systematic phase difference caused by the propagation through snow. This phase difference can be exploited to directly achieve an unbiased SWE change estimate, bypassing the need for spatial phase unwrapping and a reference point within the scene. Beyond, the differential sensitivity can be used as a direct measure of the snow permittivity (i.e., the snow density), which is an important parameter for the D-InSAR SWE retrieval, but also for other sensor concepts and many snow modeling approaches. Comparable to the single-image approaches described in Section 3.1, future systems like Harmony, or very-high-resolution systems, will operate in suitable configurations, providing a considerable squint diversity (e.g., beyond 20° for the Harmony case).

3.4.2 Key Contributions

The key contributions of [Pub6] and [Pub7] toward are robust D-InSAR snow parameter retrieval are summarized below:

- A novel explanation of the dry snow decorrelation effect on D-InSAR acquisitions has been provided, linking a snow density change to a decorrelation of the SAR signals. A decorrelation model has been established and a data-based analysis has been conducted, showing evidence of the dry snow decorrelation effect.

- The influence of SWE changes on a squinted D-InSAR acquisition has been modeled and the sensitivity of the phase difference between multiple D-InSAR acquisitions with different squints has been assessed.

- Two novel multiple-squint D-InSAR SWE retrieval approaches have been developed, capable of recovering potential phase offsets or even allowing SWE change measurements without spatial phase unwrapping (at the cost of spatial resolution).

- Additionally, a novel multiple-squint D-InSAR approach for a direct measurement of the snow permittivity (i.e., the snow density) has been proposed.

- The accuracy of the approaches has been modeled and the algorithms have been verified on simulated data of ESA's Harmony mission, showing a convincing sensitivity, given the large squint diversity of the Harmony constellation.

3.4.3 Application Scenarios

Future missions like Harmony or the Co-Fliers concepts of NASA JPL [132] with companion satellites to the upcoming ROSE-L mission of ESA will operate in suitable configurations, providing a large squint angle diversity. Hence, the proposed approaches can be applied in such missions without further adaption of the system and operational concepts. Among current sensors, very-high-resolution spaceborne SAR systems from the commercial sector could be used to synthesize multiple acquisitions with large squint angle differences (see the discussion in Section 3.1), at the penalty of a small swath width. Testing the developed approaches on very-high-resolution SAR systems is suggested for future studies to further validate the concept.

The proposed concepts can be extended to systems that acquire D-InSAR data simultaneously with significant incident angle differences beyond a few degree. Note that in the case of across-track interferometers like TanDEM-X, which have baselines of a few hundred meters, the differential sensitivity to snow parameters is expected to be negligible. However, if the two D-InSAR acquisitions are generated from different orbits, resulting in significantly different incident angles, the acquisitions could be utilized for the proposed approaches, provided they are obtained simultaneously or quasi-simultaneously. This can be achieved through the use of a constellation of satellites deployed in different orbits or by different orbit passes of a single satellite (see the discussion in 3.3 along with Figure 3.6). However, using different orbit passes of a single satellite does not allow for a simultaneous acquisition. The simultaneous acquisition of data is crucial for two main reasons: i) acquiring data at the same time ensures that the snow conditions are almost identical for both D-InSAR acquisitions, which is essential for the snow parameter retrieval using multiple incident angles (i.e., multiple squint angles) and ii) simultaneous data acquisition helps to minimize the impact of atmospheric effects, since they are partially correlated among the different acquisition geometries. Still, investigating the potential of different orbit passes is suggested for future studies.

The relation between a density change of the snow cover and the decorrelation of the SAR signals of a D-InSAR pair, described in [Pub6], may be further extended toward a snow density retrieval approach. Such retrieval is expected to be complicated by the necessity of separating the dry snow decorrelation from other decorrelation sources as well as estimating the backscatter distribution of the underlying ground, which influences the decorrelation. Dedicated campaigns with accompanying ground measurements of snow density and ground surface roughness are necessary to further consolidate the concept.

4 Conclusion

The work conducted in the frame of this thesis was aimed at advancing the state-of-the-art of SAR for the observation and exploration of terrestrial and planetary snow and ice. The developments are mainly focused on future SAR mission scenarios that provide novel observation capabilities. In the context of Earth Observation, the investigations were targeted at sensors that operate at low frequencies (e.g., upcoming L- and P-band missions), provide very high resolution, and/or measure simultaneously in multiple acquisition geometries (e.g., multiple squints). In the context of planetary exploration, the developments were aimed at novel SAR remote sensing techniques for the exploration of icy moons, addressing the recent commitment of the space agencies to future missions to icy moons, in particular, Saturn's moon Enceladus.

Two pathways were followed. First, providing a description of signal propagation effects in snow and ice on SAR measurements, alongside with dedicated approaches to exploit or compensate those effects in the frame of snow and ice applications based on simple SAR imagery, SAR interferometry (InSAR), as well as SAR tomography (TomoSAR). Second, developing strategies to enable modern radar remote sensing techniques in the form of InSAR and TomoSAR for future missions to Enceladus.

In the following, the four research objectives, stated in Section 1.2, are reiterated and the main contributions of the publications of this cumulative thesis are summarized. A more detailed description of the problem statements, contributions, as well as application scenarios and future work is provided in Chapter 3, individually for the four research objectives.

RO_1 *Modeling and exploiting SAR propagation effects in snow and ice for volumetric information retrieval from single SAR acquisitions.*

The effect of the radar signal penetration into snow, firn, and ice on the SAR signal and the impulse response has been assessed and described for the first time, showing residual phase signatures along the azimuth signal that lead to shifts and defocusing of the imaged scene features. Based on the described propagation effects, an inversion model and a SAR autofocus-based retrieval algorithm have been developed that allow the estimation of the signal penetration in snow covers, glaciers, and ice sheets, as well as the permittivity of the penetrated volume. The approaches rely on the information in single SAR images, without the need for polarimetric, interferometric, or tomographic information. The autofocus approach is based on the shift measurement between two images

generated from different portions of the sampled Doppler spectrum and can be applied on high-resolution systems and systems that acquire multiple SAR images with different squint angles (e.g., ESA's Harmony mission). Beyond, it has been shown for the first time that the sensitivity of the SAR acquisition to the permittivity of the snow/ice volume can be exploited to obtain a vertical resolution effect of targets and structures within ice sheets and glaciers, when using very-high-resolution systems. This can be considered as a single-image tomography. The developed single-image approaches can be used to provide volumetric information of ice sheets, glaciers, and snow covers (e.g., depth of scattering structures, permittivity/density, SWE) based on single SAR images as well as to calibrate interferometric and tomographic products.

RO_2 *Enabling orbital repeat-pass SAR interferometric and tomographic imaging of Enceladus: feasibility and potential.*

The orbital requirements for repeat-pass InSAR and TomoSAR at Enceladus have been derived and the strongly perturbed orbit dynamic at Enceladus has been identified as the main limiting factor for repeat-pass InSAR at Enceladus. Insufficient stability and repeat characteristic of existing solutions of high-inclined orbits around Enceladus have been demonstrated. Based on the orbit requirements, a search approach for repeat-pass orbits has been developed and a family of high-inclined orbits with a natural stability of years has been identified. These orbits fulfill the requirements for InSAR and TomoSAR in terms of small repeat-pass baselines, maximized inclination, and long-term stability. The robustness of the designed orbits against various perturbations and uncertainties (in terms of gravity field knowledge and navigation) has been demonstrated. Beyond, the suitability of the designed orbits for repeat-pass InSAR and TomoSAR has been demonstrated and the performance of a dedicated InSAR mission scenario for Enceladus (in development at JPL) that is based on the designed orbits has been assessed, indicating the general feasibility of the mission concept.

RO_3 *Compensating and exploiting propagation effects for accurate single-pass InSAR elevation measurements of ice sheets and glaciers.*

The penetration of the SAR signals into snow and ice has been identified and addressed in many research works as the main limiting factor in robust InSAR elevation and elevation change measurements over ice sheets and glaciers. In the frame of this thesis, the additional impact of commonly neglected propagation effects on InSAR elevation products over ice sheets and glaciers has been assessed and quantified, showing considerable geolocation errors of meters to few tens of meters beyond the well-known penetration bias. Multiple adapted processing approaches have been proposed, capable of accommodating the propagation effects in terms of range and phase offsets with suf-

ficient accuracy. The developed approaches are simple to integrate in existing InSAR processors and have been validated on simulated InSAR acquisitions of the upcoming Harmony mission by ESA, showing good performance compared to the state-of-the-art penetration bias correction. Together with the single-image techniques in [Pub1, Pub2] and established coherence-based penetration bias estimators, the developed processing approaches provide an important step toward a robust penetration bias calibration in InSAR elevation products.

RO_4 *Modeling and exploiting propagation effects in differential InSAR for snow parameter retrieval.*

Snow parameter retrieval using D-InSAR directly exploits the signal delay introduced by the propagation through the snow cover. A robust retrieval is often hindered by a low temporal coherence and the 2π phase ambiguity of the interferometric measurement. A novel explanation for the dry snow decorrelation effect in D-InSAR acquisitions has been provided, linking a snow density change to a decorrelation of the SAR signals that is caused by a change of the wavenumber within the snow volume. A decorrelation model has been established and a data-based analysis has been conducted, showing evidence of the dry snow decorrelation effect and hinting toward a novel snow density retrieval approach. Beyond, the influence of a SWE change on a squinted D-InSAR acquisition has been modeled and novel multiple-squint D-InSAR SWE retrieval approaches have been developed, capable of recovering potential phase offsets or even allowing SWE change measurement without spatial phase unwrapping. Additionally, a novel multiple-squint D-InSAR approach for a direct measurement of the snow permittivity (i.e., the snow density) has been developed. The upcoming Harmony mission is a suitable candidate to implement the developed concepts, given the large squint diversity among the Harmony constellation.

The simultaneous developments in the frame of Earth Observation and icy moon mission scenarios showed great synergies. On the one hand, the stringent boundary conditions of an Enceladus mission scenario (e.g., low instrument complexity and limited navigation capability) inspired novel SAR techniques like the single-image approaches described in [Pub1,Pub2] that have a high relevance also in the context of Earth Observation for the calibration of interferometric and tomographic products, or potentially the estimation of the snow water equivalent (SWE). On the other hand, by enabling the imaging of icy moons with SAR techniques like InSAR and TomoSAR that are considered standard in Earth Observation but rather exotic among the planetary community, the way how we explore icy moons can be fundamentally changed.

List of Symbols and Acronyms

Symbols

Symbol	Unit	Description
A		image pixel amplitude
B	Hz	chirp bandwidth
B_{D}	Hz	Doppler bandwidth
$B_{\perp}$	m	perpendicular baseline
c	$\mathrm{m/s}$	propagation velocity
c_0	$\mathrm{m/s}$	speed of light in free space
$\vec{E}$	$\mathrm{V/m}$	electrical field
f	Hz	frequency
f_{D}	Hz	Doppler frequency
f_{DC}	Hz	Doppler centroid frequency
f_{R}	$1/\mathrm{s}^2$	Doppler rate
HoA	m	height of ambiguity
j		imaginary unit
$\vec{k}$		complex propagation vector
$\hat{k}$		unit vector describing the direction of propagation
k_0	$\mathrm{rad/m}$	wave number in free-space
k_{c}		propagation constant
k_{r}	$1/\mathrm{s}^2$	chirp rate
L_{a}	m	antenna size in azimuth
L_{e}	m	antenna size in elevation
L_{s}	m	synthetic aperture length
n		refractive index
$\vec{n}$		normal vector
$n(t)$		noise signal
PRF	Hz	pulse repetition frequency
r	m	distance
$\vec{r}$	m	position vector

r_0	m	minimal distance in range history
t	s	range time
t_a	s	azimuth time
T	s	travel time
T_int	s	integration time
v	$\mathrm{m/s}$	effective velocity of the platform
$w(t_\mathrm{a})$		antenna pattern amplitude modulation in azimuth direction
α	$1/\mathrm{m}$	attenuation constant
β	$1/\mathrm{m}$	phase constant
γ		complex coherence
δr	m	range resolution
δr_g	m	ground range resolution
δx	m	azimuth resolution
Δ		difference operator
Δk_z	$\mathrm{rad/m}$	vertical interferometric wave number
Δr	m	differential range distance
$\Delta\varphi$	rad	interferometric phase
ε_c		complex permittivity
ε	$\mathrm{F/m}$	permittivity
ε_0	$\mathrm{F/m}$	permittivity in free space
ε_r'		real part of the relative permittivity
ε_r''		imaginary part of the relative permittivity
λ	m	wavelength
μ	$\mathrm{H/m}$	permeability
μ_0	$\mathrm{H/m}$	permeability in free space
μ_r		relative permeability
ρ	$\mathrm{kg/m^3}$	density
σ	$\Omega\,\mathrm{m}$	conductivity
τ	s	travel time
τ_0	s	travel time corresponding to r_0
τ_p	s	pulse duration
θ_i	rad	incidence angle
θ_l	rad	look angle
θ_r	rad	refraction angle
φ_r	rad	phase information corresponding to the target range
φ_scatter	rad	random phase component from the scattering process
ψ	rad	squint angle

ω	$\mathrm{rad/s}$	angular frequency
ω_c	$\mathrm{rad/s}$	angular frequency of carrier
∇		nabla operator

Acronyms and Abbreviations

AWGN	Additive White Gaussian Noise
ALOS	Advanced Land Observing Satellite
DLR	German Aerospace Center
D-InSAR	Differential SAR Interferometry
EO	Earth Observation
HF	High Frequency
InSAR	SAR Interferometry
ISRO	Indian Space Research Organisation
JAXA	Japan Aerospace Exploration Agency
JPL	Jet Propulsion Laboratory
NASA	National Aeronautics and Space Administration
NISAR	NASA-ISRO SAR Mission
PRF	Pulse Repetition Frequency
RCM	Range Cell Migration
SAR	Synthetic Aperture Radar
SNR	Signal to Noise Ratio
SWE	Snow Water Equivalent
TanDEM-X	TerraSAR-X add-on for Digital Elevation Measurement
TomoSAR	SAR Tomography
VHF	Very High Frequency
3-D	Three-Dimensional

List of Publications

[Pub1] A. Benedikter, M. Rodriguez-Cassola, F. Betancourt-Payan, G. Krieger, and A. Moreira, "Autofocus-based estimation of penetration depth and permittivity of ice volumes and snow using single SAR images," *IEEE Transactions on Geoscience and Remote Sensing*, vol. 60, pp. 1–15, 2022.

[Pub2] A. Benedikter and M. Rodriguez-Cassola, "A volumetric P-band imaging concept for the SAR exploration of Saturn's moon Enceladus," in *EUSAR 2021; 13th European Conference on Synthetic Aperture Radar*, pp. 842–847, 2021.

[Pub3] A. Benedikter, K. Wickhusen, H. Hussmann, A. Stark, F. Damme, M. Rodriguez-Cassola, and G. Krieger, "Periodic orbits for interferometric and tomographic radar imaging of Saturn's moon Enceladus," *Acta Astronautica*, vol. 191, pp. 326–345, 2022.

[Pub4] A. Benedikter, P. Rosen, M. Simons, R. Park, M. Rodriguez-Cassola, P. Prats-Iraola, G. Krieger, and J. Matar, "Performance analysis of a repeat-pass InSAR mission for deformation and topography mapping of Saturn's moon Enceladus," in *IGARSS 2023 - 2023 IEEE International Geoscience and Remote Sensing Symposium*, pp. 4177–4180, 2023.

[Pub5] A. Benedikter, M. Rodriguez-Cassola, P. Prats-Iraola, G. Krieger, and G. Fischer, "On the processing of single-pass InSAR data for accurate elevation measurements of ice sheets and glaciers," *IEEE Transactions on Geoscience and Remote Sensing*, vol. 62, pp. 1–10, 2024.

[Pub6] A. Benedikter, M. Rodriguez-Cassola, P. Prats-Iraola, K. Belinska, and G. Krieger, "On the decorrelation effect of dry snow in differential SAR interferometry," in *IGARSS 2023 - 2023 IEEE International Geoscience and Remote Sensing Symposium*, pp. 8323–8326, 2023.

[Pub7] A. Benedikter, K. Belinska, M. Rodriguez-Cassola, P. Prats-Iraola, G. Fischer, G. Krieger, and I. Hajnsek, "Toward dry snow parameter estimation by simultaneous multiple squint differential InSAR," *IEEE Transactions on Geoscience and Remote Sensing*, vol. 62, pp. 1–15, 2024.

Bibliography

[1] C. A. Wiley, "Pulsed Doppler radar methods and apparatus," US Patent US3196436A, 1954.

[2] NASA, "Seasat." `www.jpl.nasa.gov/missions/seasat/`, visited in September 2024.

[3] A. Moreira, P. Prats-Iraola, M. Younis, G. Krieger, I. Hajnsek, and K. P. Papathanassiou, "A tutorial on synthetic aperture radar," *IEEE Geoscience and Remote Sensing Magazine*, vol. 1, pp. 6–43, Mar. 2013.

[4] J.-S. Lee and E. Pottier, *Polarimetric radar imaging: From basics to applications*. CRC Press, 2009.

[5] P. A. Rosen, S. Hensley, I. R. Joughin, F. K. Li, S. N. Madsen, E. Rodriguez, and R. M. Goldstein, "Synthetic aperture radar interferometry," *Proceedings of the IEEE*, vol. 88, no. 3, pp. 333–382, 2000.

[6] R. Bamler and P. Hartl, "Synthetic aperture radar interferometry," *Inverse Problems*, vol. 14, pp. R1–R54, aug 1998.

[7] S. Cloude and K. Papathanassiou, "Polarimetric SAR interferometry," *IEEE Transactions on Geoscience and Remote Sensing*, vol. 36, no. 5, pp. 1551–1565, 1998.

[8] A. Reigber and A. Moreira, "First demonstration of airborne SAR tomography using multi-baseline L-band data," *IEEE Transactions on Geoscience and Remote Sensing*, vol. 38, no. 5, pp. 2142–2152, 2000.

[9] DLR, "TerraSAR-X." `https://www.dlr.de/de/forschung-und-transfer/projekte-und-missionen/terrasar-x`, visited in September 2024.

[10] DLR, "TanDEM-X." https://www.dlr.de/de/forschung-und-transfer/projekte-und-missionen/tandem-x, visited in September 2024.

[11] ESA, "Sentinel-1." https://sentiwiki.copernicus.eu/web/s1-mission, visited in September 2024.

[12] JAXA, "ALOS-2." https://www.eorc.jaxa.jp/ALOS-2/en/about/overview.htm, visited in September 2024.

[13] O. Rzhiga, "Venera-15 and -16 spacecraft: Images and maps of Venus," *Advances in Space Research*, vol. 7, no. 12, pp. 269–278, 1987.

[14] NASA, "Magellan." https://science.nasa.gov/mission/magellan/, visited in September 2024.

[15] NASA, "Cassini." https://science.nasa.gov/mission/cassini/, visited in September 2024.

[16] R. Bindschadler, K. Jezek, and J. Crawford, "Glaciological investigations using the synthetic aperture radar imaging system," *Annals of Glaciology*, vol. 9, p. 11–19, 1987.

[17] K. C. Jezek, M. R. Drinkwater, J. P. Crawford, R. Bindschadler, and R. Kwok, "Analysis of synthetic aperture radar data collected over the southwestern Greenland ice sheet," *Journal of Glaciology*, vol. 39, no. 131, p. 119–132, 1993.

[18] E. Rignot, K. Jezek, J. van Zyl, M. Drinkwater, and Y. Lou, "Radar scattering from snow facies of the Greenland ice sheet: results from the AIRSAR 1991 campaign," in *Proceedings of IGARSS '93 - IEEE International Geoscience and Remote Sensing Symposium*, pp. 1270–1272 vol.3, 1993.

[19] Y.-L. S. Tsai, A. Dietz, N. Oppelt, and C. Kuenzer, "Remote sensing of snow cover using spaceborne SAR: A review," *Remote Sensing*, vol. 11, no. 12, 2019.

[20] T. Nagler and H. Rott, "Retrieval of wet snow by means of multitemporal SAR data," *IEEE Transactions on Geoscience and Remote Sensing*, vol. 38, no. 2, pp. 754–765, 2000.

[21] J. Shi and J. Dozier, "Estimation of snow water equivalence using SIR-C/X-SAR. I. inferring snow density and subsurface properties," *IEEE Transactions on Geoscience and Remote Sensing*, vol. 38, no. 6, pp. 2465–2474, 2000.

[22] J. Koskinen, J. Pulliainen, and M. Hallikainen, "The use of ERS-1 SAR data in snow melt monitoring," *IEEE Transactions on Geoscience and Remote Sensing*, vol. 35, no. 3, pp. 601–610, 1997.

[23] M. Bernier and J.-P. Fortin, "The potential of times series of C-band SAR data to monitor dry and shallow snow cover," *IEEE Transactions on Geoscience and Remote Sensing*, vol. 36, no. 1, pp. 226–243, 1998.

[24] H. Rott and C. Mätzler, "Possibilities and limits of synthetic aperture radar for snow and glacier surveying," *Annals of Glaciology*, vol. 9, p. 195–199, 1987.

[25] T. Strozzi, R. Caduff, N. Jones, C. Barboux, R. Delaloye, X. Bodin, A. Kääb, E. Mätzler, and L. Schrott, "Monitoring rock glacier kinematics with satellite synthetic aperture radar," *Remote Sensing*, vol. 12, no. 3, 2020.

[26] S. D. Jawak, T. G. Bidawe, and A. J. Luis, "A review on applications of imaging synthetic aperture radar with a special focus on cryospheric studies," *Advances in Remote Sensing*, vol. 4, pp. 163–175, 06 2015.

[27] K. C. Jezek, "Glaciological properties of the Antarctic ice sheet from RADARSAT-1 synthetic aperture radar imagery," *Annals of Glaciology*, vol. 29, p. 286–290, 1999.

[28] H. Pritchard, T. Murray, A. Luckman, T. Strozzi, and S. Barr, "Glacier surge dynamics of Sortebræ, east Greenland, from synthetic aperture radar feature tracking," *Journal of Geophysical Research: Earth Surface*, vol. 110, no. F3, 2005.

[29] DLR, "TerraSAR-X image of the month: The Drygalski Glacier in Antarctica." `https://www.dlr.de/en/latest/news/2009/20090312_terrasar-x-image-of-the-month-the-drygalski-glacier-in-antarctica_16350`, visited in September 2024.

[30] DLR, "Rate of elevation change over the Northern Patagonian Ice Field between 2000 and 2012." `https://www.dlr.de/en/latest/news/2019/04/20191210_patagonian-ice-fields-reveals-complexity-of-physical-interactions`, visited in September 2024.

[31] E. Weber Hoen and H. Zebker, "Penetration depths inferred from interferometric volume decorrelation observed over the Greenland ice sheet," *IEEE Transactions on Geoscience and Remote Sensing*, vol. 38, no. 6, pp. 2571–2583, 2000.

[32] J. Dall, "InSAR elevation bias caused by penetration into uniform volumes," *IEEE Transactions on Geoscience and Remote Sensing*, vol. 45, no. 7, pp. 2319–2324, 2007.

[33] G. Fischer, M. Jäger, K. P. Papathanassiou, and I. Hajnsek, "Modeling the vertical backscattering distribution in the percolation zone of the Greenland ice sheet with SAR tomography," *IEEE Journal of Selected Topics in Applied Earth Observations and Remote Sensing*, vol. 12, no. 11, pp. 4389–4405, 2019.

[34] G. Fischer, K. P. Papathanassiou, and I. Hajnsek, "Modeling and compensation of the penetration bias in InSAR DEMs of ice sheets at different frequencies," *IEEE Journal of Selected Topics in Applied Earth Observations and Remote Sensing*, vol. 13, pp. 2698–2707, 2020.

[35] S. Tebaldini, T. Nagler, H. Rott, and A. Heilig, "Imaging the internal structure of an alpine glacier via L-band airborne SAR tomography," *IEEE Transactions on Geoscience and Remote Sensing*, vol. 54, no. 12, pp. 7197–7209, 2016.

[36] Z. Martins *et al.*, "Report of the expert committee for the large-class mission in ESA's Voyage 2050 plan covering the science theme "Moons of the Giant Planets"," tech. rep., European Space Agency (ESA), 2024.

[37] J. R. Spencer and F. Nimmo, "Enceladus: An active ice world in the Saturn system," *Annual Review of Earth and Planetary Sciences*, vol. 41, no. 1, pp. 693–717, 2013.

[38] C. C. Porco, P. Helfenstein, P. C. Thomas, *et al.*, "Cassini observes the active south pole of Enceladus," *Science*, vol. 311, no. 5766, pp. 1393–1401, 2006.

[39] F. Postberg, J. Schmidt, J. Hillier, *et al.*, "A salt-water reservoir as the source of a compositionally stratified plume on Enceladus," *Nature*, vol. 474, pp. 620–622, 2011.

[40] F. Postberg, N. Khawaja, B. Abel, *et al.*, "Macromolecular organic compounds from the depths of Enceladus," *Nature*, vol. 558, pp. 564–568, 2018.

[41] A. Coustenis, S. Atreya, T. Balint, *et al.*, "TandEM: Titan and Enceladus mission," *Exp Astron*, vol. 23, pp. 893–946, 2009.

[42] K. Konstantinidis, C. L. F. Martinez, B. Dachwald, *et al.*, "A lander mission to probe subglacial water on Saturn's moon Enceladus for life," *Acta astronautica*, vol. 106, pp. 63–89, 2015.

[43] K. Reh *et al.*, "Enceladus Life Finder: The search for life in a habitable moon," in *2016 IEEE Aerospace Conference*, pp. 1–8, 2016.

[44] S. MacKenzie *et al.*, "Enceladus Orbilander: A flagship mission concept for astrobiology," planetary mission concept study for the 2023-2032 decadal survey, Johns Hopkins University Applied Physics Laboratory, 2020.

[45] M. Simons, B. Anderson, A. Benedikter, *et al.*, "Crustal deformation derived from repeat-pass interferometric SAR at Enceladus – why and how?," *Bulletin of the AAS*, vol. 55, oct 23 2023.

[46] E. R. Stofan, C. Elachi, J. I. Lunine, *et al.*, "The lakes of Titan," *Nature*, vol. 445, no. 7123, pp. 61–64, 2007.

[47] M. Sori, J. T. Keane, and A. Ermakov, "Next generation planetary geodesy," , Keck Institute for Space Studies (KISS), 2023.

[48] NASA/JPL-Caltech/ASI, "Titan: Larger and larger lakes." `https://photojournal.jpl.nasa.gov/catalog/PIA09180`, visited in September 2024.

[49] NASA/JPL-Caltech/ASI, "Southern Enceladus in radar view." `https://science.nasa.gov/resource/southern-enceladus-in-radar-view/`, visited in September 2024.

[50] J. C. Curlander and R. N. McDonough, *Synthetic aperture radar: Systems and signal processing*. Wiley-Interscience, 1991.

[51] F. Ulaby, M. C. Dobson, and J. L. Álvarez-Pérez, *Handbook of radar scattering statistics for terrain*. Artech House, 2019.

[52] M. Soumekh, *Synthetic aperture radar signal processing*, vol. 7. New York: Wiley, 1999.

[53] R. Touzi, A. Lopes, J. Bruniquel, and P. Vachon, "Coherence estimation for SAR imagery," *IEEE Transactions on Geoscience and Remote Sensing*, vol. 37, no. 1, pp. 135–149, 1999.

[54] F. T. Ulaby, *Microwave remote sensing: Active and passive, Volume I: Fundamentals and radiometry*. Artech House Publishers, 1986.

[55] M. Born, E. Wolf, and A. B. Bhatia, *Principles of optics*. Cambridge University Pr., 2002.

[56] C. M. Huber, A. Benedikter, G. Krieger, and M. Rodriguez-Cassola, "Radar travel time tomography for subsurface ice exploration at Saturn's moon Enceladus," in *2021 18th European Radar Conference (EuRAD)*, pp. 433–436, 2022.

[57] C. Mätzler, "Applications of the interaction of microwaves with the natural snow cover," *Remote sensing reviews*, vol. 2, no. 2, pp. 259–387, 1987.

[58] C. Mätzler and U. Wegmüller, "Dielectric properties of fresh-water ice at microwave frequencies," *Journal of Physics D: Applied Physics*, vol. 21, no. 11, p. 1660, 1988.

[59] M. Tiuri, A. Sihvola, E. Nyfors, and M. Hallikaiken, "The complex dielectric constant of snow at microwave frequencies," *IEEE Journal of oceanic Engineering*, vol. 9, no. 5, pp. 377–382, 1984.

[60] A. Kovacs, A. J. Gow, and R. M. Morey, "The in-situ dielectric constant of polar firn revisited," *Cold Regions Science and Technology*, vol. 23, no. 3, pp. 245–256, 1995.

[61] S. Leinss, A. Wiesmann, J. Lemmetyinen, and I. Hajnsek, "Snow water equivalent of dry snow measured by differential interferometry," *IEEE Journal of Selected Topics in Applied Earth Observations and Remote Sensing*, vol. 8, no. 8, pp. 3773–3790, 2015.

[62] G. Hufford, "A model for the complex permittivity of ice at frequencies below 1 THz," *Int J Infrared Milli Waves*, vol. 12, p. 677–682, 1991.

[63] E. Rignot, "Backscatter model for the unusual radar properties of the Greenland ice sheet," *Journal of Geophysical Research: Planets*, vol. 100, no. E5, pp. 9389–9400, 1995.

[64] E. J. Rignot, S. J. Ostro, J. J. van Zyl, and K. C. Jezek, "Unusual radar echoes from the Greenland ice sheet," *Science*, vol. 261, no. 5129, pp. 1710–1713, 1993.

[65] J. J. Sharma, I. Hajnsek, K. P. Papathanassiou, and A. Moreira, "Polarimetric decomposition over glacier ice using long-wavelength airborne PolSAR," *IEEE Transactions on Geoscience and Remote Sensing*, vol. 49, no. 1, pp. 519–535, 2011.

[66] G. Parrella, I. Hajnsek, and K. P. Papathanassiou, "Polarimetric decomposition of L-band PolSAR backscattering over the Austfonna ice cap," *IEEE Transactions on Geoscience and Remote Sensing*, vol. 54, no. 3, pp. 1267–1281, 2016.

[67] S. Leinss, G. Parrella, and I. Hajnsek, "Snow height determination by polarimetric phase differences in X-band SAR data," *IEEE Journal of Selected Topics in Applied Earth Observations and Remote Sensing*, vol. 7, no. 9, pp. 3794–3810, 2014.

[68] S. Manickam, A. Bhattacharya, G. Singh, and Y. Yamaguchi, "Estimation of snow surface dielectric constant from polarimetric SAR data," *IEEE Journal of Selected Topics in Applied Earth Observations and Remote Sensing*, vol. 10, no. 1, pp. 211–218, 2017.

[69] A. Patil, G. Singh, and C. Rüdiger, "Retrieval of snow depth and snow water equivalent using dual polarization SAR data," *Remote Sensing*, vol. 12, no. 7, 2020.

[70] G. Singh, A. Verma, S. Kumar, Snehmani, A. Ganju, Y. Yamaguchi, and A. V. Kulkarni, "Snowpack density retrieval using fully polarimetric TerraSAR-X data in the Himalayas," *IEEE Transactions on Geoscience and Remote Sensing*, vol. 55, no. 11, pp. 6320–6329, 2017.

[71] D. Varade, G. Singh, O. Dikshit, and S. Manickam, "Identification of snow using fully polarimetric SAR data based on entropy and anisotropy," *Water Resources Research*, vol. 56, no. 2, p. e2019WR025449, 2020.

[72] L. Huang, Z. Li, B.-S. Tian, Q. Chen, J.-L. Liu, and R. Zhang, "Classification and snow line detection for glacial areas using the polarimetric SAR image," *Remote Sensing of Environment*, vol. 115, no. 7, pp. 1721–1732, 2011.

[73] E. Berthier, D. Floricioiu, A. S. Gardner, *et al.*, "Measuring glacier mass changes from space—A review," *Reports on Progress in Physics*, vol. 86, no. 3, 2023.

[74] B. Wessel, A. Bertram, A. Gruber, S. Bemm, and S. Dech, "A new high-resolution elevation model of Greenland derived from TanDEM-X," *ISPRS Annals of the Photogrammetry, Remote Sensing and Spatial Information Sciences*, vol. III-7, pp. 9–16, 2016.

[75] M. Rankl and M. Braun, "Glacier elevation and mass changes over the central Karakoram region estimated from TanDEM-X and SRTM/X-SAR digital elevation models," *Annals of Glaciology*, vol. 57, no. 71, p. 273–281, 2016.

[76] P. Malz, W. Meier, G. Casassa, R. Jaña, P. Skvarca, and M. H. Braun, "Elevation and mass changes of the southern Patagonia icefield derived from TanDEM-X and SRTM data," *Remote Sensing*, vol. 10, no. 2, 2018.

[77] H. Rott, W. Abdel Jaber, J. Wuite, S. Scheiblauer, D. Floricioiu, J. M. van Wessem, T. Nagler, N. Miranda, and M. R. van den Broeke, "Changing pattern of ice flow and mass balance for glaciers discharging into the Larsen A and B embayments, Antarctic Peninsula, 2011 to 2016," *The Cryosphere*, vol. 12, no. 4, pp. 1273–1291, 2018.

[78] W. Abdel Jaber, H. Rott, D. Floricioiu, J. Wuite, and N. Miranda, "Heterogeneous spatial and temporal pattern of surface elevation change and mass balance of the Patagonian ice fields between 2000 and 2016," *The Cryosphere*, vol. 13, no. 9, pp. 2511–2535, 2019.

[79] P. Rizzoli, M. Martone, H. Rott, and A. Moreira, "Characterization of snow facies on the Greenland ice sheet observed by TanDEM-X interferometric SAR data," *Remote Sensing*, vol. 9, no. 4, 2017.

[80] S. Hensley, D. Moller, S. Oveisgharan, T. Michel, and X. Wu, "Ka-band mapping and measurements of interferometric penetration of the Greenland ice sheets by the GLISTIN radar," *IEEE Journal of Selected Topics in Applied Earth Observations and Remote Sensing*, vol. 9, no. 6, pp. 2436–2450, 2016.

[81] E. Rignot, K. Echelmeyer, and W. Krabill, "Penetration depth of interferometric synthetic-aperture radar signals in snow and ice," *Geophysical Research Letters*, vol. 28, no. 18, pp. 3501–3504, 2001.

[82] S. Oveisgharan and H. A. Zebker, "Estimating snow accumulation from InSAR correlation observations," *IEEE Transactions on Geoscience and Remote Sensing*, vol. 45, no. 1, pp. 10–20, 2007.

[83] S. Abdullahi, B. Wessel, M. Huber, A. Wendleder, A. Roth, and C. Kuenzer, "Estimating penetration-related X-band InSAR elevation bias: A study over the Greenland ice sheet," *Remote Sensing*, vol. 11, no. 24, 2019.

[84] A. Dehecq, R. Millan, E. Berthier, N. Gourmelen, E. Trouvé, and V. Vionnet, "Elevation changes inferred from TanDEM-X data over the Mont-Blanc area: Impact of the X-band interferometric bias," *IEEE Journal of Selected Topics in Applied Earth Observations and Remote Sensing*, vol. 9, no. 8, pp. 3870–3882, 2016.

[85] B. Wessel, M. Huber, C. Wohlfart, A. Bertram, N. Osterkamp, U. Marschalk, A. Gruber, F. Reuß, S. Abdullahi, I. Georg, and A. Roth, "TanDEM-X PolarDEM 90 m of Antarctica: generation and error characterization," *The Cryosphere*, vol. 15, no. 11, pp. 5241–5260, 2021.

[86] A. Lambrecht, C. Mayer, A. Wendt, D. Floricioiu, and C. Völksen, "Elevation change of Fedchenko glacier, Pamir Mountains, from GNSS field measurements and TanDEM-X elevation models, with a focus on the upper glacier," *Journal of Glaciology*, vol. 64, no. 246, p. 637–648, 2018.

[87] H. Rott, S. Scheiblauer, J. Wuite, L. Krieger, D. Floricioiu, P. Rizzoli, L. Libert, and T. Nagler, "Penetration of interferometric radar signals in Antarctic snow," *The Cryosphere*, vol. 15, no. 9, pp. 4399–4419, 2021.

[88] R. M. Goldstein, H. Engelhardt, B. Kamb, and R. M. Frolich, "Satellite radar interferometry for monitoring ice sheet motion: Application to an Antarctic ice stream," *Science*, vol. 262, no. 5139, pp. 1525–1530, 1993.

[89] A. Hooper, D. Bekaert, K. Spaans, and M. Arıkan, "Recent advances in SAR interferometry time series analysis for measuring crustal deformation," *Tectonophysics*, vol. 514-517, pp. 1–13, 2012.

[90] E. Rignot, K. C. Jezek, and H. G. Sohn, "Ice flow dynamics of the Greenland ice sheet from SAR interferometry," *Geophysical Research Letters*, vol. 22, no. 5, pp. 575–578, 1995.

[91] P. Prats, R. Scheiber, A. Reigber, C. Andres, and R. Horn, "Estimation of the surface velocity field of the Aletsch glacier using multibaseline airborne SAR interferometry," *IEEE Transactions on Geoscience and Remote Sensing*, vol. 47, no. 2, pp. 419–430, 2009.

[92] S. Palmer, A. Shepherd, H. Björnsson, and F. Pálsson, "Ice velocity measurements of Langjökull, Iceland, from interferometric synthetic aperture radar (InSAR)," *Journal of Glaciology*, vol. 55, no. 193, p. 834–838, 2009.

[93] P. Sánchez-Gámez and F. J. Navarro, "Glacier surface velocity retrieval using D-InSAR and offset tracking techniques applied to ascending and descending passes of Sentinel-1 data for southern Ellesmere ice caps, Canadian Arctic," *Remote Sensing*, vol. 9, no. 5, 2017.

[94] T. Nagler, H. Rott, M. Hetzenecker, J. Wuite, and P. Potin, "The Sentinel-1 mission: New opportunities for ice sheet observations," *Remote Sensing*, vol. 7, no. 7, pp. 9371–9389, 2015.

[95] P. López-Dekker, J. Biggs, B. Chapron, A. Hooper, A. Kääb, S. Masina, J. Mouginot, B. B. Nardelli, C. Pasquero, P. Prats-Iraola, P. Rampal, J. Stroeve, and B. Rommen, "The Harmony mission: End of Phase-0 science overview," in *2021 IEEE International Geoscience and Remote Sensing Symposium IGARSS*, pp. 7752–7755, 2021.

[96] T. Guneriussen, K. Hogda, H. Johnsen, and I. Lauknes, "InSAR for estimation of changes in snow water equivalent of dry snow," *IEEE Transactions on Geoscience and Remote Sensing*, vol. 39, no. 10, pp. 2101–2108, 2001.

[97] H. Rott, T. Nagler, and R. Scheiber, "Snow mass retrieval by means of SAR interferometry," in *3rd Fringe Workshop Eur. Space Agency Earth Observ.*, 2004.

[98] G. Engen, T. Guneriussen, and Y. Overrein, "Delta-K interferometric SAR technique for snow water equivalent (SWE) retrieval," *IEEE Geoscience and Remote Sensing Letters*, vol. 1, no. 2, pp. 57–61, 2004.

[99] S. Leinss, A. Wiesmann, J. Lemmetyinen, and I. Hajnsek, "Snow water equivalent of dry snow measured by differential interferometry," *IEEE Journal of Selected Topics in Applied Earth Observations and Remote Sensing*, vol. 8, no. 8, pp. 3773–3790, 2015.

[100] T. Nagler, H. Rott, S. Scheiblauer, L. Libert, N. Mölg, R. Horn, J. Fischer, M. Keller, A. Moreira, and J. Kubanek, "Airborne experiment on InSAR snow mass retrieval in alpine environment," in *IGARSS 2022 - 2022 IEEE International Geoscience and Remote Sensing Symposium*, pp. 4549–4552, 2022.

[101] S. Oveisgharan, R. Zinke, Z. Hoppinen, and H. P. Marshall, "Snow water equivalent retrieval over Idaho – Part 1: Using Sentinel-1 repeat-pass interferometry," *The Cryosphere*, vol. 18, no. 2, pp. 559–574, 2024.

[102] B. Rekioua, M. Davy, L. Ferro-Famil, and S. Tebaldini, "Snowpack permittivity profile retrieval from tomographic SAR data," *Comptes Rendus Physique*, vol. 18, no. 1, pp. 57–65, 2017.

[103] H. Qiao, P. Zhang, Z. Li, L. Huang, C. Zhao, S. Gao, C. Liu, Z. Wu, S. Liang, J. Zhou, W. Sun, and L. Wang, "Snow profile reconstruction from tomographic UAV SAR," *International Journal of Applied Earth Observation and Geoinformation*, vol. 118, p. 103291, 2023.

[104] T. G. Yitayew, L. Ferro-Famil, T. Eltoft, and S. Tebaldini, "Lake and fjord ice imaging using a multifrequency ground-based tomographic SAR system," *IEEE Journal of Selected Topics in Applied Earth Observations and Remote Sensing*, vol. 10, no. 10, pp. 4457–4468, 2017.

[105] G. D. Martin-del Campo-Becerra, A. Benedikter, J. Amao-Oliva, and R. Scheiber, "Subsurface TomoSAR imaging of the Mittelbergferner glacier in the Austrian Alps," in *EUSAR 2021; 13th European Conference on Synthetic Aperture Radar*, pp. 1–6, 2021.

[106] F. Banda, J. Dall, and S. Tebaldini, "Single and multipolarimetric P-band SAR tomography of subsurface ice structure," *IEEE Transactions on Geoscience and Remote Sensing*, vol. 54, no. 5, pp. 2832–2845, 2016.

[107] M. Pardini, G. Parrella, G. Fischer, and K. Papathanassiou, "A multi-frequency SAR tomographic characterization of sub-surface ice volumes," in *Proceedings of EUSAR 2016: 11th European Conference on Synthetic Aperture Radar*, pp. 1–6, 2016.

[108] T. L. Toan, J. Chave, J. Dall, K. Papathanassiou, P. Paillou, M. Rechstein, S. Quegan, S. Saatchi, K. Seipel, H. Shugart, S. Tebaldini, L. Ulander, and M. Williams, "The Biomass mission: Objectives and requirements," in *IGARSS 2018 - 2018 IEEE International Geoscience and Remote Sensing Symposium*, pp. 8563–8566, 2018.

[109] R. Orosei, R. Jordan, D. Morgan, *et al.*, "Mars advanced radar for subsurface and ionospheric sounding (MARSIS) after nine years of operation: A summary," *Planetary and Space Science*, vol. 112, pp. 98–114, 2015.

[110] R. Seu, R. J. Phillips, D. Biccari, *et al.*, "SHARAD sounding radar on the Mars Reconnaissance Orbiter," *Journal of Geophysical Research: Planets*, vol. 112, no. E5, 2007.

[111] D. B. Campbell, N. J. S. Stacy, W. I. Newman, R. E. Arvidson, E. M. Jones, G. S. Musser, A. Y. Roper, and C. Schaller, "Magellan observations of extended impact crater related features on the surface of Venus," *Journal of Geophysical Research: Planets*, vol. 97, no. E10, pp. 16249–16277, 1992.

[112] C. Elachi, S. Wall, M. Allison, *et al.*, "Cassini radar views the surface of Titan," *Science*, vol. 308, no. 5724, pp. 970–974, 2005.

[113] R. M. C. Lopes, R. L. Kirk, K. L. Mitchell, *et al.*, "Cryovolcanism on Titan: New results from Cassini RADAR and VIMS," *Journal of Geophysical Research: Planets*, vol. 118, no. 3, pp. 416–435, 2013.

[114] K. Mitchell, U. Khankhoje, J. Castillo-Rogez, and S. Wall, "Enceladus' brilliant surface: Cassini RADAR observations and interpretation," pp. 2902–, 03 2013.

[115] S. J. Ostro, R. D. West, M. A. Janssen, *et al.*, "Cassini RADAR observations of Enceladus, Tethys, Dione, Rhea, Iapetus, Hyperion, and Phoebe," *Icarus*, vol. 183, no. 2, pp. 479–490, 2006.

[116] S. Ostro, R. West, L. Wye, *et al.*, "New Cassini RADAR results for Saturn's icy satellites," *Icarus*, vol. 206, no. 2, pp. 498–506, 2010.

[117] J. D. Hofgartner and K. P. Hand, "A continuum of icy satellites' radar properties explained by the coherent backscatter effect," *Nature Astronomy*, vol. 7, no. 5, pp. 534–540, 2023.

[118] M. Stefko, S. Leinss, O. Frey, and I. Hajnsek, "Coherent backscatter enhancement in bistatic Ku- and X-band radar observations of dry snow," *The Cryosphere*, vol. 16, no. 7, pp. 2859–2879, 2022.

[119] S. Smrekar, S. Hensley, R. Nybakken, *et al.*, "VERITAS (Venus Emissivity, Radio Science, InSAR, Topography, and Spectroscopy): A Discovery mission," in *2022 IEEE Aerospace Conference (AERO)*, pp. 1–20, 2022.

[120] J. Mittermayer, S. Wollstadt, P. Prats-Iraola, and R. Scheiber, "The TerraSAR-X staring spotlight mode concept," *IEEE Transactions on Geoscience and Remote Sensing*, vol. 52, no. 6, pp. 3695–3706, 2014.

[121] ICEYE, "ICEYE introduces first-in-market satellite radar dwell capability." `https://www.iceye.com/press/press-releases/dwell-mode`, visited in September 2024.

[122] A. Kääb, J. Mouginot, P. Prats-Iraola, E. Rignot, B. Rabus, A. Benedikter, H. Rott, T. Nagler, B. Rommen, and P. Lopez-Dekker, "Potential of the bi-static SAR satellite companion mission Harmony for land-ice observations," *Remote Sensing*, vol. 16, no. 16, 2024.

[123] J. Mittermayer, S. Wollstadt, P. Prats-Iraola, P. Lopez-Dekker, G. Krieger, and A. Moreira, "Bidirectional SAR imaging mode," *IEEE Transactions on Geoscience and Remote Sensing*, vol. 51, no. 1, pp. 601–614, 2013.

[124] A. Manappatty, A. Benedikter, M. Rodriguez-Cassola, P. Prats-Iraola, and G. Krieger, "SAR signal penetration estimation over ice sheets and glaciers using multiple squints and incoherent shift measurements," in *EUSAR 2024; 15th European Conference on Synthetic Aperture Radar*, pp. 1–6, 2024.

[125] A. Benedikter, M. Rodriguez-Cassola, G. Krieger, A. Moreira, and M. Vossiek, "Verfahren zur rechnergestützten Verarbeitung von SAR-Rohdaten," German Patent 10 2022 133 858.4.

[126] R. S. Park, N. Mastrodemos, R. A. Jacobson, A. Berne, A. T. Vaughan, D. J. Hemingway, E. J. Leonard, J. C. Castillo-Rogez, C. S. Cockell, J. T. Keane, A. S. Konopliv, F. Nimmo, J. E. Riedel, M. Simons, and S. Vance, "The global shape, gravity field, and libration of Enceladus," *Journal of Geophysical Research: Planets*, vol. 129, no. 1, p. e2023JE008054, 2024.

[127] A. I. Ermakov, R. S. Park, J. Roa, J. C. Castillo-Rogez, J. T. Keane, F. Nimmo, E. S. Kite, C. Sotin, T. J. W. Lazio, G. Steinbrügge, S. M. Howell, B. G. Bills, D. J. Hemingway, V. Viswanathan, G. Tobie, and V. Lainey, "A recipe for the geophysical exploration of Enceladus," *The Planetary Science Journal*, vol. 2, p. 157, aug 2021.

[128] D. Sandwell, P. Rosen, W. Moore, and E. Gurrola, "Radar interferometry for measuring tidal strains across cracks on Europa," *Journal of Geophysical Research: Planets*, vol. 109, no. E11, 2004.

[129] G. Black, D. Campbell, and L. Carter, "Arecibo radar observations of Rhea, Dione, Tethys, and Enceladus," *Icarus*, vol. 191, no. 2, pp. 702–711, 2007.

[130] J. Eppler, B. Rabus, and P. Morse, "Snow water equivalent change mapping from slope-correlated synthetic aperture radar interferometry (InSAR) phase variations," *The Cryosphere*, vol. 16, no. 4, pp. 1497–1521, 2022.

[131] K. Belinska, G. Fischer, and I. Hajnsek, "Differential SAR interferometry and co-polar phase differences for snow water equivalent estimation," in *EUSAR 2022; 14th European Conference on Synthetic Aperture Radar*, pp. 1–4, 2022.

[132] M. Lavalle *et al.*, "Co-fliers concepts formulation for NISAR and ROSE-L to address SDC and STV needs," in *IGARSS 2023 - 2023 IEEE International Geoscience and Remote Sensing Symposium*, 2023.

A Annex

The publications in the frame of the cumulative thesis are attached below. The following copyrights apply to each publication:

- For the publication [Pub1], *"Autofocus-based estimation of penetration depth and permittivity of ice volumes and snow using single SAR images"*, the following copyright applies: This work is licensed under a Creative Commons Attribution-NonCommercial-NoDerivatives 4.0 License.
- For the publication [Pub2], *"A volumetric P-band imaging concept for the SAR exploration of Saturn's moon Enceladus"*,the following copyright applies: © 2021 VDE Verlag GmbH, Berlin, Offenbach. Reprinted, with permission, from [Pub2].
- For the publication [Pub3], *"Periodic orbits for interferometric and tomographic radar imaging of Saturn's moon Enceladus"*, the following copyright applies: This work is licensed under a Creative Commons Attribution-NonCommercial-NoDerivatives 4.0 License.
- For the publication [Pub4], *"Performance analysis of a repeat-pass InSAR mission for deformation and topography mapping of Saturn's moon Enceladus"*, the following copyright applies: © 2023 IEEE. Reprinted, with permission, from [Pub4].
- For the publication [Pub5], *"On the processing of single-pass InSAR data for accurate elevation measurements of ice sheets and glaciers"*, the following copyright applies: This work is licensed under a Creative Commons Attribution-NonCommercial-NoDerivatives 4.0 License.
- For the publication [Pub6], *"On the decorrelation effect of dry snow in differential SAR interferometry"*, © 2023 IEEE. Reprinted, with permission, from [Pub6].
- For the publication [Pub7], *"Towards dry snow parameter estimation by simultaneous multiple squint differential InSAR"*, the following copyright applies: This work is licensed under a Creative Commons Attribution-NonCommercial-NoDerivatives 4.0 License.

Autofocus-Based Estimation of Penetration Depth and Permittivity of Ice Volumes and Snow Using Single SAR Images

Andreas Benedikter, Marc Rodriguez-Cassola, Felipe Betancourt-Payan, Gerhard Krieger, *Fellow, IEEE*, and Alberto Moreira, *Fellow, IEEE*

***Abstract*— An intrinsic challenge in the geophysical interpretation of low-frequency synthetic aperture radar (SAR) imagery of semitransparent media, such as ice sheets, is the position ambiguity of the scattering structures within the glacial volume. Commonly tackled by applying interferometric and tomographic techniques, their spaceborne implementation exhibits by orders higher complexity compared to missions relying on single SAR images, making them cost expensive or, in the context of planetary missions, even impossible due to limited navigation capability. Besides, even these sophisticated techniques are commonly biased due to inaccurate permittivity estimates, leading to geometric distortions up to several meters. We present a novel inversion procedure to estimate volume parameters of ice sheets, namely, the depth of the scattering layer within the glacial volume and the dielectric permittivity of the ice, based on single-image single-polarization SAR acquisitions. The information is inherent in the processed SAR data as phase errors on the azimuth signals resulting from uncompensated nonlinear propagation of the radar echoes through ice. We suggest a local map-drift autofocus approach to quantify and spatially resolve the phase errors and an inversion model to relate them to the penetration depth and permittivity. Testing the proposed technique using P-band SAR data acquired using DLR's airborne sensor F-SAR during the ARCTIC15 campaign in Greenland shows promising results and good agreement with tomographic products of the analyzed test site.**

***Index Terms*— Autofocus, cryosphere, depth, glacier, penetration, permittivity, synthetic aperture radar (SAR), tomography.**

I. Introduction

SYNTHETIC aperture radar (SAR) is a well-established remote sensing technique for the exploration of terrestrial and planetary ice sheets. This outstanding position builds upon several SAR-specific characteristics, such as metric or even submetric resolution, large spatial coverage, and operability almost independent of atmospheric conditions and solar illumination. Furthermore, electromagnetic waves with wavelengths in the microwave regime partially penetrate into optical nontransparent natural media, such as snow, ice, sand, dry soil, and vegetation. Considering snow and ice environments that are the focus of this study, this characteristic provides sensitivity of the SAR acquisition to both surface backscatter and scattering phenomena within the snow/ice sheet. Signal backscatter is expected to arise from 1) interfaces separating regions with dielectric contrast, e.g., air/snow, snow/ice, ice/water, and ice/bedrock; 2) ice inclusions in form of volumetric scattering; and 3) subsurface ice layers. This gives access to information about the vertical structure of ice sheets, which, in the terrestrial context, is of fundamental importance for glacier mass balance and dynamics and to gain understanding about the interrelation between the ice masses and environmental processes such as climate change [1], [2]. In the context of planetary exploration, the characterization of the internal structure of planetary ice sheets is a major element in understanding the geology and geophysical processes of planetary bodies and has been pioneered by the exploration of the Martian polar caps [3], [4]. With the rising scientific interest in the active icy moons such as Saturn's Enceladus and Jupiter's Europa, modalities for planetary subsurface ice exploration may play a central role in future missions.

In situ ground-penetrating radar sensors or airborne ice-sounding radars are most frequently used for measuring the internal structure of terrestrial ice sheets [5]–[7]. For the exploration of the Martian subsurface two radar sounding instruments have been deployed in orbit [8], [9]. Ice sounders allow for the imaging of the ice sheet subsurface along the radar track by operating a low-frequency nadir-looking radar at low altitude. They offer a particular sensitivity to specular scattering occurring at interfaces such as at the bedrock and internal ice layers, providing information on the thickness of the layers. The application of ice sounders is restricted by the limited coverage and backscattering profile estimation owing to the nadir-looking imaging geometry, not allowing for 3-D measurement of the ice sheet. In contrast, the side-looking geometry of spaceborne SAR is able to provide global coverage of terrestrial or planetary ice masses on a regular basis. Various experimental studies have been reported

Manuscript received June 8, 2021; revised October 4, 2021; accepted December 6, 2021. Date of publication December 13, 2021; date of current version March 1, 2022. This work was supported by the German Space Agency at the German Aerospace Center (DLR) with funds from the German Federal Ministry for Economic Affairs and Energy (BMWi) through the Project EnEx-AsGAr under Grant 50NA1708. *(Corresponding author: Andreas Benedikter.)*

Andreas Benedikter and Gerhard Krieger are with the Institute of Microwaves and Photonics (LHFT), Friedrich-Alexander University Erlangen-Nürnberg (FAU), 91058 Erlangen, Germany, and also with the Microwaves and Radar Institute, German Aerospace Center (DLR), 82234 Weßling, Germany (e-mail: andreas.benedikter@dlr.de).

Marc Rodriguez-Cassola, Felipe Betancourt-Payan, and Alberto Moreira are with the Microwaves and Radar Institute, German Aerospace Center (DLR), 82234 Weßling, Germany.

Digital Object Identifier 10.1109/TGRS.2021.3135026

in the literature to overcome the limitation of traditional 2-D SAR imaging, by applying polarimetric and interferometric SAR techniques, allowing for the retrieval of volumetric properties of ice sheets [10]–[12]. Extending the synthetic aperture in elevation direction by multiple acquisitions gathered from slightly displaced radar tracks allows for direct 3-D resolved measurement of ice sheets. This technique is commonly referred to as tomographic SAR (TomoSAR) imaging. TomoSAR allows for the direct retrieval of the vertical ice structure over wide swaths. It has been successfully applied in several airborne experiments for imaging the internal structure of Alpine glaciers and the Greenland ice sheet [13]–[15] and can be utilized as a robust basis for validation due to its direct 3-D capability.

In this article, we present an inversion procedure to estimate volume parameters of ice sheets, namely, the depth of the scattering scene within the glacial volume and the dielectric permittivity of the ice, based on a single-image single-polarization SAR acquisition. The information is inherent in the processed SAR data as phase errors on the azimuth signals resulting from uncompensated nonlinear propagation of the radar echoes through ice. We suggest a local map-drift autofocus approach to quantify and spatially resolve the phase errors and simple inversion models to relate these errors to the volume parameters. SAR autofocus algorithms have been used over decades to estimate residual platform motion errors [16]–[18] and have been suggested to correct ionospheric-induced phase errors [19], [20], both with the primary goal of recovering the contrast in the SAR image. In the case of a snow/ice scene, besides a corrected radiometry, the measured phase errors can be linked to the underlying physical scene properties, as introduced above. The approach relies on SAR systems with decent Doppler bandwidth to ensure sufficient sensitivity in the phase error measurement. This requirement is met by current airborne sensors such as DLR's F-SAR and spaceborne systems such as TerraSAR-X in staring spotlight mode or ALOS-2 in spotlight mode. The suggested single-image inversion approach may be applied complementary to polarimetric, interferometric, and tomographic imaging, or in applications in which these sophisticated technologies are not implementable such as in planetary missions. We use P-band SAR data acquired by DLR's airborne sensor F-SAR during the ARC-TIC15 campaign in Greenland to validate the proposed technique. The considered data consist of repeat-pass acquisitions from the K-transect test site forming a tomographic stack, which will be used to validate the results obtained with the single-image approach.

This article is organized in six sections. In Section II, the problem statement driving the proposed approach is discussed. Section III describes the modeling of the signal propagation, scattering, and resulting phase errors. The concept of the single SAR image inversion approach is presented in Section IV. Results from the airborne data are presented and discussed in Section V. Conclusions are drawn in Section VI.

II. Problem Statement

An important geophysical distinction of SAR image features in the assessment of ice sheets is their characterization as surface or volume structures and, furthermore, their exact position within the ice. The intrinsic difficulty in SAR imaging of semitransparent media, such as snow or ice, is the ambiguity in the position of the scattering structures within the media, even if the topography of the surface is known. An example of the complex backscatter situation of an ice sheet is illustrated in Fig. 1, where different features may contribute to the return signal in a single-resolution element, which extends in elevation direction and is only bounded by the antenna beamwidth. This feature can reach from the surface to the bedrock underneath the ice.

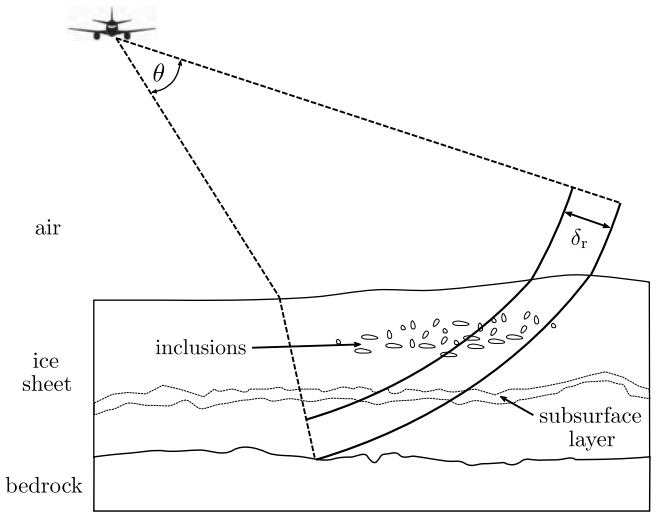

Fig. 1. Illustration of the potentially complex backscatter scenario of an ice sheet. Scattering sources from various depths may contribute in the SAR resolution cell, indicated by the range resolution δ_r and bounded by the antenna beamwidth θ.

As introduced above, the elevation ambiguity may be resolved by applying SAR interferometric or tomographic techniques that require the use of several satellites or coherent repeat passes. Although considered standard in the context of Earth observation missions, e.g., TanDEM-X and Sentinel-1, when considering planetary missions, the implementation of interferometric techniques may fail due to exceeding cost and complexity, as well as the limited accuracy in navigation and orbit determination. The stress here on the planetary context is due to the frame out of which this study emerges: a radar mission concept investigation for the exploration of Saturn's ice-covered moon Enceladus [21], where possible spacecraft orbits experience strong perturbation by Saturn's mass and the strongly nonspherical gravity field of Enceladus. Combined with the limited spacecraft navigation accuracy for outer solar system missions, the stringent navigation requirements for interferometric missions are expected to be difficult to meet. This drives the need for the proposed approach to infer the scattering position from single SAR images.

Besides the position of scattering features, the composition, i.e., the density of ice sheets is a significant geophysical parameter as it allows for example to distinguish between snow, firn, and ice. Radar acquisitions are inherently sensitive to the density of a glacial volume as it is directly related to the dielectric permittivity and therefore the propagation velocity

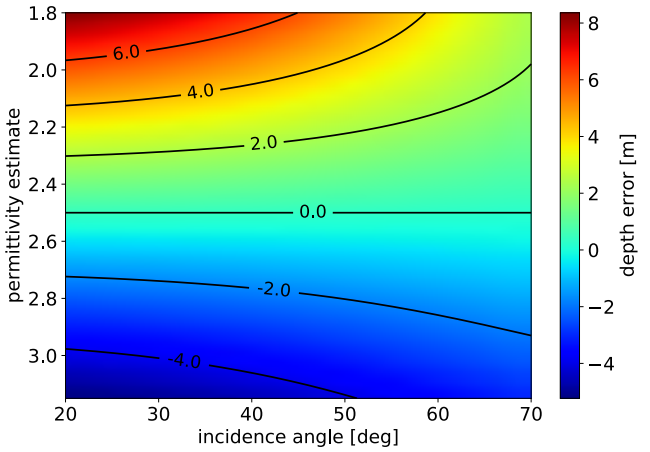

Fig. 2. Error in the estimation of the depth of a target retrieved from a tomographic product caused by inaccurate permittivity estimates. Results are shown for a target located 50 m deep in an ice sheet with averaged permittivity of 2.5. Positive values indicate an overestimation. Note the dependence with incidence angle on the ice sheet surface.

of radar signals. This sensitivity may be exploited to obtain permittivity estimates.

Moreover, an accurate permittivity knowledge is crucial for providing reliable interferometric penetration estimates and tomographic acquisitions, as the vertical wavenumber is directly related to it [11]. Permittivity values are commonly only available as rough estimates. Considering tomography, permittivity is commonly incorporated in the form of a geometric correction step after tomographic processing assuming free space propagation [15]. Derived from the relations given in [15], Fig. 2 displays the tomographic estimation errors of the depth of a structure located 50 m deep in an ice sheet with mean permittivity of 2.5, i.e., a permittivity corresponding to medium dense firn. Errors are analyzed for permittivity estimates spanning a range from slightly dense firn (i.e., 1.8) to solid ice (i.e., 3.15), and incidence angles on the surface between 20° and 70°. For different depths, the error is varying linearly. Significant errors can be expected in cases where no additional measurements constrain the permittivity range. A further independent approach for penetration estimation, as discussed in this study, can allow for the estimation of the permittivity.

III. Propagation and Phase Error Model

A. Propagation and Scattering in Snow and Ice

Considering radar systems operating in commonly used frequency bands, e.g., from P to X, when the radar echo impinges on the interface between air and snow/ice a significant part of the energy is not scattered but penetrates into the glacial volume [22]. The ratio of scattered and penetrating signal energy is dependent on the signal frequency, the dielectric permittivity of the surface layer, and the surface roughness [22]. Low values of these quantities lead to strong signal penetration. The penetrating electromagnetic wave experiences a change in propagation velocity, which, under the assumption of snow and ice as a low-loss material, can be written as [23]

$$c_{\text{ice}} = \frac{c_0}{\sqrt{\varepsilon_{r,\text{ice}}}} = \frac{c_0}{n_{\text{ice}}} \tag{1}$$

where c_0 is the speed of light in free space, $\varepsilon_{r,\text{ice}}$ the real part of the permittivity of snow/ice, and n_{ice} the corresponding refractive index, which is mainly used throughout this article, as it eases the description of propagation phenomena. The index ice is from here on used to indicate parameters describing the glacial volume. The velocity change results in a direction change of the penetrating wave, which can be described using Snell's law of refraction [23]

$$n_{\text{air}} \cdot \sin\theta_i = n_{\text{ice}} \cdot \sin\theta_r \tag{2}$$

with θ_i being the incident angle of the echo at a surface point with respect to the surface normal and θ_r the refraction angle.

Within the glacial volume the propagating signal may be backscattered by volumetric distributed inclusions, such as air inclusions, ice lenses and pipes, and depth hoar, in the form of volume scattering. Furthermore, backscatter occurs in form of surface scattering at interfaces separating layers with dielectric contrast, i.e., snow/firn, snow/ice, water bodies, refrozen wet snow or firn, and glacier/bedrock. Along its propagation path, the signal experiences an attenuation that results from scattering and dielectric absorption losses. Both processes increase with higher frequencies. In P and L bands, commonly used for ice-penetrating SAR systems, ice sheets are relatively transparent when compared to other natural media and studies record backscatter signatures in SAR acquisitions down to several tens of meters [13]–[15]. Above two GHz the absorption losses rise drastically due to increasing dielectric losses, represented by the imaginary part of the permittivity. Besides, the scattering losses show a strong dependence on the frequency, commonly modeled with a f^4 proportionality [24]. The propagation velocity within the glacial volume changes according to (1) with the refractive index, which can be assumed to be frequency independent in the microwave region with a slight temperature dependence [25]. The value for n_{ice} of pure ice is typically assumed to be around $(3.15)^{1/2}$ [26]. However, the n_{ice} of snow and firn strongly depends on its density and water content. Assuming cold conditions, ice sheets are commonly modeled as a with-depth-increasing density, leading to an equivalent n_{ice} profile with common starting values for snow of about $\sqrt{1.4}$ [26] and saturating at the refractive index of pure ice. Real ice sheets may exhibit more complex refractive index distributions, especially in regions where melting and refreezing events lead to strongly heterogeneous density distributions, e.g., highly reflecting layers.

The travel path of the radar echoes in complex n_{ice} distributions is nonlinear and can be approximated by Fermat's principle of least time, which states that the path of a ray taken between two points in an arbitrary heterogeneous medium is the one for which the ray takes the least time compared to adjacent paths [23]. The approximation made is to treat the traveling wave as propagating rays, which are perpendicular to the wave fronts. It is almost perfect if the wavelength is small compared to the structures with which it

interacts, but it cannot account for effects such as diffraction and interference [23]. Also Snell's law in (2) is subject to this high-frequency approximation. Generally speaking, the authors see the approximation applicable for ice-penetrating radar applications, as the small-scale variations within the glacial volume, i.e., the conglomerate of ice particles and air, are sufficiently small compared to radar wavelengths to be assumed homogeneous, whereas the interfaces between layers and permittivity profiles vary in large spatial extents compared to radar wavelengths. The validity of the approximation may be proven wrong if wavelength-sized structures are present, such as ice lenses or pipes. Nonetheless, it is an indispensable tool for approximating the travel time and path of the radar echoes through the glacial volume and is frequently used in the community.

B. SAR Signal Model

The received SAR signal echoed from a point target after demodulation can be modeled as [27]

$$s_{\mathrm{rx}}(t,t_a) = \mathrm{rect}\left[\frac{t-\tau(t_a)}{\tau_p}\right] \cdot \exp\left[j\cdot\pi\cdot k_r\cdot(t-\tau(t_a))^2\right] \cdot w^2(t_a)\cdot\exp[-j\cdot 2\cdot\pi\cdot f\cdot\tau(t_a)] \quad (3)$$

where t is the slant range time, t_a the azimuth time, τ_p the pulse duration, k_r the chirp rate, $w(t_a)$ the illumination footprint of the antenna over the scene, and $\tau(t_a)$ the variation of the two-way travel time to the target along azimuth, which is referred to as travel time history from here on. The backscatter coefficient of the target is set to unity. The signal model is equivalently applicable for conventional SAR acquisitions assuming free space propagation and for subsurface imaging through a dielectric heterogeneous propagation medium such as ice. The only difference lies in the formation of the travel time history, further discussed below. If not considering a discrete point target but a complex glacial volume as backscattering source, as depicted in Fig. 1, the return of all targets within the resolution cell integrates into the echo. The resolution cell extends in elevation direction and is only bounded by the antenna beamwidth, leading to a superposition of backscatter sources from different depths through the ice sheet. Commonly, the signal is dominated by specific scattering sources. For P- and L-band frequencies, subsurface scattering often contributes the strongest returns, whereas at higher frequencies, the backscatter arises mainly at the surface. For conventional SAR imaging, the vertical position of the scattering source is not accessible.

SAR data are commonly processed assuming free-space propagation between radar and target allowing for a trivial computation of the travel time history and therefore the phase history. For a target located within an ice sheet, $\tau(t_a)$ experiences additional influence by the change in propagation velocity and travel path nonlinearity, according to the relations discussed in Subsection III-A. The resulting mismatch between the processing kernel and the phase history of the target leads to defocusing in the processed SAR image depending on the magnitude and shape of the phase error history. Commonly perceived as an undesired effect, the defocusing may be exploited to gain information about the ice permittivity and target depth, if precisely measured and modeled.

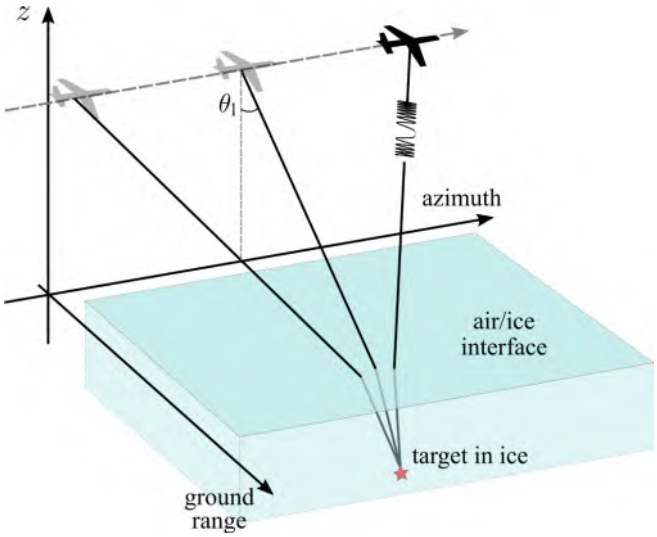

Fig. 3. Simplified acquisition geometry for a target located within an ice sheet of constant refractive index and flat surface, illustrating the refraction effect on the ice surface.

TABLE I
F-SAR P-BAND ACQUISITION PARAMETERS

Parameter	Value
Center frequency	435 MHz
Processed azimuth resolution	1.0 m
Processed range resolution	3.84 m
Sensor altitude	4000 m
Incidence angle range	25° to 60°

The acquisition geometry for a simplified scenario with a linear radar track, a flat interface between air and the ice sheet, and a constant refractive index n_{ice} is illustrated in Fig. 3, where the refraction on the surface leads to a nonlinear travel path of the echoes. For a target located within an ice sheet the derivation of the travel time history and therefore the phase history is nontrivial. Even for the simple scenario in Fig. 3, a closed form expression is not possible, as the derivation of the travel time along a single ray path requires the computation of the intercept point on the surface, leading to the determination of the roots of a fourth-order polynomial [28], which results in unpractical analytical expressions.

1) Phase Error Simulation: The simulated travel time history for a point target located 50 m deep in ice is shown in Fig. 4 (top panel) and is compared to a target at the same slant range time in a free space surrounding, i.e., the assumption made in processing. The simulation geometry is comparable to the one in Fig. 3 with a constant refractive index $n_{\mathrm{ice}} = (3.1)^{1/2}$ and an incidence angle on ice of 50°. System parameters such as sensor altitude, frequency, and integration time are chosen according to the analyzed data in Section V of the F-SAR flight campaign and listed in Table I. The computation of travel times was performed using a numerical minimization according to Fermat's principle. The difference between the two travel time histories is shown in the

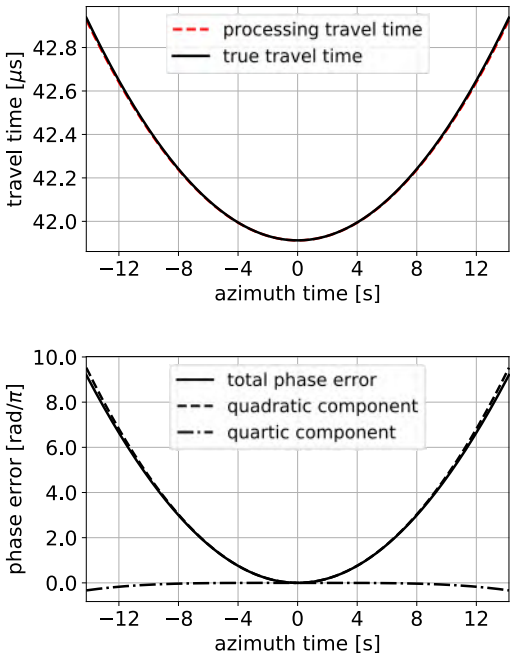

Fig. 4. (Top) simulated travel time history for a target located 50 m deep in an ice sheet of refractive index $(3.1)^{1/2}$ according to F-SAR acquisition parameters in Table I in black, compared to the travel time history used for processing assuming free space in dashed red. (Bottom) Phase error between the two histories and its quadratic and quartic component.

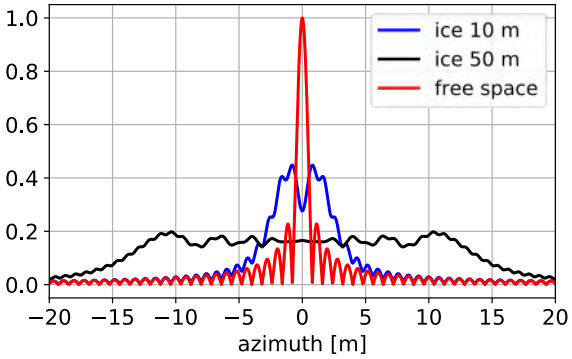

Fig. 5. Simulated azimuth IRF of a target located 10 and 50 m deep in an ice sheet with a refractive index of $(3.1)^{1/2}$, processed assuming free-space propagation, and compared to a target at equivalent slant range time located in free space. F-SAR P-band acquisition parameters are used for the simulation, depicted in Table I. Note the strong defocusing, even for the target at 10 m depth.

bottom panel of Fig. 4 in the form of a phase error describing the difference between the two corresponding phase histories. Furthermore, the two most significant polynomial terms of the phase error, i.e., the quadratic and quartic components are derived from an order-ten polynomial fit. The hyperbolic appearance of the phase error is well described by its quadratic component, even for the relatively large Doppler bandwidth of the F-SAR P-band acquisition. At the borders of the synthetic aperture a maximum phase error of $\approx 9.1\pi$ is reached. The effect of the phase error on the azimuth impulse response

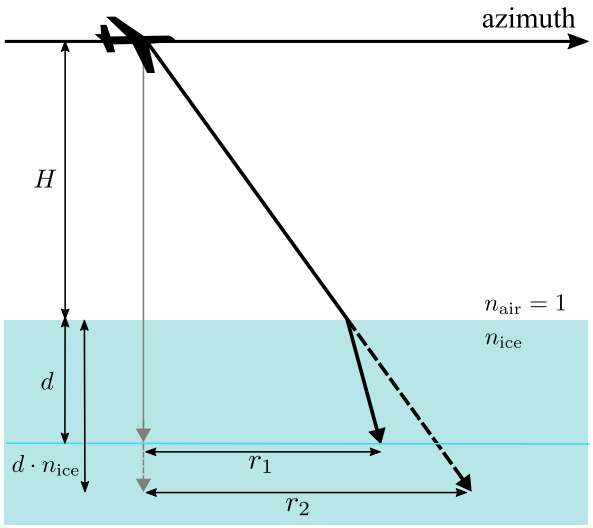

Fig. 6. Geometric relations for the derivation of the Doppler rate.

function (IRF) is depicted in Fig. 5 for a target 50 m deep in ice (corresponds to results in Fig. 4) and 10 m deep. The IRFs are compared to the one of a target located at the same slant range time but in free space, which appears well focused. The severe phase errors lead to a heavy defocusing of the IRF even for the target located 10 m under ice. This effect for subsurface SAR imaging of ice sheets has also been mentioned in [15], but regarded as negligible for the processed azimuth resolution of 5 m. For finer nominal azimuth resolution, as in the present dataset, the phase error cannot be neglected and increases proportional to $1/\delta_a^2$, with δ_a being the azimuth resolution. In [29], it is shown that for very fine azimuth resolution (i.e., <0.5 m in P-band) the defocusing effect may be even exploited to obtain a 3-D metric resolution effect.

2) Phase Error Model: As outlined in the discussion of Fig. 4, the phase error is well described by its quadratic component. This facilitates to approximate the phase history by an order-two polynomial. For non-squinted acquisitions the phase history may be approximated as [27]

$$\Phi(t_a) \approx \tau_0 \cdot f \cdot 2 \cdot \pi + f_R \cdot \pi \cdot t_a^2 \tag{4}$$

where τ_0 is the minimum of the travel time history and f_R is the Doppler rate. From a target's perspective, the Doppler rate describes the changing rate of Doppler frequency under which it is observed. For a target in free space it is given by [27]

$$f_{R,\text{fs}} = \frac{4 \cdot v_e^2}{\lambda_0 \cdot c_0 \cdot \tau_0} \tag{5}$$

with λ_0 being the wavelength in free space and v_e the effective velocity between sensor and target. A target located in ice perceives a faster changing Doppler frequency due to a compacting of the azimuth sampling and therefore a higher Doppler rate. The Doppler rate may be derived by quantifying the compacting. In Fig. 6, the distances between two Doppler frequency samples for a depth d in the ice are illustrated for the actual case of $n_{\text{ice}} > n_{\text{air}}$ and $n_{\text{ice}} = n_{\text{air}}$, r_1 and r_2, respectively. For the latter case, d is scaled with n_{ice} to account

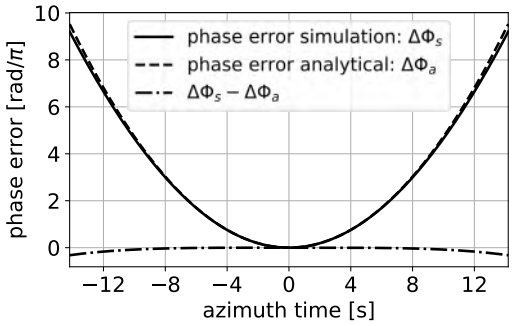

Fig. 7. Comparison of the simulated phase error history according to Fig. 4 and the analytical expression in (8).

for the higher propagation velocity. The ratio (r_2/r_1) relates the Doppler rate for a target in ice to the Doppler rate of a free space assumption, i.e., the Doppler rate used in processing

$$f_R = f_{R,\mathrm{fs}} \cdot \frac{r_2}{r_1} = f_{R,\mathrm{fs}} \cdot \zeta \tag{6}$$

where ζ is used from here on as a short-hand notation. For deriving ζ, the side-looking geometry and refraction in the slant range plane have to be taken into account, resulting in

$$\zeta \simeq \frac{\left(H + d \cdot n_{\mathrm{ice}} \cdot \frac{\cos\theta_i}{\cos\theta_r}\right) \cdot n_{\mathrm{ice}}}{H \cdot n_{\mathrm{ice}} + d \cdot \frac{\cos\theta_i}{\cos\theta_r}} \tag{7}$$

where H is the sensor altitude and θ_i and θ_r are the incidence and refraction angle in the slant range plane at boresight. Following, the phase error can be modeled as:

$$\Delta\Phi(t_a) = f_{R,\mathrm{fs}} \cdot \pi \cdot (\zeta - 1) \cdot t_a^2. \tag{8}$$

Together with the derived model parameter in (7), the expression in (8) provides an estimation of the phase error to be expected for targets located in an ice sheet of constant refractive index when the processing of the data is performed under the common assumption of free space propagation. The model is used in the following sections as inversion model for estimating the depth of an imaged feature d and the refractive index of the ice sheet n_{ice}. To validate the phase error model, in Fig. 7, the analytical expression of (8) is used to replicate the phase error from the analysis of Fig. 4. Obviously, the analytical expression only accounts for the quadratic component, leaving a quartic component after forming the difference.

3) Discussion: The derived relations allow for a simple modeling of the quadratic phase error induced by the propagation of the echoes through ice. For realistic acquisition scenarios, violating the flat Earth assumption in the derivation of the model, the topography can be locally approximated by tangential planes. This approximation holds under the assumption that the topography is varying insignificantly within the area where the echoes of a target impinge on the glacial surface. Considering realistic penetration depths down to 100 m, this area extends in the order of tens of meters, making the approximation tolerable in a wide range of cryospheric application scenarios. The accommodation of realistic refractive index distributions follows a similar rationale. A distribution that is laterally varying insignificantly within the spatial extent spanned by the echo ray paths may be approximated by a constant refractive index even if heterogeneous in vertical dimension. Errors in both approximations result in linear and higher-order phase terms additional to the modeled quadratic term.

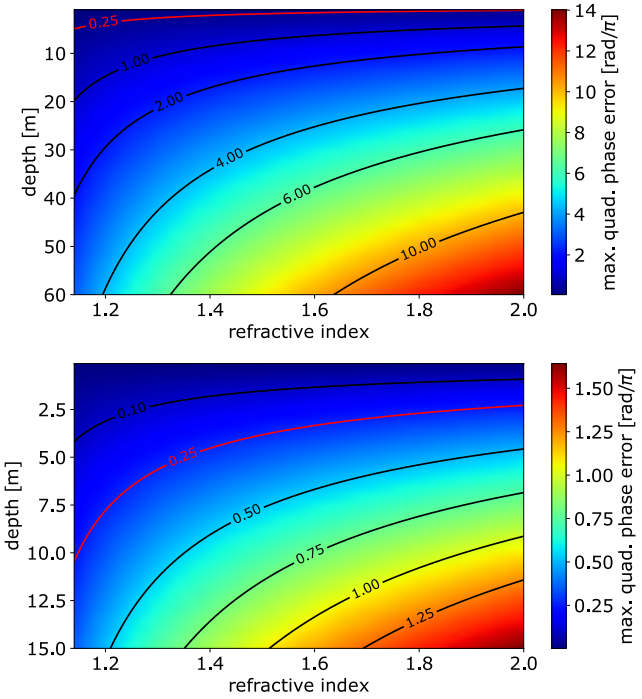

Fig. 8. Maximum quadratic phase error between the correct phase history of a target located in an ice sheet and the phase history of the processing kernel (assuming free space) for varying refractive indices and target depths. (Top) Acquisition parameters chosen according to the F-SAR P-band data depicted in Table I and (bottom) parameters according to TerraSAR-X staring spotlight depicted in Table II.

TABLE II
EXEMPLARY TERRASAR-X STARING SPOTLIGHT ACQUISITION PARAMETERS

Parameter	Value
Center frequency	9.65 GHz
Processed azimuth resolution	0.24 m
Sensor altitude	514 km
Incidence angle	50°

The expression in (8) is used in Fig. 8 to model the maximum quadratic phase error for a wide span of target depths and refractive indices, with the maximum error located at the borders of the synthetic aperture. In the top panel, system parameters correspond to the F-SAR P-band acquisition depicted in Table I with an incident angle on the surface of 50°. The 0.25π contour (red) marks the phase error that is commonly regarded as the limit at which a visual degradation of the SAR image starts and is also frequently stated as an empirical estimation of the accuracy limit of autofocus algorithms. For the F-SAR parameters, almost all constellations in the analyzed parameter space surpass this border. The bottom panel of Fig. 8 displays for TerraSAR-X staring spotlight system parameters, depicted in Table II, that significant phase errors can be expected

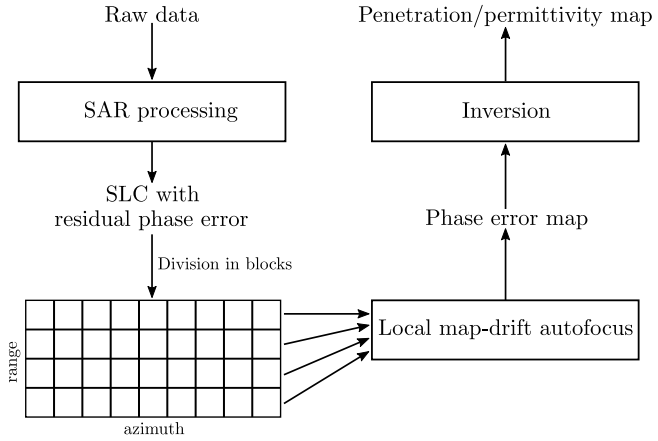

Fig. 9. Block diagram of the proposed single-image inversion approach. Note that the blocks are treated separately in the local map-drift autofocus.

even with the limited penetration expected for X-band signals, if sufficient Doppler bandwidth is available. Computations were performed assuming a spherical Earth approximated by a tangential plane at the point of incidence.

IV. Inversion Approach

Inverting the penetration and permittivity from the phase error present in SAR images necessarily follows a three-stage approach:

1) SAR processing,
2) phase error estimation using autofocus algorithm,
3) inversion of phase errors.

The general procedure of the single-image inversion approach is depicted in Fig. 9. The first stage, SAR processing, describes conventional SAR focusing of the acquired raw data assuming free-space propagation. One preliminary assumption of the approach is that nominal calibration has already been applied on the data, to make sure most of the residual phase signatures are due to the propagation within the volumes of interest. In a second stage, phase errors are estimated using a SAR autofocus algorithm, namely, a local map-drift autofocus applied on the focused single-look complex SAR image (SLC). The autofocus is applied block-wise on the focused data, resulting in a spatially resolved phase error map over the imaged scene. Finally, the estimated phase errors are fed into an inversion model based on the results presented in Section III, which allows the generation of penetration maps or permittivity estimates.

A. Local Map-Drift Autofocus

SAR autofocus approaches are broadly used for the estimation and correction of phase errors to produce high-resolution SAR imagery. The two most commonly applied approaches are the phase gradient autofocus (PGA) and the map-drift autofocus (MDA) [16]. PGA allows for the estimation of arbitrary phase error functions [17], but the necessity of bright, point-like targets restricts the applicability for glacial terrain. Moreover, as the aim of the suggested approach is to estimate and invert scene-induced phase errors, point-like features

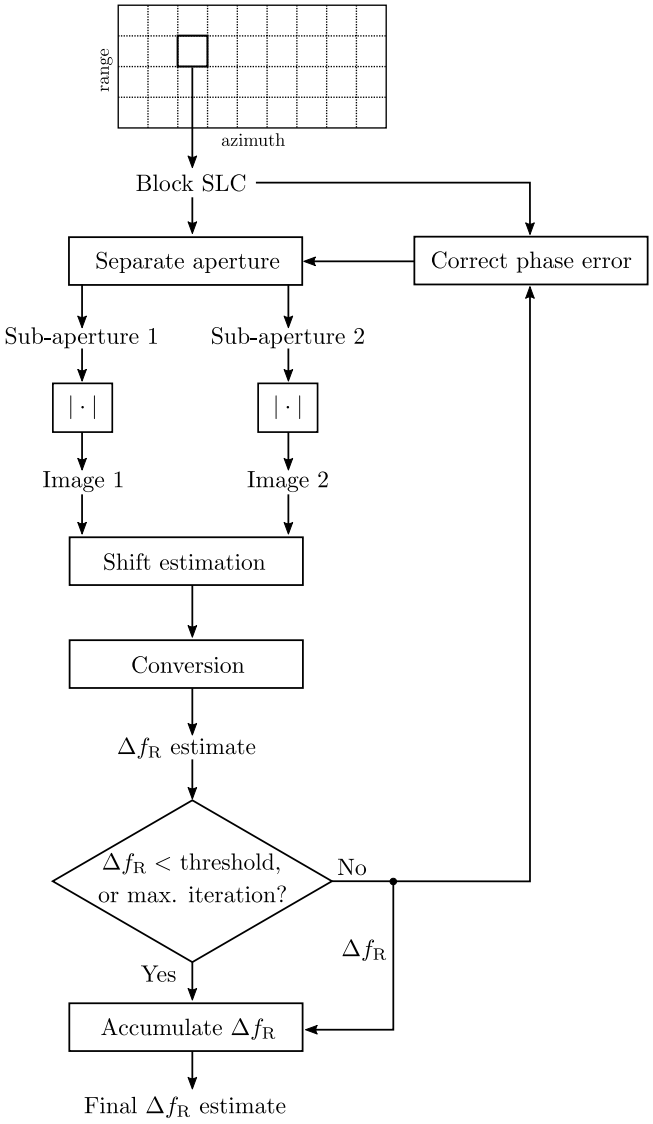

Fig. 10. Block diagram of the local map-drift approach.

would need to be well distributed over the scene. Therefore, an MDA method is preferred, which requires only the presence of contrast features in the scene, such as edges, shadows, and other details. Contrast may be found in subsurface glacial scenes in the form of bed rock reflection or reflection from volume structures. MDA, in its basic form, estimates the second derivative of the phase error function by measuring a linear shift between two images generated from two azimuth sublooks [16]. When considering a phase error dominated by a quadratic term -as described above-, the second derivative is proportional to the error in Doppler rate Δf_R between the processing kernel and the actual phase history, which has been shown in Section III to be roughly proportional to the penetration depth and the permittivity of the volume. This becomes evident by taking a look at the phase history formulation in (4).

In Fig. 10, the basic steps of the developed MDA method are displayed. The autofocus is applied in blocks to get local estimates of the propagation errros. For every block, the shift

between the amplitude images generated from the two azimuth sublooks is estimated using a 2-D cross correlation. Subpixel accuracy is reached by evaluating the slope of the phase of the cross-correlation spectrum, with the slope being connected to the shift of the cross-correlation peak over Fourier theorems. When considering the images formed from two equally sized, non-overlapping sublooks spanning together the whole aperture, the azimuth pixel shift Δx can be related to the Doppler rate error over [30]

$$\Delta f_R = \frac{2 \cdot \Delta x}{B_D^2 \cdot \text{osf}} \cdot f_{R,\text{proc}}^2 \tag{9}$$

where B_D stands for the Doppler bandwidth, osf is the oversampling factor, and $f_{R,\text{proc}}$ describes the Doppler rate used for processing. The MDA is applied in an iterative manner, in which the estimated Δf_R after each iteration is used to correct the quadratic phase error in the spectrum of the block SLC. Typically, this leads to an improvement of the Δf_R estimate, because each correction step leads to a contrast enhancement in the image, allowing a higher accuracy shift measurement. In each iteration k, $f_{R,\text{proc}}$ is updated according to

$$f_{R,\text{proc};k} = f_{R,\text{proc};k-1} + \Delta f_{R;k-1} \tag{10}$$

and Δf_R is accumulated to obtain the total Doppler rate error. The process is terminated when Δf_R reaches a lower threshold, or after a maximum number of iterations. Commonly, after two or three iterations of corrections, the measurement converges and does not improve further. Each block is treated separately and the Doppler rate error is assumed constant over the block. The initial value of $f_{R,\text{proc}}$ is calculated according to (5) at midrange of the considered block. For a thorough description of the particularities and implementation of the map-drift algorithm the reader is referred to Carrara *et al.* [16].

B. Inversion

Based on the error model presented in Section III, we can relate the output of the autofocus to the penetration and the permittivity of the ice volume. According to (6) the model parameter ζ can be estimated as

$$\zeta = 1 + \frac{\Delta f_R}{f_{R,\text{fs}}}. \tag{11}$$

Therefrom, based on (7) the depth of the dominantly scattering scene (i.e., the penetration depth) d is expressed as

$$d = \frac{n_{\text{ice}} \cdot (H - H \cdot \zeta)}{\frac{\cos\theta_i}{\cos\theta_r} \cdot \left(\zeta - n_{\text{ice}}^2\right)}. \tag{12}$$

For obtaining the refractive index n_{ice}, the refraction angle θ_r in (7) has to be expressed according to Snell's law. Solving for n_{ice} results in four roots of which only one takes physical values and has the form

$$n_{\text{ice}} = \sqrt{\frac{-b + \sqrt{b^2 - 4 \cdot a \cdot c}}{2 \cdot a}} \tag{13}$$

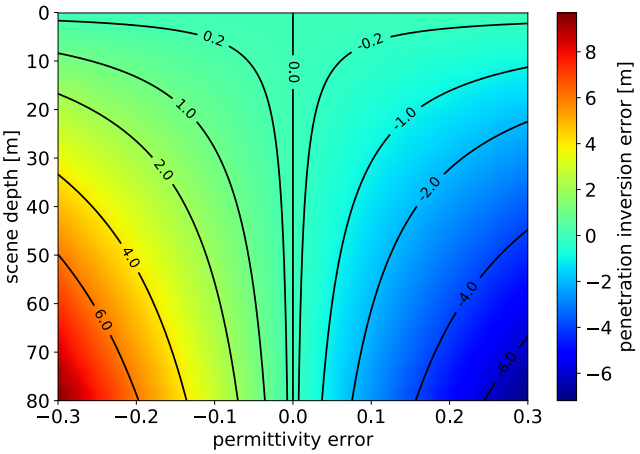

Fig. 11. Error in the penetration depth inversion using the single-image approach resulting from errors in the permittivity knowledge, shown for the F-SAR acquisition geometry, different depths of the scattering scene within the ice sheet, an incident angle on the surface of 45°, and an exemplary true permittivity of the ice sheet of 2.5.

with

$$a = \cos^2(\theta_i) \cdot d^2 \tag{14}$$

$$b = -2 \cdot \zeta \cdot \cos^2(\theta_i) \cdot d^2 - H^2 \cdot (1 - \zeta)^2, \quad \text{and} \tag{15}$$

$$c = \cos^2(\theta_i) \cdot d^2 \cdot \zeta^2 + \sin^2(\theta_i) \cdot H^2 \cdot (1 - \zeta)^2. \tag{16}$$

The dependence of the phase error to both, the depth and the refractive index does not allow for the joint estimation of both parameters from a single acquisition. Previous knowledge of one of them or additional acquisitions are required.

1) Single Image Inversion: Considering a single SAR image being the only available measurement, a penetration depth inversion according to (12) is the primary application scenario of the inversion approach as the refractive index of a snow and ice sheet may be bound to a certain range depending on weather conditions and geographic location. The sensitivity of the penetration inversion to errors in the refractive index (i.e., permittivity) knowledge is shown in Fig. 11 for the example case of an ice sheet with mean permittivity of 2.5, corresponding to medium dense firn. The results are shown for the F-SAR acquisition geometry with a sensor altitude of 4000 m, different depths of the scattering scene within the ice sheet, and an incident angle on the surface of 45°. For penetration depths in the range of several tens of meters, as expected for example in P-band, and representative permittivity error magnitudes up to 0.3, inversion errors with magnitudes up to few meters are to be expected. Note that the sensitivity to permittivity errors of the single-image approach is higher compared to interferometric or tomographic techniques. However, the magnitude of the analyzed penetration errors does not seem to drastically limit the usability for the exploration of ice sheets. Note also that permittivity distributions within ice sheets may exhibit a significant vertical heterogeneity, as introduced in Section III-A. Such permittivity profiles can be naturally incorporated in the form of an effective constant permittivity if an estimate of the vertical profile is available.

For a refractive index inversion, hardly any bound can be put on an estimate of the penetration depth. Additional

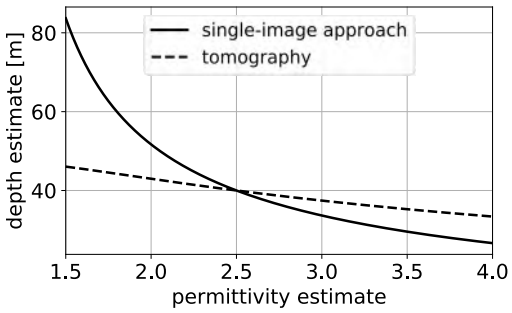

Fig. 12. Depth estimate for erroneous permittivity estimates for a target located 40 m deep in firn of permittivity 2.5, comparing the single-image approach and tomographic products. Note the difference in the sensitivity to the permittivity errors.

in situ measurements are required to constrain the expected penetration.

2) Multiple Image Inversion: If more than one SAR image with different aspect angles on the scene are available, the geometric diversity may be exploited to jointly estimate the penetration and permittivity. At this point the potential of a joint estimation using the single-image approach and the information from multiple acquisitions is outlined briefly. A dedicated assessment is left for future research.

Considering coherent acquisitions in the form of SAR interferometry or tomography, the single-image approach may be used to calibrate the refractive index estimate to obtain unbiased penetration estimates and tomographic imaging. The calibration relies on the above introduced property that interferometry and tomography exhibit a different sensitivity to permittivity errors than the single-image approach, leading to diverging depth estimates for erroneous permittivity estimates. This characteristic is displayed in Fig. 12, comparing the depth estimate of a target using permittivity corrected tomography and the single-image approach. The target is located in firn of permittivity 2.5 at a depth of 40 m acquired with an incidence angle of 50°. Results are shown for a wide span of permittivity estimates. The correct permittivity can be calibrated according to the best agreement between the two estimates. The calibration is unambiguous but is limited by the accuracy of the two measurements.

Besides coherent acquisitions, repeat-pass acquisitions with large baselines may be exploited to jointly solve the system of depth and permittivity by additionally evaluating the range shift of subsurface image features between the geometrically coregistered acquisitions. The range shift is a consequence of the sensitivity of the refraction effect to the incidence angle on the ice surface.

V. Validation With F-SAR Data

A. Experimental Data

The experimental dataset utilized in this study was acquired in May 2015 in the frame of the ARCTIC15 campaign by DLR's airborne sensor F-SAR [31]. The test site is the K-transect in South-West Greenland (67°4′ N, 49°23′ W) and its location is depicted in Fig. 13. The analyzed data

Fig. 13. Location of the K-transect test site in South-West Greenland (67°4′ N, 49°23′ W).

are multibaseline, fully polarimetric P-band acquisitions over approximately 100 km with a swath of 3 km from the west coast to the inner part of the ablation zone of the ice sheet. The campaign consisted of eight parallel flight tracks at an altitude of approximately 4000 m with a maximum horizontal separation of 270 m. The acquisition parameters are depicted in Table I. A single-pass X-band digital elevation model (DEM) was acquired and used for processing and geocoding. The DEM is referenced to corner reflectors on the ice sheet surface. Topography-dependent, navigation-based motion compensation was carried out during processing.

The imaged area is part of the ablation zone of the glacier consisting of solid glacier ice covered with a dry snow layer [32]. An ice-free (i.e., surface) section is located on the left side of the images. Only few snow and ice fields are scattered in this area. The test site was chosen for this article due to its large spatial extent, the predictable refractive index of solid ice, and the transition between ice-free terrain and the ice sheet. An overview on the imaged scene and first insight in the scattering behavior is provided by the quick looks in Fig. 14, showing an amplitude image in HH polarization and a polarimetric decomposition, i.e., Fig. 14(a) and (b), respectively. On the left-hand side of the swath, the ice-free section is located. The ice-covered area, taking the largest part of the scene, may be roughly distinguished into two different backscatter behaviors. A SAR tomographic analysis of the test site in [33] displays that the dark regions in the amplitude image, corresponding to the blue colored areas in the Pauli image, are dominated by scattering from near surface layers, whereas the bright areas, i.e., green colored, can be attributed to volumetric scattering from subsurface layers.

B. Penetration Inversion Using the Single-Image Approach

For simplicity reasons, a rectangular crop of the imaged scene is utilized to test the single-image approach. The image crop extends 2.5 km in range and 100 km in azimuth and is shown in Fig. 15(a). HV polarization is chosen, due to

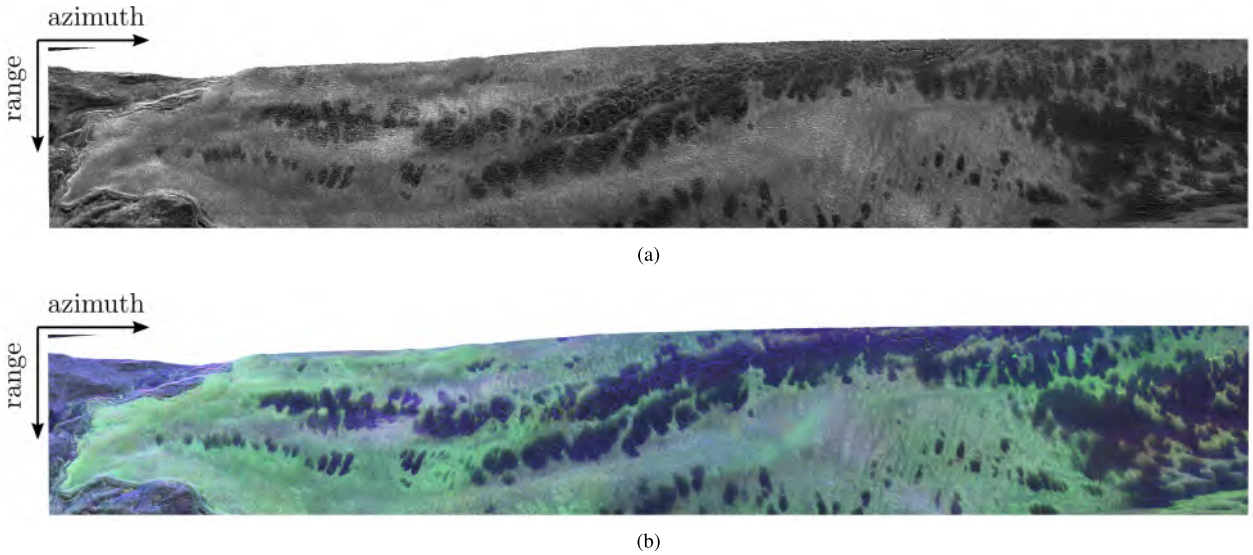

Fig. 14. (a) P-band amplitude image of the K-transect scene in HH polarization. (b) Pauli polarimetric decomposition of the scene. The blue color indicates a backscatter behavior dominated by surface scattering and the green color indicates dominant volume scattering.

the high sensitivity to volumetric scattering and therefore enhanced probability for subsurface features dominating the backscatter. The local map-drift approach is applied in a block-wise manner on the processed data. Blocks have a size of 2048 × 256 samples in azimuth and range, respectively. The choice of block size is a trade-off between spatial resolution and accuracy, or rather reliability, of the measurement. A block needs to be sufficiently large to contain enough contrast features for the cross correlation to provide reliable shift estimates. Especially in the low-contrast case of an ice sheet, relatively large blocks have to be used. The sensitivity of the cross correlation to low-amplitude features is strengthened by applying it on the square-root of the amplitude image. In order to track the changes of the autofocus estimates, 90% overlap between consecutive blocks is used.

Three iterations of local corrections are carried out for each block in the present example and azimuth shifts, i.e., corresponding Doppler rate errors, are accumulated. Despite the relatively large block size, 1.2% of the blocks provided erroneous measurements that do not converge throughout the iterations or exhibit invalid shift values. The estimates from those blocks are discarded and not shown in the results of Fig. 15. In Fig. 15(b) the resulting map of accumulated azimuth shifts is shown. It is evident that the measurement undoubtedly replicates the physical appearance of the ice sheet. The rocky terrain with scattered snow fields on the left-hand side leads to almost no shifts, whereas the area spanned by the ice sheet results in varying negative shifts. The dark areas in the amplitude image, dominated by surface scattering, provide mainly small shifts. Overall, shift magnitudes are increasing toward the right-hand side. Measured azimuth shifts, i.e., corresponding Doppler rate errors, are inverted to depth estimates of the scattering scene within the glacial volume, where the refractive index is chosen as $n_{\text{ice}} = (3.1)^{1/2}$ corresponding to almost solid ice. For each block, the inversion model in (12) requires estimates of the sensor altitude with respect to a tangential plane at the point where the echoes impinge on the surface and the local incidence angle on the surface with respect to the surface normal. This information is provided from the X-band DEM in X-band and from the geocoding process during the P-band SAR data processing. Local incidence angles, used in the inversion, are averaged over the block and depicted in Fig. 15(c). The final depth inversion is displayed in Fig. 15(d), showing penetration depths down to −84 m. The general appearance replicates that of the azimuth shifts. Note the slight dependence with the incidence angle if comparing the color scale of Fig. 15(b) and (d), especially noticeable in far-range. The residual estimate after all corrective iterations in the map-drift approach is shown in Fig. 15(e). It provides a fair estimate of the possibly present measurement noise. Obviously, the error is lower for less penetration, i.e., smaller azimuth shifts. Overall, it does not exceed 4.5 m in the present scene and the mean error amounts to 0.52 m.

C. Validation With Tomograms

Due to the availability of tomographic acquisitions of the analyzed scene, we have conducted a qualitative validation of the single-image approach. The multibaseline acquisitions in P-band are coregistered and tomographic processing is performed using all available baselines and a Capon beamformer for focusing in elevation dimension. Multilooking with a 2048 × 256 window (azimuth × range) is performed to increase correlation with the block-wise map-drift measurement of equivalent size. Tomographic focusing is performed assuming free space propagation. The tomographic products represent 3-D images of the scattering glacial volume. Fig. 16 shows three vertical slices along azimuth of the glacial volume together with the overlaid depth estimates of the single-image approach. The tomograms are registered to the acquired

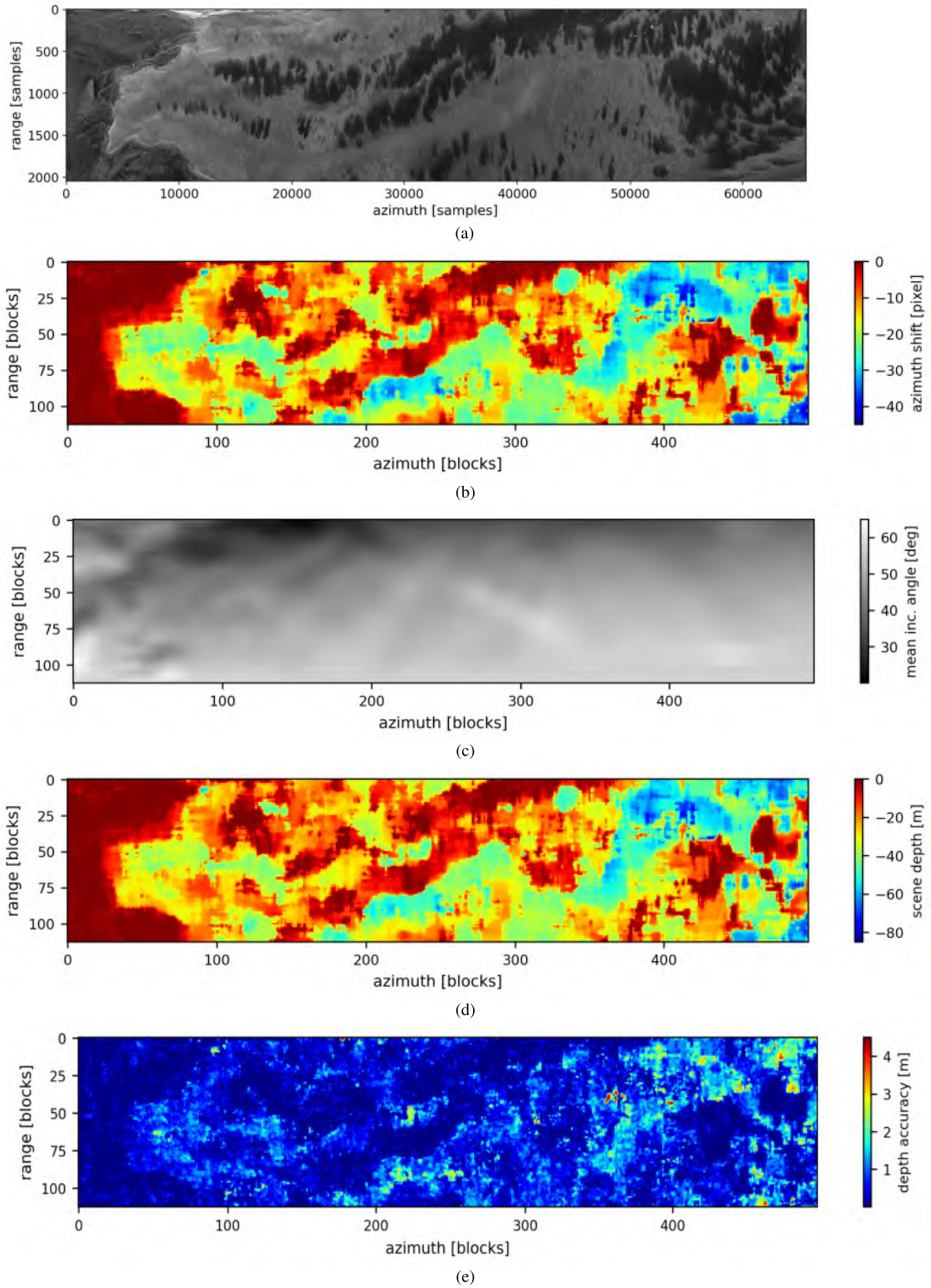

Fig. 15. Depth inversion results using the new single SAR image inversion approach on a scene from the K-transect in South-West Greenland showing: (a) amplitude image of the scene in HV polarization; (b) estimated azimuth shifts accumulated over three iterations of the local map-drift approach; (c) local incidence angles averaged in each block; (d) estimated scattering depth; and (e) accuracy of depth estimate derived from residual Doppler rate error estimate after the last iteration of the local map-drift algorithm.

X-band DEM, so that the zero position of the vertical coordinate z corresponds to the surface and negative values indicate the subsurface. Furthermore, an amplitude normalization along z for every azimuth sample is performed to enhance the interpretability of the backscatter distribution. To account for the reduced propagation velocity in the ice sheet and refraction

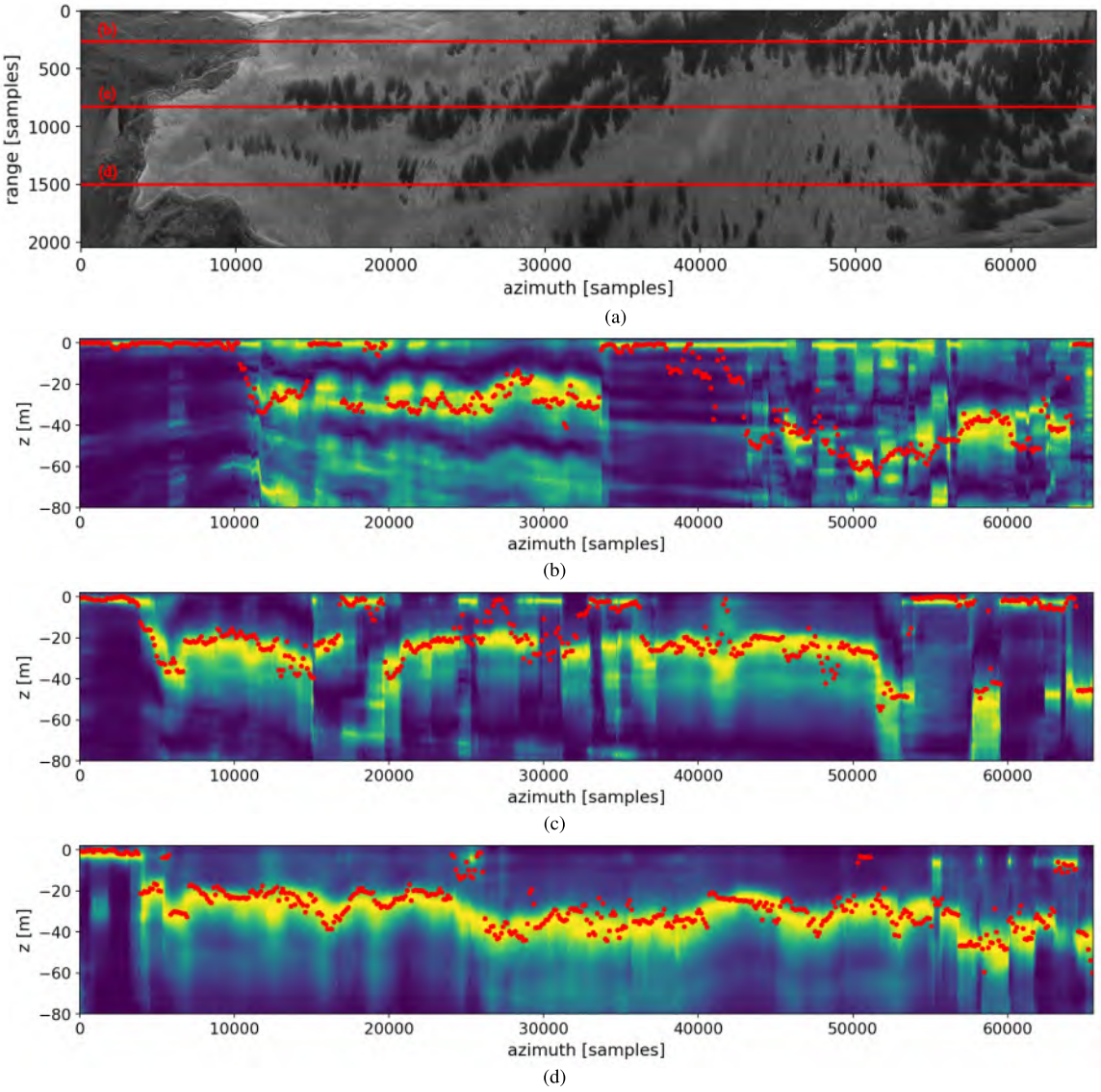

Fig. 16. Tomographic validation of the new single SAR image inversion approach showing three tomograms [(b)–(d)] through the whole azimuth extent of the scene [shown in (a)] along the red lines. The zero position of the z coordinate is registered to the surface and negative z values indicate the subsurface. Tomograms are normalized along z. Red dots indicate the depth estimate using the single-image approach.

on the surface, a geometric correction is applied according to the relations given in [15], using the corresponding local incidence angles and the same refractive index as used for the single-image approach, i.e., $n_{\text{ice}} = (3.1)^{1/2}$. Overlaying the tomograms, the corresponding depth estimates using the single-image approach are plotted as red dots. The tomograms are located at the range position coinciding with a block center. Note the overall good correspondence between the tomograms and the depth estimates using the single-image approach. Especially in areas where the backscatter is dominated by either a surface or distinct subsurface return, the agreement shows good consistency. Discrepancies mainly arise if multiple scattering sources at different depths are present [i.e., in Fig. 16(d) around azimuth sample 25 000], leading to an averaging effect in the depth inversion, or if the depth of the dominant backscatter sources changes laterally fast [i.e. in Fig. 16(c) from azimuth samples 25 000 to 35 000]. The strong inconsistency in Fig. 16(b) around sample 40 000 may be explained by the fact that nearby subsurface scene features within the range extent of the analyzed block influenced the map-drift measurement even if not visible in the strongly multilooked tomograms. A similar argumentation may be used to explain other deviations in the two measurements. Note that high backscatter intensity does not necessarily imply good contrast, which controls the quality of the autofocus results. According to the concept for permittivity calibration introduced in Section IV-B, the refractive index of $n_{\text{ice}} = (3.1)^{1/2}$ for both, the depth inversion using the single-image approach and the correction of the tomograms is chosen according to a visual calibration, by maximizing the apparent correlation between the measurements. The permittivity value fits remarkably well to the properties of solid ice in the ablation zone.

VI. Conclusion and Discussion

Inspired by the difficulty of designing interferometric and tomographic SAR missions for planetary exploration, a strategy for the imaging of volumetric structures using low-frequency SAR images with moderate to good resolution has been presented. The developed approach is based on an inversion procedure relying on single-image single-polarization SAR acquisitions to estimate volume parameters of ice sheets, namely, the penetration and the dielectric permittivity of the ice. It exploits phase errors present in the SAR image resulting from uncompensated nonlinear propagation of the radar echoes through ice.

As part of the single-image approach, a simple inversion model has been presented, allowing to link the phase errors to the depth of the scattering scene within an ice sheet, the average refractive index of the penetrated glacial volume, and the acquisition geometry. Based on the derived model it has been demonstrated that severe phase errors are to be expected in high-resolution SAR acquisitions of ice sheets, leading to strong defocusing of subsurface scenes. The phase errors can be effectively quantified and spatially resolved with the proposed local map-drift autofocus algorithm, from which penetration and permittivity estimates can be derived via the phase error model. Using high-resolution airborne P-band SAR data acquired over the Greenland ice sheet it has been demonstrated that the single-image approach delivers largely reliable penetration estimates when comparing them to tomographic products. The simplicity promotes the approach for SAR mission scenarios aimed at the exploration of planetary ice sheets such as the ice crust of Saturn's moon Enceladus or Jupiter's moon Europa. Furthermore, the potential capability of the single-image approach for calibrating the permittivity estimate for interferometric and tomographic acquisitions may be highly relevant for mitigating interferometric estimation biases over ice sheets in missions such as TanDEM-X or future missions such as Biomass and the Earth Explorer 10 candidate Harmony. A thorough assessment is left for future work.

The fact that the accuracy and reliability of the single-image approach is bounded by the map-drift shift estimation performance using a cross correlation suggests that the approach may fail in highly homogeneous cryospheric scenes where not sufficient contrast is present. However, the analyzed scene comprises a wide spectrum of contrast level, promoting it as a suitable example for a variety of cryospheric scenes. The use of SAR acquisitions in cross-polarization is recommended to provide a higher sensitivity to subsurface features compared to acquisitions in copolarization. Though, there is no general constraint on the polarization for the applicability of the single-image approach. The presented validation of the single-image approach using P-band SAR tomographic products provides a qualitative demonstration of its validity and potential. As part of future activities, further cryospheric F-SAR campaigns with the collection of ground measurements are planned. In particular, the measurements of the local permittivity and the deployment of reference targets within boreholes in the ice sheet may support a consistent data-driven quantitative assessment of the accuracy and precision of the single-image approach.

Obviously, the proposed technique is not restricted to cryospheric applications but may be suitable for other semi-transparent natural media with significant permittivity difference to air, i.e., sand or soil. Furthermore, inverting atmospheric parameters from propagation induced phase errors may be achieved in similar manner.

Acknowledgment

This study was financially supported by the German Space Agency at the German Aerospace Center (DLR) with funds from the German Federal Ministry for Economic Affairs and Energy (BMWi) under the Project EnEx-AsGAr, registration no. 50NA1708. The authors would like to thank M. Stelzig (LHFT, FAU) and Prof. M. Vossiek (LHFT, FAU) for the support in the EnEx Project. They would also like to thank everyone involved in the ARCTIC15 campaign, which was conducted by DLR and ETH Zurich, Zurich, Switzerland. They would also like to thank Dr. G. Fischer (DLR) for the valuable discussions and support with the F-SAR data.

References

[1] D. G. Vaughan *et al.*, "Observations: Cryosphere," in *Climate Change 2013: The Physical Science Basis. Contribution of Working Group I to the Fifth Assessment Report of the Intergovernmental Panel on Climate Change*, T. F. Stocker *et al.*, Eds. Cambridge, U.K.: Cambridge Univ. Press, 2015.

[2] J. A. MacGregor *et al.*, "Radiostratigraphy and age structure of the Greenland ice sheet," *J. Geophys. Res., Earth Surf.*, vol. 120, no. 2, pp. 212–241, Feb. 2015.

[3] R. Orosei *et al.*, "Radar evidence of subglacial liquid water on Mars," *Science*, vol. 361, no. 6401, pp. 490–493, 2018.

[4] I. B. Smith, N. E. Putzig, J. W. Holt, and R. J. Phillips, "An ice age recorded in the polar deposits of Mars," *Science*, vol. 352, no. 6289, pp. 1075–1078, May 2016.

[5] F. Hélière, C.-C. Lin, H. Corr, and D. Vaughan, "Radio echo sounding of pine Island Glacier, West Antarctica: Aperture synthesis processing and analysis of feasibility from space," *IEEE Trans. Geosci. Remote Sens.*, vol. 45, no. 8, pp. 2573–2582, Aug. 2007.

[6] J. J. Legarsky, S. P. Gogineni, and T. L. Akins, "Focused synthetic aperture radar processing of ice-sounder data collected over the Greenland ice sheet," *IEEE Trans. Geosci. Remote Sens.*, vol. 39, no. 10, pp. 2109–2117, Oct. 2001.

[7] S. Shabtaie and C. R. Bentley, "Ice-thickness map of the West Antarctic ice streams by radar sounding," *Ann. Glaciol.*, vol. 11, pp. 126–136, Jan. 1988.

[8] R. Jordan *et al.*, "The Mars express MARSIS sounder instrument," *Planet. Space Sci.*, vol. 57, nos. 14–15, pp. 1975–1986 2009.

[9] R. Seu *et al.*, "SHARAD sounding radar on the Mars reconnaissance orbiter," *J. Geophys. Res.*, vol. 112, no. E5, 2007.

[10] E. W. Hoen and H. A. Zebker, "Penetration depths inferred from interferometric volume decorrelation observed over the Greenland ice sheet," *IEEE Trans. Geosci. Remote Sens.*, vol. 38, no. 6, pp. 2571–2583, Nov. 2000.

[11] J. J. Sharma, I. Hajnsek, K. P. Papathanassiou, and A. Moreira, "Estimation of glacier ice extinction using long-wavelength airborne Pol-InSAR," *IEEE Trans. Geosci. Remote Sens.*, vol. 51, no. 6, pp. 3715–3732, Jun. 2013.

[12] G. Parrella, I. Hajnsek, and K. P. Papathanassiou, "Polarimetric decomposition of L-band PolSAR backscattering over the Austfonna ice cap," *IEEE Trans. Geosci. Remote Sens.*, vol. 54, no. 3, pp. 1267–1281, Mar. 2016.

[13] S. Tebaldini, T. Nagler, H. Rott, and A. Heilig, "Imaging the internal structure of an Alpine glacier via L-band airborne SAR tomography," *IEEE Trans. Geosci. Remote Sens.*, vol. 54, no. 12, pp. 7197–7209, Dec. 2016.

[14] M. Pardini, G. Parrella, G. Fischer, and K. Papathanassiou, "Single and multipolarimetric P-band SAR tomography of subsurface ice structure," in *Proc. 11th Eur. Conf. Synth. Aperture Radar (EUSAR)*, 2016, pp. 1–6.

[15] F. Banda, J. Dall, and S. Tebaldini, "Single and multipolarimetric P-band SAR tomography of subsurface ice structure," *IEEE Trans. Geosci. Remote Sens.*, vol. 54, no. 5, pp. 2832–2845, May 2016.

[16] W. Carrara, R. Goodman, and R. Majewski, *Spotlight Synthetic Aperture Radar: Signal Processing Algorithms* (Artech House Remote Sensing Library). Norwood, MA, USA: Artech House, 1995.
[17] D. E. Wahl, F. H. Eichel, D. C. Ghiglia, and C. V. Jakowatz, "Phase gradient autofocus—A robust tool for high resolution SAR phase correction," *IEEE Trans. Aerosp. Electron. Syst.*, vol. 30, no. 3, pp. 827–835, Jul. 1994.
[18] O. O. Bezvesilniy, I. M. Gorovyi, and D. M. Vavriv, "Estimation of phase errors in SAR data by local-quadratic map-drift autofocus," in *Proc. 13th Int. Radar Symp.*, May 2012, pp. 376–381.
[19] D. P. Belcher, "Theoretical limits on SAR imposed by the ionosphere," *IET Radar, Sonar Navigat.*, vol. 2, no. 6, pp. 435–448, Dec. 2008.
[20] Z. Li, S. Quegan, J. Chen, and N. C. Rogers, "Performance analysis of phase gradient autofocus for compensating ionospheric phase scintillation in BIOMASS P-band SAR data," *IEEE Geosci. Remote Sens. Lett.*, vol. 12, no. 6, pp. 1367–1371, Jun. 2015.
[21] A. Benedikter *et al.*, "Potential of a multimodal orbital radar mission for the exploration of Enceladus," in *Proc. EGU Gen. Assem. Conf. Abstr.*, May 2002, p. 19621.
[22] F. Ulaby, M. C. Dobson, and J. L. Á. Pérez, *Handbook of Radar Scattering Statistics for Terrain*. Norwood, MA, USA: Artech, 2019.
[23] M. Born *et al.*, *Principles of Optics: Electromagnetic Theory of Propagation, Interference and Diffraction of Light*, 7th ed. Cambridge, U.K.: Cambridge Univ. Press, 1999.
[24] C. Mätzler, "Improved born approximation for scattering of radiation in a granular medium," *J. Appl. Phys.*, vol. 83, no. 11, pp. 6111–6117, Jun. 1998.
[25] C. Matzler and U. Wegmuller, "Dielectric properties of freshwater ice at microwave frequencies," *J. Phys. D, Appl. Phys.*, vol. 20, no. 12, pp. 1623–1630, Dec. 1987.
[26] A. Kovacs, A. J. Gow, and R. M. Morey, "The *in-situ* dielectric constant of polar firn revisited," *Cold Regions Sci. Technol.*, vol. 23, no. 3, pp. 245–256, May 1995.
[27] J. C. Curlander and R. N. McDonough, *Synthetic Aperture Radar: Systems and Signal Processing*. Hoboken, NJ, USA: Wiley, 1991.
[28] G. Glaeser and H. Schröcker, "Reflections on refractions," *J. Geometry Graph.*, vol. 4, no. 1, pp. 1–18, 2000.
[29] A. Benedikter and M. Rodriguez-Cassola, "A volumetric P-band imaging concept for the SAR exploration of Saturn's moon Enceladus," in *Proc. 13th Eur. Conf. Synth. Aperture Radar (EUSAR)*, 2016, pp. 1–6.
[30] F.-K. Li, D. Held, J. Curlander, and C. Wu, "Doppler parameter estimation for spaceborne synthetic-aperture radars," *IEEE Trans. Geosci. Remote Sens.*, vol. GRS-23, no. 1, pp. 47–56, Jan. 1985.
[31] R. Horn, A. Nottensteiner, and R. Scheiber, "F-SAR-DLR's advanced airborne SAR system onboard DO228," in *Proc. 7th Eur. Conf. Synth. Aperture Radar*, 2008, pp. 1–4.
[32] G. Parrella, G. Fischer, I. Hajnsek, and K. P. Papathanassiou, "Mapping the ice zones of West Greenland using multi-frequency polarimetric SAR data," in *Proc. 12th Eur. Conf. Synth. Aperture Radar (EUSAR)*, 2018, pp. 1–6.
[33] G. Parrella, G. Fischer, M. Pardini, K. Papathanassiou, and I. Hajnsek, "Interpretation of polarimetric and tomographic signatures from glacier subsurface: The K-transect case study," in *Proc. IEEE Int. Geosci. Remote Sens. Symp. (IGARSS)*, Jul. 2019, pp. 4927–4930.

Andreas Benedikter was born in Munich, Germany, in 1994. He received the B.Sc. degree in medical engineering and the M.Sc. degree (Hons.) in electrical engineering and information technology from Friedrich-Alexander University Erlangen-Nürnberg (FAU), Erlangen, Germany, in 2017 and 2019, respectively, where he is currently pursuing the Ph.D. degree with the Institute of Microwaves and Photonics.

In 2017, he was with the University of Bristol, Bristol, U.K. Since 2018, he has been with the Microwaves and Radar Institute, German Aerospace Center (DLR), Oberpfaffenhofen, Germany, as a Research Scientist. His research interests include radar signal processing, SAR autofocus techniques, and the study of future radar mission concepts, especially in the context of planetary exploration missions.

Mr. Benedikter received the ARGUS Science Award by Hensoldt and the VDE-Award, both in 2019.

Marc Rodriguez-Cassola was born in Barcelona, Spain, in 1977. He received the Ingeniero degree in telecommunication engineering from the Universidad Pública de Navarra, Pamplona, Spain, in 2000, the Licenciado (M.Sc.) degree in economics from the Universidad Nacional de Educación a Distancia, Madrid, Spain, in 2012, and the Ph.D. degree in electrical engineering from the Karlsruhe Institute of Technology, Karlsruhe, Germany, in 2012.

From 2000 to 2001, he was a Radar Hardware Engineer with the Study Center of Terrestrial and Planetary Environments (CETP)/French National Center for Scientific Research (CNRS), Saint Maur des Fosses, France. From 2001 to 2003, he was a Software Engineer with Altran Consulting, Munich, Germany. Since 2003, he has been with the German Aerospace Center, Microwaves and Radar Institute, Weßling, Germany, where he is leading the SAR Missions Group. His research interests include radar signal processing, SAR end-to-end simulation, SAR processing and calibration algorithms, crisis theory, and radar mission analysis and applications.

Felipe Betancourt-Payan was born in Colombia in 1993. He received the bachelor's degree in aerospace engineering from Carlos III University, Madrid, Spain, in 2017, and the master's degree in space science and technology (SpaceMaster) from the Luleå University of Technology, Sweden and Université Toulouse III—Paul Sabatier, France, in 2019. He is currently pursuing the Ph.D. degree with Microwaves and Radar Institute, German Aerospace Center (DLR-HR), Weßling, Germany.

Since 2019, he has been with the Microwaves and Radar Institute, German Aerospace Center (DLR-HR). His research interests involve the use of autofocus techniques for characterization of geophysical parameters using low frequency SAR.

Gerhard Krieger (Fellow, IEEE) received the Dipl.-Ing. (M.S.) and Dr.-Ing. (Ph.D.) (Hons.) degrees in electrical and communication engineering from the Technical University of Munich, Munich, Germany, in 1992 and 1999, respectively.

From 1992 to 1999, he was with the Ludwig Maximilians University, Munich, where he conducted multidisciplinary research on neuronal modeling and nonlinear information processing in biological and technical vision systems. Since 1999, he has been with the Microwaves and Radar Institute of the German Aerospace Center (DLR), Oberpfaffenhofen, Germany, where he started as a Research Associate developing signal processing algorithms for a novel forward-looking radar system employing digital beamforming on receive. From 2001 to 2007, he led the New SAR Missions Group, which pioneered the development of advanced bistatic and multistatic radar systems, such as TanDEM-X, as well as innovative multichannel SAR techniques and algorithms for high-resolution wide-swath SAR imaging. Since 2008, he has been the Head of the Radar Concepts Department, which hosts about 40 scientists focusing on new SAR techniques, missions, and applications. He has been serving as Mission Engineer for TanDEM-X and he also made major contributions to the development of the Tandem-L mission concept, where he led the Phase-0 and Phase-A studies. Since 2019, he holds also professorship with the Friedrich-Alexander University Erlangen-Nürnberg (FAU), Erlangen, Germany. He is the author or coauthor of more than 100 peer-reviewed journal papers, nine invited book chapters, more than 400 conference papers, and more than 20 patents.

Prof. Krieger has been an Associate Editor for the IEEE TRANSACTIONS ON GEOSCIENCE AND REMOTE SENSING since 2012. In 2014, he served as the Technical Program Chair for the European Conference on Synthetic Aperture Radar and as a Guest Editor for the IEEE JOURNAL OF SELECTED TOPICS IN APPLIED EARTH OBSERVATIONS AND REMOTE SENSING. He received several national and international awards, including two Best Paper Awards at the European Conference on Synthetic Aperture Radar, two Transactions Prize Paper Awards of the IEEE Geoscience and Remote Sensing Society, and the W.R.G. Baker Prize Paper Award from the IEEE Board of Directors.

Alberto Moreira (Fellow, IEEE) received the B.S.E.E. and M.S.E.E. degrees from the Aeronautical Technological Institute (ITA), São José dos Campos, Brazil, in 1984 and 1986, respectively, and the Dr.Eng. degree (Hons.) from the Technical University of Munich, Munich, Germany, in 1993.

From 1996 to 2001, he was the Chief Scientist and Engineer with the SAR Technology Department, German Aerospace Center (DLR), Oberpfaffenhofen, Germany. Under his leadership, the DLR airborne SAR system has been upgraded to operate in innovative imaging modes, such as polarimetric SAR interferometry, tomography, and holography. Since 2001, he has been the Director of the Microwaves and Radar Institute, DLR, and a Full Professor of microwave remote sensing with the Karlsruhe Institute of Technology (KIT), Karlsruhe, Germany. His DLR's Institute contributes to several scientific programs and projects for spaceborne SAR missions, such as TerraSAR-X, TanDEM-X, SAR-Lupe, and SARah, as well as Kompsat-6, PAZ, Sentinel-1, BIOMASS, and ROSE-L. The mission TanDEM-X, led by his institute, has generated a global, high-resolution digital elevation model of the Earth with unprecedented accuracy. He is the initiator and a principal investigator (PI) for this mission. He is the author or a coauthor of more than 450 publications in international conferences and journals and eight book chapters. He holds more than 40 international patent grants in the radar and antenna field. His professional interests and research areas encompass spaceborne radar end-to-end system design, microwave techniques and system concepts, signal processing, and remote sensing applications.

Dr. Moreira was a recipient of several international awards, including the IEEE AESS Nathanson Award in 1999 for the Young Radar Engineer of the Year, the IEEE Kiyo Tomiyasu Field Award in 2007, the IEEE W. R. G. Baker Award from the IEEE Board of Directors in 2012, and the IEEE GRSS Distinguished Achievement Award in 2014. He and his colleagues received the GRSS Transactions Prize Paper Awards in 1997, 2001, and 2007 and the GRSS Letters Prize Paper Award in 2015 and 2017. He has served as the President of the IEEE Geoscience and Remote Sensing (GRS) Society in 2010 and the General Co-Chair of IGARSS in 2012. He has been serving as the Chair of the Major Awards of the GRS Society since 2017. He was the Founder and Chair of the GRSS German Chapter from 2003 to 2008 and has served as an Associate Editor for the IEEE GRS LETTERS from 2003 to 2007 and the IEEE TRANSACTIONS ON GEOSCIENCE AND REMOTE SENSING since 2005. From 2012 to 2017, he has served as a Principal Investigator for the Helmholtz Alliance Remote Sensing and Earth System Dynamics and is currently the PI for Tandem-L, a radar mission proposal for the global observation of dynamic processes on Earth's surface with unprecedented quality and resolution.

EUSAR 2021 . ISBN 978-3-8007-5457-1 / ISSN 2197-4403 . ©VDE VERLAG GMBH . Berlin . Offenbach

A Volumetric P-band Imaging Concept for the SAR Exploration of Saturn's Moon Enceladus

Andreas Benedikter[a,b] and Marc Rodriguez-Cassola[a]
[a]Microwaves and Radar Institute, German Aerospace Center (DLR), Germany, andreas.benedikter@dlr.de
[b]Institute of Microwaves and Photonics, University of Erlangen-Nuremberg (FAU), Germany

Abstract

In the frame of the Enceladus Explorer Initiative (EnEx) conducted at the German Aerospace Center (DLR), we are currently investigating the potential of an orbital Synthetic Aperture Radar (SAR) instrument to contribute in the understanding of the surface and subsurface structure and composition of the Enceladean ice crust and the involved geophysical processes. The proximity of Saturn constrains the stable solutions for an Enceladus SAR orbiter. The resulting orbit geometries offer the possibility to exploit extremely wide angular observations, with typical integration times of about 800 s to 6000 s, which can be used for a single-pass volumetric imaging approach to provide 3-D metric resolution imagery of the ice crust. The approach is based on the sensitivity of the SAR surveys to the permittivity profiles of the ice. Additionally, we explore the potential of multi-pass acquisitions to provide both accurate imaging and permittivity estimation.

1 Introduction

Saturn's ice-covered moon Enceladus became the focus of great scientific attention, since during the NASA Cassini mission geyser-like jets were discovered, erupting through the few kilometer thick ice crust in the south polar region [1]. Backed by gravitational measurements, this discovery suggests the presence of a global ocean underneath the ice crust. With the Enceladus Explorer Initiative (EnEx), the German Aerospace Center (DLR) is currently developing a mission concept comprising a landing on Enceladus close to one of the jets and a subsequent probing of the Enceladean ice and water. Filling the present gap of knowledge about the surface and subsurface ice structure and composition is crucial for the realisation of such a lander mission and is fundamental for understanding the geophysical processes on the moon.

In the frame of EnEx, we are currently investigating the potential of a multi-modal orbital radar instrument to be used as a companion to the lander mission. Among other modes, the radar is intended to work as multi-frequency SAR instrument (e.g., Ka and P-band) to image ice features on both surface and subsurface. It is well known that low frequency SAR systems offer a unique capability to reveal subsurface ice structures, due to the penetration capabilities of electromagnetic waves up to few gigahertz. Especially tomographic SAR imaging offers the opportunity to observe the vertical structure of ice sheets, which allows for the discrimination of interfaces (e.g., space/ice, internal layers, permittivity profiles), water content or subsurface features. Tomographic SAR imaging over ice has been demonstrated in several airborne campaigns [2], [3].

In the case of Enceladus, the orbit characteristics, coupled with uncertain spacecraft control accuracy, may prevent the possibility of consistent tomographic acquisitions. We are currently analysing the potential of subsurface -or even volumetric- imaging concepts adapted to the specific orbit geometry and control capabilities. The aim of this paper is to discuss general mission aspects for a P-band SAR orbiter, including orbit considerations, coverage, resolution and sensitivity. Besides, we investigate the potential of a volumetric imaging concept and processing approach using single and multiple acquisitions, relying on the phase inconsistencies introduced on the radar echoes by the propagation within the ice due to permittivity changes.

2 Mission Aspects

The design of radars for planetary missions is usually subject to tight restrictions concerning mass and allocated space. At the current state, the development of the different mission components for EnEx is carried out as separated conceptional studies. Subject to current estimates, the P-band SAR system described in **Table 1** represents a conservative assumption for the purpose of the study. Note the suggested reflector antenna may allow for the operation of the radar with two different frequencies for simultaneous surface imaging.

2.1 Orbit Considerations

The orbit selection plays a fundamental role in the performance of the system and its ability to fulfill the observation requirements. The proximity of Saturn has a strong influence on the orbital mechanics, constraining the stable solutions for an Enceladus SAR orbiter.

The dynamics describing the motion of an orbiter about Enceladus are subject to the so-called restricted-

Parameter	Value
Average transmit power $P_{\mathrm{tx,avg}}$	50 W
Center frequency f	435 MHz
Pulse bandwidth B_{p}	10 MHz
Pulse duration τ_{p}	10 µs
Antenna size (reflector)	2 m
Receiver equivalent noise temperature T_{n}	300 K
Receiver noise factor F	3 dB

Table 1 System parameters for an example P-band SAR to be used in the subsequent analysis. Note the suggested values appear reasonable given the mass, power and space restrictions of planetary missions. Note too the suggested reflector antenna architecture may allow the simultaneous use for another frequency band.

three-body-problem, which is commonly characterized in a body-fixed frame by the following set of equations:

$$\ddot{x} = 2 \cdot n \cdot \dot{y} + \frac{\delta \Gamma}{\delta x}, \qquad \ddot{y} = 2 \cdot n \cdot \dot{x} + \frac{\delta \Gamma}{\delta y}, \qquad \ddot{z} = \frac{\delta \Gamma}{\delta z}, \quad (1)$$

where x, y, and z are the body-fixed coordinates, the dots denote the first and second derivative with respect to time, n is the mean motion of Enceladus and Γ indicates the gravitational potential, which can be written as

$$\Gamma = \frac{1}{2} \cdot n^2 \cdot \left(3 \cdot x^2 - z^2\right) + \frac{\mu_{\mathrm{g}}}{\sqrt{x^2 + y^2 + z^2}} + U. \quad (2)$$

Here, μ_{g} is the Enceladus gravitational parameter and the term U accounts for the non-spherical shape of Enceladus. From a global search for orbits about Enceladus [4], a so-called periodic orbit (orbit which repeats its trajectory after a certain time) with an average inclination of 61°, an average altitude of 240 km, and an orbital period of 10.3 days was found to be the highest inclined orbit which still provides long-term stability even in higher fidelity models, involving additional perturbations by the Sun, Jupiter, and Titan.

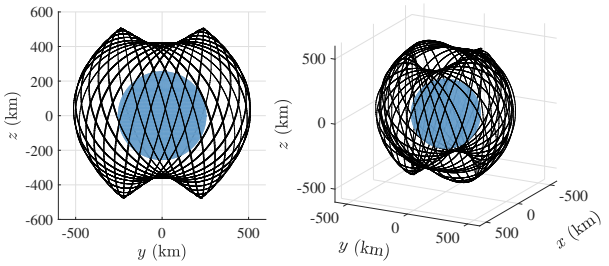

Figure 1 Propagated orbit about Enceladus. Note the changes in height caused by the presence of Saturn.

The high inclination combined with the moderate altitude allows for global coverage, including the most interesting south polar region. We use this orbit as basis for our subsequent analysis. The orbit can be propagated by solving the system in (1). In **Figure 1** the propagated orbit over one period is shown. The orbit shows varying orbital parameters, whereof the most relevant ones are depicted in **Table 2**.

Parameter	Range
Altitude	180 km - 300 km
Velocity	100 m s^{-1} - 140 m s^{-1}
Inclination	55° - 65°
Eccentricity	0.02 - 0.23

Table 2 Ranges of variation of the orbital parameters of the solution in [4].

2.2 Observation Opportunities

The periodic nature of the orbit in the body-fixed frame provides a repeated ground track, which allows the schedule of acquisitions. The ground track is shown in **Figure 2** overlaying an optical image of the Enceladean surface [5]. The light blue lines in the south polar region indicate the aforementioned jets. The coverage provided by the reference P-band system and orbit in left-looking geometry is illustrated in **Figure 3**. A range of incident angles between

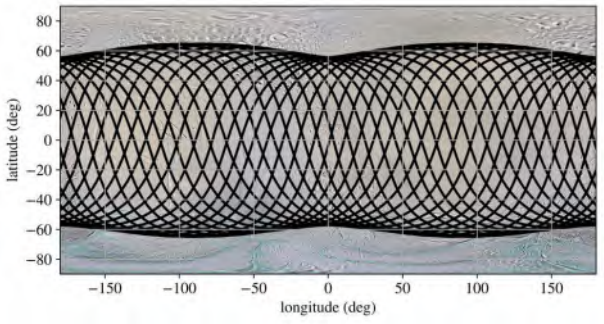

Figure 2 Orbit ground track on the surface of Enceladus.

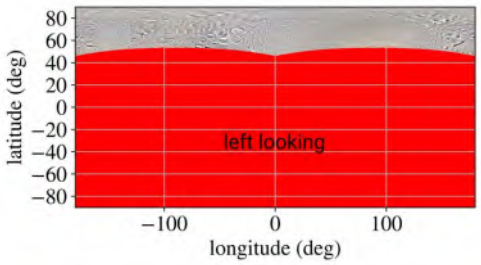

Figure 3 Coverage of the Enceladean surface simulated for the P-band system depicted by Table 1 in a left-looking geometry for incidence angles ranging from 25° to 45°.

25° and 45° has been assumed. The left-looking geometry allows for covering the most interesting south polar regions.

The unique shape of the orbit together with the small antenna size of the reference system can be exploited to obtain SAR acquisitions with outstandingly long integration times, showing strong similarities with spotlight acquisitions, especially in polar regions. In the upper part of **Figure 4** the available integration time for the P-band system is plotted for two exemplary incidence angles over one orbit period. It ranges from 800 s to a maximum of

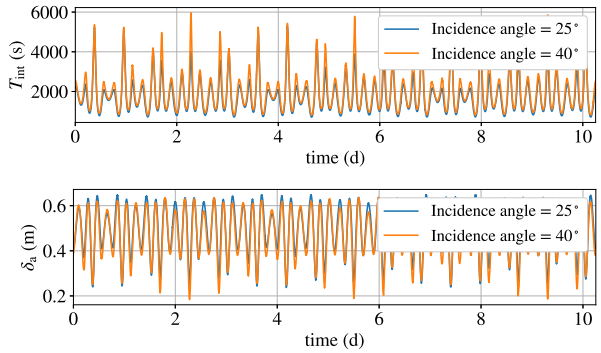

Figure 4 Maximal integration time T_{int} and azimuth resolution δ_{a} over one orbit period for two incidence angles. Note the extreme peaks in the integration time are linked to polar passes and correspond to the azimuth resolution minima.

almost 6000 s, where the extreme peaks are linked to polar passes. The available integration time directly influences the possible azimuth resolution δ_{a}, achievable by the reference system. The azimuth resolution is shown in the lower part of Figure 4 and has been derived for targets placed on the surface of the moon, but provides an almost exact estimate of the values in the subsurface. The range resolution scales with the relative permittivity of the ice ε_{r} according to

$$\delta_{\text{r}} = \frac{c_0}{2 \cdot B_{\text{p}}} \cdot \frac{1}{\sqrt{\varepsilon_{\text{r}}}}, \tag{3}$$

where c_0 is the speed of light in free space. Enceladean ice is known to be water ice, what leads to typical ε_{r} values between 1.6 and 3.2 depending on the density. For the 10 MHz bandwidth this translates in δ_{r} values between 11.9 m and 8.4 m, respectively.

2.3 Sensitivity for Subsurface Imaging

The sensitivity is mainly determined by the propagation losses of the radar echos in the ice and constrained by the orbit and system parameters. The model we use is based on knowledge about ice and snow on Earth and adapted to the special conditions on Enceladus, such as the extremely low temperatures ranging from 80 K at the surface to 273 K at the interface between ice and water. Due to this low temperatures, the absorption losses are expected to be extremely small and outreached by the scattering losses. Simulations show that for worst-case modelling with a predominate scatterer size of several centimeter, penetration down to 150 m can be expected for the P-band system in Table 1.

3 Volumetric Imaging Concept

SAR tomography provides 3-D imaging of semi-transparent media by exploiting multiple coherent passes of a radar at different positions over the same scene. Repeat-pass tomographic SAR modes will be used in future missions such as ESA's BIOMASS [6] or Tandem-L [7]. However, parking tomographic orbits about Enceladus

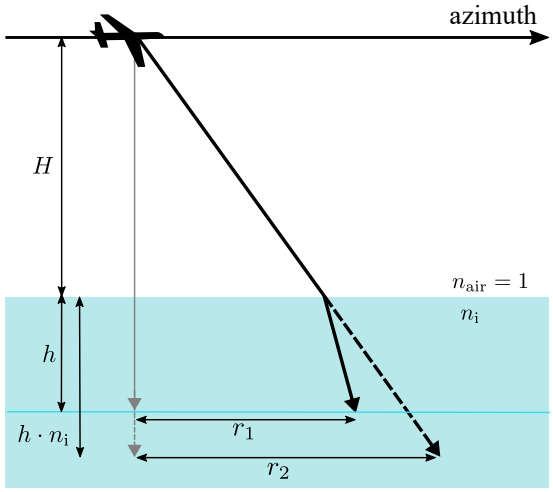

Figure 5 Compaction of effective azimuth sampling caused by propagation through two different media to illustrate the effect on the Doppler rate for the imaging of subsurface ice structures.

is highly questionable, due to the strong -and not accurately known- gravitational perturbations and the associated impact on the orbit control accuracy. This aspect challenges our ability to propose a purely tomographic SAR mission concept. We present in this section alternative concepts for the imaging of Enceladean volumetric structures. In particular, a single-pass volumetric imaging concept, based on exploiting the unique orbit geometry and the sensitivity of the Doppler rate to the ice crust permittivity is discussed, beginning with a derivation of the vertical resolution.

Let us recall the expression of the phase history of a target:

$$\Phi(t_{\text{a}}) \approx r_0 \cdot \frac{4 \cdot \pi}{\lambda} + f_{\text{DC}} \cdot 2 \cdot \pi \cdot t_{\text{a}} + f_{\text{R}} \cdot \pi \cdot t_{\text{a}}^2 + \ldots, \tag{4}$$

where r_0 is the minimum of the range history and needs to be considered as optical length for subsurface imaging. The linear term is characterised by the Doppler centroid f_{DC}, which can be assumed to be zero for non-squinted acquisitions. The Doppler rate f_{R} determines the quadratic term and can be written for propagation in free-space as

$$f_{\text{R,fs}} = \frac{2 \cdot v_{\text{e}}^2}{\lambda \cdot r_0}, \tag{5}$$

where v_{e} is the effective velocity of the survey. Compared to targets located in free-space, targets embedded in ice experience an increased Doppler rate due to a compacting of the azimuth sampling. **Figure 5** illustrates the effect for a two-layered model with horizontal interface and linear radar track, where $n_{\text{i}} = \sqrt{\varepsilon_{\text{r,i}}}$ describes the refractive index of the ice layer. We will use the model in Figure 5 to get estimates of the vertical resolution which can be achieved using the reference system and orbit of Section 2. The Doppler rate for a target in ice may be derived by quantifying aforementioned compacting of the azimuth sampling. In Figure 5 the distance between two Doppler frequency samples for a depth h in the ice is illustrated for the actual

case of $n_\mathrm{i} > n_\mathrm{air}$ and $n_\mathrm{i} = n_\mathrm{air}$, r_1 and r_2, respectively. For the latter case, h is scaled with n_ice to account for the higher propagation velocity. The ratio $\frac{r_2}{r_1}$ relates the Doppler rate for a target in ice to the Doppler rate of a free space assumption:

$$f_\mathrm{R} = f_{\mathrm{R,\,fs}} \cdot \frac{r_2}{r_1} = f_{\mathrm{R,\,fs}} \cdot \frac{\left(H + h \cdot n_\mathrm{i} \cdot \frac{\cos\theta_\mathrm{i}}{\cos\theta_\mathrm{r}}\right) \cdot n_\mathrm{i}}{H \cdot n_\mathrm{i} + h \cdot \frac{\cos\theta_\mathrm{i}}{\cos\theta_\mathrm{r}}}, \quad (6)$$

where H is the sensor altitude and θ_i and θ_r are the incidence and refraction angle in the slant range plane at boresight. This leads to the fact that two targets on the same constant-r_0 curve, which under a free-space assumption cannot be distinguished by a SAR system, are observed with unique Doppler rates depending on their depth h. In analogy to the Doppler resolution in azimuth direction, we name this concept Doppler rate resolution. Note that even if the dependence with h is common to any orbital geometry [8], the changes in the Doppler rate caused by the propagation in ice for the considered case will be significantly higher.

The Doppler rate resolution can be exploited by incorporating the varying Doppler rate into the image formation. This leads to unique azimuth filter functions for different points along a constant-r_0 curve, where the filter functions differ from each other by their quadratic component. In other words, the azimuth signal generated by a target at a point on a specific constant-r_0 curve experiences only at this point a matched filter, where at all other positions along the curve a quadratic mismatch between the azimuth signal and the filter function is present. This quadratic phase error leads to a defocusing of the azimuth impulse response, where the degree of defocusing is characterised by the maximal quadratic phase error at the borders of the phase history ($t_\mathrm{a} = \frac{T_\mathrm{int}}{2}$):

$$\Delta\Phi_\mathrm{max} = \pi \cdot \Delta f_\mathrm{R} \cdot \left(\frac{T_\mathrm{int}}{2}\right)^2, \quad (7)$$

where Δf_R is the difference in Doppler rate. Among other effects, the defocusing of the impulse response results in a decreasing main-lobe magnitude, leading to a spatial resolution along the constant-r_0 curve and therefore, a resolution in elevation. From equations (5) and (6) a vertical resolution δ_h along a constant r_0-curve can be approximated by

$$\delta_h \approx \delta_{f_\mathrm{R}} \cdot \left(\frac{\delta f_\mathrm{R}}{\delta h}\right)^{-1}, \quad (8)$$

where δ_{f_R} is the Doppler rate resolution, which can be derived according to (7) as

$$\delta_{f_\mathrm{R}} = \Delta\Phi_{\mathrm{max},-3\,\mathrm{dB}} \cdot \frac{1}{\pi} \cdot \left(\frac{2}{T_\mathrm{int}}\right)^2, \quad (9)$$

where $\Delta\Phi_{\mathrm{max},-3\,\mathrm{dB}}$ indicates the maximal quadratic phase error which leads to a decrease of the azimuth impulse response main-lobe by $-3\,\mathrm{dB}$ and can be approximated as $\Delta\Phi_{\mathrm{max},-3\,\mathrm{dB}} \approx 0.87\pi$. The derivation in (8) results in

$$\frac{\delta f_\mathrm{R}}{\delta h} \approx \frac{2 \cdot v_\mathrm{e}^2}{\lambda \cdot r_0} \cdot \frac{H \cdot n_\mathrm{i} \cdot \frac{\cos\theta_\mathrm{i}}{\cos\theta_\mathrm{r}} \cdot \left(n_\mathrm{i}^2 - 1\right)}{\left(H \cdot n_\mathrm{i} + h \cdot \frac{\cos\theta_\mathrm{i}}{\cos\theta_\mathrm{r}}\right)^2}, \quad (10)$$

wherefrom, the vertical resolution along a constant-r_0 curve may be approximated as

$$\delta_h \approx 0.87 \cdot \left(\frac{2}{T_\mathrm{int}}\right)^2 \cdot \frac{\lambda \cdot r_0}{2 \cdot v_\mathrm{e}^2} \cdot \frac{\left(H \cdot n_\mathrm{i} + h \cdot \frac{\cos\theta_\mathrm{i}}{\cos\theta_\mathrm{r}}\right)^2}{H \cdot n_\mathrm{i} \cdot \frac{\cos\theta_\mathrm{i}}{\cos\theta_\mathrm{r}} \cdot \left(n_\mathrm{i}^2 - 1\right)}. \quad (11)$$

The vertical resolution is nearly independent of the depth h for realistic scenarios, where $h \ll H$. The resolution along the constant-r_0 curve (in elevation) can be approximated by projecting the depth resolution according to the refraction angle θ_r:

$$\delta_\mathrm{el} \approx \frac{\delta_h}{\sin\theta_\mathrm{r}}. \quad (12)$$

The long integration times, provided by the orbit geometry and the wide antenna beam, may lead to metric resolutions for the Enceladean case. **Figure 6** shows the vertical resolution δ_h in relation to the integration time for an orbiter velocity of $100\,\mathrm{m\,s^{-1}}$, an altitude of 250 km, an incidence angle of 35° and different refractive indices, representing the permittivity range of ice and snow.

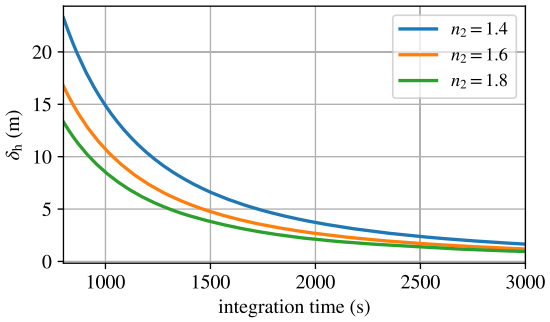

Figure 6 Vertical resolution over integration time for an orbiter velocity of $100\,\mathrm{m\,s^{-1}}$, an altitude of 250 km, an incidence angle of 35° and refractive indices, representing the permittivity range of ice and snow.

In order to validate the derived concept for the more complex acquisition scenario of an Enceladus SAR orbiter, we present a simulation of the 3-D impulse response of a point target in the ice crust. The target is located at −40° latitude, in a depth of 170 m and is illuminated with an incidence on the surface of 35°. The results were produced using a raw data simulator, which incorporates the orbit geometry and the propagation effects on the radar echoes introduced by the ice permittivity. The permittivity distribution was modeled according to dry ice sheets on Earth, increasing with depth and saturating at the level of pure ice. The wave propagation in the ice is approximated by means of an Eikonal solver, which is capable of modeling almost arbitrary permittivity distributions. The raw data were focused using a time-domain back-projection approach. **Figure 7** shows the resulting 3-D impulse response in a local reference frame for an integration time of 1000 s. Two different iso-surfaces are shown, to illustrate the shape of the impuls response and the focusing along elevation. The $-3\,\mathrm{dB}$ iso-surface gives an impression of the resolution, which takes the following values: $\delta_\mathrm{r} \approx 8.4\,\mathrm{m}$, $\delta_\mathrm{a} \approx 0.6\,\mathrm{m}$, and $\delta_h \approx 13\,\mathrm{m}$. The $-19\,\mathrm{dB}$ iso-surface clearly shows an

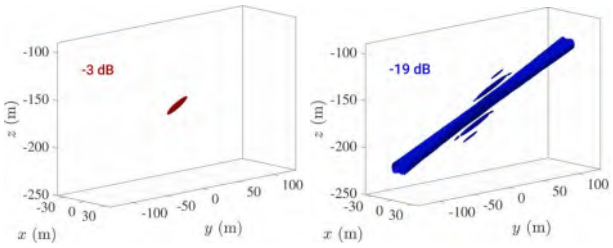

Figure 7 Iso-surface representation of the 3-D impulse response of a point target located at $-40°$ latitude, 170 m deep and illuminated with an incidence on the surface of $35°$ for an integration time of 1000 s. Iso-surfaces of -3 dB and -19 dB are shown to illustrate the focusing along elevation. The coordinates describe a local reference frame, where the x-axis is aligned with azimuth and $z = 0$ corresponds to the surface.

expansion in elevation and the side-lobes along the vertical coordinate. The authors are aware that also the curved orbit contributes to the resolution effect, but simulations show that this factor is small compared to the permittivity contribution.

4 Processing Approach

As a consequence of the above, the lack of precise knowledge about the permittivity distribution in the ice crust may introduce a geometrical displacement and defocusing of the scene, if the permittivity estimate for the image formation disaccords with the real conditions. The defocusing of the scene contains valuable information about the actual target position and real ice crust permittivity. Exploiting this defocusing confronts us with the challenge of separating the two factors. We want to suggest a processing approach, which iteratively estimates the correct ice permittivity by merging the information from an inversion model and the triangulation between different acquisitions with angular diversity.

4.1 Inversion Model

The inversion model is intended to relate the degree of defocusing in the SAR image to its geometrical displacement in elevation. The degree of defocusing can be estimated by means of a SAR autofocus algorithm. In the case under analysis, it can be expressed in terms of a Doppler rate error Δf_{R}. According to the derivation in the previous section the relation between vertical displacement and Doppler rate error can be approximated as

$$\Delta z \approx \Delta f_{\mathrm{R}} \cdot \frac{\lambda \cdot r_0}{2 \cdot v_{\mathrm{e}}^2} \cdot \frac{\left(H \cdot n_{\mathrm{i}} + h \cdot \frac{\cos\theta_{\mathrm{i}}}{\cos\theta_{\mathrm{r}}}\right)^2}{H \cdot n_{\mathrm{i}} \cdot \frac{\cos\theta_{\mathrm{i}}}{\cos\theta_{\mathrm{r}}} \cdot \left(n_{\mathrm{i}}^2 - 1\right)}, \qquad (13)$$

where z is the vertical coordinate. The inversion procedure is illustrated in **Figure 8**. Let us consider a case in which the permittivity is known and the focusing is performed in a horizontal plane at depth z_{f}. If z_{f} disaccords with the depth of the considered feature, it will appear defocused in the image. By using the information provided by the autofocus and the inversion model in (13) the vertical error Δz can be estimated. The performance of this approach depends on the accuracy of the autofocus, which scales with the contrast in the scene.

4.2 Multi-Pass Processing Approach

In the case of an error in the permittivity, the prediction of the inversion model will lead to a wrong position. An additional acquisition from a different geometry (e.g., from a repeat pass) may provide sufficient diversity to solve for permittivity and positioning errors. The geometrical offsets between the two images can be combined with the inversion model in an iterative processing approach, in which the correct permittivity is found if the triangulation between the two images and the inversion model point to the same position. Note this triangulation may be realized in form of across-track SAR interferometry or radargrammetry. SAR interferometry is expected to provide better accuracy by orders of magnitude, but requires stringent orbit control.

To proof the potential of the approach, we conducted a simulation using the aforementioned raw data simulator with the given orbit geometry and a constant refractive index of the ice $n_{\mathrm{i}} = 1.7$. The simulation consists of two acquisitions separated by an incidence of $15°$, where we assume that some common features will appear within the images. **Figure 9** shows the results of the simulation, where the black curve indicates the true depth of the imaged scene and the dashed line indicates the horizontal plane in which the focusing is performed. The top plot shows the results of the inversion of the location error (red) under the assumption of a refractive index of 1.65 in the processing. Noise was applied on the inversion output to account for the limited accuracy of the autofocus algorithm, where the noise is bounded by an autofocus accuracy characterised by a residual of 0.25π maximal quadratic phase error. Note the result of the inversion differs with respect to the measurement of the location errors of the two images (blue), which suggests the processing should be repeated with a different permittivity value. The bottom plot shows the agreement between the inversion model and the location errors measured from the two images under the assumption of the correct permittivity in the processing.

The suggested approach works simultaneously as a processing approach for the generation of reliable radiometry and as a physical inversion model of the dielectric characteristics of the Enceladean ice crust. Its performance depends on the autofocus accuracy, number and geometry (i.e., coherent or incoherent) of acquisitions, and the error arising from averaging the permittivity distribution in the ice to a constant permittivity.

5 Concluding Remarks

This paper provides first steps towards a systematic assessment of a subsurface imaging concept for the P-band SAR

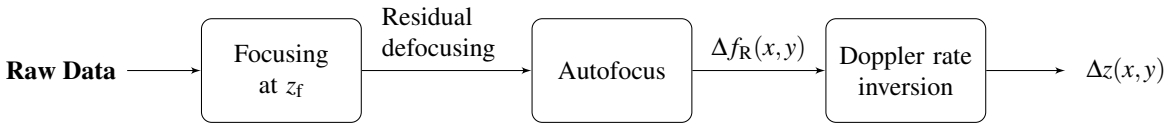

Figure 8 Flowchart of the Doppler rate inversion procedure for a single image assuming the permittivity profile of the scene is known.

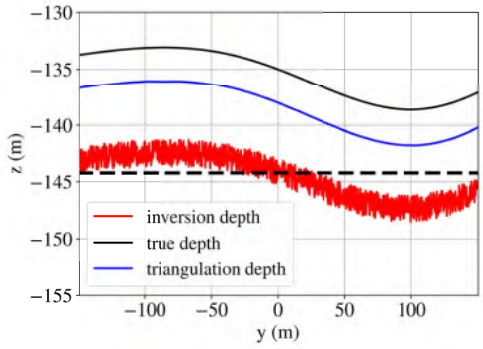

(a) $\Delta n = 1.7 - 1.65 = 0.05$.

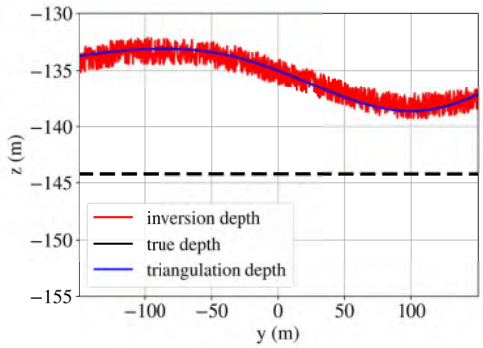

(b) $\Delta n = 1.7 - 1.7 = 0.0$.

Figure 9 Simulation of the location predictions by the inversion model (red) and the triangulation between two acquisitions with incidence angle difference of 15° (blue) for a misestimation of the correct refractive index of $\Delta n = 0.05$ (a) and a correct estimation (b). The dashed line indicates the focusing plane. Note that for the misestimation the two predictions diverge and do not align with the true depth of the imaged scene (black), whereas for the correct refractive index, both predictions align with the scene.

exploration of Enceladus. Making use of the unique observation opportunities, given by the orbit trajectory, the influence of the permittivity on the propagation of the radar echoes can be exploited to allow for 3-D metric resolution imagery of the Enceladean ice crust. The uncertainty in the knowledge about the permittivity may be compensated by combining the information of different passes, coherently or incoherently.

6 Acknowledgements

The authors would like to thank Gerhard Krieger, Rolf Scheiber and Gustavo Martin del Campo Becerra and Ralf Horn for their contributions.

7 Literature

[1] C. Porco, P. Helfenstein, P. Thomas, *et al.*, "Cassini observes the active south pole of Enceladus," *Science*, vol. 311, no. 5766, pp. 1393–1401, 2006.

[2] S. Tebaldini, T. Nagler, H. Rott, and A. Heilig, "Imaging the internal structure of an alpine glacier via L-band airborne SAR tomography," *IEEE Transactions on Geoscience and Remote Sensing*, vol. 54, pp. 7197–7209, Dec 2016.

[3] M. Pardini, G. Parrella, G. Fischer, and K. Papathanassiou, "A multi-frequency SAR tomographic characterization of sub-surface ice volumes," in *European Conference on Synthetic Aperture Radar (EUSAR)*, pp. 1–6, Juni 2016.

[4] R. P. Russell and M. Lara, "On the design of an Enceladus science orbit," *Acta Astronautica*, vol. 65, no. 1, pp. 27 – 39, 2009.

[5] NASA/JPL, "Color map of Enceladus," 2014. [Online; accessed October 31, 2019].

[6] "BIOMASS – An Earth Explorer to observe forest biomass. Report for Mission Selection," Techincal Report, ESA SP-1324/1, May 2012.

[7] A. Moreira, G. Krieger, I. Hajnsek, *et al.*, "Tandem-L: A highly innovative bistatic SAR mission for global observation of dynamic processes on the Earth's surface," *IEEE Geoscience and Remote Sensing Magazine*, vol. 3, pp. 8–23, June 2015.

[8] M. Rodriguez-Cassola, P. Prats-Iraola, F. De Zan, *et al.*, "Doppler-related distortions in TOPS SAR images," *IEEE Transactions on Geoscience and Remote Sensing*, vol. 53, pp. 25–35, Jan 2015.

Acta Astronautica 191 (2022) 326–345

Contents lists available at ScienceDirect

Acta Astronautica

journal homepage: www.elsevier.com/locate/actaastro

Research paper

Periodic orbits for interferometric and tomographic radar imaging of Saturn's moon Enceladus

Andreas Benedikter [a,b,*], Kai Wickhusen [c], Hauke Hussmann [c], Alexander Stark [c], Friedrich Damme [d], Marc Rodriguez-Cassola [a], Gerhard Krieger [a,b]

[a] Microwaves and Radar Institute, German Aerospace Center (DLR), 82234 Wessling, Germany
[b] Institute of Microwaves and Photonics (LHFT), Friedrich-Alexander University Erlangen-Nürnberg (FAU), 91058 Erlangen, Germany
[c] Institute of Planetary Research, German Aerospace Center (DLR), 12489 Berlin, Germany
[d] Institute of Geodesy and Geoinformation Science, Technical University Berlin, 10553 Berlin, Germany

ARTICLE INFO

Keywords:
Enceladus
Orbit
Orbit design
Radar
SAR interferometry
SAR tomography

ABSTRACT

Spaceborne synthetic aperture radar interferometry and tomography are well-established techniques for the exploration of terrestrial ice sheets. In the frame of DLR's mission concept Enceladus Explorer (EnEx), these techniques are considered for providing topography, deformation, and composition measurements, as well as 3-D metric-resolution imaging of the Enceladean ice crust. However, the formation of repeat-pass interferometric and tomographic acquisitions requires spacecraft orbits with almost perfectly repeating ground tracks and sufficient inclination for providing access to the most-interesting south polar region with its plumes. Unfortunately, the low Enceladus mass and its proximity to Saturn commonly lead to extreme instabilities for orbit inclinations beyond 60°. We show that existing orbit solutions close to this inclination barrier resulting from searches in simplified dynamic models do not exhibit sufficient stability in realistic n-body ephemeris simulations for providing the necessary repeat characteristic. We present a grid-search strategy in an ephemeris model for identifying highly-stable, periodic orbits satisfying the repeating ground track requirement. The resulting orbit solutions are assessed regarding their stability, repeat characteristic, and robustness to uncertainties in the gravitational model, navigation inaccuracies, and drag by the ejected gas and dust of the plumes. Global simulations of interferometric and tomographic acquisition geometries are used to assess the suitability of the orbits. The identified orbits provide sufficient inclination and long-term stability to sustain the required repeat characteristic up to few hundreds of days with repeat-pass baselines in the order of hundreds of meters. This may allow a consistent implementation of radar interferometric and tomographic imaging modes for a future Enceladus mission. Besides, the high stability may offer favorable conditions for other remote sensing modalities.

1. Introduction

1.1. Enceladus radar orbiter

With only about 500 km in diameter, Saturn's moon Enceladus is a differentiated geological active body, most likely comprising a porous rocky core and an ice shell, separated by a global subsurface salt-water ocean [1]. The discovery of plumes ejecting gas and ice particles through cracks within the ice crust in the south polar region and the presence of complex organic molecules within have quickly thrust Enceladus in the spotlight of the planetary science community [2–4]. Consequently, these discoveries have assigned a high priority to the moon among exploratory mission plans in the frame of investigations of habitability in other worlds, among others: [5–8]. Under the name Enceladus Explorer Initiative (EnEx), the German Aerospace Center (DLR) is developing a mission concept comprising a landing close to the plumes and a subsequent probing of the Enceladean ice and water with an ice-penetrating melting robot [6]. Such a lander mission requires a preceding orbiter-based mapping of Encledus' topography as well as surface and subsurface ice crust structure and composition, focused on the south polar region. Note that determining these geophysical properties is furthermore a frequently stated science objective for future Enceladus exploration. Especially measuring the dynamics of the ice, caused by tidal deformation, and the shape and geomorphology of the plumes and the plume source region is crucial for understanding the observed cryovolcanism [8]. The poor solar illumination of the

* Corresponding author at: Microwaves and Radar Institute, German Aerospace Center (DLR), 82234 Wessling, Germany.
E-mail address: andreas.benedikter@dlr.de (A. Benedikter).

https://doi.org/10.1016/j.actaastro.2021.10.041
Received 11 August 2021; Received in revised form 15 October 2021; Accepted 25 October 2021
Available online 9 November 2021

Enceladus south polar region with complete winter darkness from year 2039 to 2054 and a maximum Sun elevation during southern solstice of 26.73° at the South Pole [9] prevents consistent optical imaging and almost drives the need for an imaging radar system, i.e., a synthetic aperture radar (SAR) system, for the mapping task. A SAR system is based on a pulsed radar which operates in a side-looking geometry providing two-dimensional metric-resolution imagery over tens of kilometer wide swaths independent of solar illumination. The 2-D resolution is provided by means of pulse compression in line-of-sight direction (i.e., range) and coherent integration of consecutive radar echoes along the motion direction of the orbiter (i.e., azimuth) to form a long synthetic aperture. The amplitude of a SAR image provides a backscatter map (i.e., reflectivity map) of the imaged scene. Radar signals in the frequency range below few GHz significantly penetrate into optical non-transparent natural media such as snow and ice, providing sensitivity of the SAR acquisition to both surficial backscatter and other scattering structures within the ice crust. In the frame of EnEx a multi-modal radar orbiter is considered [10], operating mainly as a dual-frequency SAR instrument (i.e., Ka and P-band) to image ice features on the surface and subsurface, respectively. Spaceborne SAR instruments in planetary missions have been successfully operated for imaging, among others, the surface of Venus during the Venera 15, Venera 16, and Magellan mission [11,12] and for revealing the surface of Saturn's moon Titan through its dense atmosphere during the Cassini mission [13].

1.2. Interferometric and tomographic repeat-pass SAR

If two SAR images are acquired from mutually displaced flight tracks, the phase difference between the two (i.e., the interferometric phase) carries information about the surface and subsurface topography, deformation, and composition. SAR interferometry (InSAR) may be implemented in two basic manners: (i) single-pass InSAR, using simultaneous acquisitions by two spatially separated receiving antennas on one spacecraft (as implemented for the SRTM mission [14]) or on two spacecraft flying in close formation (as implemented for the TanDEM-X mission [15]), and (ii) repeat-pass InSAR as illustrated in Fig. 1, with the two acquisitions separated by an instance of time, e.g., the repeat cycle of a repeating ground track orbit. This approach has been implemented for several Earth observation missions, e.g., ERS-1/2, Envisat, and Sentinel-1. The advantage of the repeat-pass approach, especially in the context of planetary missions with tight restrictions concerning mass and allocated space, is that a single spacecraft with a single receiving unit is sufficient. Furthermore, the temporal separation between the acquisitions allows for deformation and change detection measurements. Spaceborne repeat-pass InSAR is nowadays considered a routine method for measuring Earth's topography at high spatial resolution and vertical accuracy over wide areas and detecting surface change due to volcanoes, earth quakes, glacier movement, and other ground deformation within a fraction of the wavelength [16–18]. Repeat-pass InSAR systems for planetary exploration have been suggested for topographic mapping and change detection at Venus [19–21] and Mars [22,23]. Orbital InSAR at Enceladus may be an indispensable tool for topography estimation, measuring tidal deformation processes in the ice crust, and the inversion of ice composition parameters. The two basic requirements for repeat-pass InSAR at Enceladus are:

- The reference and repeat orbit trajectory, viewed in an Enceladus body-fixed frame, must be almost parallel and the distance between the orbital tracks (i.e., baseline), projected on a line perpendicular to the radar line-of-sight, must be less than the critical baseline which is a function of the wavelength, signal bandwidth, distance to the scene and incidence angle on the scene, with higher values of these quantities resulting in longer critical baselines [16,24]. Typical critical baseline values for orbits analyzed in this study are in Ka-band tens to a few hundred meters and on the order of several kilometers for P-band frequencies. This constraint imposes challenging requirements on orbit characteristics and navigation performance.
- The backscatter distribution of the scene cannot change significantly between reference and repeat acquisition. In the context of Earth observation, this commonly leads to problems in vegetated areas and glacial areas with heavy snow accumulation or melting processes. With a snow deposit maximum rate of 1 mm/year [25] these effects are expected to be small at Enceladus and may be reduced by shortening the orbital repeat cycle.

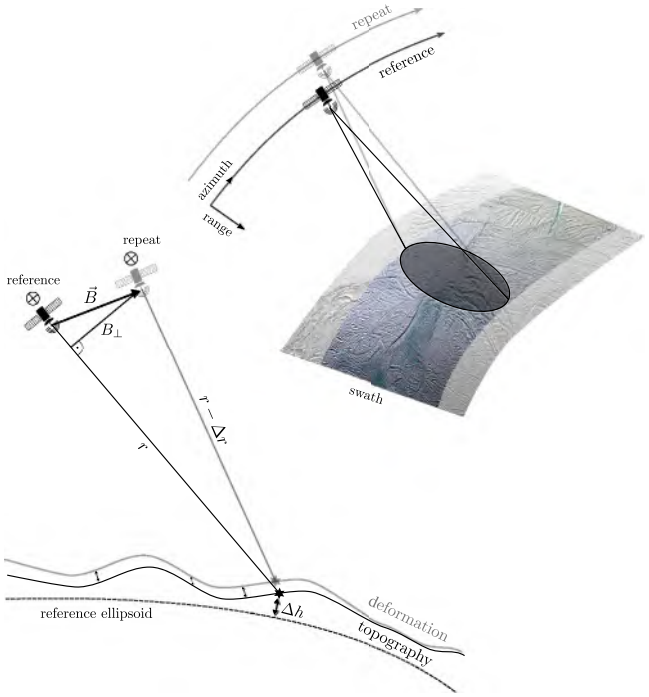

Fig. 1. Illustration of the repeat-pass SAR interferometry imaging geometry. Note that the reference and repeat pass are separated in time.

Extending the concept by additional repeat passes allows the formation of a synthetic antenna aperture in the cross-track direction perpendicular to the radar line-of-sight (i.e., elevation). The concept is illustrated in Fig. 2. Thus, besides the 2-D capability of traditional SAR, the backscatter distribution of the scene can be resolved in the elevation direction. In combination with the aforementioned penetration capability of the radar waves, this approach, which is commonly referred to as tomographic SAR (TomoSAR), enables direct 3-D imaging of the glacial volume structure. TomoSAR has been successfully applied in several airborne campaigns for imaging the internal structure of alpine glaciers and the Greenland ice sheet [26–30] and provides the unique capability (compared to other sensors) of 3-D metric resolution measurements of the Enceladean ice crust along kilometer wide swaths. TomoSAR would allow the imaging of the subsurface expansion of the plumes and other subsurface features, such as cracks, layers, or water bodies. The requirements for repeat-pass TomoSAR are similar to the InSAR case in the sense that reference and repeat orbits must be almost parallel and no significant changes in the backscatter distribution can be present. Though the maximum baseline between orbital tracks is not limited by the critical baseline, it is constrained by the necessity of sufficiently dense sampling of the synthetic antenna aperture in elevation to avoid ambiguities (i.e., ghost images).

1.3. Enceladus orbits

InSAR and TomoSAR require repeat ground track orbits with almost perfect repeat characteristic to fulfill the baseline requirements and

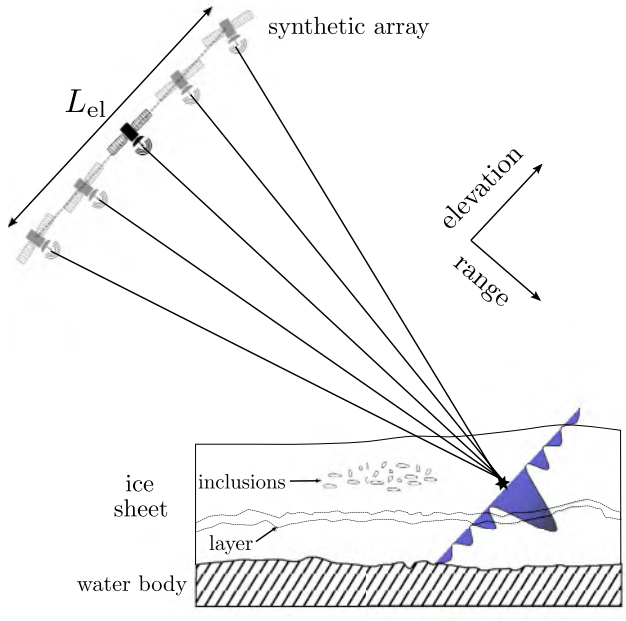

Fig. 2. Illustration of the SAR tomography imaging geometry. The impulse response in elevation direction for a target in the ice crust is sketched in blue.

short repeat periods to mitigate decorrelation effects due to a changing backscatter distribution. Furthermore, the candidate orbits must have sufficient inclination to provide coverage of the most-interesting south polar regions. The design of science orbits around planetary satellites has been extensively studied in recent years [31–36]. Unfortunately, it is well known that most high-inclined orbits suffer from instability caused by the third body effect of the planet leading to highly eccentric and eventually impacting orbits. At Enceladus, its small mass and the proximity to Saturn lead to impact times of few days for polar orbits [33]. The relevant dynamic parameters of Enceladus are given in Table 1. Past studies have identified long-term stable orbits through averaging techniques in the Saturn-Enceladus Hill model [34,35] with maximum inclinations reaching up to 62 ° for low-eccentricity orbits with semi-major axes of roughly two times the Enceladus radius [35]. However, the significant non-sphericity of Enceladus' gravitational field has not been considered in the averaging model. A thorough assessment of possible science orbits at Enceladus was performed by Russell and Lara [36] in the form of a global search for periodic orbits, i.e., orbits with repeating trajectories in the body-fixed frame. Note that the periodicity in the body-fixed frame implies a repeating ground track, the desired condition for InSAR and TomoSAR. The solutions in [36] are based on an unaveraged Hill model including the large J_2 term alongside other higher-order terms of Enceladus spherical harmonic gravity field. A class of highly inclined stable orbits emerged from this search whereof an exemplary candidate orbit with a maximum inclination of roughly 64° and an average altitude of 245 km was proven long-term stable over a course of 6 months in n-body ephemeris propagation involving gravitational perturbation by Saturn, Titan, Jupiter, the Sun, and oblateness effects from Saturn and Enceladus. With inclinations around 60°, altitudes comparable to the Enceladus radius and orbital velocities around $100\,\mathrm{m\,s^{-1}}$, the solutions in [36] may provide a favorable platform for SAR imaging of the south polar region, allowing measurements of the plume region with incidence angles on the surface ranging from roughly 20° to 50°. However, even though the solutions in [36] are almost perfectly periodic in the simplified Hill model, the propagation in the perturbed ephemeris model does not provide repeating ground tracks. Note that the orbital stability formulation for SAR interferometry and tomography has to be more stringent than commonly framed in the context of planetary science orbit design.

Table 1
Enceladus parameters.

Parameter	Unit	Value
orbital period	day	1.370218
orbital eccentricity	–	0.0049
distance to Saturn	km	237,250 - 239,570
mean radius	km	252.1
mass	kg	1.0805E+20
mass ratio Saturn	–	1.90115E−7
rotational period	–	synchronous, i.e., equal to orbital period

In [33–36] orbits are considered stable as long as no impact or escape occurs, whereas for InSAR a stable orbit should provide a repeating trajectory within an imaginary orbital tube, corresponding to the above introduced baseline requirements.

In this work, we shift our focus away from simplified dynamic models and tackle the orbit design problem through a grid search for periodic orbits in an ephemeris model including all relevant gravitational perturbations. The main advantage of this approach proves to be the accurate incorporation of the non-circular orbit of Enceladus. To limit the parameter space, the grid search is performed around the well-suited (concerning the SAR imaging geometry) solutions of [36] in three dimensions, namely, the semi-major axis, inclination, and eccentricity. Highly stable periodic orbits appear with almost equally spaced repeat periods at integer multiples of nearly the Enceladus period. Found solutions sustain InSAR stability characteristics up to 200 days and conventional stability requirements beyond 15 years at maximum inclinations of 62°. Furthermore, Monte Carlo simulations show robustness to uncertainties in the Enceladus gravity field and potential navigation inaccuracies.

The remaining paper is organized in six sections. In Section 2, the InSAR and TomoSAR driven orbit design problem statement is discussed including insight into the imaging concepts, resulting orbit requirements, and deficiencies of existing orbit solutions. Section 3 outlines the periodic orbit search methodology based on a grid search approach in the ephemeris model with a discussion on relevant perturbations and the considered parameter space. Resulting periodic solutions are presented in Section 4 and assessed regarding their provided observation opportunities, repeat quality, stability, and robustness. In Section 5 the potential of the identified orbits for InSAR and TomoSAR is analyzed based on representative SAR system parameters. The implications of the derived results are discussed in Section 6. Conclusions are drawn in Section 7.

2. Problem statement

2.1. InSAR requirements

The pixels of a complex SAR image contain information about the signal amplitude and its phase. The amplitude A is a measure of the reflectively of the scene and the phase φ a measure of the two-way distance between the antenna and the scene with a 2π ambiguity. The information in one pixel is the superposition of the signals from all scattering elements within this cell, all contributing with a geometry dependent random phase leading to random-like phase information over the SAR image. If a second SAR image is acquired from an almost identical vantage point and the backscatter distribution has not changed, forming the phase difference $\Delta\varphi$ between the two images removes the scattering inherent phase, leaving a component that mainly depends on the acquisition geometry, topography, and deformation. This phase component is proportional to the difference in range distance between the acquisitions Δr, as indicated in Fig. 1, according to the relation [37]

$$\Delta\varphi = \frac{4\cdot\pi}{\lambda}\cdot\Delta r, \tag{1}$$

with λ as the signal's wavelength. The interferometric phase is a linear combination of the following components [24]:

$$\Delta\varphi = \varphi_{\text{ref}} + \varphi_{\text{topo}} + \varphi_{\text{defo}} + \varphi_{\text{atm}} + \varphi_{\text{noise}}, \tag{2}$$

where φ_{ref} represents the component of a reference digital elevation model (DEM), e.g., an ellipsoid as indicated in Fig. 1, and is removed in processing to reveal the component of the topography relative to the reference φ_{topo} and of the deformation φ_{defo}. The phase information is commonly corrupted by system noise φ_{noise} and phase components caused by propagation delays in the atmosphere φ_{atm}. The φ_{atm} component may be neglected at Enceladus due to the low density of both the neutral and ionized atmosphere formed by the plumes and Saturn's E-ring, with density values several orders of magnitude lower than Earth's atmosphere [38,39]. The measurement accuracy of the interferometric phase in (2), i.e., the amount of phase noise φ_{noise} is determined by the interferometric coherence, i.e., the degree of correlation between the two SAR images. Several factors may contribute to a decorrelation of the two images. The coherence can be summarized as [37]

$$\gamma = \gamma_{\text{noise}} \cdot \gamma_{\text{temp}} \cdot \gamma_{\text{coreg}} \cdot \gamma_{\text{geo}}, \tag{3}$$

where the different factors have magnitudes between zero and unity and describe the limited coherence due to the receiver noise γ_{noise}, temporal changes of the scene microstructure between the two acquisitions γ_{temp}, limited co-registration accuracy γ_{coreg}, and acquisition geometry dependent baseline, rotation, and volume decorrelation summarized as γ_{geo} and discussed in the following subsections. At this point, relevant InSAR concepts driving the orbit considerations shall be further outlined. For a complete review on InSAR methodology the reader is referred to *Bamler and Hartl* [37] or *Rosen* et al. [16].

Under the assumption that no deformation occurred between the reference and repeat acquisition and that the phase component of the reference DEM φ_{ref} is removed, the interferometric phase is formed out of the topographic phase φ_{topo} and can be linked to the height of the scattering scene above the reference DEM Δh by [37]

$$\varphi_{\text{topo}} = \frac{4 \cdot \pi \cdot B_{\perp}}{\lambda \cdot r \cdot \sin(\theta)} \cdot \Delta h, \tag{4}$$

where r is the range distance of the reference acquisition, θ is the incidence angle with respect to the surface normal vector, and $B_{\perp}$ is the effective (i.e., perpendicular) baseline as depicted in Fig. 1. Note that for a glacial scene, the position of the dominantly scattering scene features (i.e., the scattering phase center) may be located within the ice sheet due to the partial penetration of the radar signals. Still, the contribution is referred to as topographic phase throughout the paper. Besides the topography, the interferometer is sensitive to the deformation of the scattering scene in range direction. At Enceladus significant tidal-driven deformation in the order of a few meters is to be expected [40], both deforming the surface and replicating in the ice crust volume. Under the assumption of $B_{\perp} = 0$, the topographic phase component vanishes and the deformation in range can be directly retrieved over the relation in (1). As the baseline cannot be controlled to zero for an Enceladus orbiter, to separate topography and deformation, multiple acquisitions with different baselines may be used. An acquisition pair with large baseline increases the sensitivity to the topography and can be used for refining the reference DEM. The refined DEM may be used in a small baseline pair to remove the topographic component for deformation estimation. Alternatively, a deformation model may be fit to multiple acquisitions to solve for topography and estimate the model parameters for deformation estimation [41]. Both approaches require a minimum of three acquisitions to solve for topography and deformation. A larger number of coherent acquisitions can be used to improve the accuracy of both topographic and deformation measurements and may allow a higher complexity of the deformation model. Besides geometric information, measuring the coherence between one or more interferometric pairs allows the estimation of surface and volume composition parameters and their changes.

2.1.1. Baseline requirements

As discussed above, for deformation measurements, small baselines tending toward zero are favorable. For topography estimation, it is obvious from (4) that the height sensitivity $\Delta\varphi/\Delta h$ of the interferometer can be improved by increasing $B_{\perp}$. However, the maximum useful baseline is constrained by the necessity of the two acquisitions to be phase coherent. By increasing the perpendicular baseline and therefore the incidence angle difference of the two acquisitions, the geometry dependent factor of the coherence γ_{geo} in (3) decreases systematically due to an increasing difference of the scattering inherent phase contribution [42]. From a signal processing perspective, the band-limited radar signals from the two acquisitions map different portions of the observed ground scattering spectrum if acquired with different incidence angles [43]. Only for identical incidence angles the spectra overlap completely. With increasing baseline the spectra shift apart and γ_{geo} drops. A reduced γ_{geo} can be mitigated by filtering the non-overlapping parts of the spectra, but with the penalty of worsening the resolution in the range direction. The so-called critical baseline $B_{\perp,\text{crit}}$ describes the separation limit at which the spectral support between the acquisitions vanishes completely, and can be written as [24]

$$B_{\perp,\text{crit}} = \frac{W \cdot r \cdot \lambda \cdot \tan(\theta)}{c}, \tag{5}$$

where W is the signal bandwidth, c the propagation velocity of the electromagnetic waves, i.e., the speed of light. The critical baseline constitutes a theoretical upper limit until which InSAR is possible. However, several practical considerations show that the maximum baseline requirement is commonly more stringent: (i) band filtering to reduce decorrelation is only possible to a degree such that the range resolution requirements are still satisfied; (ii) decorrelation due to volume scattering effects grows for increasing baselines (relevant for low frequencies where significant penetration occurs, such as the suggested P-band); (iii) additional decorrelation due to noise γ_{noise}, mis-registration γ_{coreg}, and temporal changes γ_{temp} further degrades the coherence and requires sufficient spectral support to compensate for it by averaging; and (iv) the phase-to-height conversion in (4) provides ambiguous height measurements at multiples of [24]

$$h_{\text{amb}} = \frac{\lambda \cdot r \cdot \sin(\theta)}{2 \cdot B_{\perp}}, \tag{6}$$

because of the 2π ambiguity of the interferometric phase measurements. This problem is commonly tackled by so-called phase unwrapping, which may lead to problems in mountainous areas and may pose a more stringent requirement on $B_{\perp}$ than the critical baseline. This concern may be relevant in the Enceladus plume region with its mountainous topography. Since the factors listed above are mainly driven by system parameters and requirements on the resulting image products (e.g., resolution and vertical accuracy), and since the present paper does not aim to provide a mission performance assessment but a feasibility study for interferometric/tomographic Enceladus orbits and missions, we simplify the baseline assessment by the requirement to be within a conservative fraction of the critical baseline, such as $B_{\perp,\text{crit}}/2$. Fig. 3 gives insight into the critical baseline value range to be expected for typical Enceladus orbits. An orbital height of 200 km, incidence angles between 30° and 50° on a spherical Enceladus model, and 3 example values for the slope of the local topography are assumed. This spherical Enceladus acquisition model is illustrated in Fig. 4 and is used throughout the Section as an representative example. The left plot in Fig. 3 depicts the results for the P-band system parameters in Table 2. A strong dependence on the local incidence angle is visible with the most stringent values of a few kilometers at low incidence angles. The right plot shows the same analysis for the Ka-band system parameters in Table 2. Compared to P-band, the shorter wavelength, only slightly compensated by the larger bandwidth, results in critical baselines starting from a few hundred meters. Note that the analyzed P-band and Ka-band system parameters are taken as representative example cases throughout the paper. However, conclusions to other

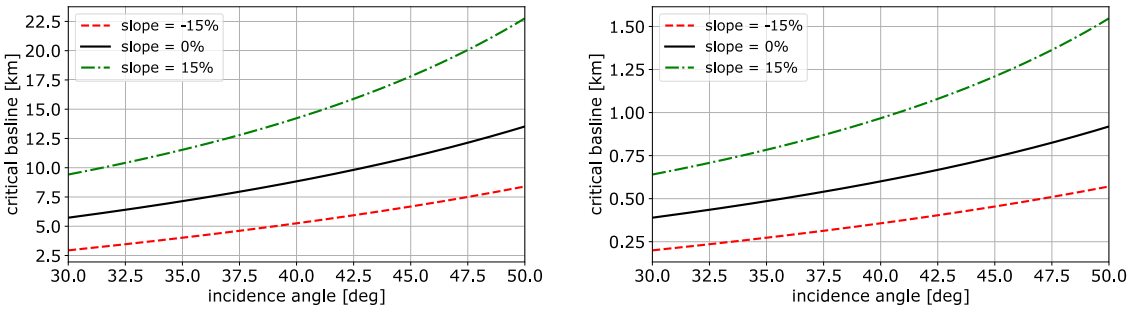

Fig. 3. Critical baseline for different incidence angles and local slopes computed for the spherical Enceladus model shown in Fig. 4 and the system parameters depicted in Table 2: P-band (left) and Ka-band (right).

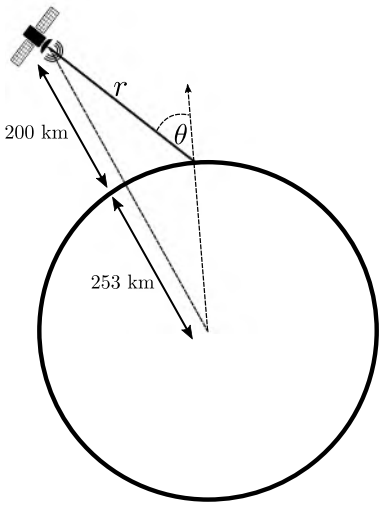

Fig. 4. Spherical Enceladus acquisition model.

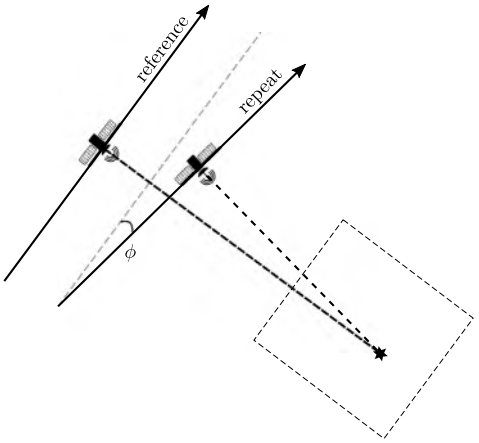

Fig. 5. Illustration of orbital convergence and the convergence angle ϕ.

Table 2
Example SAR system parameters as suggested for the EnEx concept.

Parameter	P-band	Ka-band
center frequency	435 MHz	32 GHz
bandwidth	20 MHz	100 MHz

system specifications may be drawn easily as the critical baseline varies linearly with frequency and bandwidth (cf. Eq. (5)).

The discussed baseline limitation requires the repeat orbit to be within an imaginary orbital tube around the reference orbit, with a size depending on the system and imaging geometry. Note that the critical baseline refers to the perpendicular baseline. Thus, an orbital displacement in the line of sight is less critical.

2.1.2. Parallel orbit requirement

Geometric decorrelation (i.e., a reduced γ_{geo}) between reference and repeat-pass acquisition also results from non-parallel orbit trajectories [42], as depicted in Fig. 5. Comparable to the above outlined decorrelation effect due to an increasing baseline, non-parallel trajectories result in slightly different rotational aspect angles on the scene, thus, a different realization of the scattering inherent phase. Again, the effect can be considered as a mapping of different portions of the ground scattering spectrum, but in the azimuthal direction. Similar to the critical baseline we can approximate a critical rotation angle ϕ, i.e., orbital convergence angle, that results in complete decorrelation of the two SAR images. Following [42],

$$\phi_{\text{crit}} = \frac{\lambda}{2 \cdot \sin(\theta) \cdot \delta_{\text{a}}}, \tag{7}$$

where δ_{a} is the azimuth resolution of the system that is indirectly proportional to the processed bandwidth in azimuth. The decorrelation effect can be almost completely compensated for by squinting the antenna, i.e., steering the spacecraft in the azimuthal direction in order to introduce an opposing azimuthal frequency shift. Hence, the parallel orbit requirement can be replaced, within a certain extent, to a relative pointing accuracy requirement of the spacecraft between reference and repeat pass. At this point, only a brief feasibility assessment is given. In Fig. 6 the critical convergence angle, in radians, is depicted for the P-band and Ka-band system parameters for a range of feasible values of azimuth resolution. Note that for P-band the reduced wavelength due to propagation in ice with a relative dielectric permittivity of $\varepsilon_{\text{r}} \approx 3.1$ [44] has to be accounted for, according to $\lambda = \lambda_0/\sqrt{\varepsilon_{\text{r}}}$, where λ_0 is the wavelength in free space. Angle values lie in the tenths of radians range for the P-band parameters and in the order of several milliradians for Ka-band. Comparing these values to pointing requirements stated for NASA's Cassini mission in the Saturn system (i.e., 2 mrad [45]) and the mission proposal *Enceladus Orbilander* (i.e., 350 µrad [8]), an accurate compensation of not perfectly parallel orbits is expected to be achievable, yet at the accuracy limit for Ka-band. The parallel orbit requirement is therefore governed by practical considerations such as providing suitable baselines over time frames allowing consistent acquisitions over long swaths and minimizing the required squint angles. Generally speaking, a minimized orbital convergence is desirable but small deviations from the parallel orbit assumption are not expected to hinder interferometric imaging.

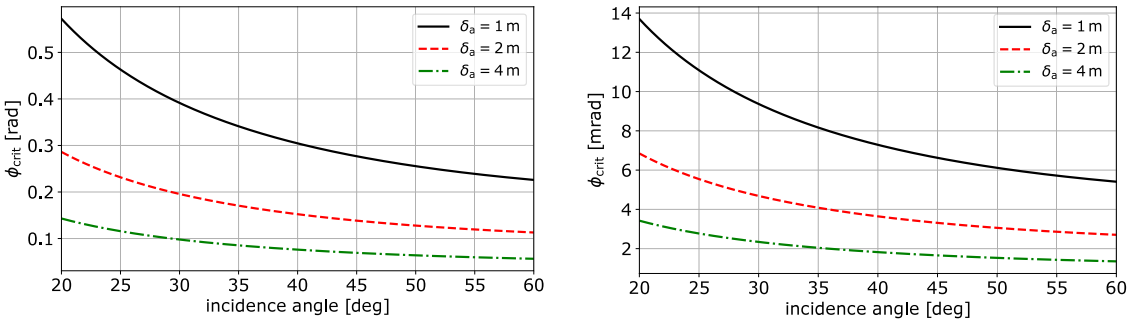

Fig. 6. Critical rotation angle for different incidence angles and example values of azimuth resolution for the spherical Enceladus model shown in Fig. 4 and the system parameters depicted in Table 2: P-band (left) and Ka-band (right).

2.2. TomoSAR requirements

Considering P-band acquisitions of an ice sheet, InSAR only provides a mean height of all backscatter contributions within the glacial volume. In order to resolve the whole vertical distribution of scatterers, multiple passes over the same area can be used to form a synthetic aperture, i.e., a synthetic antenna array, in the elevation direction. The concept is illustrated in Fig. 2. The resolution in elevation depends on the synthetic aperture length L_{el} [46],

$$\delta_{el} = \frac{\lambda \cdot r}{2 \cdot L_{el}}. \tag{8}$$

Note that L_{el} represents the aperture length perpendicular to the line-of-sight direction. For the spherical Enceladus acquisition model in Fig. 4, the elevation resolution is depicted in Fig. 7 for the P-band parameters and varying array lengths L_{el}. The reduced wavelength due to propagation in ice is accounted for. The red contour indicates the resolution in the range direction for the P-band system, given by

$$\delta_r = \frac{c_0}{2 \cdot W \cdot \sqrt{\varepsilon_r}}, \tag{9}$$

where c_0 is the speed of light in free space. It may be considered as a useful lower limit below which an enhanced elevation resolution does not provide major improvement for volumetric imaging. Note the same order of magnitude of critical baseline values (Fig. 3, left panel) and tomographic aperture lengths leading to useful elevation resolution. This correspondence allows for the assumption that acquisitions suitable for InSAR may also be used to form a tomographic aperture. To avoid ambiguities in the elevation direction, the tomographic aperture has to be sampled with a sufficient number of passes. Assuming uniform spacing, the minimum required distance between passes is given by [46]

$$d \leq \frac{\lambda \cdot r \cdot \sin\theta}{2 \cdot h_v}, \tag{10}$$

where h_v is the depth of the volume to be imaged unambiguously. Meaningful values of h_v are limited by the depth down to which significant backscattered power is to be expected. In glacial terrain this depth is mainly governed by the power extinction within the ice and depends on the composition and the temperature of the ice. Values in the tens of meters to a few hundred meters are to be expected for the P-band frequencies. Fig. 8 depicts the minimum required distance d for the P-band parameters and three example values of unambiguous volume depth h_v. In reality, the limited spacecraft navigation capability may not allow a uniform sampling of the tomographic aperture. For a non-uniform sampled aperture, defining a sampling requirement is complex. Nevertheless, the depicted minimum distances in Fig. 8 in the order of a few hundred meters give a fair estimate of the minimum required pass spacing that should be contained within the tomographic aperture. An unevenly sampled aperture results in a higher sidelobe level in elevation. Commonly, TomoSAR focusing of data acquired over ice sheets is achieved using a Matched Spatial Filter (MSF) or Capon beam forming [47]. Capon is frequently used in TomoSAR for mitigating

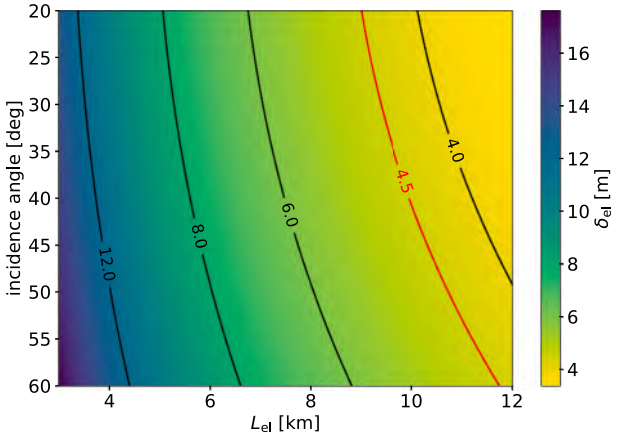

Fig. 7. Elevation resolution for different incidence angles and tomographic aperture lengths L_{el} computed for the spherical Enceladus model in Fig. 4 and the P-band system parameters depicted in Table 2. The red contour indicates the range resolution for the P-band system. (For interpretation of the references to color in this figure legend, the reader is referred to the web version of this article.)

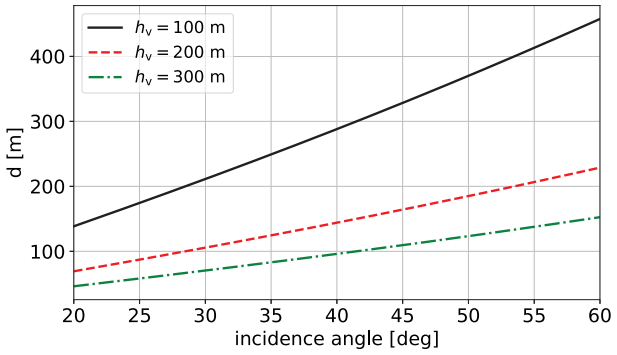

Fig. 8. Minimum required distance between passes for different incidence angles and unambiguous heights h_v computed for the spherical Enceladus model in Fig. 4 and the P-band system parameters depicted in Table 2.

the increased sidelobe level from uneven sampling and overcoming the Rayleigh resolution in (8). Hence, a shorter tomographic aperture length L_{el} and a reduced number of passes is sufficient. However, Capon as a non-linear technique does not provide radiometrically correct imaging.

Since the elevation separation between passes for an Enceladus orbiter is not expected to be controlled within meters or even tens of meters, the formation of a tomographic aperture has to follow to a certain extent an opportunity driven approach. The resolution driven aperture length L_{el} in the few kilometer range may be roughly controlled by a drift of the orbit over time. The necessary number of

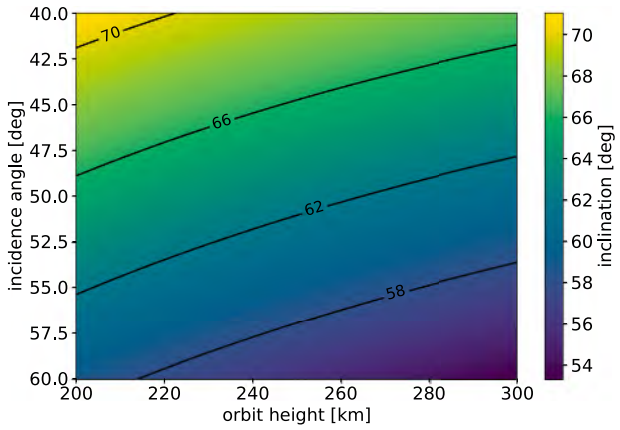

Fig. 9. Required orbit inclination for different incidence angles and orbit heights computed for the spherical Enceladus model in Fig. 4. (For interpretation of the references to color in this figure legend, the reader is referred to the web version of this article.)

passes within the tomographic aperture $N > L_{el}/d$ lies in the order of tens of passes and poses an orbital repeat quality requirement similar to the InSAR baseline requirement. The exact distribution of the passes is expected to happen in a random-like manner driven by the orbit stability, spacecraft navigation accuracy, and maneuver event timing. The estimation of the baselines for InSAR and TomoSAR processing may be achieved by well-established approaches based on the acquired SAR images as described in [48–50].

2.3. General orbit considerations

2.3.1. Coverage

To ensure coverage of the most-interesting south polar region (plumes are located at < −70° latitude) with incidence angles suitable for interferometric and tomographic SAR imaging (i.e., 25° - 60°), orbits are required to have sufficient inclination and height. Orbits analyzed in this study have altitudes above the surface of 200 km to 300 km. Fig. 9 depicts required orbit inclinations for imaging a surface point at the South Pole (most stringent point) with an incidence angle from 40° to 60°. The spherical model from Fig. 4 is assumed, with varying orbit height. Note that especially for TomoSAR, incidence angles beyond 50° are less favorable, due to significantly less vertical penetration into the ice crust for larger incidence angles and a reduced system sensitivity because of the resulting larger range distances. This requires orbit inclinations above 60°. This condition proves to be at the feasibility limit. Covering areas outside the plume region (> −70° latitude) is not stated as main objective for EnEx, which is focused on a lander mission in the plume region. However, global mapping and exploration may be an objective for other mission concepts and is considered in the following sections.

2.3.2. Stability

To minimize the Δv for station keeping, orbits that maintain the InSAR and TomoSAR required repeat characteristic over long periods are favorable. In the context of planetary orbit design, orbits are commonly considered stable as long as no impact or escape occurs. We refer to this characteristic as common orbital stability from here on. However, for InSAR and TomoSAR, a stable orbit should provide a repeating trajectory within an imaginary orbital tube, corresponding to the baseline requirements. We refer to this characteristic as orbital InSAR stability from here on. The size of the tube depends on the system frequency, system bandwidth, distance to the scene, and local incidence angle.

Table 3
8:35 periodic orbit from [36]. Initial conditions given in inertial, non-rotating frame aligned with the IAU defined Enceladus body fixed frame at epoch.

Parameter	Unit	Value
a_0	km	0.4987636181497566E+03
e_0	–	0.7594742316109369E−01
i_0	deg	0.5872499513454099E+02
ω_0	deg	−0.9185596836014398E+02
Ω_0	deg	0.2417191769293457E+03
ν_0	deg	$-\omega_0$
T_{rep}	day	0.1026020511894865E+02

2.4. Existing solutions

Of the Enceladus orbits in the literature, the periodic solutions proposed by *Russell and Lara* in [36] are closest to meeting the above outlined requirements due to the inherent repeat ground track characteristic in periodic orbits. The solutions are designed regarding a maximized inclination and long-term stability. The design was performed in the Enceladus-Saturn Hill model, implying a circular orbit of Enceladus around Saturn. For details on Hill's approximation to the three-body-problem, see for example [51]. The non-spherical Enceladus gravity was included in terms of J_2, J_3, and C_{22} contributions (see [36] for details). In [36] a periodic 8:35[1] orbit was proposed as a compromise between high inclination and proven long-term stability over 6 months in an n-body ephemeris propagation. The initial conditions for the 8:35 orbit are depicted in Table 3.

Fig. 10 shows characteristics of the 8:35 orbit propagated in the Hill's plus non-spherical gravity model over one repeat period of $T_{rep} \approx 10.26$ days. The orbit has a mean altitude of 245 km and mean inclination of 62°. The third body influence results in a strong variation of altitude and inclination. The perfect repeat characteristic is evident in the ground track, where the first and last points of one repeat period overlap precisely. Fig. 11 shows an ephemeris propagation of the 8:35 orbit in Table 3 including the ephemerides of Enceladus and Saturn and the influence of Enceladus' non-spherical gravitational field. Throughout the paper, the ephemeris states are based on publicly available[2] data of the Jet Propulsion Laboratory and we use the Particle Integrator (PInt) developed at DLR's Institute of Planetary Research (described in [52,53]) for the orbit propagation. The non-spherical gravity contribution is based on the harmonic coefficient determination by [54]. The coefficients are listed in Table 4 and their central values are used. Note that for the ephemeris propagation in [36] older data were used. For simplicity and without loss of generality, the propagation is started at January 1, 2000 (J2000) and propagated over two repeat periods ($2T_{rep} \approx 20.52$ days). The left panel of Fig. 11 shows that the general appearance of the orbit is similar to the nominal solution in Fig. 10 (propagation in Hill's model), however, the ground track shows that the repeat characteristic is lost, i.e., the first (black) and second (red) repeat cycle diverge significantly. Note that the difference to the nominal solution can be mainly attributed to the non-circular orbit of Enceladus around Saturn with an eccentricity of roughly 0.0047 that is approximated as circular in Hill's model. The eccentricity results in a varying acceleration on the orbiter caused by Saturn's gravity. The refined Enceladus gravity field has a secondary effect.

The non-repeating ground track in the ephemeris propagation allows the qualitative conclusion that the analyzed 8:35 orbit does not

[1] 35 spacecraft revolutions around Enceladus and $8 + \Delta\Omega$ revolutions of Enceladus around Saturn within one repeat period. $\Delta\Omega$ denotes a fraction of the Enceladus orbit period.

[2] URL: https://naif.jpl.nasa.gov/naif/spiceconcept.html ; ftp://naif.jpl.nasa.gov/pub/naif/generic_kernels/spk/planets/de438.bsp; ftp://naif.jpl.nasa.gov/pub/naif/generic_kernels/spk/satellites/sat427.bsp; ftp://naif.jpl.nasa.gov/pub/naif/generic_kernels/pck/pck00010.tpc

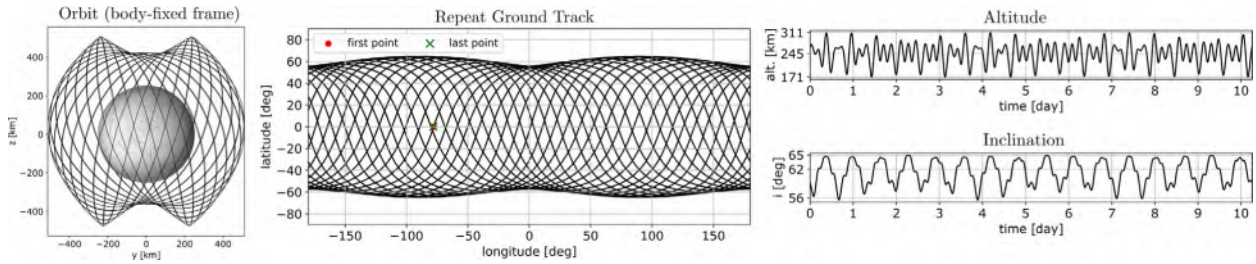

Fig. 10. One period of the 8:35 orbit from [36] propagated in Hill's model plus the non-spherical gravity of Enceladus. (For interpretation of the references to color in this figure legend, the reader is referred to the web version of this article.)

Table 4
Estimated Enceladus gravity harmonic coefficients from [54].

Coefficient	Central value $\pm 1\sigma$
$J_2(\times 10^{-6})$	5435.2 ± 34.9
$C_{21}(\times 10^{-6})$	9.2 ± 11.6
$S_{21}(\times 10^{-6})$	39.8 ± 22.4
$C_{22}(\times 10^{-6})$	1549.8 ± 15.6
$S_{22}(\times 10^{-6})$	22.6 ± 7.4
$J_3(\times 10^{-6})$	−115.3 ± 22.9

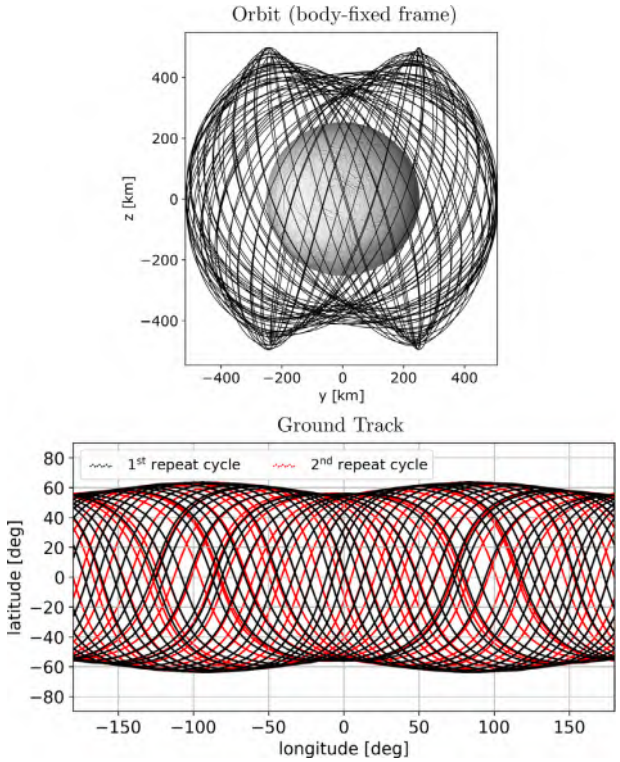

Fig. 11. Two repeat periods of the 8:35 orbit from [36] propagated in the ephemeris model. Note the divergence of the ground track of the first and second repeat cycle. (For interpretation of the references to color in this figure legend, the reader is referred to the web version of this article.)

allow the implementation of a consistent interferometric or tomographic SAR mission. Other periodic orbits from [36] are expected to show comparable repeat characteristic degradation in ephemeris propagation, as their design is performed in the same simplified model. Besides, a faster repeat period than the 10.25 days of the 8:35 orbit is desirable, especially for TomoSAR purposes where an aperture out of several repeat passes has to be constructed. To meet the InSAR and TomoSAR requirements, periodic orbits that provide repeat ground track characteristic in realistic dynamic models are required.

3. Orbit search methodology

In this section, the developed methodology for identifying orbits suited for InSAR and TomoSAR is outlined. Despite the fact that a certain baseline between reference and repeat passes may be required, the search is targeted on identifying perfectly periodic orbits. The required baselines in the order of hundreds of meters to few kilometers are expected to form naturally due to the complexity of the dynamic system, uncertainty in the gravitational field, and navigation inaccuracy. In addition, divergence from perfect periodicity may be achieved by slightly deviating from the optimum orbit solution.

3.1. Model and parameters

In order to account for the non-circular orbit of Enceladus around Saturn and all relevant perturbations, the periodic orbit search is performed in an ephemeris model. The used model is restricted to the ephemeris of Enceladus and Saturn and perturbation by the non-spherical gravity of Enceladus and Saturn, neglecting, e.g., perturbations by the other moons and planets. This simplification is justified by the magnitudes of acceleration acting on the spacecraft, shown in Fig. 12. As an example case, the spacecraft is propagated starting from the initial conditions for the 8:35 orbit and the accelerations attributed to the masses of Enceladus, Saturn, the Sun, the Jupiter barycenter, and the 6 Saturn moons closest to Enceladus are shown. Additionally, the accelerations caused by the higher-order terms of the non-spherical gravity field of Enceladus and Saturn are depicted. The used higher terms of Enceladus correspond to Table 4 and of Saturn to the values provided in [55]. Enceladus, Saturn, and their higher terms exceed the acceleration of other bodies by several orders of magnitude.

3.2. Grid search approach

Due to the complexity of the ephemeris model, a brute-force grid search approach is implemented for identifying periodic solutions. The search parameter space spans around the initial conditions of the 8:35 orbit depicted in Table 3. This approach is chosen to limit the parameter space and is justified by the fact that the 8:35 orbit provides well suited characteristics for SAR imaging. The parameter space is restricted to 3 dimensions – namely, the initial values of the semi-major axis a_0, inclination i_0, and eccentricity e_0 – as they are the determining parameters for the orbit shape.

The desired periodicity can be described in a body fixed frame by the fact that after the repeat period T_{rep} the state vector (position and velocity) is approximately equal to the initial state vector:

$$\begin{aligned} \mathbf{S}_{\text{rep}} &\approx \mathbf{S}_0 \\ \left[x_{\text{rep}}, y_{\text{rep}}, z_{\text{rep}}, u_{\text{rep}}, v_{\text{rep}}, w_{\text{rep}}\right]^{\text{T}} &\approx \left[x_0, y_0, z_0, u_0, v_0, w_0\right]^{\text{T}}. \end{aligned} \tag{11}$$

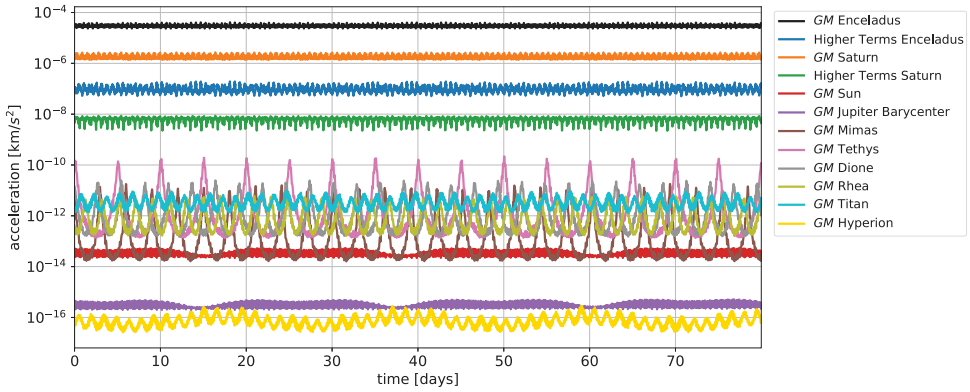

Fig. 12. Accelerations acting on the orbiter for a propagation starting from the initial conditions of the 8:35 orbit from [36]. (For interpretation of the references to color in this figure legend, the reader is referred to the web version of this article.)

Algorithm 1: Grid search algorithm

Input: Initial state parameter space: $\mathbf{a}_0$ of size N_a, $\mathbf{i}_0$ of size N_i, $\mathbf{e}_0$ of size N_e
Number of orbiter revolutions: N
Output: Optimization metric array: $\mathbf{M}_{\mathrm{N_a}\times\mathrm{N_i}\times\mathrm{N_e}}$

```
for a_0 in a_0 (increment ia) do
    T̃_rep = N · sqrt(4·π²·a_0³ / μ_E);
    for i_0 in i_0 (increment ii) do
        for e_0 in e_0 (increment ie) do
            Propagate orbit from t = T_0 to t = T_0 + T̃_rep + ΔT;
            if no impact then
                Provide initial state vector A_{6×1} and state vectors in B_{6×K} in body-fixed frame (Fig. 13) ;
                Upsample B_{6×K} using spline interpolation ⟶ B̂_{6×K̂} ;
                Compute angle between position vector in A and all position vectors in B̂ ⟶ χ_{1×K̂} ;
                Compute angle between velocity vector in A and all velocity vectors in B̂ ⟶ ν_{1×K̂} ;
                M[ia, ii, ie] = min(|χ| + |ν|)
            end
        end
    end
end
```

To constrain the possible T_rep values, an estimate can be provided according to

$$\widetilde{T}_\mathrm{rep} = N \cdot \widetilde{T}_\mathrm{E} = N \cdot \sqrt{\frac{4 \cdot \pi^2 \cdot a_0^3}{\mu_\mathrm{E}}}, \tag{12}$$

where N is the number of revolutions of the orbiter around Enceladus prior to repeat, $\widetilde{T}_\mathrm{E}$ is the estimated revolution period around Enceladus, a_0 is the initial value of the semi-major axis, and μ_E is the Enceladus gravitational parameter. Note that $\widetilde{T}_\mathrm{E}$ is only a rough estimate, because the considered orbits are significantly non-Keplerian, i.e., the semi-major axis a largely changes over time, as indicated in Fig. 10.

The concept of the grid search approach is to identify initial state values $\{a_0, i_0, e_0\}$ that result in orbit solutions satisfying the condition in (11) after a desired number of orbiter revolutions N. The main steps are described in the form of pseudo code in Algorithm 1, and Fig. 13 illustrates the concept for the case of $N = 1$.

For every constellation in the parameter space $\{a_0, i_0, e_0\}$, first an estimate of the expected repeat period $\widetilde{T}_\mathrm{rep}$ is provided according to (12). The current increment values of $\{a_0, i_0, e_0\}$ and the values $\{\omega_0, \Omega_0, \nu_0\}_{8:35}$ of the 8:35 orbit, depicted in Table 3, are used as initial state for the orbit propagation. Starting at epoch $t = T_0$ as stated for Table 3, the orbit is propagated until a time $t = T_0 + \widetilde{T}_\mathrm{rep} + \Delta T$. The time interval ΔT is added to compensate for the inaccurate $\widetilde{T}_\mathrm{rep}$ estimate due to the non-Keplerian orbit dynamics, as visualized in Fig. 13. A value of $\Delta T = 3\,\mathrm{h}$ has proven to be a good choice for the analyzed orbits. If the orbit impacts Enceladus, the current iteration is skipped. If no impact occurs, a metric is provided to test the similarity between the state vector $\mathbf{A}$ at $t = T_0$ and the most similar state vector in the time interval $t_\mathrm{K} = [T_0 + \widetilde{T}_\mathrm{rep} - \Delta T, T_0 + \widetilde{T}_\mathrm{rep} + \Delta T]$. For this purpose, temporally even-spaced state vectors $\mathbf{B}_{6\times\mathrm{K}}$ in t_K are provided by the propagator and are interpolated to a finer temporal sampling using a spline interpolation, resulting in $\hat{\mathbf{B}}_{6\times\hat{\mathrm{K}}}$. A sample spacing in the order of 1 s was found to be sufficient. In order to account with equivalent sensitivity for the similarity regarding position and velocity between the state $\mathbf{A}$ and states in $\hat{\mathbf{B}}$, the angle between the position and velocity vectors is used as a metric rather than the absolute values. The metric

$$\mathbf{M} = \min\left(|\boldsymbol{\chi}| + |\boldsymbol{\nu}|\right), \tag{13}$$

describes the similarity between state $\mathbf{A}$ and the most similar state in $\hat{\mathbf{B}}$, where $\boldsymbol{\chi}_{1\times\hat{\mathrm{K}}}$ is the angle between the position vectors and $\boldsymbol{\nu}_{1\times\hat{\mathrm{K}}}$ the angle between the velocity vectors. The results of every parameter constellation are stored in the optimization metric array $\mathbf{M}_{\mathrm{N_a}\times\mathrm{N_i}\times\mathrm{N_e}}$.

The orbit solution with the best repeat characteristic for a given N corresponds to the parameters $\{a_0, i_0, e_0\}$ that minimize $\mathbf{M}$:

$$a_{0,\min}, i_{0,\min}, e_{0,\min} = \underset{\mathbf{a}_0, \mathbf{i}_0, \mathbf{e}_0}{\arg\min}\, \mathbf{M}. \tag{14}$$

For the example case of $N = 14$ the grid search result is shown in Fig. 14 in form of a slice through $\mathbf{M}$ along the a_0, i_0-plane at $e_{0,\min} = 0.0759$. The considered parameter space spans over an initial semi-major axis from 400 km to 520 km and an initial inclination between 48°

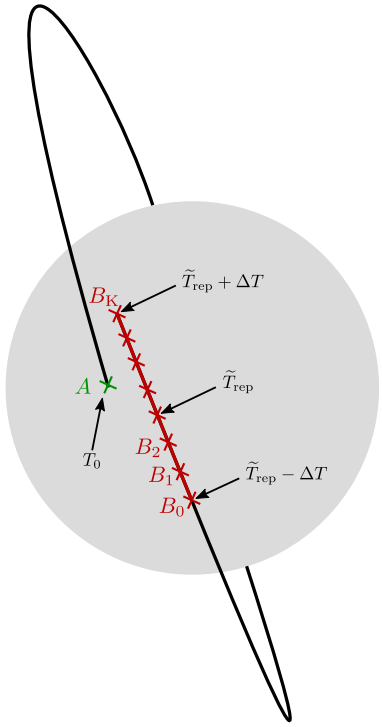

Fig. 13. Illustration of the state vectors of interest for Algorithm 1.

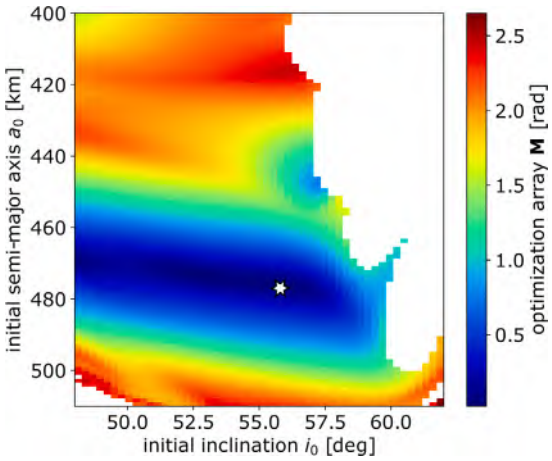

Fig. 14. Result of the grid search algorithm for $N = 14$ orbiter revolutions. A slice through the 3-D optimization space **M** is shown at the minimum position of the initial eccentricity e_0. The white star indicates the minimum and thus the parameter constellation of semi-major axis a_0, inclination i_0, and e_0 resulting in the most accurate repeat characteristic. White areas indicate parameter constellations leading to impacting orbits. (For interpretation of the references to color in this figure legend, the reader is referred to the web version of this article.)

and 62°. The white areas indicate parameter constellations resulting in impacting orbits and the white star is located at the minimum position. A general tendency that inclinations above a certain limit lead to severe instability is evident and corresponds to the findings in the literature, e.g., [36]. The minimum area extends over roughly 5° of initial inclination and a few kilometers of semi-major axis, suggesting that a range of orbit solutions with similar repeat quality exist. This range may offer a certain freedom in orbit design around the optimal solution.

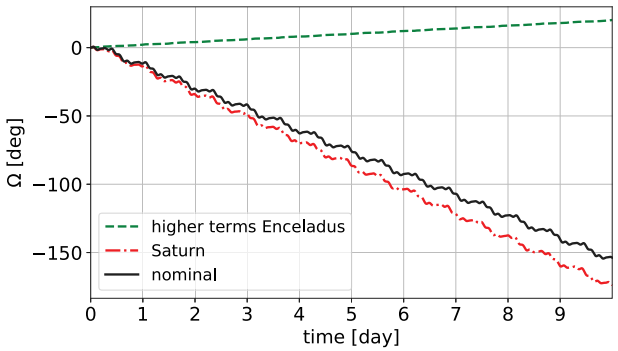

Fig. 15. Drift of the longitude of the ascending node Ω caused by the higher terms of Enceladus, Saturn, and both combined (nominal).

4. Periodic orbit solutions

The periodic orbit search was performed for integer values of N from 1 to 40 over the intervals

$$\begin{aligned} a_0 &= [400\,\mathrm{km},\ 550\,\mathrm{km}], \\ i_0 &= [50°,\ 65°], \text{and} \\ e_0 &= [0,\ 0.1], \end{aligned} \tag{15}$$

with a sample spacing of $\delta a_0 = 1\,\mathrm{km}$, $\delta i_0 = 0.25°$, and $\delta e_0 = 0.01$. The interval range of a_0 and i_0 is chosen due to the coverage requirement of the south polar region with decent incidence angles. Higher inclinations consistently lead to impacting orbits. Also eccentricities beyond 0.1 result in impacts or escapes. In a second iteration the sample spacing was refined by a factor of 10 around the minimum. A qualitative assessment was performed for every N to check if the $\{a_{0,\min}, i_{0,\min}, e_{0,\min}\}$-solution resulted in a periodic behavior.

4.1. General orbit characteristics

Periodic orbits consistently emerge from the search, with repeat periods of

$$T_{\mathrm{rep}} \approx K \cdot 1.29\,\mathrm{d}, \tag{16}$$

where $K \geq 1$ takes integer values. Without the perturbation by Saturn and the higher terms of the Enceladus gravity field the repeat period would correspond to a multiple of the Enceladus rotation period of 1.37 days, leading to the required repeating trajectory in the Enceladus body-fixed frame. The deviation of approximately two hours results from a drift of the longitude of the ascending node Ω in the Enceladus inertial frame, shown in Fig. 15 over 10 days for the orbit that repeats after $T_{\mathrm{rep}} \approx 1 \cdot 1.29\,\mathrm{d}$. The drift of Ω is mainly caused by the third body effect of Saturn (dash–dot, red line in Fig. 15). The higher terms of Enceladus' gravity field result in an opposing drift with significantly lower magnitude (dashed, green line in Fig. 15). A combined drift (solid, black line in Fig. 15) of $\dot{\Omega} = 21.1°/1.37\,\mathrm{d}$ is present, confirming the observed deviation according to

$$1.37\,\mathrm{d} \cdot \left(1 - \frac{21.1°}{360°}\right) \approx 1.29\,\mathrm{d}. \tag{17}$$

The two-hour difference to the Enceladus orbital period of 1.37 days may allow to effectively track the tidal deformation processes that are locked to the Enceladus period.

From here on the assessment is restricted to the three orbits with the fastest repeat period ($K = 1, 2, 3$) as the short repeat periods are favorable for both, a shorter time for generating interferometric and tomographic products and reducing the effect of temporal decorrelation of the backscatter distribution in the scene between repeating passes. The K1 orbit repeats after $N = 5$ orbiter revolutions, the K2 orbit after $N = 9$, and the K3 orbit after $N = 14$. Fig. 16 shows characteristics of

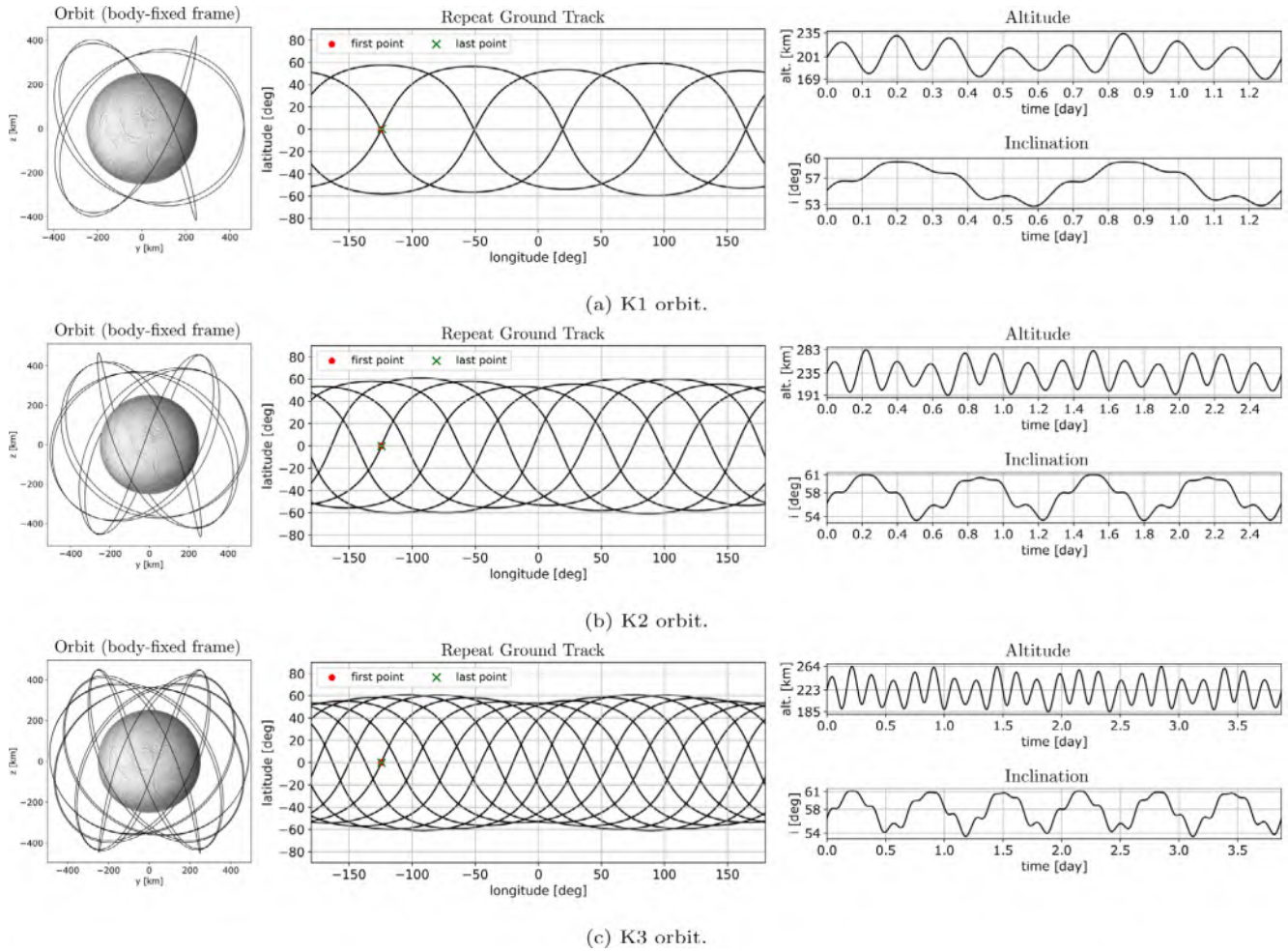

Fig. 16. One period of the example K1, K2, and K3 orbits. Note the precise overlap of first and last point of the ground track.

Table 5
Orbit solutions. Initial conditions given in inertial, non-rotating frame aligned with the IAU defined Enceladus body fixed frame at epoch.

Parameter	Unit	K1	K2	K3
a_0	km	0.45362E+03	0.49041E+03	0.47752E+03
e_0	–	0.7594E−01	0.7594E−01	0.7594E−01
i_0	deg	0.5517E+02	0.5625E+02	0.5648E+02
T_{rep}	day	1.2919	2.5788	3.8744
mean i	deg	56.4	57.7	57.8
max. i	deg	59.5	61.0	61.1
mean altitude	km	200.6	234.1	222.5
max. altitude	km	234.3	283.0	264.0
min. altitude	km	169.8	191.2	185.7

the three solutions and Table 5 depicts the initial conditions and relevant properties. Note that the illustrated orbits are examples of classes of solutions with similar shape emerging from the minimum region of the optimization space **M**. The solutions in Fig. 16 are examples within the minimum region of **M** optimized toward a maximum inclination. Note also that the periodicity is not perfect, as the condition in (11) is only approximated by the grid search approach.

The repeat characteristic is demonstrated in the ground tracks shown in Fig. 16, where the first point and last point after one repeat period overlay. The orbits reach maximum inclinations of 59.5°, 61.0°, and 61.1° for the K1, K2, and K3 orbit, respectively. Combined with the relatively high altitudes of the orbits between 170 km and 283 km, these inclinations allow for a consistent coverage of the south polar region. Fig. 17 shows the coverage on the Enceladus surface for the three orbits within one repeat period for a right-looking system and incidence angles on the surface in the range of 25° to 60°. Coverage values greater than 1 indicate access to the surface point from multiple different orbit positions. Note that the coverage pattern for a left-looking system is almost identical but mirrored at the equator, giving access to the northern hemisphere. The K3 orbit provides almost global coverage, whereas K1 and K2 show significant gaps. However, all three orbits allow for a consistent coverage of the most-interesting plume region (<−70° latitude). The access to certain regions from multiple parts of the orbit may be beneficial in areas with strong topographic variations to mitigate shadow effects. Fig. 18 shows the minimum incidence angle with which the south polar region can be imaged. The black dots indicate the positions of the plumes according to [56]. For the K1 case, the coverage of a significant part of the plume region around the South Pole requires incidence angles beyond 50°, with a maximum of 59° suggesting unfavorable conditions for tomographic imaging. Still, the major part of the plume region can be imaged with incidence angles below 50°. For the K2 and K3 cases, the higher altitude and higher inclination compared to K1 allow for a coverage with incidence angles below 50° over the whole plume region.

4.2. Stability assessment

For a qualitative stability assessment, the evolution of the orbits over 200 days is shown in Fig. 19. Unlike in the dynamic model for the orbit search, all accelerations shown in Fig. 12 are included in the orbit propagation. However, the influence of the additional forces is barely noticeable in comparison to the results when only Enceladus and Saturn

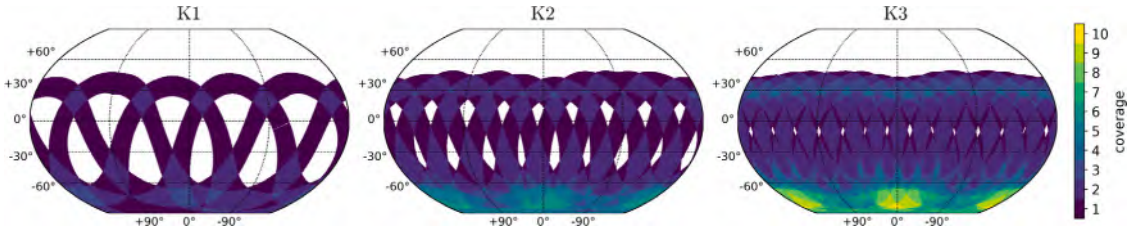

Fig. 17. Coverage opportunity of the K1, K2, and K3 orbit for a right looking system and incidence angles from 25° to 60°. Values > 1 indicate access to the region from multiple parts of the orbit. (For interpretation of the references to color in this figure legend, the reader is referred to the web version of this article.)

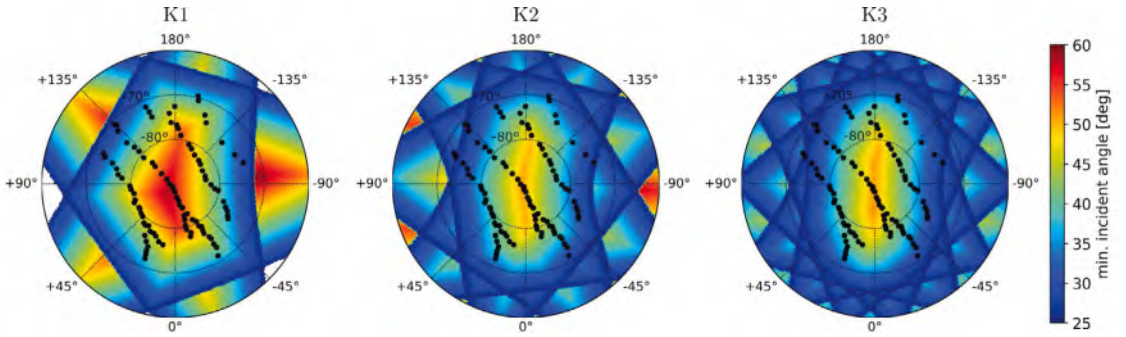

Fig. 18. Minimum incidence angle in the south polar region for the K1, K2, and K3 orbit. Black dots indicate the plume locations. (For interpretation of the references to color in this figure legend, the reader is referred to the web version of this article.)

are considered (further discussed in Section 4.3). All three orbits keep their general shape over 200 days and beyond. K2 specially provides an almost perfect repeat characteristic over the whole course. K1 shows a drift over time and loses the repeat characteristic after approximately 40 days. Each orbit is proven stable according to common stability requirements (no impact, no escape) in long-term propagations beyond 15 years.

To evaluate the InSAR stability characteristic, Fig. 20 shows the distance of the orbiter to a reference trajectory over time. The reference is chosen as the trajectory of the first repeat cycle of the orbit. The distance instead of the perpendicular baseline $B_\perp$ is considered here as $B_\perp$ depends on the incidence angle and therefore does not allow a general description of the repeat stability, i.e., InSAR stability. Though, the distance can be considered as the maximum possible value of $B_\perp$. For the three orbits, the distance varies around a mean value of approximately 3 km over few to several tens of days and then increases after a certain time. The 3 km distance lies well within the critical baseline values for the low-frequency P-band system shown in the left panel of Fig. 3, but significantly exceeds the critical baselines for the high-frequency Ka-band system shown in the right panel of Fig. 3. This suggests that no consistent repeat-pass InSAR acquisitions in Ka-band are possible. To compare the orbits, we define the InSAR stability so that the 20 day distance average does not surpass 8 km. According to this criterion, K1 provides InSAR stability over 47 days, K2 over 262 days, and K3 over 82 days. The shorter stability time of K1 may be related to the lower altitude compared to K2 and K3 and therefore stronger perturbation by Enceladus' non-spherical gravity field.

4.3. Robustness assessment

As possible sources of perturbation on the orbit solutions we evaluate the influence of the Saturnian moons, Jupiter, and the Sun, the drag caused by the ejected gas and dust of the plumes, the uncertainty in the Enceladus gravity field, and possible navigation inaccuracies. The assessment is mainly done on the example case of the K2 orbit.

4.3.1. Moons, Jupiter, and the Sun

The analyzed orbits resulted from an orbit search in an ephemeris model including Enceladus and Saturn and perturbation by the higher terms of their gravity fields. Fig. 21 shows the distance d to the nominal orbit (i.e., the solution from the search model) over 40 days when propagating in a model including the 6 closest Saturnian moons, the Jupiter barycenter, and the Sun. Example cases of the acceleration magnitudes of the perturbations are shown in Fig. 12. d is rising over time but does not exceed 200 m over the 40 days. When comparing it to the non-perfect repeat characteristic with distances between reference and repeat passes up to few kilometers (cf. Fig. 20), the perturbation by the moons, Jupiter, and the Sun may be neglected.

4.3.2. Drag by plumes

The plumes in the south polar region eject gas and dust into space introducing a perturbing drag force on the spacecraft when passing by. Spatial and temporal samples of the combined gas and dust density were derived from Cassini attitude control data during 6 flybys at Enceladus [38,57]. The derived density varies significantly with time and with the altitude and latitude of the measurement position. The assessment of the perturbation by the plumes is restricted here to a worst-case estimate with a maximum density of $47 \times 10^{-12}\,\mathrm{kg\,m^{-3}}$ at an altitude of 99 km and a latitude of −90° reported in [38]. The acceleration of the drag force can be estimated according to [57]

$$a_\mathrm{D} = \frac{F_\mathrm{D}}{M_\mathrm{SC}} = \frac{1}{2 \cdot M_\mathrm{SC}} \cdot \rho \cdot v^2 \cdot C_\mathrm{D} \cdot A, \tag{18}$$

where F_D is the drag force, M_SC the mass of the spacecraft, ρ the density, v the velocity, C_D the drag coefficient, and A the cross-sectional area of the spacecraft projected in the direction of the velocity vector. As an example case, a Cassini-like spacecraft with $A = 18.6\,\mathrm{m^2}$, $C_\mathrm{D} = 2.2$, and $M_\mathrm{SC} = 2150\,\mathrm{kg}$ is assumed [57]. The maximum velocity of the 3 orbits with $v = 139\,\mathrm{m\,s^{-1}}$ is used for the worst-case estimate resulting in an acceleration of $a_\mathrm{D} = 8.6 \times 10^{-12}\,\mathrm{km\,s^{-2}}$. This value lies within the magnitudes of acceleration caused by the Saturnian moons (cf. Fig. 12) and may be regarded as negligible, as discussed in Section 4.3.1. Note that the drag is expected to be significantly lower due to the higher altitudes and lower absolute latitudes of the analyzed orbits and therefore lower plume density.

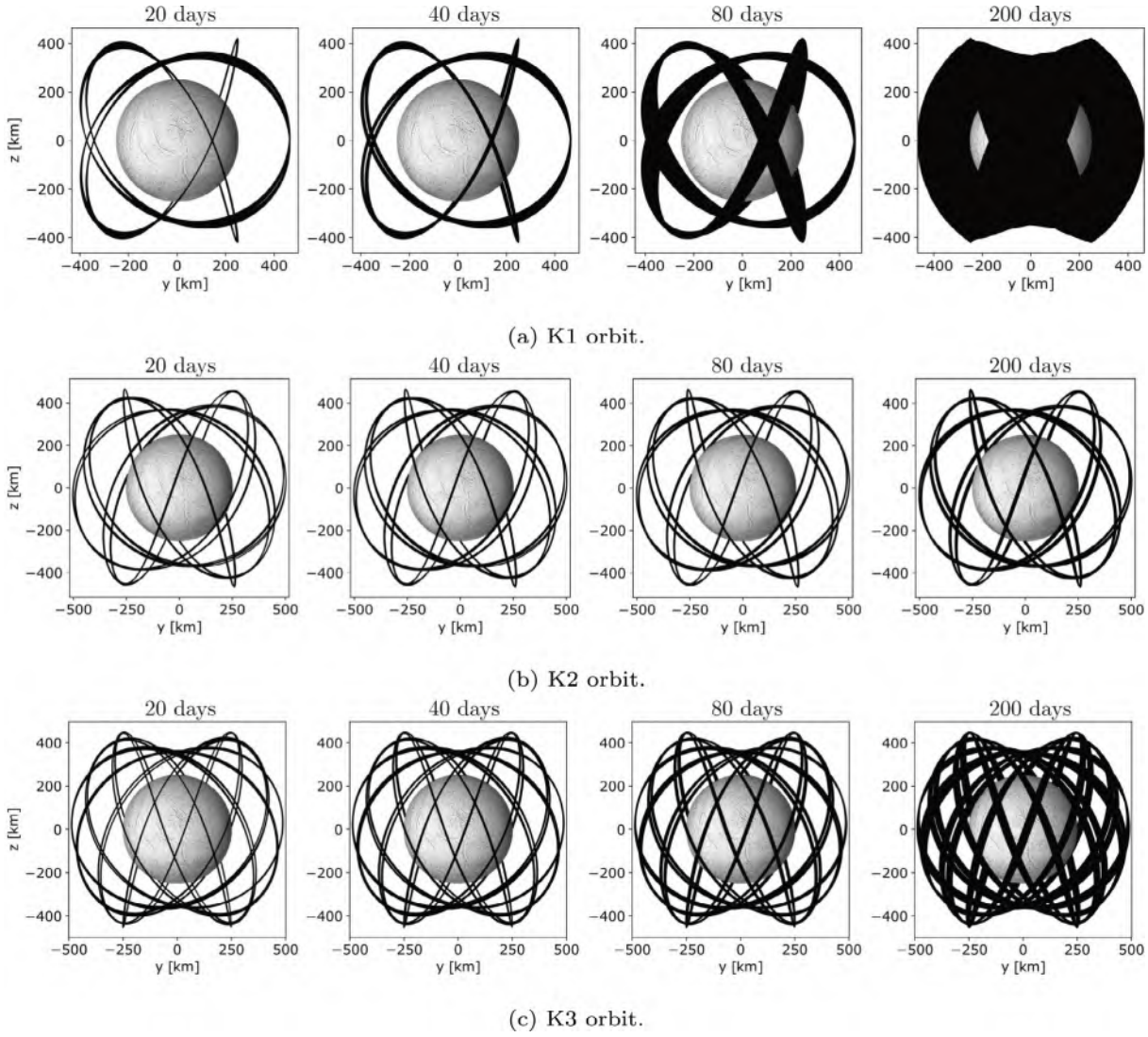

Fig. 19. Evolution of the K1, K2, and K3 orbit over 200 days.

4.3.3. Gravity field uncertainty

The Enceladus gravity field used in the orbit search has been derived from radio tracking measurements during several Enceladus flybys of the Cassini spacecraft [54]. The harmonic coefficients and the related inaccuracies are depicted in Table 4. Fig. 22 shows the results of a Monte Carlo analysis for which the K2 orbit was propagated repeatedly over 40 days including all forces shown in Fig. 12. In each Monte Carlo iteration, the higher terms of the Enceladus gravity were varied within the 1σ bound given in Table 4. 1000 iterations were performed. The solid black line shows the mean value of the distance to the nominal orbit trajectory over all Monte Carlo iterations and the gray range indicates the standard deviation. The nominal orbit is taken as the solution for the central values in Table 4. The upper panel in Fig. 22 shows 6 days of propagation and overlaid the latitude of the orbiter in red. The mean distance increases over time and varies with the latitude of the orbiter. High orbiter latitudes correlate with small distances suggesting a higher robustness for the near-polar passes, a favorable characteristic for a mission focused on the south polar region. The 40 day mean distance amounts to 552 m. For orbiter positions with absolute latitude values above 50° the 40 day mean distance amounts to 242 m. A similar Monte Carlo simulation using the K1 orbit resulted in slightly higher distance values, i.e., a 40 day mean of 699 m and 298 m for latitudes above 50°. This increased distance may be attributed to the lower orbit altitude of the K1 orbit. Similar to the rationale in Section 4.3.1, when comparing to the non-perfect repeat characteristic with distances between reference and repeat passes up to few kilometers (cf. Fig. 20), the possible perturbation by the uncertainty in the gravity field has a secondary effect.

4.3.4. Navigation inaccuracy

Navigation maneuvers are required at orbit insertion and for station keeping, i.e., for keeping the orbiter on the nominal trajectory after deviations due to perturbations. The accuracy with which the orbiter can be placed on the nominal trajectory is a combination of the orbit determination accuracy and maneuver execution accuracy. Navigation inaccuracies result in a diverging orbit evolution after a maneuver compared to the nominal orbit. As an example case, we assume a navigation accuracy according to the results presented for the mission proposal *Enceladus Orbilander* [8], stating position and velocity errors within 3σ bounds of approximately 250 m and $0.02\,\mathrm{m\,s^{-1}}$, respectively. Fig. 23 shows the results of a similar Monte Carlo simulation as in Section 4.3.3 for assessing the orbit robustness against navigation inaccuracies. The K2 orbit was propagated 1000 times over 40 days. In each iteration, the initial state was perturbed by a randomly directed position and velocity error with normal distributed magnitudes, with a standard deviation equal to the above stated 3σ values. The resulting mean distance over time to the nominal orbit shows a similar behavior as in the analysis for the uncertainty in the gravity field. High latitudes of the

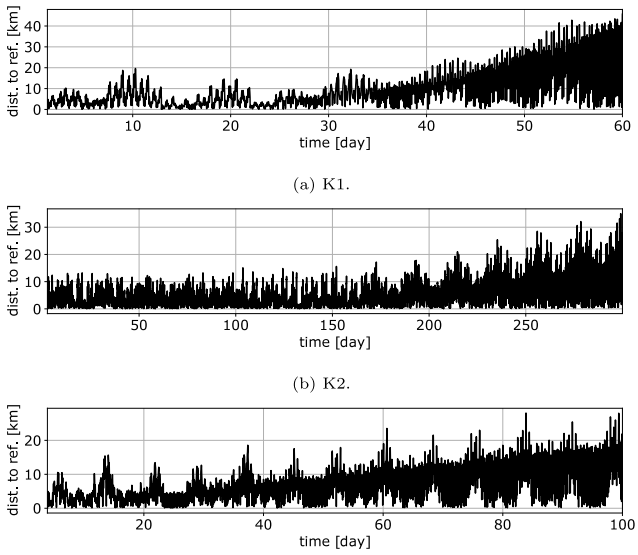

(a) K1.

(b) K2.

(c) K3.

Fig. 20. Distance of the orbiter to the reference trajectory. The reference is the trajectory of the first repeat cycle. The results are shown for the K1, K2, and K3 orbit.

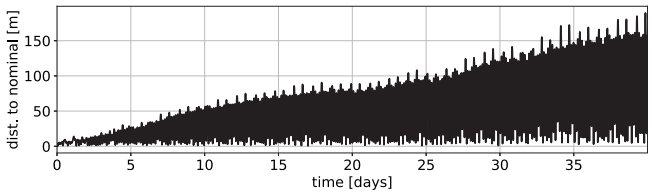

Fig. 21. Distance of the orbiter to the nominal orbit trajectory of K2 when incorporating all perturbations according to the accelerations shown in Fig. 12.

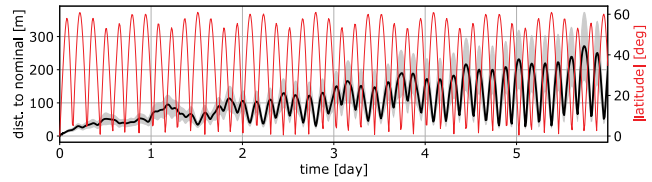

(a) Propagation over 6 days, overlaid in red the latitude of the orbiter.

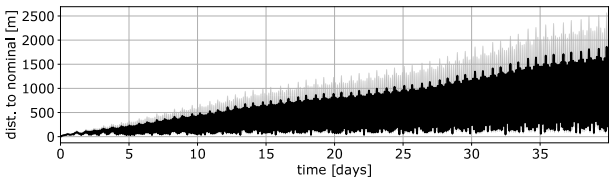

(b) Propagation over 40 days.

Fig. 22. Results of the Monte Carlo simulation for evaluating the perturbation by potential uncertainties in the Enceladus gravity field (see text for explanation). (For interpretation of the references to color in this figure legend, the reader is referred to the web version of this article.)

orbiter correspond to a smaller distance to the nominal orbit, i.e., more robustness. However, the perturbing effect is stronger, leading to a 40 day mean distance of 10.52 km and 7.67 km for absolute latitudes above 50°. A mean distance of 3 km (i.e., the mean distance between reference and repeat orbit as shown in Section 4.2) to the nominal orbit is reached after approximately 8 days for latitudes above 50°. This result suggests the execution of navigation events with similar accuracy every few days

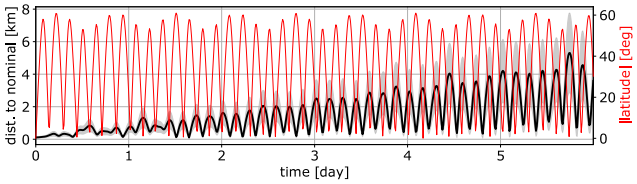

(a) Propagation over 6 days, overlaid in red the latitude of the orbiter.

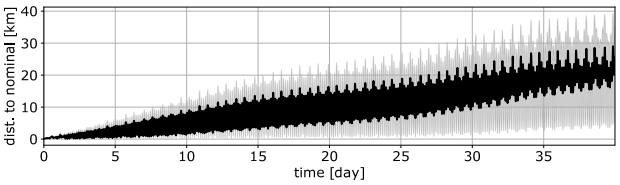

(b) Propagation over 40 days.

Fig. 23. Results of the Monte Carlo simulation for evaluating the perturbation by potential navigation inaccuracies (see text for explanation). (For interpretation of the references to color in this figure legend, the reader is referred to the web version of this article.)

to prevent a degradation of the repeat quality. The analyzed navigation inaccuracy has by far the strongest perturbing effect on the orbits. Assuming the 1σ bounds instead of 3σ reduces the perturbing effect drastically. If the orbiter could be placed accurately on the nominal trajectory, navigation events separated by several tens to few hundreds of days would be sufficient to guarantee InSAR stability characteristics.

5. Interferometry and tomography assessment

The suitability of the proposed orbits for the implementation of repeat-pass SAR interferometric and tomographic imaging modes is assessed for the south polar plume region (i.e., for latitudes $< -60°$). The assessment is restricted to geometric considerations concerning the number and distribution of interferometric and tomographic baselines provided by the orbits.

5.1. Interferometry

As outlined in more detail in Section 2.1.1, the perpendicular baseline between a reference and repeat-pass acquisition has to be well within the critical baseline to allow for InSAR. Throughout this section the perpendicular baseline is required to be smaller than $B_{\perp,\mathrm{crit}}/2$, as a conservative upper limit until which robust interferometric imaging is to be expected. Furthermore, the orbital convergence angle between reference and repeat acquisition is required to be smaller than its critical value (here 2 m azimuth resolution is assumed) to allow for consistent InSAR acquisitions over long swaths. The residual orbit convergence is expected to be compensated for by squinting of the antenna.

To assess the potential of the orbits for InSAR, the number of possible interferometric acquisitions is evaluated. For each point on a surface grid over the south polar region[3], the positions along the orbit trajectory from which the specific point is acquired with a zero-Doppler[4] imaging geometry are determined. Following, the perpendicular baseline and convergence between these orbiter positions is computed. For

[3] Enceladus is modeled as a triaxial ellipsoid with the radii $a = 256.6$ km, $b = 251.4$ km, and $c = 248.3$ km [58].

[4] The orbiter position of closest approach to the considered point on ground within a SAR acquisition. Corresponds to the azimuth position in the SAR image at which a target located at the considered surface point appears after SAR image formation.

orbits that are not perfectly parallel, the perpendicular baseline can be computed as

$$B_\perp = \sqrt{\left|\vec{B}\right|^2 - B_\parallel^2}, \tag{19}$$

with the baseline component parallel to the line-of-sight vector

$$B_\parallel = \left\langle \vec{B}, \vec{r} \right\rangle, \tag{20}$$

where $\langle \cdot, \cdot \rangle$ denotes the inner product and $\vec{r}$ is the line-of-sight vector from the reference orbit position to the considered surface point. The following results are shown for the P-band and Ka-band system parameters for the EnEx mission concept (cf. Table 2). However, conclusions may be drawn for other system specifications as the critical baseline scales linearly with frequency and bandwidth (cf. Eq. (5)). Fig. 24 shows for each surface point the number of interferometric pairs, i.e., pairs of reference and repeat orbit positions satisfying the baseline and convergence requirements. The incidence angle on the surface is constrained to be within 25° and 60°. The results are shown for K1 and K2 in Fig. 24(a) and Fig. 24(b), respectively. The K3 orbit does not provide a significant difference to K1 and K2 regarding the south polar InSAR coverage. In the left panels of Fig. 24 the number of interferometric pairs for the P-band system parameters after 2 repeat periods are shown. The 2 repeat periods ideally result in one reference and one repeat trajectory over the whole orbit course. Numbers of InSAR pairs greater than one result from the fact that certain surface points are accessible from more than one part of the orbit. Both K1 and K2 result in consistent P-band InSAR coverage of the plume region. Note that the shown results do not indicate that the whole region can be imaged within 2 repeat periods, but demonstrate the potential InSAR coverage opportunity for each surface point. K2 provides access from more different orbit parts than K1, resulting in a higher number of InSAR pairs for 2 repeat periods. Replicating the analysis for the Ka-band system parameters results in no InSAR pairs for the 2 repeat periods due to the more stringent baseline requirements. The middle and right panels show the number of InSAR pairs after a representative time of 40 days for P-band and Ka-band, respectively. For P-band, K1 results in more InSAR pairs within 40 days due to the faster repeat period. Within 40 days a few baselines even satisfy the stringent conditions for Ka-band. K2 provides slightly more consistent coverage in Ka-band due to the higher-quality repeat characteristic as appreciated in Fig. 19. However, reliable repeat-pass Ka-band InSAR does not seem to be feasible when also considering the partly uncontrollable deviations from the nominal trajectory due to navigation inaccuracies, allowing at most for opportunity-driven acquisitions.

As outlined in Section 2.1, several applications require multi-baseline InSAR acquisitions, i.e., more than one coherent repeat acquisition. For the P-band parameters, the left panels of Fig. 25 show over a course of 40 days for each surface point the maximum number of coherent baselines, i.e., the maximum number of coherent repeat acquisitions corresponding to one reference. Within the 40 days, K1 provides a maximum of 30 baselines, i.e., 31 coherent acquisitions. K2 provides maximum half the baselines because of the twice as long repeat period but results in a more consistent coverage of the south polar region. In the middle panel, the smallest baseline within the stack is shown in percentage of the critical baseline. Both K1 and K2 contain small baselines below 10 % for almost the whole plume region. The largest baselines are shown in the right panels with a maximum value of roughly 50 % of the critical baseline, corresponding to the posed requirement: $B_\perp < B_{\perp,\mathrm{crit}}/2$. The more stable repeat characteristic of K2 leads to smaller maximum baselines compared to K1.

5.2. Tomography

The suitability of the orbits for SAR tomography purposes is mainly determined by the length and the sampling of the synthesized aperture in elevation. In this work, we only provide a general assessment of the usability of the analyzed orbits in terms of sampling and vertical resolution. Note, however, that contrary to the InSAR case, larger baselines between the reference and repeat trajectories than provided by the non-perfect repeat characteristic may be desirable to optimize the SAR tomography performance. These larger baselines may require a dedicated orbit design where a small orbit drift in the body-fixed frame is generated to provide larger baselines, i.e., a worse repeat characteristic. A dedicated SAR tomography orbit design is left for future research.

The non-perfect repeat characteristic results in a non-uniform sampling of the tomographic aperture not allowing for an analytic description of the resolution and the sampling requirement. Therefore, the assessment is performed on simulated vertical impulse response functions (IRFs) for targets located at the Enceladus surface according to the following steps:

1. for each point on a surface grid in the south polar region, the orbit positions forming tomographic apertures[5] (i.e., positions with zero-Doppler imaging geometry on almost parallel trajectories) are determined;
2. using the P-band system parameters, the receive signal for a point-like target is simulated for each tomographic aperture and then focused along the vertical axis (parallel to the surface normal vector) using a matched spatial filter, providing the IRFs for the different tomographic apertures;
3. the resolution and the magnitude of the IRF side lobes are determined. To avoid ambiguities, tomographic apertures resulting in side lobes higher than half the main lobe power within 200 m along the vertical axis are neglected. 200 m is chosen as an example value for the depth down to which significant backscatter is expected for the P-band system.

Fig. 26 shows for the K1 orbit and for each surface point the best achievable vertical resolution (left panels), the magnitude of the highest side lobe of the corresponding IRF (middle panels), and example IRFs (right panel) from the region within lat $= [-80°, -70°]$ and lon $= [-135°, -180°]$. The results are shown for a propagation over 15 and 30 orbital repeat cycles in Fig. 26(a) and Fig. 26(b), respectively. The natural spread of the orbit repeat cycles due to the non-perfect repeat characteristic provides for certain regions a relatively fine vertical resolution below 10 m. For other regions, the repeat trajectories are mainly separated in line-of-sight direction resulting in small effective apertures and therefore a coarse vertical resolution up to several tens of meters. Already the 15 repeat cycles (i.e., a maximum of 15 acquisitions) allow for a consistent coverage of the plume region with IRF side lobes below −3 dB of the main lobe. However, the overall side lobe level is significantly reduced when synthesizing the tomographic apertures with acquisitions over 30 repeat cycles.

Fig. 27 shows the same analysis for the K2 orbit. Note that the K2 repeat period is approximately twice as long as for K1. Hence, forming equivalent tomographic apertures requires doubling the time. K2 does not provide a fine vertical resolution below 10 m. This characteristic can be attributed to the more accurate repeat characteristic. However, the bigger choice from multiple tomographic apertures from different orbit positions for each surface point provides a higher flexibility. Therefore, the resolution can be kept below 35 m by choosing the best suited set of acquisitions.

The results show that with the natural spread of the repeat trajectories, significant resolution may be achieved for certain parts of the south polar region. In order to achieve better resolution, the maximum trajectory separation perpendicular to the line-of-sight has to be increased, e.g., by degrading the orbital repeat quality. The sampling of the tomographic aperture, even if not perfectly uniform, contains for

[5] Multiple tomographic apertures may be formed from different parts of the orbit.

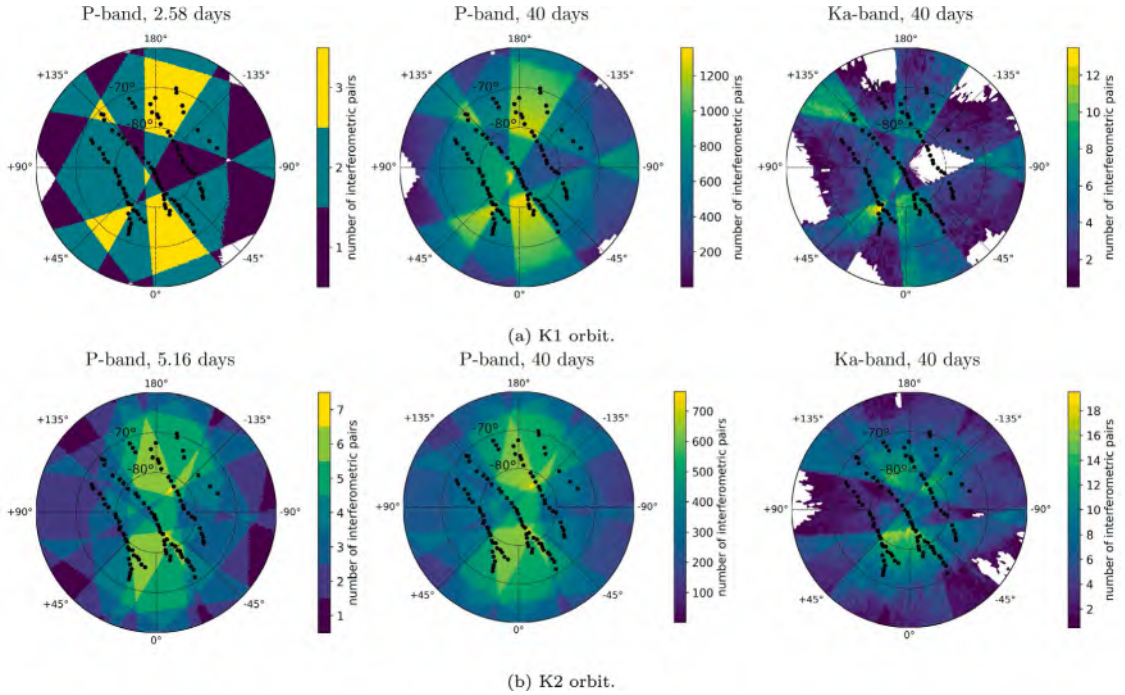

Fig. 24. Interferometric coverage of the south polar region for the K1 (a) the K2 (b) orbit showing: 2 repeat periods of propagation and the P-band parameters (left), 40 days of propagation and the P-band parameters (middle), and 40 days of propagation and the Ka-band parameters (right). Note that fewer interferometric pairs are forming for the Ka-band parameters due to the significantly smaller critical baseline compared to the P-band parameters. (For interpretation of the references to color in this figure legend, the reader is referred to the web version of this article.)

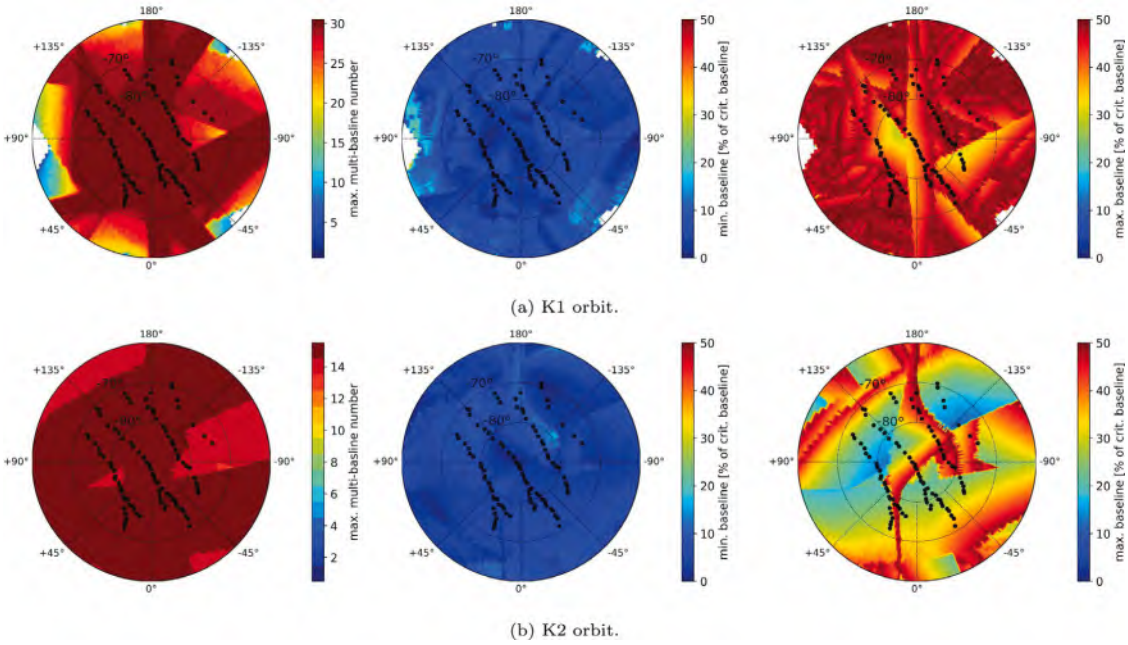

Fig. 25. Multi-baseline P-band interferometric coverage of the south polar region for the K1 (a) the K2 (b) orbit propagated over 40 days showing: the maximum number of coherent baselines (left), the smallest baseline in the coherent set (middle), and the largest baseline in the coherent set (right). (For interpretation of the references to color in this figure legend, the reader is referred to the web version of this article.)

most parts of the orbit trajectory separations in the range of several tens to a few hundred meters corresponding to the reference values for uniform sampling shown in Fig. 8. This sampling results in the overall acceptable side lobe level. Super-resolution techniques such as Capon for tomographic focusing can be used to significantly improve the resolution and side lobe level in order to reduce the required number of repeat cycles for forming tomographic acquisitions.

6. Discussion

6.1. Practical mission scenario

The InSAR and TomoSAR assessment in Section 5 has been performed with the nominal orbit solutions including perturbations by the Enceladean moons, Jupiter, and the Sun. In Section 4.3.4 we have outlined that navigation inaccuracies may introduce a significant

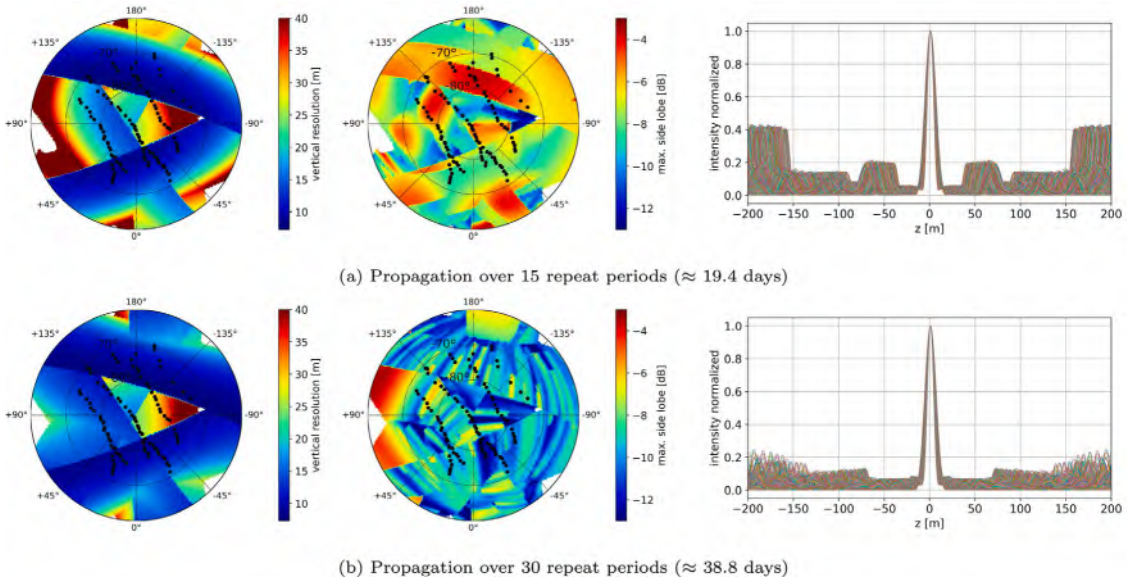

Fig. 26. Tomographic coverage of the south polar region for the K1 orbit (see text for explanation). (For interpretation of the references to color in this figure legend, the reader is referred to the web version of this article.)

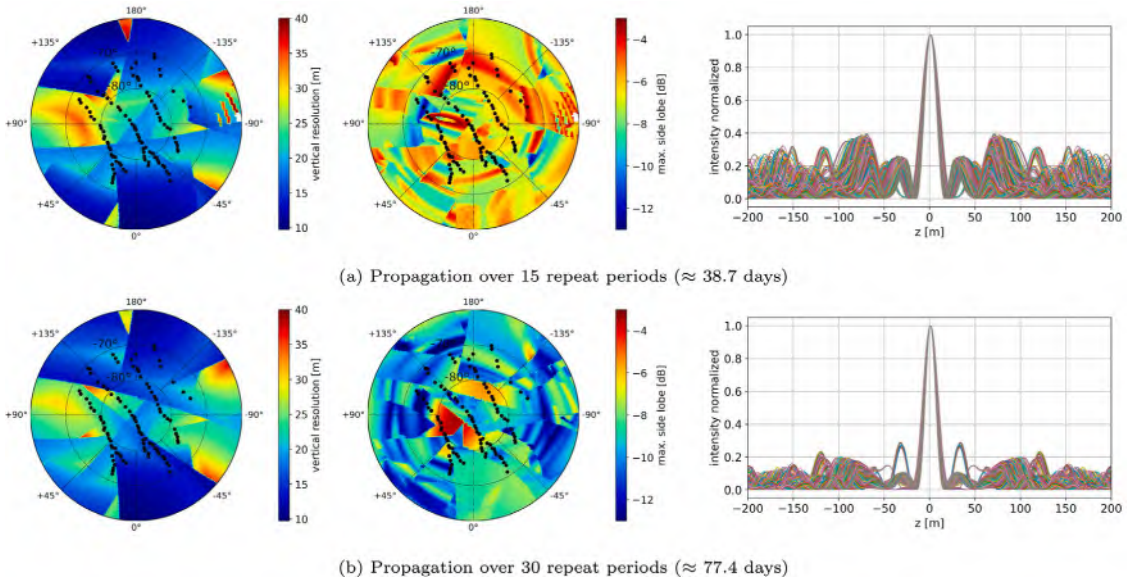

Fig. 27. Tomographic coverage of the south polar region for the K2 orbit (see text for explanation). (For interpretation of the references to color in this figure legend, the reader is referred to the web version of this article.)

perturbation leading to deviations from the nominal trajectory on the order of a few kilometers within several days when assuming the navigation accuracy from [8]. The perturbation is on the same order of magnitude as the natural separation between the reference and repeat passes, allowing the assumption that the formation of interferometric and tomographic baselines should not be significantly hindered and in some cases even enhanced. However, navigation events every few days are required to keep the deviation from the nominal orbit within few kilometers (cf. Fig. 23). As an example case the K1 orbit is propagated over 40 days with artificial navigation events every 3 days. Note that no realistic maneuvers are simulated but the orbiter is placed back on the nominal trajectory every 3 days with a position and velocity error according to the parameters given in Section 4.3.4. The resulting trajectory is used to replicate the multi-baseline analysis from Fig. 25(a). The results are shown in Fig. 28 alongside the resulting trajectory (left panel). The overall maximum multi-baseline number is comparable to the unperturbed case in Fig. 25(a). In some regions the number of coherent baselines decreased, in others an increase is visible. This variation suggests locally a larger or smaller separation of the repeat trajectories, respectively. The minimum and maximum baselines are comparable to the results for the nominal orbit. Note that only an example case is analyzed here. Stronger or weaker perturbations are to be expected depending on the magnitude and direction of the position and velocity errors. However, no drastic limitation for InSAR and TomoSAR is expected. In any case, if the orbiter can be placed on the nominal trajectory with a high accuracy, a maneuver-free operation is favorable.

6.2. Orbit selection

We have shown that the 3 analyzed orbits (K1, K2, and K3) may enable consistent interferometric and tomographic imaging of the south polar region. The fast repeat period of K1 is favorable for providing

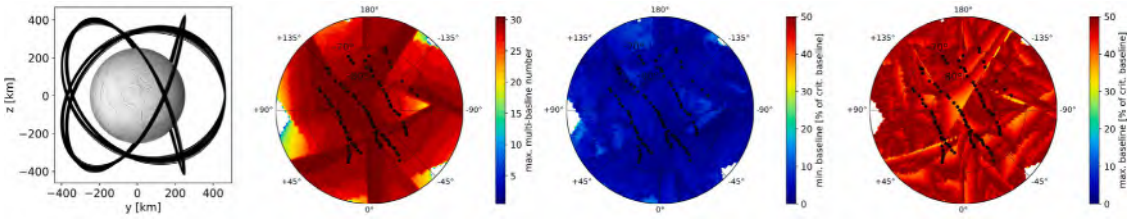

Fig. 28. Replicated analysis of Fig. 25(a) with artificial navigation events every 3 days. (For interpretation of the references to color in this figure legend, the reader is referred to the web version of this article.)

InSAR and TomoSAR products within a short time and to reduce the temporal decorrelation between the acquisitions. However, it is the least stable solution and provides unfavorable incidence angles at latitudes $< -80°$ (cf. Fig. 18). K2 is the most stable solution and allows access to the South Pole with incidence angles $< 50°$. Furthermore, K2 allows access to the same regions from more parts of the orbit than K1. This greater access may be favorable to mitigate shadow effects and offer more flexibility in the choice of interferometric and tomographic acquisition geometries. Compared to K1 and K2, K3 exhibits intermediate stability and comparable incidence angles at the South Pole as K2, but it allows for almost global coverage. Against this background, no general suggestion for the orbit choice is given here, as it will be largely driven by mission aspects concerning regions of interest and product specifications. Also, orbits with longer repeat periods (i.e., $K > 3$) are expected to provide sufficient inclination and orbital InSAR stability, but are not expected to bring significant additional value. Changing between K1, K2, and K3 may be accomplished with relatively little Δv. Simulations using ESA's Lambert solver *pykep* [59] result in Δv values in the order of 10 m/s for transfer times of a few hours, promoting this option for a mission scenario.

6.3. Usability for other modalities

In addition to radar applications, the high stability (i.e., low-maintenance) of the orbits compared to existing solutions in the literature and the access to the south polar region suggests utility as general mapping orbits and as communication relay for a lander mission close to the plumes. However, the limited maximum inclination of approximately 60° prevents access to the plume region with nadir-pointing instruments such as altimeters or radar sounders. Furthermore, sampling of plume ejecta at its maximum density is not possible. Dedicated polar tours are required for such science. The repeat characteristic may offer favorable conditions for a thermal infrared imager to monitor the activity in the plume region as a function of time at different tidal phases. The thermal activity could thus be set into context with the tidal cycles and the resulting deformation. Furthermore, the repeat orbits would be favorable for stereo imaging which would provide digital terrain models from camera data. Using Doppler tracking, the gravity field could be mapped in the equatorial region (between +/- 60° latitude). This would allow for measuring the degree-2 tidal potential including the sub- and anti-Saturnian points at which the tidal signal reaches its maximum.

7. Conclusion

Driven by the stringent requirement of almost perfectly repeating ground track orbits for repeat-pass interferometric and tomographic SAR imaging of the Enceladus south polar region, a set of highly stable periodic orbits around Enceladus has been presented. The orbits result from a developed grid-search approach for periodic orbits. In contrast with solutions in the literature, the search has been performed in a realistic ephemeris model to account for the non-circular Enceladus orbit and the non-spherical gravity fields of Enceladus and Saturn. The resulting orbits have altitudes of approximately 200 km and reach maximum inclinations of 61°, allowing to access the most-interesting south polar region with its plumes. Three orbits have been analyzed in detail regarding their stability, robustness to perturbations, and suitability for interferometric and tomographic SAR imaging. The orbits sustain the required repeat characteristic over tens to hundreds of days with baselines on the order of hundreds to a few thousands of meters between the orbital repeat cycle trajectories. The orbits are proven long-term stable (no impact, no escape) beyond 15 years. This result constitutes a significant improvement to existing orbits with similar inclination resulting from searches in simplified dynamic models, which lead to impacts within tens of days to several months when propagating in an ephemeris model.

The repeat quality of the orbits is sufficient to form interferometric baselines well within the critical baseline for the example case of the low frequency (i.e., P-band) SAR system suggested for the EnEx mission concept, providing a consistent interferometric coverage of the south polar region with its plumes. However, the divergence between the orbital repeat cycles is too strong to consistently provide baselines smaller than the critical baselines of the suggested high frequency system (i.e., Ka-band) on the order of tens of meters. Such small baselines form only sporadically, preventing consistent Ka-band InSAR coverage of the south polar region. Nonetheless, local coverage of regions of interest seems to be feasible. A single-pass Ka-band system is suggested here as a robust option for providing high-frequency SAR interferometry at Enceladus.

The natural spread of the repeat cycles allows for the formation of baselines ranging from tens of meters to few kilometers. It has been shown that this natural spread provides useful tomographic apertures allowing for unambiguous SAR tomographic imaging of the ice crust with a vertical resolution below 10 m for certain areas in the plume region. However, the vertical resolution capability may be largely improved by a dedicated orbit design for SAR tomography where a larger maximum separation between the repeat cycles (i.e., a worse repeat characteristic) is generated. Such orbit design is left for future research.

In addition to radar applications, the long-term stability and high inclination of the orbits promotes them as general science orbits and as a communication relay for a potential lander mission.

Declaration of competing interest

The authors declare that they have no known competing financial interests or personal relationships that could have appeared to influence the work reported in this paper.

Acknowledgments

This study was financially supported by the German Space Agency at the German Aerospace Center (DLR) with funds from the German Federal Ministry for Economic Affairs and Energy (BMWi) under the project EnEx-AsGAr, registration no. 50NA1708. Part of this research was carried out with support from the DFG project 'Saturn's moon after Cassini: geodetic parameters, interior structure and dynamics'.

The Authors would like to thank M. Stelzig (LHFT, FAU) and Prof. Dr.-Ing. M. Vossiek (LHFT, FAU) for their support in the EnEx project. A. Benedikter would also like to give a special thanks to E. Rodrigues Silva Filho (DLR) for the valuable discussions. The authors would also like to thank the two anonymous reviewers for their effort and constructive comments.

References

[1] J.R. Spencer, F. Nimmo, Enceladus: An active ice world in the Saturn system, Annu. Rev. Earth Planet. Sci. 41 (1) (2013) 693–717, http://dx.doi.org/10.1146/annurev-earth-050212-124025.

[2] C.C. Porco, P. Helfenstein, P.C. Thomas, A.P. Ingersoll, J. Wisdom, R. West, G. Neukum, T. Denk, R. Wagner, T. Roatsch, S. Kieffer, E. Turtle, A. McEwen, T.V. Johnson, J. Rathbun, J. Veverka, D. Wilson, J. Perry, J. Spitale, A. Brahic, J.A. Burns, A.D. DelGenio, L. Dones, C.D. Murray, S. Squyres, Cassini observes the active South Pole of Enceladus, Science 311 (5766) (2006) 1393–1401, http://dx.doi.org/10.1126/science.1123013.

[3] F. Postberg, J. Schmidt, J. Hillier, et al., A salt-water reservoir as the source of a compositionally stratified plume on Enceladus, Nature 474 (2011) 620–622, http://dx.doi.org/10.1038/nature10175.

[4] F. Postberg, N. Khawaja, B. Abel, et al., Macromolecular organic compounds from the depths of Enceladus, Nature 558 (2018) 564–568, http://dx.doi.org/10.1038/s41586-018-0246-4.

[5] A. Coustenis, S. Atreya, T. Balint, et al., TandEM: Titan and Enceladus mission, Exp. Astron. 23 (2009) 893–946, http://dx.doi.org/10.1007/s10686-008-9103-z.

[6] K. Konstantinidis, C.L. Flores Martinez, B. Dachwald, A. Ohndorf, P. Dykta, P. Bowitz, M. Rudolph, I. Digel, J. Kowalski, K. Voigt, R. Förstner, A lander mission to probe subglacial water on Saturn's moon Enceladus for life, Acta Astronaut. 106 (2015) 63–89, http://dx.doi.org/10.1016/j.actaastro.2014.09.012.

[7] K. Reh, et al., Enceladus Life Finder: The search for life in a habitable Moon, in: 2016 IEEE Aerospace Conference, 2016, pp. 1–8, http://dx.doi.org/10.1109/AERO.2016.7500813.

[8] S. MacKenzie, et al., Enceladus Orbilander: A flagship mission concept for astrobiology, in: Planetary mission concept study for the 2023–2032 decadal survey, Johns Hopkins University Applied Physics Laboratory, 2020, URL https://lib.jhuapl.edu/media/filer_public/5a/bb/5abbf99c-cbf7-49df-a420-e64add0e6e0c/enceladusorbilander_2020pmcs.pdf.

[9] J. Oberst, H. Hussmann, B. Giese, F. Sohl, D. Shoji, A. Stark, K. Wickhusen, M. Wählisch, Enceladus geodetic framework, Int. Arch. Photogramm. Remote Sens. Spatial Inf. Sci. XLII-3/W1 (2017) 113–118, http://dx.doi.org/10.5194/isprs-archives-XLII-3-W1-113-2017.

[10] A. Benedikter, M. Rodriguez-Cassola, G. Krieger, R. Scheiber, G.M. del Campo Becerra, R. Horn, M. Stelzig, A. Moreira, M. Vossiek, Potential of a multimodal orbital radar mission for the exploration of Enceladus, in: EGU General Assembly 2020, Online, http://dx.doi.org/10.5194/egusphere-egu2020-19621.

[11] O. Rzhiga, Venera-15 and -16 spacecraft: Images and maps of Venus, Adv. Space Res. 7 (12) (1987) 269–278, http://dx.doi.org/10.1016/0273-1177(87)90229-8.

[12] W.T.K. Johnson, Magellan imaging radar mission to Venus, Proc. IEEE 79 (6) (1991) 777–790, http://dx.doi.org/10.1109/5.90157.

[13] C. Elachi, M. Allison, L. Borgarelli, et al., Radar: The Cassini Titan radar mapper, Space Sci. Rev. 115 (2004) 71–110, http://dx.doi.org/10.1007/s11214-004-1438-9.

[14] J.J. van Zyl, The shuttle radar topography mission (SRTM): a breakthrough in remote sensing of topography, Acta Astronaut. 48 (5) (2001) 559–565, http://dx.doi.org/10.1016/S0094-5765(01)00020-0.

[15] G. Krieger, M. Zink, M. Bachmann, B. Bräutigam, D. Schulze, M. Martone, P. Rizzoli, U. Steinbrecher, J. Walter Antony, F. De Zan, I. Hajnsek, K. Papathanassiou, F. Kugler, M. Rodriguez Cassola, M. Younis, S. Baumgartner, P. López-Dekker, P. Prats, A. Moreira, TanDEM-X: A radar interferometer with two formation-flying satellites, Acta Astronaut. 89 (2013) 83–98, http://dx.doi.org/10.1016/j.actaastro.2013.03.008.

[16] P.A. Rosen, S. Hensley, I.R. Joughin, F.K. Li, S.N. Madsen, E. Rodriguez, R.M. Goldstein, Synthetic aperture radar interferometry, Proc. IEEE 88 (3) (2000) 333–382, http://dx.doi.org/10.1109/5.838084.

[17] D. Massonnet, M. Rossi, C. Carmona, et al., The displacement field of the Landers earthquake mapped by radar interferometry, Nature 364 (1993) 138–142, http://dx.doi.org/10.1038/364138a0.

[18] R.M. Goldstein, H. Engelhardt, B. Kamb, R.M. Frolich, Satellite radar interferometry for monitoring ice sheet motion: Application to an Antarctic ice stream, Science 262 (5139) (1993) 1525–1530, http://dx.doi.org/10.1126/science.262.5139.1525.

[19] F.J. Meyer, D.T. Sandwell, SAR interferometry at Venus for topography and change detection, Planet. Space Sci. 73 (1) (2012) 130–144, http://dx.doi.org/10.1016/j.pss.2012.10.006.

[20] R. Ghail, C. Wilson, M. Galand, et al., EnVision: taking the pulse of our twin planet, Exp. Astron. 33 (2012) 337–363, http://dx.doi.org/10.1007/s10686-011-9244-3.

[21] S. Hensley, S. Smrekar, S. Shaffer, M. Paller, H. Figueroa, A. Freeman, R. Hodges, P. Walkemeyer, VISAR: A next generation interferometric radar for Venus exploration, in: 2015 IEEE 5th Asia-Pacific Conference on Synthetic Aperture Radar, APSAR, 2015, pp. 362–366, http://dx.doi.org/10.1109/APSAR.2015.7306225.

[22] P. Paillou, T. Thompson, J. Plaut, P. Rosen, S. Hensley, C. Elachi, D. Massonnet, J. Achache, MEEM: An orbital synthetic aperture radar for Mars exploration, in: Conference on the Geophysical Detection of Subsurface Water on Mars, Vol. 1095, 2001, pp. 78–79.

[23] P. Rosen, P. Paillou, S. Hensley, D. Massonnet, T. Thompson, Imaging radar interferometry for the exploration of Mars, AGU Fall Meeting Abstracts, 2001.

[24] A. Moreira, P. Prats-Iraola, M. Younis, G. Krieger, I. Hajnsek, K.P. Papathanassiou, A tutorial on synthetic aperture radar, IEEE Geosci. Remote Sens. Mag. 1 (1) (2013) 6–43, http://dx.doi.org/10.1109/MGRS.2013.2248301.

[25] S. Kempf, U. Beckmann, J. Schmidt, How the Enceladus dust plume feeds Saturn's E ring, Icarus 206 (2) (2010) 446–457, http://dx.doi.org/10.1016/j.icarus.2009.09.016, Cassini at Saturn.

[26] X. Wu, K.C. Jezek, E. Rodriguez, S. Gogineni, F. Rodriguez-Morales, A. Freeman, Ice sheet bed mapping with airborne SAR tomography, IEEE Trans. Geosci. Remote Sens. 49 (10) (2011) 3791–3802, http://dx.doi.org/10.1109/TGRS.2011.2132802.

[27] S. Tebaldini, T. Nagler, H. Rott, A. Heilig, Imaging the internal structure of an Alpine glacier via L-band airborne SAR tomography, IEEE Trans. Geosci. Remote Sens. 54 (12) (2016) 7197–7209, http://dx.doi.org/10.1109/TGRS.2016.2597361.

[28] F. Banda, J. Dall, S. Tebaldini, Single and multipolarimetric P-band SAR tomography of subsurface ice structure, IEEE Trans. Geosci. Remote Sens. 54 (5) (2016) 2832–2845, http://dx.doi.org/10.1109/TGRS.2015.2506399.

[29] M. Pardini, G. Parrella, G. Fischer, K. Papathanassiou, A multi-frequency SAR tomographic characterization of sub-surface ice volumes, in: Proceedings of EUSAR 2016: 11th European Conference on Synthetic Aperture Radar, 2016, pp. 1–6.

[30] G. Fischer, M. Jäger, K.P. Papathanassiou, I. Hajnsek, Modeling the vertical backscattering distribution in the percolation zone of the Greenland ice sheet with SAR tomography, IEEE J. Sel. Top. Appl. Earth Obs. Remote Sens. 12 (11) (2019) 4389–4405, http://dx.doi.org/10.1109/JSTARS.2019.2951026.

[31] D.J. Scheeres, Orbital Motion in Strongly Perturbed Environments: Applications to Asteroid, Comet and Planetary Satellite Orbiters, Springer, Berlin, Heidelberg, 2012, http://dx.doi.org/10.1007/978-3-642-03256-1.

[32] M.E. Paskowitz, D.J. Scheeres, Design of science orbits about planetary satellites: Application to Europa, J. Guid. Control Dyn. 29 (5) (2006) 1147–1158, http://dx.doi.org/10.2514/1.19464.

[33] D.J. Scheeres, M.D. Guman, B.F. Villac, Stability analysis of planetary satellite orbiters: Application to the Europa orbiter, J. Guid. Control Dyn. 24 (4) (2001) 778–787, http://dx.doi.org/10.2514/2.4778.

[34] R.P. Russell, A.T. Brinckerhoff, Circulating eccentric orbits around planetary moons, J. Guid. Control Dyn. 32 (2) (2009) 424–436, http://dx.doi.org/10.2514/1.38593.

[35] M. Lara, J. Palacián, R. Russell, Mission design through averaging of perturbed Keplerian systems: the paradigm of an Enceladus orbiter, Celestial Mech. Dynam. Astronom. 108 (2010) 1–22, http://dx.doi.org/10.1007/s10569-010-9286-2.

[36] R.P. Russell, M. Lara, On the design of an Enceladus science orbit, Acta Astronaut. 65 (1) (2009) 27–39, http://dx.doi.org/10.1016/j.actaastro.2009.01.021.

[37] R. Bamler, P. Hartl, Synthetic aperture radar interferometry, Inverse Problems 14 (4) (1998) R1–R54, http://dx.doi.org/10.1088/0266-5611/14/4/001.

[38] A.Y. Lee, E.K. Wang, E.B. Pilinski, G.A. Macala, A.W. Feldman, Estimation and modeling of Enceladus plume jet density using Cassini flight data, J. Spacecr. Rockets 50 (2) (2013) 317–325, http://dx.doi.org/10.2514/1.A32344.

[39] W.M. Farrell, W.S. Kurth, D.A. Gurnett, R.E. Johnson, M.L. Kaiser, J.-E. Wahlund, J.H. Waite Jr., Electron density dropout near Enceladus in the context of water-vapor and water-ice, Geophys. Res. Lett. 36 (10) (2009) http://dx.doi.org/10.1029/2008GL037108.

[40] M. Běhounková, O. Souček, J. Hron, O. Čadek, Plume activity and tidal deformation on Enceladus influenced by faults and variable ice shell thickness, Astrobiology 17 (9) (2017) 941–954, http://dx.doi.org/10.1089/ast.2016.1629.

[41] D. Massonnet, K.L. Feigl, Discrimination of geophysical phenomena in satellite radar interferograms, Geophys. Res. Lett. 22 (12) (1995) 1537–1540, http://dx.doi.org/10.1029/95GL00711.

[42] H.A. Zebker, J. Villasenor, Decorrelation in interferometric radar echoes, IEEE Trans. Geosci. Remote Sens. 30 (5) (1992) 950–959, http://dx.doi.org/10.1109/36.175330.

[43] F. Gatelli, A. Monti Guamieri, F. Parizzi, P. Pasquali, C. Prati, F. Rocca, The wavenumber shift in SAR interferometry, IEEE Trans. Geosci. Remote Sens. 32 (4) (1994) 855–865, http://dx.doi.org/10.1109/36.298013.

[44] A. Kovacs, A.J. Gow, R.M. Morey, The in-situ dielectric constant of polar firn revisited, Cold Reg. Sci. Technol. 23 (3) (1995) 245–256, http://dx.doi.org/10.1016/0165-232X(94)00016-Q.

[45] E.B. Pilinski, A.Y. Lee, Pointing-stability performance of the Cassini spacecraft, J. Spacecr. Rockets 46 (5) (2009) 1007–1015, http://dx.doi.org/10.2514/1.41675.

[46] A. Reigber, A. Moreira, First demonstration of airborne SAR tomography using multibaseline L-band data, IEEE Trans. Geosci. Remote Sens. 38 (5) (2000) 2142–2152, http://dx.doi.org/10.1109/36.868873.

[47] F. Lombardini, A. Reigber, Adaptive spectral estimation for multibaseline SAR tomography with airborne L-band data, in: 2003 IEEE International Geoscience and Remote Sensing Symposium. Proceedings (IEEE Cat. No.03CH37477), IGARSS 2003, vol. 3, 2003, pp. 2014–2016, http://dx.doi.org/10.1109/IGARSS.2003.1294324.

[48] A. Reigber, P. Prats, J. Mallorqui, Refined estimation of time-varying baseline errors in airborne SAR interferometry, IEEE Geosci. Remote Sens. Lett. 3 (1) (2006) 145–149, http://dx.doi.org/10.1109/LGRS.2005.860482.

[49] P. Prats, J. Mallorqui, Estimation of azimuth phase undulations with multisquint processing in airborne interferometric SAR images, IEEE Trans. Geosci. Remote Sens. 41 (6) (2003) 1530–1533, http://dx.doi.org/10.1109/TGRS.2003.814140.

[50] S. Mancon, S. Tebaldini, A.M. Guarnieri, D. Giudici, Orbit accuracy estimation by multi-squint phase: First Sentinel-1 results, in: 2015 IEEE International Geoscience and Remote Sensing Symposium, IGARSS, 2015, pp. 1276–1279, http://dx.doi.org/10.1109/IGARSS.2015.7326007.

[51] V. Szebehely, Theory of Orbits, the Restricted Problem of Three Bodies, Academic Press, New York, 1967, pp. 556–652.

[52] H. Hussmann, J. Oberst, K. Wickhusen, X. Shi, F. Damme, F. Lüdicke, V. Lupovka, S. Bauer, Stability and evolution of orbits around the binary asteroid 175706 (1996 FG3): Implications for the MarcoPolo-R mission, Planet. Space Sci. 70 (1) (2012) 102–113, http://dx.doi.org/10.1016/j.pss.2012.04.010.

[53] M. Höschele, A. Stark, K. Wickhusen, H. Hussmann, J. Oberst, Orbital evolution of the BepiColombo Mercury Planetary Orbiter (MPO) in the gravity field of Mercury, Planet. Space Sci. 200 (2021) 105195, http://dx.doi.org/10.1016/j.pss.2021.105195.

[54] L. Iess, D.J. Stevenson, M. Parisi, D. Hemingway, R.A. Jacobson, J.I. Lunine, F. Nimmo, J.W. Armstrong, S.W. Asmar, M. Ducci, P. Tortora, The gravity field and interior structure of Enceladus, Science 344 (6179) (2014) 78–80, http://dx.doi.org/10.1126/science.1250551.

[55] L. Iess, B. Militzer, Y. Kaspi, P. Nicholson, D. Durante, P. Racioppa, A. Anabtawi, E. Galanti, W. Hubbard, M.J. Mariani, P. Tortora, S. Wahl, M. Zannoni, Measurement and implications of Saturn's gravity field and ring mass, Science 364 (6445) (2019) http://dx.doi.org/10.1126/science.aat2965.

[56] C. Porco, D. DiNino, F. Nimmo, How the geysers, tidal stresses, and thermal emission across the South Polar Terrain of Enceladus are related, Astron. J. 148 (2014) 45, http://dx.doi.org/10.1088/0004-6256/148/3/45.

[57] R.D. Lorenz, T.A. Burk, Enceladus plume density from Cassini spacecraft attitude control data, Icarus 300 (2018) 200–202, http://dx.doi.org/10.1016/j.icarus.2017.09.003.

[58] P. Thomas, J. Burns, P. Helfenstein, S. Squyres, J. Veverka, C. Porco, E. Turtle, A. McEwen, T. Denk, B. Giese, T. Roatsch, T. Johnson, R. Jacobson, Shapes of the Saturnian icy satellites and their significance, Icarus 190 (2) (2007) 573–584, http://dx.doi.org/10.1016/j.icarus.2007.03.012, Deep Impact Mission to Comet 9P/Tempel 1, Part 2.

[59] F. Biscani, D. Izzo, A parallel global multiobjective framework for optimization: pagmo, J. Open Source Softw. 5 (53) (2020) 2338, http://dx.doi.org/10.21105/joss.02338.

IGARSS 2023 - 2023 IEEE International Geoscience and Remote Sensing Symposium | 979-8-3503-2010-7/23/$31.00 ©2023 IEEE | DOI: 10.1109/IGARSS52108.2023.10281821

PERFORMANCE ANALYSIS OF A REPEAT-PASS INSAR MISSION FOR DEFORMATION AND TOPOGRAPHY MAPPING OF SATURN'S MOON ENCELADUS

Andreas Benedikter°, Paul Rosen⋆, Mark Simons†, Ryan Park⋆, Marc Rodriguez-Cassola°, Pau Prats-Iraola°, Gerhard Krieger°, Jalal Matar°

°Microwaves and Radar Institute, German Aerospace Center (DLR)
⋆Jet Propulsion Laboratory, California Institute of Technology
†Seismological Laboratory, California Institute of Technology

ABSTRACT

Over the last decades, repeat-pass SAR interferometry (InSAR) for deformation measurement and topographic mapping has revolutionized our understanding of many geophysical processes on Earth. A new mission concept, currently in development at the Jet Propulsion Laboratory (JPL) and Caltech, aims at using orbital repeat-pass InSAR for deformation and topography mapping of Saturn's ice-covered and geologically active moon Enceladus. In this paper, we present an initial performance assessment of the system and the suggested SAR processing approach, along with simulated InSAR acquisitions using a DLR in-house End-to-End performance simulator.

Index Terms— SAR, SAR interferometry, Saturn, Enceladus, Planetary Mission

1. INTRODUCTION

With a diameter of only about $500\,\mathrm{km}$, Saturn's moon Enceladus is a differentiated geologically active body, most likely comprising a porous rocky core and an ice shell, separated by a global subsurface water ocean [1] (cf. Fig. 1). The discovery of plumes ejecting gas and ice particles through cracks within the ice crust in the south polar region and the presence of complex organic molecules within [2] have assigned a high priority to Enceladus among exploratory mission plans investigating habitability of other worlds. A new mission concept, currently in development at the Jet Propulsion Laboratory (JPL) and Caltech, aims at using –among other modalities– repeat-pass SAR interferometry (InSAR) for deformation and topography mapping to understand the state of habitability of Enceladus, and to expand our knowledge on its past and present structural, dynamical, and kinematical properties.

Enceladus presents several distinctive observational characteristics that favor the use of repeat-pass InSAR. These include an almost-absent atmosphere, negligible temporal decorrelation effects in most areas, high backscatter (above $0\,\mathrm{dB}$ were measured in Ku- and S-band [3, 4]), and short orbital repeat cycles of approximately 30 hours. However,

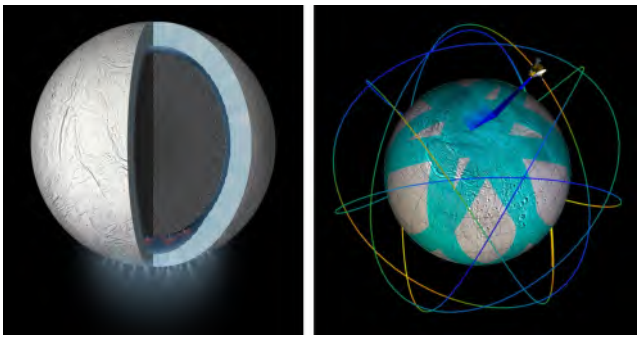

Fig. 1: (Left) artist's conception of Enceladus and its inner structure (image credit: NASA JPL) and (right) illustration of the spacecraft in the candidate orbit around Enceladus.

several aspects of the environment may lead to increased system and mission complexity that must be studied carefully and accounted for in the system design. These include: i) strong third-body gravitational perturbation from Saturn, which limits the number of feasible orbits and high orbital inclinations (e.g., above $60°$ for repeat orbits). One candidate repeat orbit has been proposed in [5] and is shown in Fig. 1 and Fig. 2; ii) the large distance to Earth paired with the uncertainties in the gravitational models limit orbit controlability and orbit determination accuracy; iii) the limited down-link capacity from the Saturnian system to Earth requires tailored on-board processing strategies for both SAR focusing and InSAR processing to reduce the data rate.

The system and performance discussions in the following are focused on aspects that are particular to SAR and InSAR surveys over Enceladus.

2. SAR SYSTEM CONSIDERATIONS AND PERFORMANCE

The preliminary radar system specifications are depicted in Table 1. An S-band frequency is chosen as a compromise among phenomenological (i.e., volume decorrelation, backscattered power, etc.) and technological (i.e., interfer-

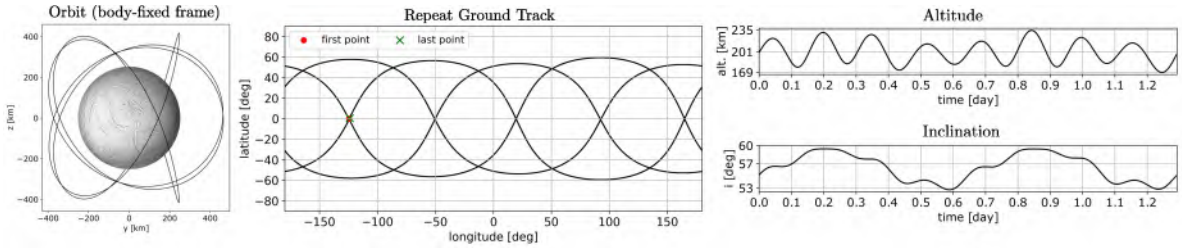

Fig. 2: One repeat cycle of the candidate orbit [5].

ometric baseline, baseline determination accuracy, on-board processing demands, etc.) constraints.

Table 1: Preliminary radar system parameters.

Parameter	Value	Comment
Wavelength	0.13 m	
Pulse repetition frequency	500 Hz	Oversampling for presumming
Range bandwidth	30 MHz	
Pulse duration	60 μs	
Tx peak power	200 W	
Receiver noise temperature	240 K	
Look angle	24.4 deg	
Equivalent antenna length	~3.5 m	Radar operated on high-gain telecom antenna (4-m reflector)
Equivalent antenna height	~0.5 m	Sub-illumination of reflector to achieve ~80 km swath width
Antenna efficiency	-3 dB	
Losses (feed, cable)	-1.5 dB	
System power margin	5 dB	

The 4-m high-gain reflector antenna will be shared for radar operations and telecommunication. In elevation direction, the reflector is partially illuminated to achieve a swath width of roughly $80\,\mathrm{km}$ in stripmap operation when pointed with a look angle of $24.4°$. The resulting coverage of the most-interesting south polar region is shown in Fig. 1. Note that this region can be potentially covered from five different passes of the orbiter. The different viewing geometries may be used to derive 3-D deformation vectors, mitigate shadow problems, and disentangle deformation and topography signatures. To reduce the data rate, both SAR and InSAR processing will be performed on board up to multi-looked interferograms.

2.1. SAR Performance Aspects

The resulting noise equivalent sigma naught (NESN) across the swath is shown in Fig. 3 (left) for the minimum, mean, and maximum orbit altitudes. The pointing of the antenna and the swath are optimized for the $200\,\mathrm{km}$ altitude to achieve the

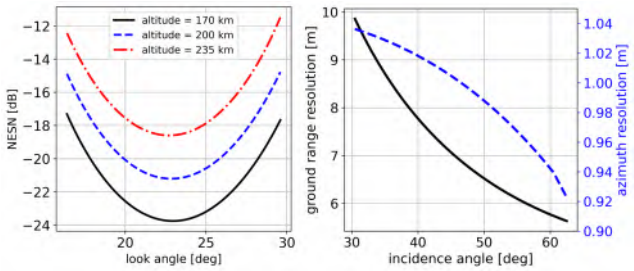

Fig. 3: SAR system performance across the swath derived from the parameters in Table 1 and for a near south polar pass of the orbit in Fig. 2: (left) the NESN for different orbit altitudes and (right) the ground resolution in range and azimuth.

$80\,\mathrm{km}$ swath width and to cover the pole. For achieving an azimuth ambiguity to signal ratio (AASR) of $-25\,\mathrm{dB}$, a pulse repetition frequency (PRF) of roughly $90\,\mathrm{Hz}$ is required. Note that the orbiter velocity is only around $120\,\mathrm{m\,s^{-1}}$. As a consequence of the small size of Enceladus, range ambiguities do not contribute to the ambiguity budget up to a PRF of approximately $900\,\mathrm{Hz}$, since they would be placed beyond the limb of the body. Hence, a substantial oversampling in azimuth with a PRF of $500\,\mathrm{Hz}$ can be used to reduce the peak power.

Fig. 3 (right) shows the potential ground resolution in range and azimuth direction for a south polar pass of the orbiter and an altitude of $200\,\mathrm{km}$, where the swath in far range is reaching beyond the South Pole (spacecraft position as illustrated in Fig. 1). The achievable azimuth resolution is significantly better compared to the standard formulation of half of the antenna length due to an almost $50\,\%$ lower ground velocity compared to the orbital velocity, caused by the relatively small body size to orbit height ratio.

2.2. SAR Focusing Aspects

The proposed SAR focusing chain is based on the chirp scaling algorithm, including two additional steps in order to accommodate the non-negligible eccentricity of the orbit paired with the relatively long integration times of the SAR surveys, namely: i) a residual hyperbolic correction in the range-Doppler domain and ii) the subaperture topography- and aperture-dependent (SATA) algorithm [6].

SATA was developed in the frame of airborne SAR systems to compensate for non-ideal trajectory deviations during

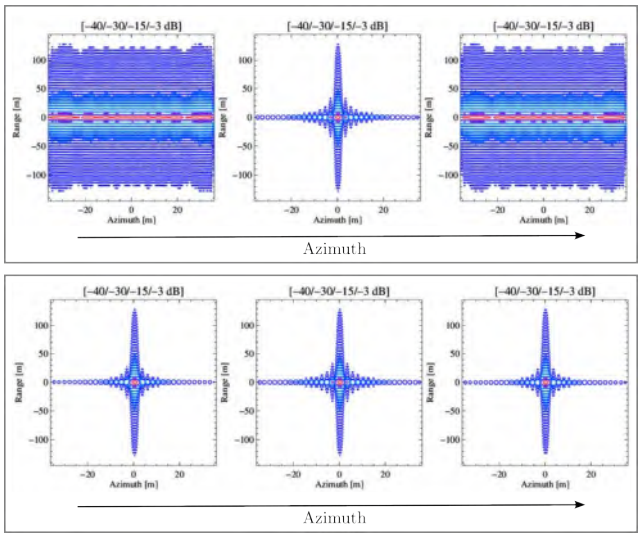

Fig. 4: Validation of the proposed SAR focusing approach using simulated point targets at mid-range of the swath, spread along a 20 km processing interval in azimuth, showing the effect of SATA [6] for compensating space-variant effects: (top) without using SATA and (bottom) when SATA is applied.

SAR focusing by considering the topography of the scene and the wide antenna beamwidth [6, 7]. SATA works with short-time Fourier transforms along azimuth before azimuth compression to compensate the non-ideal trajectory in both the space and Doppler domain. For the Enceladus SAR surveys, SATA is an efficient approach to accommodate space-variant effects within the synthetic aperture observation time resulting from the eccentricity of the orbit. Fig. 4 shows point target simulations based on the system in Table 1 and the orbit in Fig. 2. The top panel shows the results when the focusing is performed without SATA and the bottom panel when SATA is applied. The point targets are placed along the 20 km processing interval in azimuth at mid-range of the swath. Without using SATA, the point targets that are not located in the center of the azimuth interval experience strong defocusing, a direct consequence of the space-variance. Note that this effect cannot be compensated by processing smaller blocks in azimuth, since the azimuth variance occurs within the synthetic aperture observation time. With SATA, the space-variance can be efficiently compensated and the point targets appear well focused.

2.3. InSAR Performance Aspects

The orbit in Fig. 2 is periodic in an Enceladus body-fixed frame and can potentially provide repeat passes every 30 hours. However, the large distance to Earth paired with the uncertainties in the gravitational models do not allow for a very tight orbit control. The control accuracy of the baseline between repeating passes is expected to be roughly 130 m (1 sigma). In contrast to Earth observation applications, temporal decorrelation effects are expected to be negligible due to the absence of common decorrelation sources in glacial terrain (e.g., significant snow fall or melt events). The high backscatter values reported for the Enceladus surface (above 0 dB) suggest that the backscatter is dominated by efficient volume scattering in the upper part of the Enceladus ice crust [3, 4] that will introduce decorrelation for baselines greater than zero, depending on the penetration depth into the scattering volume. In the following, we assume a uniformly scattering ice volume and a 2-way penetration depth (i.e., the depth after which the power is decreased by a factor of $\frac{1}{e}$) of 15 m. This assumption is rather conservative when comparing to penetration values reported at S band in high backscatter glacial areas on Earth. However, to this date, the scattering mechanisms on Enceladus are poorly understood and mitigation strategies for potentially larger penetration need to be implemented. Fig. 5 shows the expected relative errors for the displacement and height measurement across the swath for a variety of baselines, a product resolution of 20 m x 20 m, a backscatter of 0 dB, and including common decorrelation sources except temporal decorrelation. Note that the volume decorrelation is dominating the budget. A displacement measurement error of less than few millimeters is to be expected and a topographic mapping capability with an accuracy of less than few meters. Note that the height estimated with InSAR will be systematically biased downward with respect to the surface due to the penetration into the volume and uncompensated propagation effects through the dielectric interface at the surface.

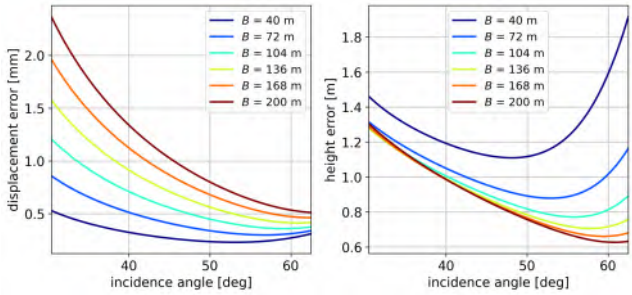

Fig. 5: InSAR performance across the swath for the system in Table 1 assuming a product resolution of 20 m x 20 m and an uniform scattering volume with exponential extinction properties with a penetration depth of 15 m: (left) displacement measurement error and (right) height measurement error for different baselines, B.

3. END-TO-END SIMULATION OF REALISTIC INSAR ACQUISITIONS

We use an in-house End-to-End (E2E) simulator developed at the Microwaves and Radar Institute of DLR [8] to generate realistic SAR products from the raw data to stacks of InSAR acquisitions. The simulations are used to evaluate the

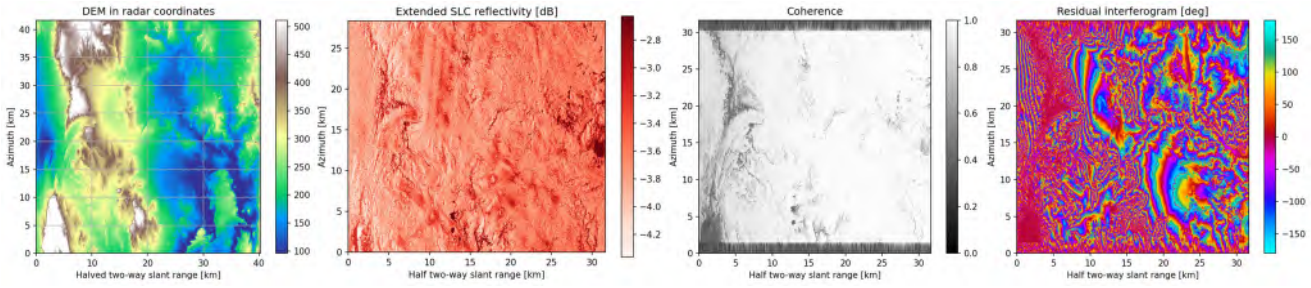

Fig. 6: First End-2-End simulation of a repeat-pass InSAR acquisition at Enceladus assuming the system in Table 1, the orbit in Fig. 2, an ellipsoidal model of Enceladus modulated with the DEM in the left panel, and a horizontal baseline of 200 m.

system performance and derive suitable interferometric processing strategies. The E2E is capable of accommodating the orbital geometries, an arbitrary topography, realistic deformation models, representative backscatter maps, and decorrelation effects, as well as any relevant instrument, baseline, and attitude errors. Fig. 6 shows first simulation results using the E2E and assuming the system in Table 1, the orbit in Fig. 2, and an ellipsoidal model of Enceladus modulated with representative topography derived from a digital elevation model (DEM) of the *Shuttle Radar Topography Mission* (SRTM). The DEM (with respect to the ellipsoid) is shown in the left panel. The reflectivity is generated synthetically, based on the local topography. The two panels on the right show the resulting interferogram and coherence for a baseline of 200 m (mostly oriented horizontally) when using the ellipsoid for the SAR focusing and InSAR processing. Only a global offset estimation for coregistration is performed. The fringes in the interferogram can be attributed to the topography. In general, the interferogram looks clean, however, in areas with strong topography the fringe rates are high for the 200 m baseline, suggesting the use of low-resolution topographic maps (available from optical stereo imaging during the Cassini mission) for the on-board InSAR processing if also strong topography regions should be recovered consistently. Note that deformation and volume decorrelation effects have not been included yet in the simulation. The volume decorrelation will have impacts on the data quality, but is not expected to significantly impact the InSAR processing assumptions, as long as sufficient coherence for the offset estimation remains.

4. CONCLUSION

We have presented a first performance assessment of an interferometric SAR mission for deformation and topography mapping of Enceladus. The orbit and the geophysical properties of Enceladus introduce unique characteristics that need to be accounted for in the system design and accommodated in the processing strategies. The End-to-End simulation results show clean interferograms, thus providing an initial validation of the system and processing concept.

5. REFERENCES

[1] J. R. Spencer and F. Nimmo, "Enceladus: An active ice world in the Saturn system," *Annual Review of Earth and Planetary Sciences*, vol. 41, no. 1, pp. 693–717, 2013.

[2] F. Postberg et al., "Macromolecular organic compounds from the depths of Enceladus," *Nature*, vol. 558, pp. 564–568, 2018.

[3] K. L. Mitchell et al., "Enceladus' brilliant surface: Cassini RADAR observations and interpretation," in *44th Lunar and Planetary Science Conference*, Houston, 2013, p. Abstract #2902, Lunar and Planetary Institute.

[4] G. J. Black, D. B. Campbell, and L. M. Carter, "Arecibo radar observations of Rhea, Dione, Tethys, and Enceladus," *Icarus*, vol. 191, no. 2, pp. 702–711, 2007.

[5] A. Benedikter et al., "Periodic orbits for interferometric and tomographic radar imaging of Saturn's moon Enceladus," *Acta Astronautica*, vol. 191, pp. 326–345, 2022.

[6] P. Prats, A. Reigber, and J.J. Mallorqui, "Topography-dependent motion compensation for repeat-pass interferometric SAR systems," *IEEE Geoscience and Remote Sensing Letters*, vol. 2, no. 2, pp. 206–210, 2005.

[7] P. Prats et al., "Comparison of topography- and aperture-dependent motion compensation algorithms for airborne SAR," *IEEE Geoscience and Remote Sensing Letters*, vol. 4, no. 3, pp. 349–353, 2007.

[8] M. Rodriguez-Cassola et al., "End-to-end level-0 data simulation tool for future spaceborne SAR missions," in *EUSAR 2018; 12th European Conference on Synthetic Aperture Radar*, 2018, pp. 1–6.

On the Processing of Single-Pass InSAR Data for Accurate Elevation Measurements of Ice Sheets and Glaciers

Andreas Benedikter, *Member, IEEE*, Marc Rodriguez-Cassola, Pau Prats-Iraola, *Senior Member, IEEE*, Gerhard Krieger, *Fellow, IEEE*, and Georg Fischer

***Abstract*— Single-pass interferometric synthetic aperture radar (InSAR) elevation measurements of dry snow, firn, and ice are known to be substantially biased downward due to a partial penetration of the radar signals into the medium, resulting in a phase center location within the volume. The so-called penetration bias, i.e., the elevation difference between surface and InSAR phase center, can be estimated from the contribution of the volume to the interferometric coherence and may be used to retrieve the surface elevation. In this article, we show that both an additional elevation bias and a horizontal shift occur in the InSAR processing for natural media with a dielectric constant different to the one of air, originating from an uncompensated stretch of the vertical wavenumber in the medium and refraction effects at the surface. This geolocation error depends on the magnitude of the penetration bias, the dielectric constant, and the acquisition geometry. It may reach up to few meters for X- and C-band frequencies and more for lower frequencies and therefore may significantly affect cryospheric elevation products from past (SRTM), current (TanDEM-X), and future (e.g., Harmony and Tandem-L) SAR interferometers. In this article, the geolocation error is assessed and an adapted interferometric processing allowing for an accurate geolocation (i.e., surface elevation measurement) is presented.**

***Index Terms*— Cryosphere, elevation bias, geocoding, glaciers, Harmony, ice sheets, penetration bias, synthetic aperture radar (SAR), SAR interferometry, TanDEM-X.**

I. Introduction

DIGITAL elevation models (DEMs) generated with single-pass interferometric synthetic aperture radar (InSAR) are a fundamental source for mapping the surface elevation and topographic changes over ice sheets and glaciers [1]. The nonnegligible penetration of radar signals into snow, firn, and ice at commonly used frequency bands, e.g., from P to X band, results in an elevation bias of the backscatter phase center versus the actual surface, typically described in the literature as penetration bias. In other words, the DEM generated from InSAR data does not replicate the surface, but it is biased downward [1], [2], [3], [4], [5], [6], [7], [8], [9], [10], [11].

Manuscript received 8 May 2023; revised 18 October 2023 and 21 November 2023; accepted 16 December 2023. Date of publication 21 December 2023; date of current version 19 January 2024. This work was supported in part by the European Space Agency under Contract 4000135083/21/NL/FF/ab. *(Corresponding author: Andreas Benedikter.)*

The authors are with the Microwaves and Radar Institute, German Aerospace Center (DLR), 82234 Weßling, Germany (e-mail: andreas.benedikter@dlr.de).

Digital Object Identifier 10.1109/TGRS.2023.3345415

In this article, we report that there is a systematic difference between the physical phase center height and the apparent phase center height measured with InSAR. This difference results from propagation effects within the glacial volume that are not accounted for in conventional InSAR processing, in particular, from a vertical wavenumber stretch in the glacial volume and refraction effects at the surface, both a direct consequence of the larger dielectric permittivity of snow, firn, and ice compared to the permittivity of air, resulting in a reduced propagation velocity. The relation between the surface height h_s, the physical height of the phase center h_{pc}, and the apparent phase center height measured with conventionally processed InSAR $h_{\mathrm{InSAR,c.}}$ can be approximated as

$$h_s \approx h_{pc} + \Delta h \approx h_{\mathrm{InSAR,c.}} - \Delta h_2 + \Delta h \tag{1}$$

where Δh is the physical penetration bias (assumed positive, according to the convention in [2] and [3]) and Δh_2 (assumed negative for biases oriented downward) represents an additional bias resulting from the abovementioned wavenumber stretch, from here on referred to as propagation bias. A comparable propagation bias effect has been reported in [12], resulting from propagation effects through the atmosphere. Commonly, Δh_2 is neglected and the assumption is that the surface height, h_s, is related to $h_{\mathrm{InSAR,c.}}$ via

$$\widetilde{h_s} \approx h_{\mathrm{InSAR,c.}} + \Delta h \tag{2}$$

where $\widetilde{\cdot}$ is used because we show in this article that the formulation does not result in an accurate surface height estimate. The approximation in (2) has been used in several research works, where the physical penetration bias Δh is estimated as the difference between an InSAR DEM (i.e., $h_{\mathrm{InSAR,c.}}$) and a surface reference DEM (i.e., h_s) generated with, e.g., optical sensors that do not penetrate the surface, to evaluate the penetration of the signals and to retrieve information on snow, firn, and ice properties [1], [4], [5], [6], [7], [8], [9]. Vice versa [5], [10], and [11] have used the inversion strategies of [2] and [3] to estimate the penetration bias Δh from the interferometric coherence to retrieve the surface elevation h_s from the TanDEM-X DEM (i.e., $h_{\mathrm{InSAR,c.}}$). Since Δh_2 is a direct consequence of the propagation through the glacial volume, it should not be neglected, but properly addressed whenever penetration into the volume occurs, especially when considering future single-pass SAR interferometers operating in lower frequency bands. Examples are Tandem-L (L band)

[13] and the Earth Explorer 10 mission Harmony (C band) [14] that is partly focused on generating elevation and elevation change products over land ice on a global scale.

It is important to note that both the penetration into the volume and the uncompensated change in propagation velocity do not only result in an elevation bias, but also a shift in horizontal, i.e., ground range, direction, as also noted in [12] in the case of propagation effects through the atmosphere. For retrieving accurate elevation estimates in cases of a spatially fast-changing topography, this horizontal shift needs to be taken into account. Hence, the DEM generation for the propagation through several media should be formulated in terms of a 3-D geolocation problem that is best addressed within the interferometric processing rather than in a secondary elevation correction.

In Section II, the geolocation error is assessed and quantified, whereas in Section III, adapted InSAR processing strategies are presented that provide an accurate geolocation for the cases in which the InSAR DEM should replicate the surface elevation or the phase center elevation. Section IV presents results generated with the Harmony End-To-End Performance Simulator (HEEPS) [15], and conclusions are drawn in Section V.

II. Assessment of the Geolocation Error

Part of a standard interferometric processing chain is shown in Fig. 1, illustrating the process from the interferogram to the retrieved DEM. The geolocation problem for glaciers and ice sheets arises within the geocoding of the interferometric information. The geocoding is commonly performed by a numerical computation of the 3-D intersect point of the interferometric phase, the range sphere, and the Doppler cone by solving the following set of equations for each pixel of the absolute phase, $\phi_{\text{abs.}}$, [16]:

$$\begin{cases} \phi_{\text{abs.}} = \dfrac{4\pi}{\lambda} \cdot \left(|\mathbf{p} - \mathbf{s}_{\text{p}}| - |\mathbf{p} - \mathbf{s}_{\text{s}}| \right) \\ r_{\text{p}} = |\mathbf{p} - \mathbf{s}_{\text{p}}| \\ f_{\text{DC,p}} = \dfrac{2}{\lambda \cdot r_{\text{p}}} \cdot \mathbf{v}_{\text{p}} \cdot (\mathbf{p} - \mathbf{s}_{\text{p}}) \end{cases} \tag{3}$$

where r_{p} is the slant range of the primary acquisition, $f_{\text{DC,p}}$ is the Doppler centroid of the primary acquisition, λ is the wavelength, $\mathbf{p}$ is the unknown point on ground, $\mathbf{s}_{\text{p}}$ is the position of the primary satellite, $\mathbf{s}_{\text{s}}$ is the position of the secondary satellite, and $\mathbf{v}_{\text{p}}$ is the velocity vector of the primary satellite.

Since for standard application scenarios, there is no a priori information on the penetration bias (i.e., the phase center depth), nor the surface elevation, free-space propagation of the radar signals between the sensor and the scatterer is typically assumed. This necessarily leads to a misinterpretation of the interferometric phase and the range for cases in which the phase center is located within the volume, because the signals experience an additional delay that is caused by the reduced propagation velocity due to the permittivity of the glacial volume.

Fig. 2 shows a simple simulation of the geocoding process and the resulting error. A simplified two-layer model (free space and glacial volume) with a constant permittivity within each layer is assumed and used in the derivations throughout this article. As an example, a horizontal snow surface, a satellite altitude of 700 km, a constant relative permittivity of the glacial volume of $\varepsilon_{\text{r}} = 2.0$, and a phase center depth of 10 m are assumed. Note that the phase center can be interpreted as the center of gravity of the backscatter distribution along the elevation direction within the volume. The blue lines represent contours of constant fast time (solid line) and interferometric phase (dashed line) when correctly accounting for the reduced propagation velocity within the volume. The contours are computed using a numerical ray tracing, based on Fermat's principle of least time. The red lines represent the equivalent contours assuming propagation only through air, i.e., the assumption made in the standard interferometric geocoding, corresponding to the first two equations in (3). Note that an acquisition geometry with a Doppler centroid equal to zero is assumed here. The shift between the blue intersect point (p_s) and the red one (p_a) represents the geolocation error, i.e., the error in the retrieved DEM. Note that the error is independent of the interferometric baseline (further discussed below) but has a strong dependence on the incident angle at the surface. Both a shift in height and ground range are present, with magnitudes depending on the phase center depth, the incident angle, and the permittivity.

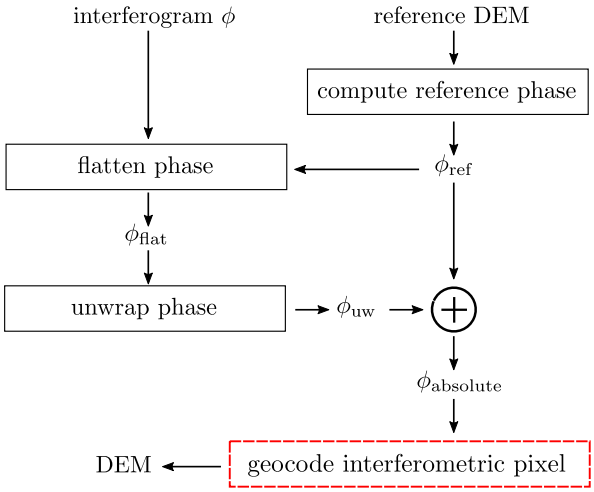

Fig. 1. Standard interferometric processing chain for generating a DEM. Calibration steps are omitted for simplicity.

For the simple propagation model used in the simulation of Fig. 2, the height error, i.e., the propagation bias Δh_2, may be quantified by evaluating the change in the interferometric vertical wavenumber k_z when propagating into the firn volume. The vertical wavenumber is stretched when penetrating in the dielectric denser medium. It can be written in terms of k_z as [17], [18]

$$k_{z,\text{vol}} = k_z \cdot \sqrt{\varepsilon_{\text{r}}} \cdot \frac{\cos\theta_{\text{i}}}{\cos\theta_{\text{r}}} \tag{4}$$

where θ_{i} is the local incident angle and θ_{r} is the refraction angle that can be computed using Snell's law. The physical contribution of the penetrated firn volume Δh (i.e., the height difference between the surface and the phase center) to the

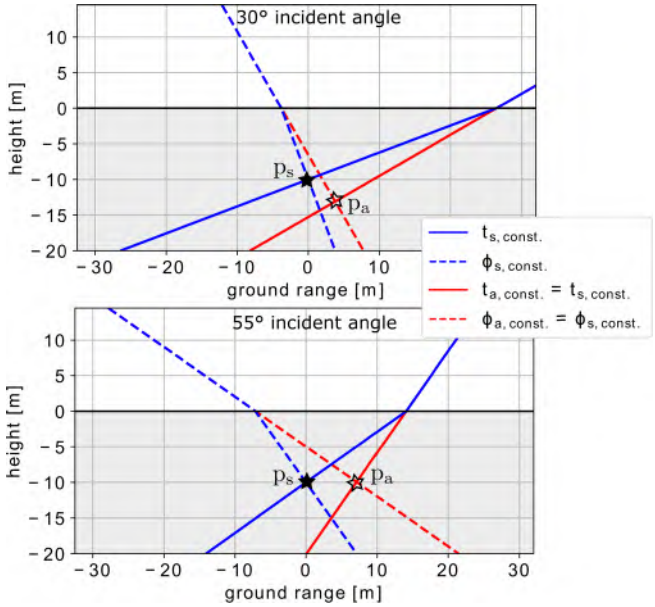

Fig. 2. Illustrative simulation of the geocoding process and the resulting geolocation error for a flat surface. Blue lines show contours of constant fast time (solid) and interferometric phase (dashed) when accounting for the propagation effects into the volume. Red lines show the corresponding contours for a free-space assumption. The shift between the blue intersect point (p_s) and the red one (p_a) represents the geolocation error.

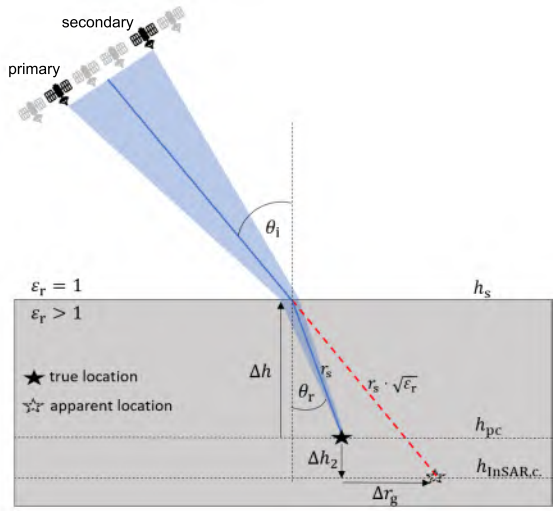

Fig. 3. Illustration for deriving the height and ground range error. The heights in the figure can be related to (1). The geometry is comparable to the 30° incident angle case in Fig. 2. For shallower incident angles, $h_{\text{InSAR,c.}}$ increases (see Fig. 2) and eventually surpasses the physical phase center height h_{pc}.

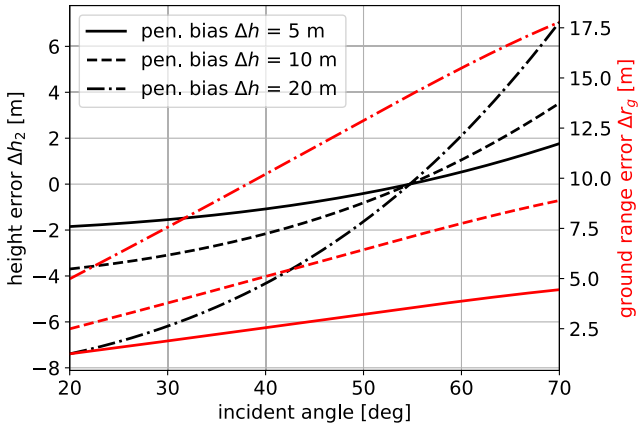

Fig. 4. Height and ground range error for different incident angles and three different penetration biases, i.e., phase center depths. A permittivity of $\varepsilon_r = 2.0$ is assumed. Note that the penetration bias corresponds to the phase center depth with respect to the surface height. A varying phase center depth may result from a varying vertical backscatter distribution in the volume or acquisition geometry.

interferometric phase can be written as $\phi_{\text{pen}} = \Delta h \cdot k_{z,\text{vol}}$. When assuming propagation through free space in the InSAR processing, ϕ_{pen} is erroneously scaled with k_z and not $k_{z,\text{vol}}$. Hence, the propagation bias Δh_2 resulting from the free-space assumption in processing may be formulated as

$$\Delta h_2 \approx \frac{\Delta h \cdot k_{z,\text{vol}}}{k_{z,\text{vol}}} - \frac{\Delta h \cdot k_{z,\text{vol}}}{k_z} = \Delta h \cdot \left(1 - \sqrt{\varepsilon_r} \cdot \frac{\cos\theta_i}{\cos\theta_r}\right). \quad (5)$$

Note again that all dependencies with the interferometric baseline cancel out. A geometrical derivation may be found when considering the interferometric pair as part of an antenna array that radiates power in the form of a collimated beam that is refracted into the glacial volume (see Fig. 3). Since the optical path lengths (i.e., the travel times) for both the physically correct propagation and the free-space assumption have to be the same, the geolocation error can be determined using the geometrical relations shown in Fig. 3, resulting in

$$\Delta h_2 = \Delta h \cdot \left(1 - \sqrt{\varepsilon_r} \cdot \frac{\cos\theta_i}{\cos\theta_r}\right) \quad (6)$$

$$\Delta r_g = \Delta h \cdot \tan\theta_r \cdot \left(\sqrt{\varepsilon_r} \cdot \frac{\sin\theta_i}{\sin\theta_r} - 1\right). \quad (7)$$

A similar derivation is provided in [19] for the SAR tomography case. Note that the expression for Δh_2 is equivalent to the wavenumber derivation in (5).

The vertical and horizontal geolocation errors are plotted in Fig. 4 as a function of the incident angle and for three different values of the penetration bias Δh. A permittivity of $\varepsilon_r = 2.0$ is assumed, representing dry firn. It is interesting to note that the intersect point of the Δh_2 curves is solely a function of the permittivity. Note also that even for the limited penetration reported for X band sensors (e.g., in [10]) down to 8–10 m, geolocation errors of several meters can be expected. Note that for the analysis above, a constant permittivity of the glacial volume is assumed. A more complex permittivity distribution may be accommodated by an effective mean value representing the volume above the phase center that may change depending on the phase center depth.

Using a backscatter model to characterize the glacial volume, the geolocation error can be linked to physical properties of the volume. For example, in [2], a model for describing the contribution of a uniform volume with exponential extinction properties to the complex interferometric coherence is given

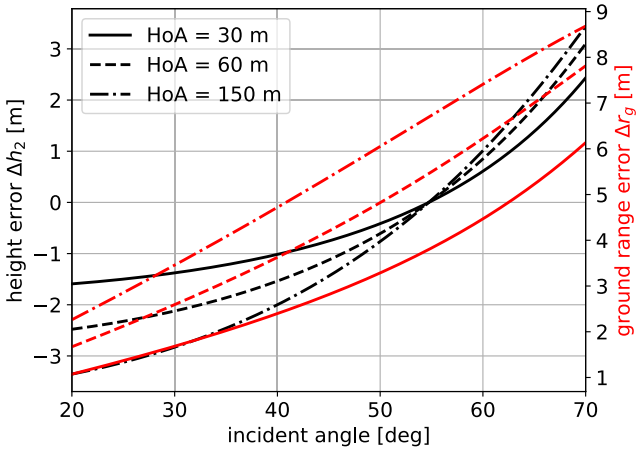

Fig. 5. Height and ground range error for different incident angles and three different heights of ambiguity. A uniform volume with a penetration depth of 10 m and a permittivity of $\varepsilon_r = 2.0$ are assumed.

as follows:

$$\gamma_{\text{vol}} = \frac{1}{1 + \mathrm{j} \cdot 2 \cdot \pi \cdot {}^{d_2}/_{\text{HoA}_{\text{vol}}}} \tag{8}$$

where j is the imaginary unit, d_2 is the two-way penetration depth [i.e., the depth after which the power is decreased by a factor of (1/e)], and $\text{HoA}_{\text{vol}} = \frac{2\pi}{k_{z,\text{vol}}}$ is the height of ambiguity in the volume. From (8), the penetration bias Δh for a uniform volume can be formulated in terms of d_2 [3]

$$\Delta h = \arctan\left(k_{z,\text{vol}} \cdot d_2\right) \cdot \frac{1}{k_{z,\text{vol}}}. \tag{9}$$

Using the formulations in (6), (7), and (9), the geolocation errors are shown in Fig. 5 for a penetration depth of $d_2 = 10$ m and three heights of ambiguity (HoA) in free space. The error for the uniform volume model is dependent on the interferometric baseline (i.e., the HoA) since the transformation from d_2 to Δh results in larger Δh values for smaller baselines.

III. Adapted Processing

In this section, we present adapted processing approaches capable of accounting for both the penetration itself and the propagation related errors presented in Section II. Two application scenarios are addressed, in which the estimated topography should replicate: 1) the phase center elevation or 2) the surface elevation. It is assumed that an accurate estimate of the penetration bias, Δh, is available, for example, by means of the inversion strategies presented in [2] and [3] that are based on the measured coherence. Note that these inversions only provide a model-based estimate of Δh with limited accuracy and may introduce systematic errors in the final DEM.

A. Topographic Height Correction

A straightforward approach is to extend the conventional processing chain in Fig. 1 by a simple elevation correction step after the DEM generation to compensate the penetration bias, Δh, and the propagation bias, Δh_2, corresponding to the relation given in (1). A DEM that approximates the phase center height can be retrieved from the conventionally processed DEM, $\text{DEM}_{\text{InSAR,c.}}$, by

$$\begin{aligned}\text{DEM}_{\text{pc}} &= \text{DEM}_{\text{InSAR,c.}} - \Delta h_2 \\ &= \text{DEM}_{\text{InSAR,c.}} - \Delta h \cdot \left(1 - \sqrt{\varepsilon_r} \cdot \frac{\cos\theta_i}{\cos\theta_r}\right)\end{aligned} \tag{10}$$

whereas a DEM approximating the surface elevation is given by

$$\begin{aligned}\text{DEM}_{\text{s}} &= \text{DEM}_{\text{InSAR,c.}} + \Delta h - \Delta h_2 \\ &= \text{DEM}_{\text{InSAR,c.}} + \Delta h \cdot \sqrt{\varepsilon_r} \cdot \frac{\cos\theta_i}{\cos\theta_r}.\end{aligned} \tag{11}$$

$\text{DEM}_{\text{InSAR,c}}$, DEM_{pc}, and DEM_{s} correspond to the heights introduced in (1): $h_{\text{InSAR,c.}}$, h_{pc}, and h_{s}, respectively. Note that such simple elevation correction does not account for the shift in ground range direction, Δr_g, and may, therefore, result in residual elevation errors for areas with strong topographic gradients.

B. Adapted InSAR Processing for Surface and Phase Center Elevation Measurement

As hinted above, penetration and propagation effects need to be accounted for within the InSAR processing. The most accurate solution is to adapt the geocoding process to incorporate the refraction at the surface and the reduced propagation velocity within the volume. However, such adaption results in a significantly higher computational complexity since the ray tracing through a multilayer medium has to be done numerically.

We suggest to perform the correction by means of a compensation of the penetration phase and a correction of the range delay in terms of an adaption of the range equation within the geocoding formalism in (3). The geocoding can then be performed conventionally, assuming free space. The adapted chain is illustrated in Fig. 6. The general approach is applicable for both the generation of a surface DEM and for a phase center DEM. Only the formulations for the computation of the phase compensation and range offsets differ.

The compensation of the penetration phase contribution ϕ_{pen} needs to account for the difference between the interferometric phase at the physical position of the phase center and the surface or phase center position for a free-space assumption. For the surface case, ϕ_{pen} can be computed as

$$\phi_{\text{pen,surface}} = -\Delta h \cdot k_{z,\text{vol}}. \tag{12}$$

For the phase center case, ϕ_{pen} can be approximated as

$$\phi_{\text{pen,pc}} = \Delta h_2 \cdot k_z. \tag{13}$$

The penetration phase can then be simply used as an offset to the absolute phase, as illustrated in Fig. 6. The range shifts may be corrected in terms of an offset on the range equation of the interferometric geocoding in (3). Again, the adaption of the range equation needs to account for the difference between the range to the physical position of the phase center and the surface or phase center position assuming free space. The range offsets can be approximated as

$$\Delta r_{\text{surface}} \approx -\sqrt{\varepsilon_r} \cdot \frac{\Delta h}{\cos\theta_r} \tag{14}$$

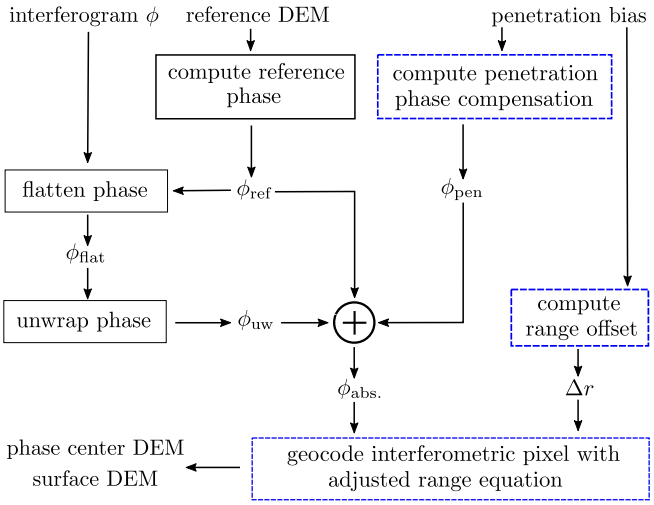

Fig. 6. Adapted interferometric processing chain for generating a DEM corresponding to the surface or the phase center, including a correction of the interferometric phase and range offsets.

TABLE I
SIMULATION PARAMETERS

Parameter	Description / Value
orbit	polar, circular, 700 km altitude
surface height	WGS 84 ellipsoid
incident angle (mean)	40°
phase center depth, Δh	-14 m to -4 m
permittivity of the penetrated volume, ε_{r}	2.0, constant

and

$$\Delta r_{\text{pc}} \approx \frac{\Delta h}{\cos\theta_{\text{r}}} \cdot (1 - \sqrt{\varepsilon_{\text{r}}}). \tag{15}$$

To apply the correction, the range equation in (3) is rewritten as

$$r_{\text{p}} + \Delta r_{\text{i}} = \left|\mathbf{p} - \mathbf{s}_{\text{p}}\right| \tag{16}$$

where the index i indicates the range offset for the surface or the phase center in (14) and (15), respectively.

Alternatively, instead of adapting the range equation in (3), the range offsets can be accounted for by interpolating the absolute phase to an adjusted range grid. Note that this approach leads to an increased computational burden and is only mentioned here since it may provide an easier integration into an existing InSAR processor.

Note that both the adaption of the range equation as well as the interpolation of the absolute phase to an adjusted range grid are first-order approximations, based on the assumption that the slope of the terrain is constant between the phase center position and the intersect point on the surface.

C. Accuracy Analysis

In order to illustrate the accuracy of the proposed approaches, they are compared within a simple simulation to an exact geocoding procedure that accounts for the refraction and propagation effects in the volume. The relevant simulation parameters are depicted in Table I. To facilitate an exact geocoding that incorporates the dielectric medium change, the surface height corresponds to the WGS 84 ellipsoid, without additional topography. The phase center height is varying between -14 and -4 m. In Fig. 7(a), the geodetic coordinates of the phase center and surface intersect points are illustrated. The coordinates correspond to the radar coordinates of a 2 km $\times$ 2 km acquisition and are computed using a Newton backgeocoding algorithm as described in [20]. Note that the backgeocoding is adapted to account for the dielectric medium change. Fig. 7(b) shows the phase center elevation in radar coordinates, and Fig. 7(c) shows the slope of the phase center elevation in range direction. The slopes up to 12 % are likely to resemble an extreme case of phase center elevation variability. However, note that the strong elevation variability may account for the effects introduced by a realistic surface topography that is absent in this simulation. Fig. 7(d) and (e) show the range offsets when comparing the correct range (resulting from the backgeocoding procedure) to the range when assuming free space, Fig. 7(d) for the phase center DEM case and Fig. 7(e) for the surface DEM case. The offsets in Fig. 7(d) are solely a consequence of the reduced propagation velocity and refraction, whereas the offsets in Fig. 7(e) additionally include the geometric distance between the surface intersect point and the phase center, together reaching up to 22 m for the present example. In the following, the resulting height errors when assuming free space in the geocoding are assessed for the cases in which the standard height correction [see (2)] is performed, or the corrections presented in Sections III-A and III-B of this work.

1) The height errors after the standard elevation correction in (2), i.e., when neglecting the propagation bias and the range offsets, are shown in Fig. 7(f) and (g) for the surface and phase center DEM case, respectively. Note that no correction is performed for the phase center DEM case. The height errors are a superposition of the erroneous height correction and the geodetic position mismatch resulting from the uncompensated range offsets (i.e., the height is not constant in the area spanned by the range offsets). The contribution due to the range offsets is stronger for the surface DEM case.
2) Fig. 7(h) and (i) show the residual height errors when applying the adapted height correction according to (10) and (11). The height estimation improved compared to the standard correction. Still, errors in the meter range are present. The residual errors can be exclusively attributed to the range offsets that translate into height errors for a topography with nonnegligible slope, as described for the previous case. Note that the pattern of the height errors resembles the one of the slopes in Fig. 7(c). For a flat topography and a constant penetration bias, no height errors would remain.
3) Fig. 7(j) and (k) show the residual height errors after applying the phase and range offset correction as described in Section III-B. The correction is not perfect because it is only a first-order approximation. Note that range offsets of few decimeters are remaining after the range correction (not explicitly shown in Fig. 7). However, even for the strong elevation variability of the present example, only height errors of few cm are still present. These are almost two orders of magnitude smaller than common height accuracy requirements.

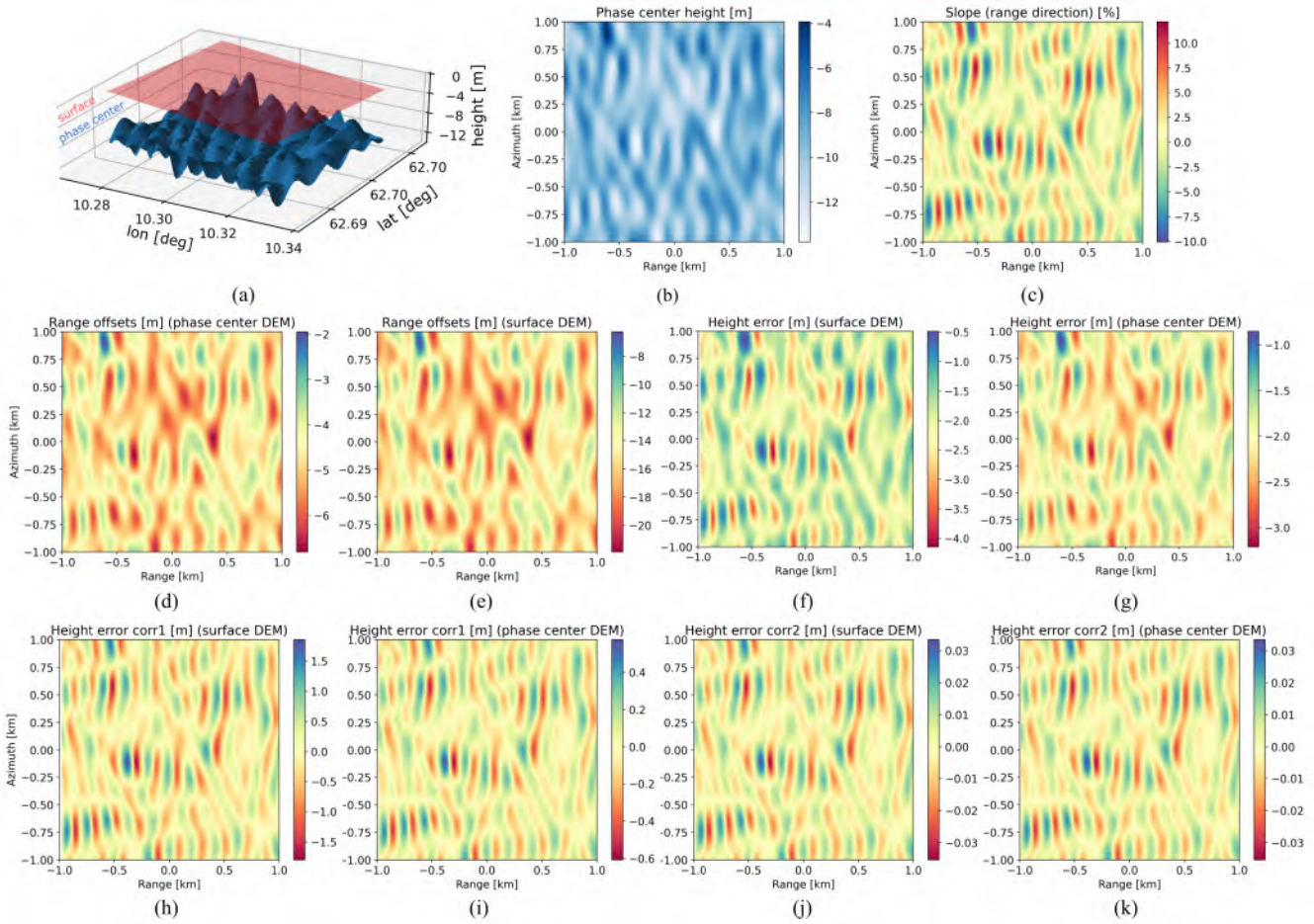

Fig. 7. Simulation for assessing the accuracy of the adapted processing approaches showing: (a) geodetic coordinates of the phase center and surface intersect points; (b) phase center elevation; (c) slope of the phase center elevation; (d) and (e) range offset between the apparent phase center position (assuming free-space propagation) and the physical phase center or the surface position, respectively; (f) and (g) height error when applying the standard elevation correction in (2) for retrieving the surface or phase center, respectively; (h) and (i) height error when applying the adapted height correction described in Section III-A; and (j) and (k) height error when applying the adapted InSAR processing described in Section III-B. Note the different range of the colorbars when comparing (h)–(k).

The discussed simulation results in Fig. 7 suggest that a height correction is not sufficient for terrains with modest to steep slopes or a spatially fast varying penetration bias. The adapted processing, as described in Section III-B, provides accurate results, even for a strongly varying topography, if a precise estimate of the penetration bias, Δh, is available.

As hinted above, biased estimates of Δh can result in systematic errors of the final DEM. Such biases may be present for heterogeneous parts of glaciers and ice sheets where model-based inversions may not replicate well enough the physical scattering and propagation properties of the glacial volume, but are expected to be small (i.e., smaller than the propagation bias, Δh_2) for rather homogeneous terrain (e.g., over the large ice sheets). Since, in the general application case with no reference date, there is no means of determining if the estimation of Δh is biased and in which direction it is biased, we suggest to always perform the adapted processing (i.e., account for the propagation bias and the range offsets) because it allows a physically correct accommodation of the propagation effects and, on average, will lead to improved elevation products.

The analyses in this article are simplified to a zero-squint acquisition geometry. For very large squint angles, also a significant geolocation error in azimuth direction is to be expected, resulting from both the incorrect geocoding and uncompensated phase residuals (due to the propagation through the glacial volume) in the SAR processing [21]. However, even for large squints of several degrees, the offsets in azimuth are marginal compared to the range offsets.

IV. Simulation Results

A reliable demonstration of the outlined effects and the proposed processing adaption on real InSAR data is challenging because a reference measurement or estimation of the penetration bias, i.e., the phase center depth, using approaches such as the inversion of the volume coherence is known to be model-dependent [22], [23]. This would necessarily result in a speculative interpretation of the results. Nevertheless, it is important to show on as much realistic as possible SAR data that the outlined effects may significantly degrade the InSAR elevation measurements of a cryospheric SAR mission.

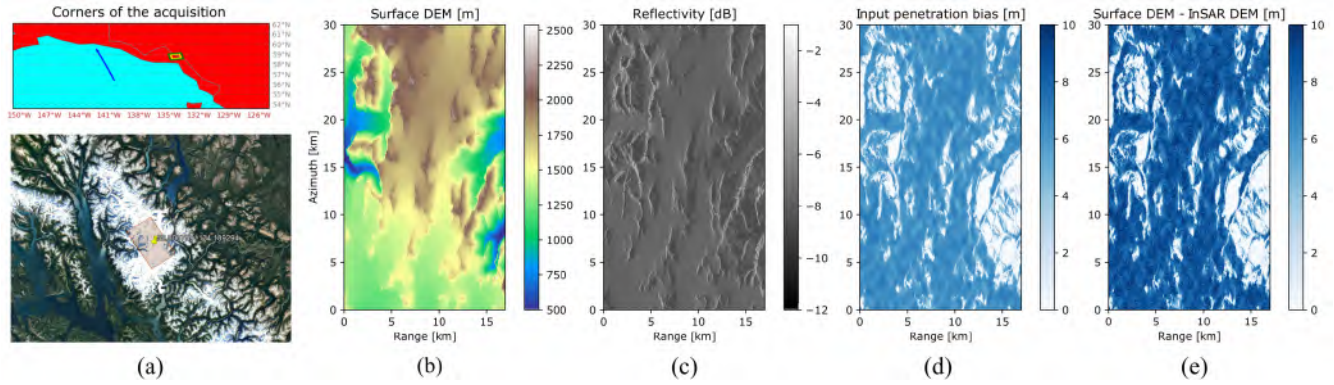

Fig. 8. Some inputs and results for the end-to-end simulation using HEEPS, showing: (a) location of the scene; (b) DEM representing the surface; (c) simulated reflectivity of the scene; (d) input penetration bias; and (e) difference between the surface DEM and the generated InSAR DEM using a conventional InSAR processing chain assuming free-space propagation.

TABLE II
HEEPS SIMULATION PARAMETERS

Parameter	Description / Value
frequency	5.405 GHz
SLC resolution (az x rg)	20 m x 5 m
interferogram resolution (az x rg)	100 m x 100 m
incident angle (mean)	30°
height of ambiguity (mean)	60 m
NESZ (mean)	−20 dB
penetration depth	0 m to 12 m
permittivity ε_r	1.8, constant
reflectivity	−12 dB to −1 dB

We use the HEEPS [15] to generate realistic SAR images and higher level products according to the Harmony system parameters. The HEEPS is based on a bistatic end-to-end (BiE2E) simulator, developed at the German Aerospace Center (DLR), Weßling, Germany [24]. The BiE2E is an integrated InSAR simulation tool with bistatic and multistatic capabilities composed of three main parts: 1) a distributed SAR raw data simulation block; 2) level 1 and level 2 processing chains; and 3) a performance evaluation module. The BiE2E allows for the efficient simulation of interferometric stacks over wide distributed areas with an exact accommodation of bistatic geometries, antenna patterns, instrument and platform effects, as well as configurable complex correlations between the simulated scenes.

The simulation parameters are chosen according to the bistatic Sentinel-1/Harmony antenna and noise behavior. The relevant simulation parameters are listed in Table II. The simulation is performed for a scene located in a mountainous glacier region in BC, Canada. The location is shown in Fig. 8(a). The glacier region is chosen as an example case. The proposed techniques are equivalently applicable to ice sheets. We use the SRTM DEM [shown in Fig. 8(b)] as the surface reference. Within the scene generation module of the raw data generator of the BiE2E, a semiphysical representation of the scene reflectivity is generated [see Fig. 8(c)] and the penetration into the glacial volume is simulated. The firn is modeled according to a uniform volume model with a varying two-way penetration depth, d_2, and a constant relative permittivity. For the given local incident angles and the height of ambiguity of 60 m, the resulting penetration bias is shown in Fig. 8(d). The penetration into the glacial volume is modeled in terms of range offsets and a complex volume coherence according to the formulation in (8). The coherence is injected in the two scenes of the interferometric pair by means of a two-image

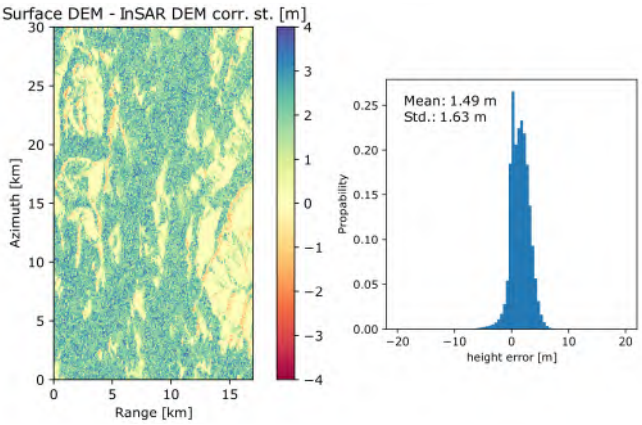

Fig. 9. Height error when applying the standard elevation correction in (2). Note the significant residual bias over the glacial areas.

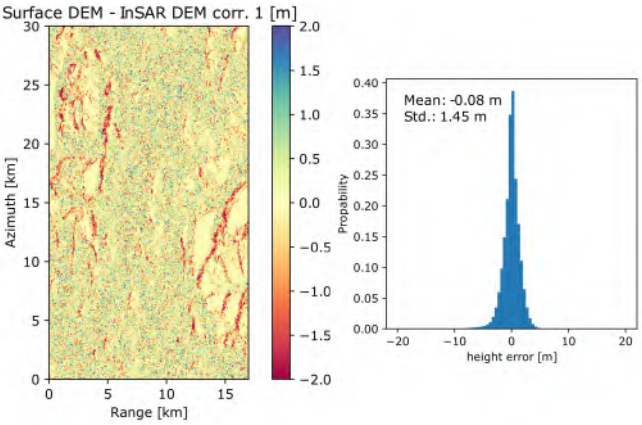

Fig. 10. Height error when applying the adapted height correction described in Section III-A. No range correction is applied.

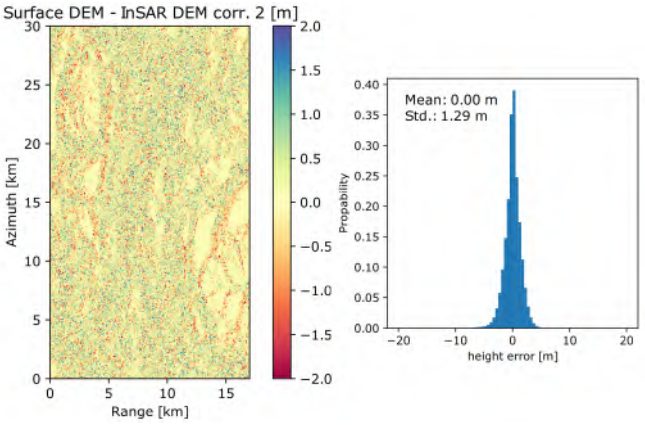

Fig. 11. Height error when applying the adapted InSAR processing described in Section III-B. Note that almost all systematic errors are removed.

Cholesky decomposition. After the scene generation and an error incorporation step (navigation, attitude, clock, etc.), the raw data are synthesized using a reverse SAR processor. Subsequently, the raw data are focused and an InSAR processor is used to generate the interferogram and DEM. For the case in which free-space propagation is assumed within the InSAR processing and no further corrections are performed, Fig. 8(e) shows the difference between the surface DEM (used as input to the simulator) and the generated InSAR DEM. Note the clear height error compared to the input penetration bias in Fig. 8(d), a direct consequence of the propagation effects into the firn volume.

Fig. 9 shows the residual height error when retrieving a surface DEM from the InSAR DEM using the standard height correction according to (2), i.e., when neglecting the propagation bias. A height offset up to 3 m over the firn areas is visible, resulting in a mean height error of 1.49 m. Note the two peaks in the histogram, corresponding to surface areas (centered around 0 m) and firn areas (centered around roughly 2.5 m). Several areas with systematic negative height offsets are visible in regions with sudden changes in the penetration bias. Those height offsets can be attributed to the uncompensated range offsets. Fig. 10 shows the results when the adapted height correction in (11) is applied, i.e., also the propagation bias is accounted for. Most of the height offsets are removed. However, the negative biases due to the range offsets are still present. Note that smaller systematic biases due to range offsets are also present in the firn areas, but not visible due to the higher phase noise caused by the volume decorrelation effects. Fig. 11 shows the results for the case in which the adapted processing, discussed in Section III-B, is applied. Almost all systematic biases have been removed. This can also be noted in the mean error of 0 m and a reduced standard deviation compared to the previous case in Fig. 10.

V. Conclusion

In this article, a bias effect (additional to the well-known penetration bias) on single-pass InSAR elevation products of glaciers and ice sheets is reported. The bias is a direct consequence of the commonly uncompensated propagation effects of the radar signals through the glacial volume, i.e., a reduced propagation velocity and refraction at the glacial surface, resulting in a 3-D geolocation error during InSAR DEM processing. If a precise estimate of the penetration bias, i.e., the phase center depth, is available, the 3-D geolocation error can be accurately corrected by means of an adapted geocoding (accounting for the propagation effects) or a compensation of the interferometric phase and range offset that are inherent to the propagation through the volume. A simple height correction may be sufficient for scenes with moderate topography. Even though the bias has not been explicitly reported in data-based research work, it should be taken into account in the generation of cryospheric elevation products from SAR interferometers (e.g., TanDEM-X, Harmony, and Tandem-L), whenever penetration into the volume occurs. Elevation errors (additional to the well-known penetration bias) up to a few meters are to be expected in C and X bands, and beyond 10 m in L band. It is important to note that the proposed processing approaches do not solve the problem of precisely estimating the penetration bias. Still, even for inaccurate penetration bias estimates, they should be applied, whenever penetration into the glacial volume occurs since they allow a physically correct accommodation of the propagation effects and, on average, will lead to improved elevation products.

Comparable propagation effects should also be observable for arid areas, where the radar signals penetrate into sand or dry soil. The problem statement can be generalized to natural media with different dielectric properties than air that are transparent or semitransparent at microwave frequencies and is applicable to delays introduced by the troposphere and ionosphere.

Acknowledgment

The authors would like to thank the two anonymous reviewers for their effort and valuable suggestions.

References

[1] E. Berthier et al., "Measuring glacier mass changes from space—A review," *Rep. Prog. Phys.*, vol. 86, no. 3, pp. 8–12, 2023.

[2] H. A. Zebker and E. W. Hoen, "Penetration depths inferred from interferometric volume decorrelation observed over the Greenland ice sheet," *IEEE Trans. Geosci. Remote Sens.*, vol. 38, no. 6, pp. 2571–2583, Nov. 2000.

[3] J. Dall, "InSAR elevation bias caused by penetration into uniform volumes," *IEEE Trans. Geosci. Remote Sens.*, vol. 45, no. 7, pp. 2319–2324, Jul. 2007.

[4] S. Abdullahi, B. Wessel, M. Huber, A. Wendleder, A. Roth, and C. Kuenzer, "Estimating penetration-related X-band InSAR elevation bias: A study over the Greenland ice sheet," *Remote Sens.*, vol. 11, no. 24, p. 2903, Dec. 2019.

[5] P. Rizzoli, M. Martone, H. Rott, and A. Moreira, "Characterization of snow facies on the Greenland ice sheet observed by TanDEM-X interferometric SAR data," *Remote Sens.*, vol. 9, no. 4, p. 315, Mar. 2017.

[6] B. Wessel et al., "TanDEM-X PolarDEM 90 m of antarctica: Generation and error characterization," *Cryosphere*, vol. 15, no. 11, pp. 5241–5260, Nov. 2021.

[7] A. Dehecq, R. Millan, E. Berthier, N. Gourmelen, E. Trouvé, and V. Vionnet, "Elevation changes inferred from TanDEM-X data over the Mont-Blanc area: Impact of the X-band interferometric bias," *IEEE J. Sel. Topics Appl. Earth Observ. Remote Sens.*, vol. 9, no. 8, pp. 3870–3882, Aug. 2016.

[8] A. Lambrecht, C. Mayer, A. Wendt, D. Floricioiu, and C. Völksen, "Elevation change of Fedchenko glacier, Pamir Mountains, from GNSS field measurements and TanDEM-X elevation models, with a focus on the upper glacier," *J. Glaciol.*, vol. 64, no. 246, pp. 637–648, Aug. 2018.

[9] Y. Dong, J. Zhao, D. Floricioiu, L. Krieger, T. Fritz, and M. Eineder, "High-resolution topography of the Antarctic peninsula combining the TanDEM-X DEM and reference elevation model of Antarctica (REMA) mosaic," *Cryosphere*, vol. 15, no. 9, pp. 4421–4443, Sep. 2021.

[10] H. Rott et al., "Penetration of interferometric radar signals in Antarctic snow," *Cryosphere*, vol. 15, no. 9, pp. 4399–4419, Sep. 2021.

[11] C. Sommer, T. Seehaus, A. Glazovsky, and M. H. Braun, "Brief communication: Increased glacier mass loss in the Russian high Arctic (2010–2017)," *Cryosphere*, vol. 16, no. 1, pp. 35–42, Jan. 2022.

[12] G. Krieger, F. De Zan, M. Bachmann, P. L. Dekker, M. R. Cassola, and J. S. Kim, "Tropospheric and ionospheric effects in spaceborne single-pass SAR interferometry and radargrammetry," in *Proc. 10th Eur. Conf. Synth. Aperture Radar*, Jun. 2014, pp. 1–4.

[13] A. Moreira et al., "Tandem-L: A highly innovative bistatic SAR mission for global observation of dynamic processes on the Earth's surface," *IEEE Geosci. Remote Sens. Mag.*, vol. 3, no. 2, pp. 8–23, Jun. 2015.

[14] P. López-Dekker, H. Rott, P. Prats-Iraola, B. Chapron, K. Scipal, and E. D. Witte, "Harmony: An earth explorer 10 mission candidate to observe land, ice, and ocean surface dynamics," in *Proc. IEEE Int. Geosci. Remote Sens. Symp.*, Jul. 2019, pp. 8381–8384.

[15] M. Rodriguez-Cassola et al., "End-to-end level-0 data simulation tool for future spaceborne SAR missions," in *Proc. 12th Eur. Conf. Synth. Aperture Radar*, Jun. 2018, pp. 1–6.

[16] E. Sansosti, "A simple and exact solution for the interferometric and stereo SAR geolocation problem," *IEEE Trans. Geosci. Remote Sens.*, vol. 42, no. 8, pp. 1625–1634, Aug. 2004.

[17] J. J. Sharma, I. Hajnsek, K. P. Papathanassiou, and A. Moreira, "Estimation of glacier ice extinction using long-wavelength airborne pol-InSAR," *IEEE Trans. Geosci. Remote Sens.*, vol. 51, no. 6, pp. 3715–3732, Jun. 2013.

[18] Y. Lei, P. Siqueira, and R. Treuhaft, "A dense medium electromagnetic scattering model for the InSAR correlation of snow," *Radio Sci.*, vol. 51, no. 5, pp. 461–480, May 2016.

[19] S. Tebaldini, T. Nagler, H. Rott, and A. Heilig, "Imaging the internal structure of an Alpine glacier via L-band airborne SAR tomography," *IEEE Trans. Geosci. Remote Sens.*, vol. 54, no. 12, pp. 7197–7209, Dec. 2016.

[20] A. Linde-Cerezo, M. Rodriguez-Cassola, P. Prats-Iraola, and M. Pinheiro, "Systematic comparison of backgeocoding algorithms for SAR processing and simulation environments," in *Proc. 13th Eur. Conf. Synth. Aperture Radar*, Mar. 2021, pp. 1–4.

[21] A. Benedikter, M. Rodriguez-Cassola, F. Betancourt-Payan, G. Krieger, and A. Moreira, "Autofocus-based estimation of penetration depth and permittivity of ice volumes and snow using single SAR images," *IEEE Trans. Geosci. Remote Sens.*, vol. 60, pp. 1–15, 2022, Art. no. 4303315.

[22] G. Fischer, M. Jäger, K. P. Papathanassiou, and I. Hajnsek, "Modeling the vertical backscattering distribution in the percolation zone of the Greenland Ice sheet with SAR tomography," *IEEE J. Sel. Topics Appl. Earth Observ. Remote Sens.*, vol. 12, no. 11, pp. 4389–4405, Nov. 2019.

[23] G. Fischer, K. P. Papathanassiou, and I. Hajnsek, "Modeling and compensation of the penetration bias in InSAR DEMs of ice sheets at different frequencies," *IEEE J. Sel. Topics Appl. Earth Observ. Remote Sens.*, vol. 13, pp. 2698–2707, 2020.

[24] *Performance Simulator for Bistatic SAR Missions*, ESA, Paris, France, DLR-HR, 4000117230/16/NL/LvH, 2020.

Andreas Benedikter (Member, IEEE) was born in Munich, Germany, in 1994. He received the B.Sc. degree in medical engineering and the M.Sc. degree (Hons.) in electrical engineering and information technology from Friedrich-Alexander University Erlangen–Nürnberg, Erlangen, Germany, in 2017 and 2019, respectively, where he is currently pursuing the Ph.D. degree.

In 2017, he spent one semester at the University of Bristol, Bristol, U.K. Since 2019, he has been a Research Scientist with the Microwaves and Radar Institute, German Aerospace Center (DLR), Weßling, Germany. His research interests include radar signal processing, synthetic aperture radar (SAR) interferometry, radar signal propagation and scattering mechanisms, and the study of future radar concepts, especially in the context of cryospheric applications and planetary exploration missions.

Mr. Benedikter was a recipient of the First Prize of the Student Paper Competition of the IEEE International Geoscience and Remote Sensing Symposium 2023 Conference held in Pasadena, CA, USA.

Marc Rodriguez-Cassola was born in Barcelona, Spain, in 1977. He received the Ingeniero degree in telecommunication engineering from the Universidad Pública de Navarra, Pamplona, Spain, in 2000, the Licenciado (M.Sc.) degree in economics from the Universidad Nacional de Educación a Distancia, Madrid, Spain, in 2012, and the Ph.D. degree in electrical engineering from the Karlsruhe Institute of Technology, Karlsruhe, Germany, in 2012.

From 2000 to 2001, he was a Radar Hardware Engineer with the Study Center of Terrestrial and Planetary Environments (CETP)/French National Centre for Scientific Research (CNRS), Saint-Maur-des-Fossés, France. From 2001 to 2003, he was a Software Engineer with Altran Consulting, Munich, Germany. Since 2003, he has been with the Microwaves and Radar Institute, German Aerospace Center, Weßling, Germany, where he is leading the Synthetic Aperture Radar (SAR) Missions Group. His research interests include radar signal processing, SAR end-to-end simulation, SAR processing and calibration algorithms, crisis theory, and radar mission analysis and applications.

Pau Prats-Iraola (Senior Member, IEEE) was born in Madrid, Spain, in 1977. He received the Ingeniero and Ph.D. degrees in telecommunications engineering from the Universitat Politècnica de Catalunya (UPC), Barcelona, Spain, in 2001 and 2006, respectively.

In 2001, he joined the Institute of Geomatics, Spain, as a Research Assistant. In 2002, he joined the Department of Signal Theory and Communications, UPC, where he worked in the field of airborne repeat-pass interferometry and airborne differential synthetic aperture radar (SAR) interferometry. From December 2002 to August 2006, he was an Assistant Professor with the Department of Telecommunications and Systems Engineering, Universitat Autònoma de Barcelona, Barcelona. In 2006, he joined the Microwaves and Radar Institute, German Aerospace Center (DLR), Weßling, Germany, where he has been the Head of the Multimodal Algorithms Group since 2009. He is the responsible and a main developer of the TanDEM-X Interferometric (TAXI) processor, an end-to-end processing chain for data acquired by the TerraSAR-X and TanDEM-X satellites, which has been used to demonstrate novel SAR acquisition modes and techniques. He is currently involved in the design and implementation of ground processor prototypes and end-to-end simulators of ESA's BIOMASS and ROSE-L missions. His research interests include high-resolution airborne/spaceborne monostatic/bistatic SAR processing, SAR interferometry, advanced interferometric acquisition modes, persistent scatterer interferometry (PSI), SAR tomography, and end-to-end SAR simulation. He has coauthored more than 60 peer-reviewed journal articles in the field.

Gerhard Krieger (Fellow, IEEE) received the Dipl.-Ing. (M.S.) and Dr.-Ing. (Ph.D.) (Hons.) degrees in electrical and communication engineering from the Technical University of Munich, Munich, Germany, in 1992 and 1999, respectively.

From 1992 to 1999, he was with Ludwig Maximilian University, Munich, where he conducted multidisciplinary research on neuronal modeling and nonlinear information processing in biological and technical vision systems. Since 1999, he has been with the Microwaves and Radar Institute, German Aerospace Center (DLR), Weßling, Germany, where he started as a Research Associate developing signal processing algorithms for a novel forward-looking radar system employing digital beamforming on receive. From 2001 to 2007, he led the New Synthetic Aperture Radar (SAR) Missions Group, which pioneered the development of advanced bistatic and multistatic radar systems, such as TanDEM-X, as well as innovative multichannel SAR techniques and algorithms for high-resolution wide-swath SAR imaging. Since 2008, he has been the Head of the Radar Concepts Department, DLR, which currently hosts about 50 scientists focusing on new SAR techniques, missions, and applications. He has been serving as a Mission Engineer for TanDEM-X and he also made major contributions to the development of the Tandem-L mission concept, where he led the Phase-0 and Phase-A studies. Since 2019, he has also been holding a professorship at Friedrich-Alexander-University Erlangen, Germany. He has authored or coauthored more than 100 peer-reviewed journal articles, nine invited book chapters, and about 500 conference papers, and holds more than 20 patents.

Prof. Krieger received several national and international awards, including two best paper awards at the European Conference on SAR, two transactions prize paper awards of the IEEE Geoscience and Remote Sensing Society, and the W.R.G. Baker Prize Paper Award from the IEEE Board of Directors. He has been an Associate Editor of IEEE TRANSACTIONS ON GEOSCIENCE AND REMOTE SENSING since 2012. He served as the Technical Program Chair for the European Conference on SAR and a Guest Editor for IEEE JOURNAL OF SELECTED TOPICS IN APPLIED EARTH OBSERVATIONS AND REMOTE SENSING in 2014.

Georg Fischer received the M.Sc. degree in geography from the Ludwig Maximilians University of Munich, Munich, Germany, in 2012, and the Ph.D. degree in environmental engineering from ETH Zurich, Zurich, Switzerland, in 2019.

From 2012 to 2013, he conducted a traineeship at the Mission Science Division, Directorate of Earth Observation Programmes, ESA, Noordwijk, The Netherlands. In 2013, he joined the Polarimetric Synthetic Aperture Radar (SAR) Interferometry Research Group, Radar Concepts Department, Microwaves and Radar Institute, German Aerospace Center (DLR), Weßling, Germany. His research interests include the characterization and modeling of polarimetric, interferometric, and tomographic SAR measurements from snow and ice and the development of methods for the estimation of geophysical properties of glaciers and ice sheets from polarimetric and interferometric SAR data.

IGARSS 2023 - 2023 IEEE International Geoscience and Remote Sensing Symposium | 979-8-3503-2010-7/23/$31.00 ©2023 IEEE | DOI: 10.1109/IGARSS52108.2023.10282149

ON THE DECORRELATION EFFECT OF DRY SNOW IN DIFFERENTIAL SAR INTERFEROMETRY

Andreas Benedikter, Marc Rodriguez-Cassola, Pau Prats-Iraola, Kristina Belinska, Gerhard Krieger

Microwaves and Radar Institute, German Aerospace Center (DLR)

ABSTRACT

Plenty of data records demonstrate that differential InSAR acquisitions of snow covered areas are often affected by severe temporal decorrelation, complicating the estimation of snow physical parameters such as the snow water equivalent. The decorrelation effect is commonly attributed to a change in the underlying scattering center distribution due to melting/refreezing, compacting of snow, or redistribution of underlying vegetation. We demonstrate that a mere change of the dielectric constant of a dry snow cover may lead to severe decorrelation, even without a change in scatterer distribution, which provides additional opportunities for the estimation of snow parameters. In this paper, a first discussion of the snow-induced decorrelation effect is provided and the derived model is evaluated against Sentinel-1 12-day coherence data using SWE measurements provided by the Copernicus Global Land Service.

***Index Terms*—** D-InSAR, SAR interferometry, snow, decorrelation, snow water equivalent

1. INTRODUCTION

The potential of differential SAR interferometry (D-InSAR) to measure snow parameters –in particular, the snow water equivalent (SWE)– has been demonstrated in several studies [1–3]. The concept relies on the penetration capability through snow at microwave frequencies and an almost linear dependence of the D-InSAR phase to a change in snow height and density between the repeat acquisitions. It has been stated in several experiments that temporal decorralation is the main limiting factor in D-InSAR SWE retrieval [1–3]. The decorrelation increases significantly for higher frequencies and longer temporal baselines. Several studies show a fairly good conservation of coherence at L band [3]. At C band and X band, severe decorrelation has been reported, especially for the 12 and 11 day repeat cycle of Sentinel-1 and TanDEM-X, respectively. The decorrelation effect is commonly attributed to a change in the underlying scattering center distribution due to melting/refreezing, snow accumulation, or redistribution of underlying vegetation [1, 2]. Let us assume dry snow conditions during the D-InSAR time interval caused by cold temperatures, where the backscatter contribution from the snow surface and volume can be expected to be much less than the backscatter from the underlying ground (e.g., rock, soil, ice, vegetation), the decorrelation explanation connected to a change in scatterer distribution feels somewhat counter-intuitive, since: i) no melting and refreezing should happen, ii) snow accumulation should not significantly contribute to the backscatter, and iii) the ground scatterer distribution (e.g., vegetation) is rather experiencing a conservation than a redistribution, compared to the snow-free case. Still, strong decorrelation is omnipresent in snow-covered areas at low temperatures.

In this paper, we provide an alternative explanation that does not require a scatterer redistribution. We show that a mere change of the snow permittivity may result in a decorrelation, due to a change of the vertical wavenumbers of the radar waves in the snow. A similar effect has been observed in [4] for the soil moisture case.

2. DECORRELATION EFFECT OF DRY SNOW

When penetrating the snow surface, the higher relative permittivity of snow, $\varepsilon_{\mathrm{r,s}}$, compared to air results in a reduced propagation velocity of the radar signals within the snow pack and, consequently, in refraction at the air-snow interface. Following [1], the additional phase delay introduced by the snow cover can be written as

$$\Delta\Phi_{\mathrm{s}} = \frac{4\cdot\pi}{\lambda_0}\cdot Z_{\mathrm{s}}\cdot\left(\sqrt{\varepsilon_{\mathrm{r,s}}(\rho_{\mathrm{s}})-\sin^2\theta_i}-\cos\theta_i\right), \quad (1)$$

where λ_0 is the wavelength, Z_{s} is the snow height, $\varepsilon_{\mathrm{r,s}}(\rho_{\mathrm{s}})$ is the density dependent relative permittivity of the snow pack, and θ_i is the incident angle. The relative permittivity of dry snow is mainly a function of the snow density and can be computed as $\varepsilon_{\mathrm{r,s}}(\rho_{\mathrm{s}}) = 1 + 1.5995\cdot\left(\rho_{\mathrm{s}}\cdot\mathrm{cm}^3\,\mathrm{g}^{-1}\right) + 1.861\cdot\left(\rho_{\mathrm{s}}\cdot\mathrm{cm}^3\,\mathrm{g}^{-1}\right)^3$ [2], where ρ_{s} is the snow density in $\mathrm{g\,cm}^{-3}$. The density of dry snow typically ranges from $0.1\,\mathrm{g\,cm}^{-3}$ for freshly fallen snow to $0.4\,\mathrm{g\,cm}^{-3}$ for heavily wind compacted snow, resulting in a relative permittivity from 1.16 to 1.76, respectively. The density of the snow pack commonly increases within days due to self-compaction, additional snow accumulation, or wind-induced compaction. Considering orbital repeat cycles of more than 10 days, it is very likely that the radar

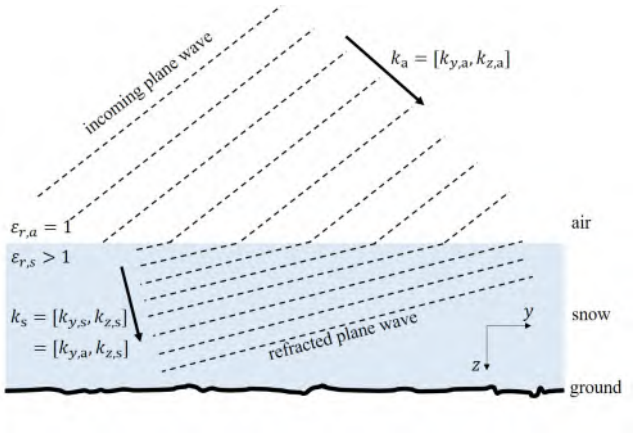

Fig. 1: Plane wave impinging on a smooth snow layer and refracting into the snow volume. Note that only the vertical wavenumber changes when propagating into the snow.

signals of the different SAR acquisitions of the D-InSAR pair will penetrate a snow volume with slightly different permittivity.

From the across-track interferometry case (non-zero baseline) it is well known that a change in the horizontal or vertical wavenumber of the SAR acquisitions with which the ground reflectivity is sampled results in decorrelation of the interferogram [5]. For the D-InSAR case (zero baseline), we note that a change of the wavenumber results from the snow cover above the ground. When observing a plane wave impinging on an air/snow interface, as illustrated in Fig. 1, it is insightful to describe the wave propagation in the wavenumber domain in a decomposed form with a horizontal component, k_y, parallel to the interface and a vertical component, k_z, perpendicular to the interface. According to [5], the wavenumbers in air can be written as $k_{y,\mathrm{a}} = \frac{2\cdot\pi}{\lambda_0}\sin\theta_i$ and $k_{z,\mathrm{a}} = \frac{2\cdot\pi}{\lambda_0}\cos\theta_i$, where θ_i is the incident angle at the air/snow interface. From electromagnetic field theory we know that the horizontal boundary conditions have to be satisfied at the dielectric interface, i.e.,

$$k_{y,\mathrm{a}} = k_{y,\mathrm{s}}, \tag{2}$$

where the indices a and s represent air and snow, respectively. Furthermore, we note that the wave equations must hold in both the air and snow volume (assuming non-magnetic media):

$$k_{y,\mathrm{a}}^2 + k_{z,\mathrm{a}}^2 = \omega^2 \cdot \varepsilon_0 \cdot \mu_0, \tag{3}$$

$$k_{y,\mathrm{s}}^2 + k_{z,\mathrm{s}}^2 = \omega^2 \cdot \varepsilon_{\mathrm{r,s}} \cdot \varepsilon_0 \cdot \mu_0, \tag{4}$$

where ω is the angular frequency and ε_0 and μ_0 are the electric and magnetic constants, respectively. Since the imaginary part of the permittivity of dry snow is negligible at microwave frequencies, (4) can be assumed real valued. From (2), (4) and the expression given in [5] for the horizontal wavenumber, the

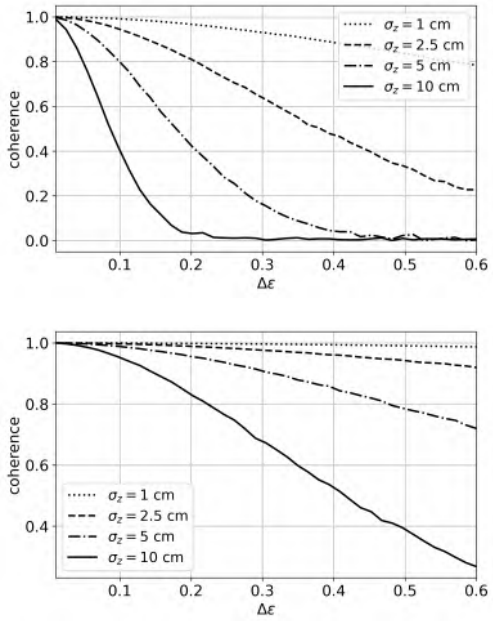

Fig. 2: Simulation of the snow-induced decorrelation effect caused by a change in the permittivity of the snow for different values of relative permittivity difference, $\Delta\varepsilon$, and ground surface roughness σ_z. (Top) C band and (bottom) L band.

vertical wavenumber in the snow can be derived as:

$$\begin{aligned} k_{z,\mathrm{s}} &= \sqrt{\omega^2 \cdot \varepsilon_{\mathrm{r,s}} \cdot \varepsilon_0 \cdot \mu_0 - k_{y,\mathrm{a}}^2} \\ &= \frac{2\cdot\pi}{\lambda_0} \cdot \sqrt{\varepsilon_{\mathrm{r,s}} - \sin^2(\theta_i)}. \end{aligned} \tag{5}$$

We can summarize that the horizontal wavenumber is not affected by the snow. However, the vertical wavenumber is altered by the permittivity of the snow. If the scattering centers within one resolution cell are distributed only horizontally, a change in snow permittivity between the two acquisitions of the D-InSAR pair is not causing decorrelation. However, if the scattering centers are also distributed vertically –even just slightly– a change in snow permittivity results in decorrelation. For a vertical backscatter density distribution $f(z)$, if we consider the two images being acquired at two different snow permittivity states, $\varepsilon_{\mathrm{r,s},1}$ and $\varepsilon_{\mathrm{r,s},2}$, the complex coherence can be written as

$$\gamma(\varepsilon_{\mathrm{r,s},1}, \varepsilon_{\mathrm{r,s},2}) = \frac{\int_0^\infty f(z) \cdot e^{\mathrm{j}2z(k_{z,\mathrm{s},2} - k_{z,\mathrm{s},1})}\mathrm{d}z}{\int_0^\infty f(z)\mathrm{d}z}. \tag{6}$$

In the following, two scattering scenarios are investigated. In the first one, a rough surface underneath the snow cover is assumed where the vertical distribution of the scattering centers is given by a zero-mean normal distribution with a standard deviation (root-mean-square error), σ_z. We have quantified the decorrelation by means of a Monte Carlo simulation. In each iteration, two SAR signals have been simulated

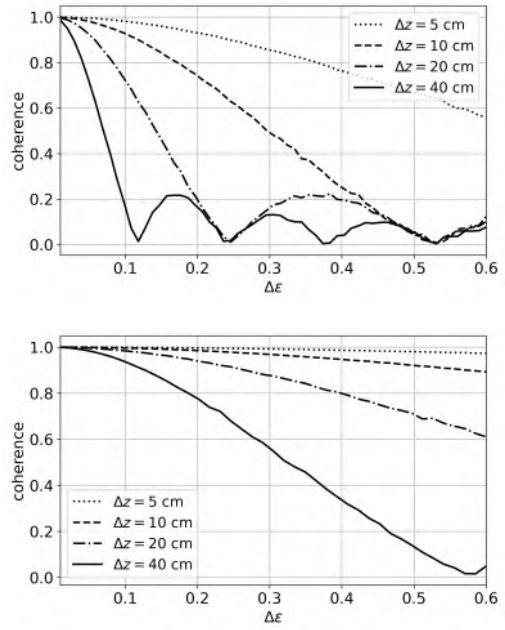

Fig. 3: Simulation of the snow-induced decorrelation effect caused by a change in the permittivity of the snow for different values of relative permittivity difference, $\Delta\varepsilon$, and vertical scattering volume extension Δz underneath the snow cover. (Top) C band and (bottom) L band.

for one realization of scattering center distribution but different relative permittivities, according to the phase delay in (1). In all cases, a zero-baseline scenario has been considered. The mean coherence is then computed over all Monte Carlo iterations. Fig. 2 shows the resulting coherence for different relative permittivity changes, $\Delta\varepsilon$, and different σ_z, where the relative permittivity of the first SAR acquisition is assumed to be 1.2. For the top plot in Fig. 2, a C-band frequency of $5.4\,\mathrm{GHz}$ (Sentinel-1) is used and for the bottom plot an L-band frequency of $1.25\,\mathrm{GHz}$ (NISAR). The decorrelation increases for larger permittivity differences until the coherence drops to zero, i.e, a complete decorrelation of the acquisitions. Also, the decorrelation increases for higher surface roughness, which is in line with the analogy to volume decorrelation in across-track InSAR. The decorrelation is significantly lower in L band. Note that the depth of the snow layer has no influence on the decorrelation.

In a second scattering scenario, a uniform vertical scattering center distribution with a certain vertical extent, Δz, is assumed to be located underneath the snow layer, representing an idealized case of vertically limited volume scattering, e.g., resulting from a vegetation layer. The resulting coherence is shown in Fig. 3 for C and L bands in the upper and lower panel, respectively. Four different uniform volume heights, Δz, are simulated. In contrast to the rough surface scenario, a sinc-like pattern results when evaluating increasing permittivity differences. The sinc-pattern is the Fourier pair to the vertically limited uniform distribution, which results as a consequence of the Fourier transform characteristic of the coherence model in (6). Also here, the analogy to the across-track InSAR case may be drawn, where an increasing permittivity difference corresponds to a larger vertical wavenumber difference (i.e., a larger baseline).

3. SENTINEL-1 DATA ANALYSIS

A validation of the above outlined effect on real D-InSAR data is rather complex since it requires accompanying snow density measurements as well as estimates of the backscatter behavior. Dedicated airborne campaigns or laboratory measurements need to be conducted for the validation of the model. For now, we try to identify evidence for the snow-induced decorrelation in a global Sentinel-1 coherence data set. For a large area in northeast Asia, we use the median 12-day coherence over three months (December, January, February) in Winter 2019/2020 from the global Sentinal-1 coherence data set generated by Kellndorfer et al. [6] with a 3 arcsecond resolution and compare it to an estimate of the median 12-day SWE change ($\Delta\mathrm{SWE}$) in the same time period derived from the *SWE-NH-5km*[1] data of the *Copernicus Global Land Services* based on microwave radiometer measurements. The data are mapped to the same grid and filtered for $\Delta\mathrm{SWE}$ values greater than $4\,\mathrm{mm}$ to ensure that only snow-covered areas are analyzed. The respective maps are shown in Fig. 4. The area under analysis has been chosen because of a high consistency of the *SWE-NH-5km* data in the considered time period. Note that no SWE is mapped over mountains or ice sheets nor in wet snow conditions. Note also that a change in SWE is caused either by a change in snow height, snow density (i.e., permittivity), or both. Snow accumulation commonly results in a snow density change, due to the different properties of freshly fallen and settled snow and the compacting of the older snow layer by the pressure of the new snow layer. Therefore, we assume that in most cases a change in SWE indicates a slight density, i.e., permittivity, change.

Fig. 5 shows the normalized (for each $\Delta\mathrm{SWE}$ bin) 2-D histogram. Coherence values between 0 and 0.75 are visible and a clear correlation between the coherence and the $\Delta\mathrm{SWE}$ can be observed. The coherence falls drastically for increasing $\Delta\mathrm{SWE}$. When looking closely, one can distinguish two patterns in the histogram. One that falls over almost the whole $\Delta\mathrm{SWE}$ extent of the histogram from a coherence value of roughly 0.7 to 0. Besides, in the $\Delta\mathrm{SWE}$ intervals $[12\,\mathrm{mm}, 21\,\mathrm{mm}]$ and $[21\,\mathrm{mm}, 28\,\mathrm{mm}]$ two side lobes of what might be interpreted as a sinc-pattern are visible, where the

[1]The product was generated by the land service of Copernicus, the Earth Observation program of the European Commission. The research leading to the current version of the product has received funding from various European Commission Research and Technical Development programs. The product is based on SWE-NH-5km data ((c) ESA and distributed by FMI).

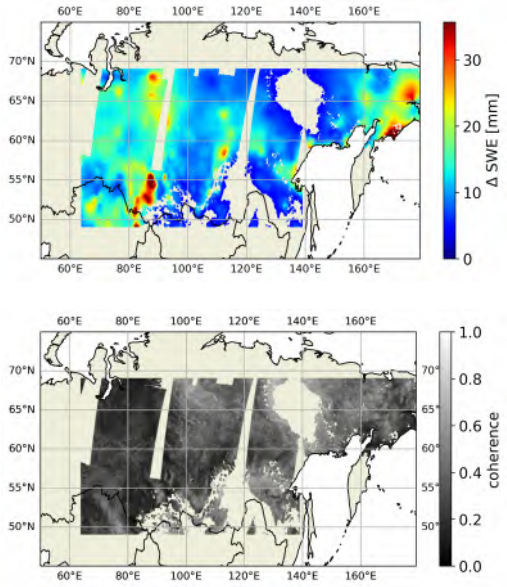

Fig. 4: Maps of median values of ΔSWE (top) and Sentinel-1 12-day coherence (bottom) for a large area in northeast Asia.

main lobe coincides with the first pattern. The two patterns may be attributed to similar scattering scenarios as discussed in the previous section, a rough surface and a volume-like scattering distribution underneath the snow cover. However, no data are available at the moment to proof this assumption and other temporal decorrelation effects, such as temporal changes of the backscatter distribution, might be present in these data. For all these reasons, an inversion of the snow parameters is not attempted in this contribution. Still, the clear correlation between the InSAR coherence and the ΔSWE, together with the similarity of the histogram and the decorrelation patterns shown in Section 2, support that the dry snow decorrelation effect might be a relevant, if not the dominating one.

4. CONCLUSION

We have shown that a permittivity change of a snow layer may result in severe decorrelation of a D-InSAR acquisition if the scattering centers within a resolution cell are not only distributed horizontally, but also vertically, even if just slightly. The decorrelation increases for higher frequencies, a larger change in permittivity, and a larger vertical extent of the backscatter distribution within one resolution cell. We have also shown that this model of snow-induced decorrelation might be compatible with the wide-area analysis of Sentinel-1 12-day coherence data. Further validation with dedicated campaigns might be helpful and will be subject of a future work. The identified correlation between coherence and ΔSWE may allow to exploit the decorrelation effect to invert snow parameters. Furthermore, the described dependence of the vertical wavenumber to the permittivity may be used to generate tomographic information from multiple zero-baseline acquisitions, similar to the virtual bandwidth concept introduced for the soil moisture case in [7].

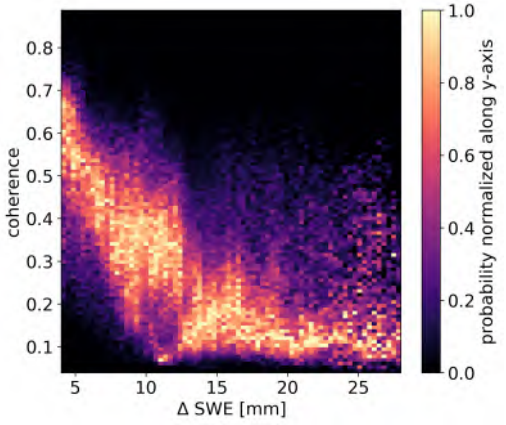

Fig. 5: 2-D histogram relating the maps in Fig. 4, normalized for each ΔSWE bin. Note that the form of the histogram is similar to the patterns shown in the analysis of Section 2.

5. REFERENCES

[1] T. Guneriussen, K.A. Hogda, H. Johnsen, and I. Lauknes, "InSAR for estimation of changes in snow water equivalent of dry snow," *IEEE TGRS*, vol. 39, no. 10, pp. 2101–2108, 2001.

[2] Silvan Leinss, Andreas Wiesmann, Juha Lemmetyinen, and Irena Hajnsek, "Snow water equivalent of dry snow measured by differential interferometry," *IEEE JSTARS*, vol. 8, no. 8, pp. 3773–3790, 2015.

[3] Kristina Belinska, Georg Fischer, and Irena Hajnsek, "Differential SAR interferometry and co-polar phase differences for snow water equivalent estimation," in *EUSAR 2022*, 2022, pp. 1–4.

[4] Francesco De Zan, Alessandro Parizzi, Pau Prats-Iraola, and Paco López-Dekker, "A SAR interferometric model for soil moisture," *IEEE TGRS*, vol. 52, no. 1, pp. 418–425, 2014.

[5] F. Gatelli, A. Monti Guarnieri, F. Parizzi, P. Pasquali, C. Prati, and F. Rocca, "The wavenumber shift in SAR interferometry," *IEEE TGRS*, vol. 32, no. 4, pp. 855–865, 1994.

[6] Josef Kellndorfer et al., "Global seasonal Sentinel-1 interferometric coherence and backscatter data set," *Scientific Data*, vol. 9, no. 1, pp. 73, Mar 2022.

[7] Keith Morrison and John Bennett, "Virtual-bandwidth SAR (VB-SAR) for sub-surface imaging," in *EUSAR 2014*, 2014, pp. 1–4.

Toward Dry Snow Parameter Estimation by Simultaneous Multiple Squint Differential InSAR

Andreas Benedikter, *Member, IEEE*, Kristina Belinska, Marc Rodriguez-Cassola, Pau Prats-Iraola, *Fellow, IEEE*, Georg Fischer, Gerhard Krieger, *Fellow, IEEE*, and Irena Hajnsek, *Fellow, IEEE*

***Abstract*— Spaceborne differential SAR interferometry (D-InSAR) has been demonstrated to potentially allow snow water equivalent (SWE) change measurements for dry snow on a spatial scale, resolution, and accuracy unprecedented by other sensor concepts. However, its operational use is hindered mainly because of: 1) low coherence areas resulting from temporal decorrelation, complicating a robust phase unwrapping and 2) an unknown phase offset due to the 2π ambiguity of the interferometric measurement and therefore a strongly biased SWE change estimate. Furthermore, conventional D-InSAR does not provide a direct measurement of the snow density, which is used in the phase-to-SWE inversion and is an important snow parameter. This article presents strategies to potentially overcome these shortcomings by exploiting simultaneously acquired interferograms with different squint angles. The different lines of sight result in differential phase delays introduced by a SWE change. The phase difference between the interferograms may be exploited to produce a low-resolution SWE estimate without the need for phase unwrapping and to resolve the 2π phase ambiguity of the single interferogram. In addition to that, the ratio between the interferograms is a measure of the dielectric permittivity of the snow and can be related to the snow density. The theoretical performance and functionality of the strategies are analyzed for the planned Harmony mission (ESA's Earth Explorer 10) based on simulated data, indicating great potential of the approach given the large squint diversity of the Harmony constellation.**

***Index Terms*— Differential SAR interferometry (D-InSAR), multiple squint, SAR interferometry, snow, snow water equivalent (SWE).**

I. Introduction

SNOW water equivalent (SWE) is defined as the depth of water which would result if all the ice contained in the snow volume were melted

$$\mathrm{SWE} = \int_0^{Z_s} \rho_s(z)dz \tag{1}$$

where Z_s is the snow depth, z the vertical coordinate, and $\rho_s(z)$ the depth-dependent snow density (defined dimensionless as the ratio of the gravimetric densities of snow and water). SWE is an important hydrological parameter used in water resources, glacier mass balance, and climate change impact. Spaceborne remote sensing of SWE allows a large coverage and potentially fast revisit time. Compared to operationally used passive microwave and gamma radiation sensors with resolutions on the kilometer scale [1], [2], [3], the potential of differential SAR interferometry (D-InSAR) to measure SWE for dry snow with a large coverage, a spatial resolution in the order of tens of meters, and a millimeter accuracy has been demonstrated in several studies [4], [5], [6], [7], [8], [9], [10], [11], [12], [13], [14], [15], [16], [17], [18], [19], [20], [21]. The concept relies on the transparency of dry snow at microwave frequencies and a linear dependence of the D-InSAR phase to the change in snow height between the repeat acquisitions of the D-InSAR pair that can be connected via (1) to the SWE change, ΔSWE. The total SWE of the snow cover needs to be inferred by accumulation of ΔSWE maps. Despite being demonstrated over 20 years ago by Guneriussen et al. [4], D-InSAR SWE monitoring is not applied operationally, mainly because of the following limiting factors.

1) Low temporal coherence areas limit the accuracy of the phase measurement and may significantly complicate the phase-unwrapping process that is commonly necessary for the spatial snow height dynamic in typical snow covers [5], [7], down to a point at which no robust SWE retrieval is possible.
2) A reference point with known ΔSWE is required in the scene to estimate the absolute phase (hence, the absolute ΔSWE). This is necessary because the D-InSAR phase may carry an unknown offset if the phase delay introduced by the propagation through snow surpasses 2π, resulting only in a relative ΔSWE estimate.

Furthermore, conventional D-InSAR does not provide a direct measurement of the snow density and permittivity, which are used in the phase-to-SWE inversion and are important snow parameters.

To overcome the need for phase unwrapping in low-coherence areas and to resolve the phase offset problem, delta-k methods have been suggested [6], [7], which are based on the comparison of the D-InSAR phase between two radar carrier frequency sub-bands. However, these approaches

Received 21 June 2024; revised 2 August 2024; accepted 19 August 2024. Date of publication 25 October 2024; date of current version 5 December 2024. This work was supported in part by European Space Agency under Contract 4000135083/21/NL/FF/ab. *(Corresponding author: Andreas Benedikter.)*

The authors are with the Microwaves and Radar Institute, German Aerospace Center (DLR), 82234 Weßling, Germany (e-mail: andreas.benedikter@dlr.de).

Digital Object Identifier 10.1109/TGRS.2024.3486328

are limited by the bandwidth of current SAR sensors. In [13], an approach is suggested that exploits the sensitivity of the snow-induced phase to the topographic slope by correlating the D-InSAR phase with DEM-derived phase sensitivity maps. The approach performs well in mountainous areas with a significant variability of terrain slopes within the estimation window, but does not provide sensitivity over flat terrain. Varade et al. [12] and Belinska et al. [16], [17] propose to exploit polarimetric information of polarimetric SAR data resulting from the commonly anisotropic dielectric properties of the snow volume to recover the potential phase offset.

In this article, we propose a novel approach for estimating the absolute ΔSWE by exploiting the differential phase sensitivity from two or more interferograms with different squint angles. The difference phase (i.e., the difference between the two interferograms) may be directly used to obtain a low-resolution ΔSWE map in low-coherence areas which do not allow a consistent phase unwrapping, or to estimate the bulk phase offset in areas with sufficient coherence for phase unwrapping, allowing a measurement of the absolute ΔSWE at the resolution and accuracy of the interferogram. A comparable approach has been suggested in [22] for measuring the absolute troposphere change. Furthermore, the ratio of two interferograms with different squint angles is a direct measure of the real part of the dielectric permittivity of the snow and can be linked to the snow density, which is not only an important input for the D-InSAR SWE mapping, but also for other sensor concepts and modeling approaches. The planned Earth Explorer 10 mission by ESA, Harmony [23], may be a suitable candidate for the proposed approach due to the large squint diversity of the constellation and is therefore chosen as an example case to analyze the potential performance and the functionality of the approach.

The article is structured as follows. Section II provides insight into the characteristics of the D-InSAR SWE measurement. Section III discusses the developed approaches for absolute ΔSWE and density retrieval exploiting multiple squints and Section IV shows results of the approaches applied on simulated Sentinel-1 and Harmony acquisitions. After a discussion on potential limitations and error sources of the proposed methodology in Section V, the article is concluded in Section VI.

II. D-InSAR ΔSWE Measurement

A. Snow Model Assumptions

The key assumption behind D-InSAR SWE retrieval is that the snow cover is almost transparent at the sensing frequency [4], [5], [6], [7], resulting in the fact that the backscatter contribution from the snow surface and volume can be expected to be much less than the backscatter from the underlying ground (i.e., rock, soil, firn, ice, and vegetation). Such conditions are commonly only met at dry snow conditions (i.e., at temperatures consistently well below 0 °C). Liquid water content at higher temperatures results in a strong absorption within the snow volume. The snow cover should be dry throughout the temporal baseline that separates the SAR acquisitions of the D-InSAR pair to avoid a change in the scattering distribution caused by, e.g., melt and refreeze events. Throughout this article, dry snow conditions are considered and the developed methodologies are expected to be applicable only under dry snow conditions, in line with D-InSAR-based SWE retrieval literature [4], [5], [6], [7], [8], [9], [10], [11], [12], [13], [14], [15], [16], [17], [18], [19], [20], [21]. The snow cover is modeled with a constant density (i.e., a mean density) in the vertical dimension, for which the formulation of the SWE in (1) reduces to

$$\mathrm{SWE} = \rho_s \cdot Z_s. \tag{2}$$

This approximation has been shown in [7] to be suitable also for stratified snow covers. Following [7], the relative permittivity of the dry snow cover can be computed as

$$\varepsilon_s(\rho_{s,\mathrm{abs.}}) = 1 + 1.5995 \cdot \rho_{s,\mathrm{abs.}} + 1.861 \cdot \rho_{s,\mathrm{abs.}}^3 \tag{3}$$

where $\rho_{s,\mathrm{abs.}}$ is the absolute, i.e., not normalized, snow density in g cm^{-3}. Note that throughout the article, we use the dimensionless density expression ρ_s from (1) that is normalized by the density of water. We consider density values of all kinds of dry snow conditions, ranging from calmly fallen fresh snow to wind slabs, i.e., a normalized density from roughly 0.1 to 0.4.

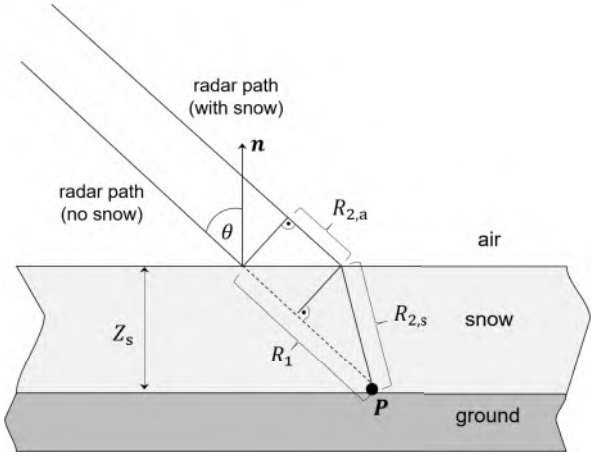

Fig. 1. Geometry of the refraction effect in snow. The solid line ($R_{2,a}+R_{2,s}$) is the signal propagation path through snow and the dashed line (R_1) is the corresponding free space path. The optical path length difference is $R_{2,a} + \sqrt{\varepsilon_s} \cdot R_{2,s} - R_1$, where ε_s is the relative dielectric permittivity of the snow layer. Adapted from [4].

B. D-InSAR Phase Model for SWE

The higher relative dielectric permittivity of snow, ε_s, compared to air results in a reduced propagation velocity of the radar signals within the snow cover and causes refraction at the air–snow interface, as shown in Fig. 1. The phase difference to the snow free state can be related from the difference in the optical path length (illustrated in Fig. 1) according to [4] as follows:

$$\Delta\Phi_s = \frac{4 \cdot \pi}{\lambda} \cdot \left[\left(R_{2,a} + \sqrt{\varepsilon_s} \cdot R_{2,s}\right) - R_1\right] \tag{4}$$

$$= \frac{4 \cdot \pi}{\lambda} \cdot Z_s \cdot \left(\sqrt{\varepsilon_s(\rho_s) - \sin^2\theta} - \cos\theta\right) \tag{5}$$

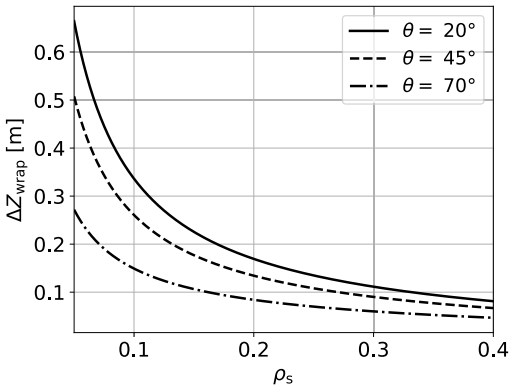

Fig. 2. Critical limit of snow height change at which the first phase wrap in the D-InSAR interferogram occurs. Shown for the Harmony/Sentinel-1 5.405 GHz center frequency, different snow densities, ρ_s, and incident angles, θ.

where λ is the wavelength, Z_s is the snow height, and θ is the incident angle. The relation in (5) is an approximation, because, in practice, the incident angles for the snow free and snow covered case differ slightly. The approximation holds for the spaceborne geometries under analysis and snow heights in the meter range. From (2) and (5), a linear relation between the phase difference and the SWE can be found

$$\Delta\Phi_s = \mathrm{SWE} \cdot \frac{4 \cdot \pi}{\lambda \cdot \rho_s} \cdot \left(\sqrt{\varepsilon_s(\rho_s) - \sin^2\theta} - \cos\theta \right). \quad (6)$$

The relation holds for the general case of D-InSAR, where the single SAR images are acquired at different snow height states (i.e., SWE states). The total SWE in (6) can be replaced with SWE change, ΔSWE, and ρ_s interpreted as the magnitude of the mean density of the snow cover. Note that throughout the article, the SWE is defined to be measured in the direction of the local slope normal vector. If instead the SWE is defined to be oriented toward the center of gravity, a cosine slope factor has to be included in (6) [13].

An unknown offset in the D-InSAR ΔSWE measurement occurs, whenever the snow height change leads to a D-InSAR phase greater than 2π. Fig. 2 shows the critical snow height change that leads to phase wrapping (ΔZ_{wrap}) for different relative snow densities ranging from calmly fallen snow to wind slabs under dry snow conditions and three incident angles. The plots are shown for the Harmony and Sentinel-1 mission center frequency of 5.405 GHz (C band). Beyond ΔZ_{wrap}, the conventional D-InSAR ΔSWE retrieval does not produce meaningful results if no reference point with known ΔSWE value is present in the scene. For most of the snow states, already a snow height change of 20 cm leads to phase wrapping. This leads to the conclusion that at C band or higher frequencies conventional D-InSAR ΔSWE mapping cannot be used for a large variety of snow accumulation events. Beyond a bulk phase offset over the scene, the spatial variability of snow height or density changes commonly results in multiple fringes over the scene [5], [7], requiring spatial phase unwrapping to recover the absolute phase.

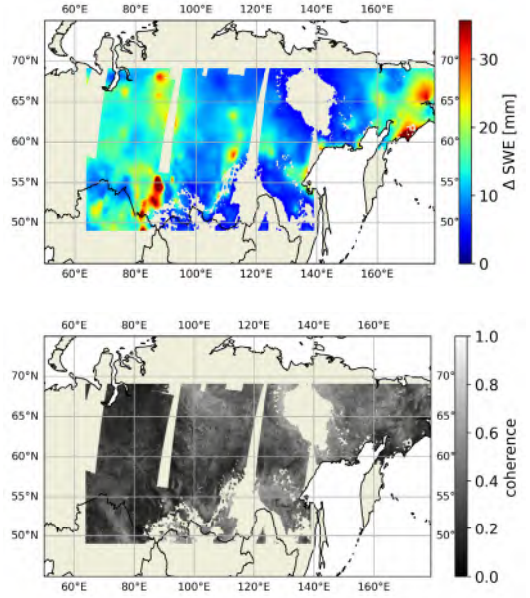

Fig. 3. Maps of median values of (top) ΔSWE and (bottom) Sentinel-1 12-day coherence for a large area in northeast Asia.

C. D-InSAR Coherence in SWE Retrieval

It has been stated in several experiments that temporal decorrelation is the main limiting factor in D-InSAR SWE retrieval, e.g., in [4], [7], [16]. Considering consistently dry snow conditions (i.e., the reference scenario outlined in Section II-A), the decorrelation may result from 1) a change in the scatterer distribution caused by wind drifts, slab releases, or a change of the scattering layer or volume underneath the snow; 2) a change in the sub-pixel scale snow height or density distribution [5]; and/or 3) a bulk change in the snow density, i.e., the permittivity [24]. The decorrelation increases significantly for higher frequencies and longer temporal baselines between the acquisitions. Several experimental studies show a relatively good conservation of coherence at L band [16]. At C band (the Harmony mission operating frequency band) and X-band, severe decorrelation has been reported, especially for the 12 and 11 day repeat cycle of Sentinel-1 and TanDEM-X, respectively. Since the bistatic Harmony constellation is bound to Sentinel-1 as transmitter, and since the approaches proposed in this article depend on the level of coherence, we present in the following a brief assessment on Sentinel-1 coherence statistics, linked to daily radiometer measurements of SWE.

For a large area in northeast Asia, we use the median 12-day coherence over 3 months (December, January, February) in Winter 2019/2020 from the global Sentinal-1 coherence dataset generated by Kellndorfer et al. [25] with a 3 arcsecond resolution and compare it to an estimate of the median 12-day ΔSWE in the same time period derived from the *SWE-NH-5* km[1] data of the *Copernicus Global Land Services* based on microwave radiometer measurements. The data are

[1]The product was generated by the land service of Copernicus, the Earth Observation program of the European Commission. The research leading to the current version of the product has received funding from various European Commission Research and Technical Development programs. The product is based on SWE-NH-5 km data (©ESA and distributed by FMI).

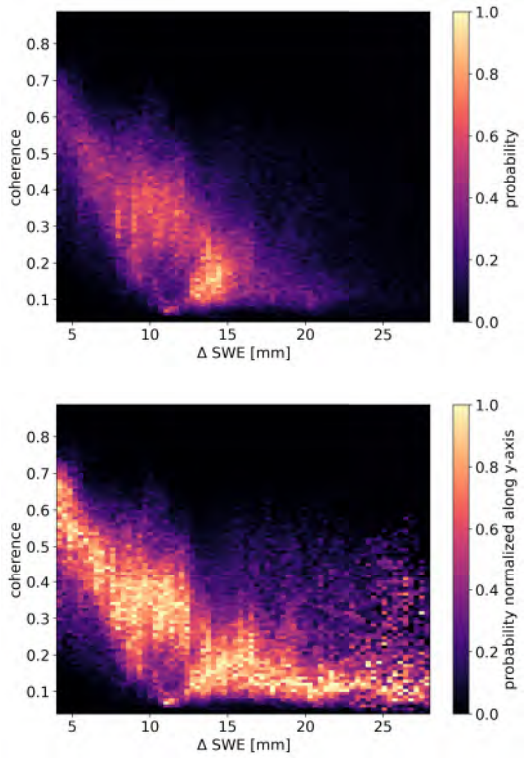

Fig. 4. (Top) 2-D histogram relating the maps in Fig. 3 and (bottom) the same histogram normalized for each ΔSWE bin.

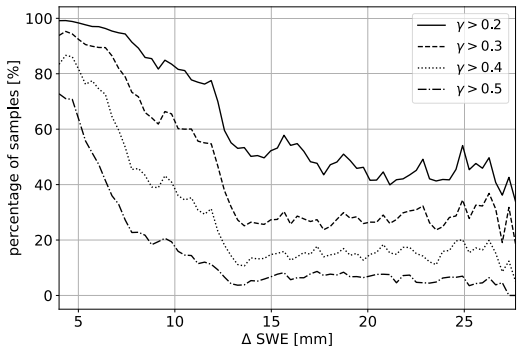

Fig. 5. Percentage of samples in the maps of Fig. 3 that are above a coherence threshold of 0.2, 0.3, 0.4, or 0.5.

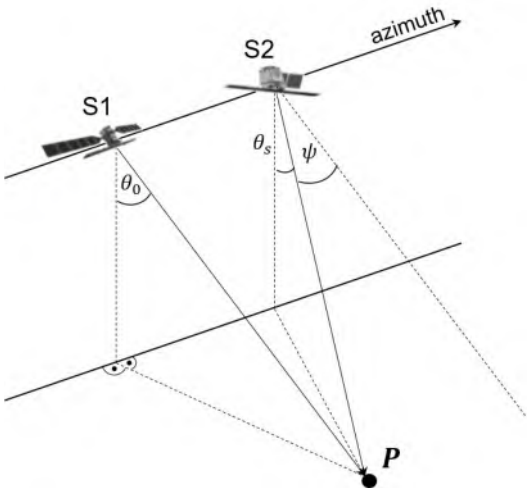

Fig. 6. Illustration of the squinted acquisition geometry (S2) compared to a zero-squint acquisition (S1).

mapped to the same grid and filtered for ΔSWE values greater than 4 mm. The respective maps are shown in Fig. 3. The area under analysis has been chosen because of a high measurement consistency of the *SWE-NH-5* km data in the considered time period, containing only few invalid measurement points. Note that no SWE is mapped over mountains or ice sheets nor in wet snow conditions. Fig. 4 shows the 2-D histogram (top panel) of the data in Fig. 3 and the normalized (for each ΔSWE bin) 2-D histogram (bottom panel). In the generation of the coherence data, large estimation windows have been used [25] to minimize the bias inherent to coherence estimation [26]. The bias over completely decorrelated areas (e.g., water bodies and layover) has been measured to be on average 0.03 [25]. The data are dominated by two main sample populations: 1) at ΔSWE ≈ 10 mm and coherence values from 0.3 to 0.4 and 2) at ΔSWE ≈ 15 mm and coherence values from 0.1 to 0.2. However, a considerable amount of samples covers a coherence range from almost 0 to 0.7 and ΔSWE values from 4 to 25 mm. The normalized histogram shows a clear tendency indicating a stronger decorrelation for larger SWE changes. Fig. 5 gives an insight into the coherence levels to expect, showing the percentage of samples above a certain coherence threshold. For example, one may expect to acquire interferograms with a coherence greater than 0.2 in roughly 50 % of cases over a variety of snow accumulation conditions.

Note that the relationship between temporal coherence and the ΔSWE of a dry snow cover is of indirect nature. However, the decorrelation effects explained at the beginning of this section are strongly correlated with SWE changes and may explain the clear correlation observable in Fig. 4. The presented statistics are not aimed on providing a conclusive analysis on the range of expectable coherence and ΔSWE values, but on demonstrating that in a considerable amount of cases and over wide areas, snow accumulation does not result in a complete decorrelation of Sentinel-1 12-day interferograms.

III. Exploiting the Squint Diversity

The phase contribution due to the signal propagation through snow depends on the local incident angle [see (6)], which, for the same target, varies along the azimuth coordinate, i.e., it varies for different squint angles. However, the net effect on the focused image phase is well approximated by considering only the Doppler centroid incident angle at the target [13]. Hence, for a squinted acquisition, the net phase corresponds to an incident angle that is larger than the boresight incident angle. Fig. 6 illustrates the concept for a zero-squint acquisition (S1) and an acquisition with a squint angle $|\psi| > 0$ (S2). Assuming a flat Earth geometry and a straight and horizontal radar track, the incident angle for the squinted acquisition can be written as

$$\theta_s = \cos^{-1}(\cos\theta_0 \cdot \cos\psi). \tag{7}$$

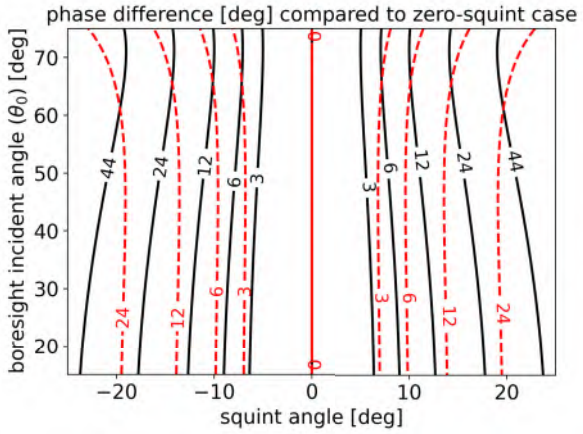

Fig. 7. Snow-induced phase difference of a squinted D-InSAR acquisition (S2) compared to the zero-squint case (S1). Values are shown for the 5.405 GHz center frequency, a ΔSWE of 3.5 cm, and two density values: $\rho_s = 0.1$ (solid, black) and $\rho_s = 0.4$ (dashed, red).

θ_s may then be inserted in (6) to describe the ΔSWE D-InSAR phase. The approaches outlined in this article are based on the different phase contributions of the snow for different squint angles. For the flat Earth geometry in Fig. 6, the difference in the D-InSAR phase between a squinted acquisition and a zero-squint acquisition is shown in Fig. 7. The 5.405 GHz frequency is used and a ΔSWE of 3.5 cm is assumed. The solid (black) contours correspond to a relative snow density of 0.1 and the dashed (red) contours to 0.4. The phase difference increases for larger squint angle differences, and hence, also the sensitivity of the differential D-InSAR phase to the ΔSWE increases. Note that the sensitivity relies on the squint magnitude diversity only. Positive and negative squints with the same magnitudes introduce equal phase signatures. The influence of the boresight incident angle θ_0 depends on the snow density, as the density not only relates the ΔSWE to the snow height, but also determines the permittivity [see (2) and (6)]. Due to the small snow height compared to the satellite altitude, it can be assumed that even for large squint angle differences, the ΔSWE seen by two simultaneous D-InSAR acquisitions will be largely correlated. In Sections III-A–III-C, three approaches for exploiting simultaneously acquired interferograms with different squint angles are analyzed for low to moderate coherence scenarios. The analyses are based on a setting with two simultaneous monostatic D-InSAR acquisitions (S1 and S2), one acquired with zero squint and the other with a squint greater than zero, as shown in Fig. 6. Further conclusions are drawn for the Harmony case, where one of the interferograms is acquired in a bistatic manner, resulting in a combination of propagation paths through the snow volume of both squint geometries, hence, leading to half the sensitivity compared to the values shown in Fig. 7 for two monostatic acquisitions. The explicit ΔSWE retrieval formula for the bistatic Harmony case is later described in (22) in Section IV.

Harmony is an upcoming ESA mission that has been selected as the tenth Earth Explorer. It consists of two companion satellites to Sentinel-1 as bistatic receivers (see Fig. 8)

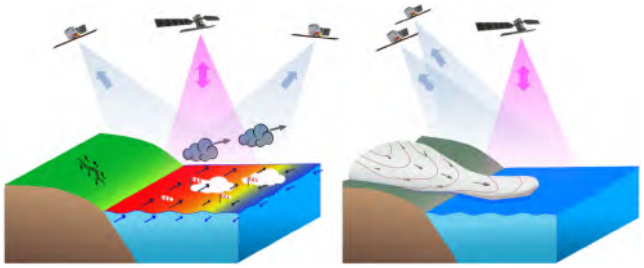

Fig. 8. Illustration taken from [27] showing the Harmony constellation in the (left) StereoSAR configuration and (right) XTI formation.

that image the same scene as Sentinel-1. The constellation is operated either in the so-called StereoSAR configuration with the two Harmony satellites flying ∼350 km in front and behind Sentinel-1, or in the so-called XTI configuration with the two Harmony satellites forming an across-track interferometer while flying ∼350 km behind Sentinel-1. In both configurations, there is a squint diversity between the Harmony satellites and Sentinel-1 of ∼22° (i.e., ∼11° effective squint due to the bistatic operation of the Harmony satellites). This large squint diversity makes the Harmony mission a suitable candidate to implement the approaches described in the following.

A. Low-Resolution ΔSWE Estimation for Low-Coherence Scenarios

ΔSWE mapping using D-InSAR commonly requires phase unwrapping to recover the spatial variation of the SWE and a reference point in the scene with known ΔSWE to recover the bulk phase offset over the scene. However, in low-coherence scenarios, it may be not feasible to perform robust phase unwrapping. In such cases, the difference phase, $\Delta\Delta\Phi_s$, between the two interferograms acquired with different squints may be exploited since it has a significantly reduced sensitivity to the ΔSWE compared to the single interferograms. Therefore, $\Delta\Delta\Phi_s$ stays within a single 2π interval for a large range of ΔSWE values. The D-InSAR phases of the two acquisitions can be written as

$$\begin{aligned}\Delta\Phi_{s,1} &= \Delta\text{SWE} \cdot \frac{4\cdot\pi}{\lambda\cdot\rho_s} \cdot \left(\sqrt{\varepsilon_s(\rho_s) - \sin^2\theta_1} - \cos\theta_1\right) \\ &= \Delta\text{SWE} \cdot \frac{4\cdot\pi}{\lambda\cdot\rho_s} \cdot \beta_1, \end{aligned} \tag{8}$$

$$\begin{aligned}\Delta\Phi_{s,2} &= \Delta\text{SWE} \cdot \frac{4\cdot\pi}{\lambda\cdot\rho_s} \cdot \left(\sqrt{\varepsilon_s(\rho_s) - \sin^2\theta_2} - \cos\theta_2\right) \\ &= \Delta\text{SWE} \cdot \frac{4\cdot\pi}{\lambda\cdot\rho_s} \cdot \beta_2 \end{aligned} \tag{9}$$

where θ_1 and θ_2 are the local incident angles of acquisitions S1 and S2, respectively, and β_1 and β_2 are used as short-hand notations from here on for the terms in the brackets. Following, the difference phase is:

$$\Delta\Delta\Phi_s = \Delta\text{SWE} \cdot \frac{4\cdot\pi}{\lambda\cdot\rho_s} \cdot (\beta_2 - \beta_1). \tag{10}$$

Fig. 9 shows the critical ΔSWE leading to a phase wrap of $\Delta\Delta\Phi_s$ for different incident angles of acquisition S1 and squint angles of S2. The Sentinel-1 frequency of 5.405 GHz

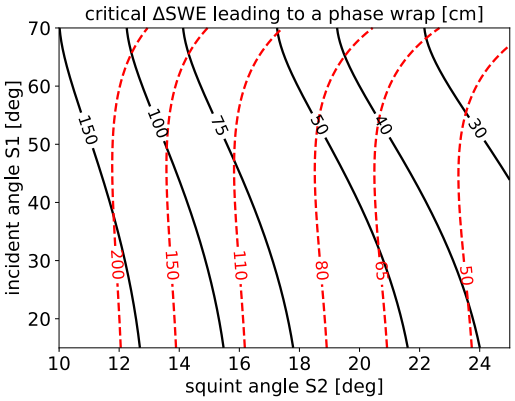

Fig. 9. Critical ΔSWE leading to a phase wrap of the difference phase $\Delta\Delta\Phi_s$. Values are shown for the 5.405 GHz center frequency and two density values: $\rho_s = 0.1$ (solid, black) and $\rho_s = 0.4$ (dashed, red).

is assumed and two density values, $\rho_s = 0.1$ (solid, black) and $\rho_s = 0.4$ (dashed, red). It requires very large ΔSWE values to produce a difference phase greater than 2π. Note that, for example, a ΔSWE of 30 cm corresponds to a snow height change of 3 m for a density of 0.1. This allows the assumption that almost all snow accumulation scenarios can be estimated unambiguously using $\Delta\Delta\Phi_s$.

The ΔSWE can be estimated from $\Delta\Delta\Phi_s$ according to

$$\Delta\text{SWE} = \frac{\lambda \cdot \rho_s}{4 \cdot \pi} \cdot \frac{\Delta\Delta\Phi_s}{\beta_2 - \beta_1} \tag{11}$$

and the standard deviation of the estimation can be written as

$$\sigma_{\Delta\text{SWE}} = \sqrt{\sigma^2_{\Delta\Phi_{s,1}} + \sigma^2_{\Delta\Phi_{s,2}}} \cdot \frac{\lambda \cdot \rho_s}{4 \cdot \pi} \cdot \frac{1}{\beta_2 - \beta_1} \tag{12}$$

where $\sigma_{\Delta\Phi_{s,i}}$ are the standard deviations of the single interferograms. Assuming the same variances for both interferograms (note that the interferograms are acquired simultaneously), the expression reduces to

$$\sigma_{\Delta\text{SWE}} = \sqrt{2} \cdot \sigma_{\Delta\Phi_s} \cdot \frac{\lambda \cdot \rho_s}{4 \cdot \pi} \cdot \frac{1}{\beta_2 - \beta_1} \tag{13}$$

where $\sigma_{\Delta\Phi_s}$ can be written in terms of the coherence, γ, and the number of samples used for multilooking (ML), N, as [28]

$$\sigma_{\Delta\Phi_s} = \frac{1}{\sqrt{2 \cdot N}} \cdot \frac{\sqrt{1 - \gamma^2}}{\gamma}. \tag{14}$$

Note that (14) is only valid for large N. From (13) and (8) or (9), one can see that the accuracy scales with the factors $\sqrt{2}$ and $(\beta_{1,2}/(\beta_2 - \beta_1))$ compared to the measurement using the single interferogram, leading to a substantial accuracy reduction. This requires significant averaging to reduce the noise. Fig. 10 shows the standard deviation of the ΔSWE estimate for a frequency of 5.405 GHz and a normalized snow density of 0.2. The top panel shows the dependence on the acquisition geometry and the bottom panel the dependence on the coherence and the size of the window used for ML (assumed quadratic). For the top panel plot, a coherence of 0.2 and a ML window size of 50 × 50 are assumed, which is roughly equivalent (in terms of number of samples) to a 500 × 500 m resolution interferogram generated from

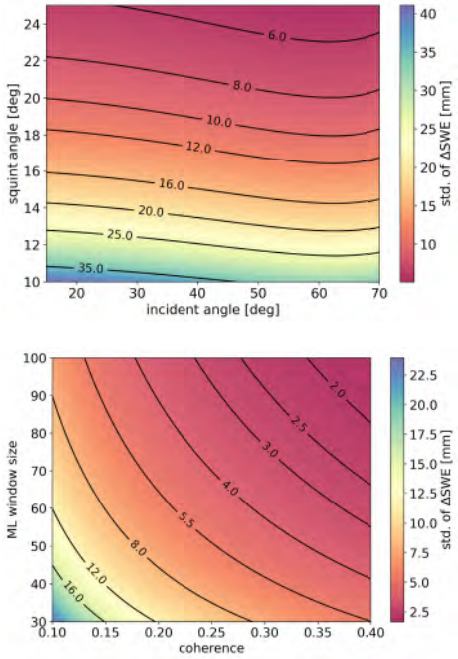

Fig. 10. Standard deviation of the ΔSWE estimate for the low-resolution estimation described in Section III-A for a frequency of 5.405 GHz and a normalized snow density of 0.2. (Top) dependence on the incident angle of acquisition S1 and the squint angle of S2 for a coherence of 0.2 and a ML window size of 50 × 50 and (bottom) dependence on the coherence and the size of the ML window (assumed quadratic) for a squint angle of S2 of 22° and an incident angle of S1 of 45°.

Sentinel-1 products acquired in interferometric wide-swath (IW) mode with a single-look resolution of 20 × 5 m. For the plot in the bottom panel, a squint angle of S2 of 22° and an incident angle of S1 of 45° are assumed. For the low-to-moderate coherence values and for the Sentinel-1/Harmony scenario in IW mode, an accuracy in the order of several mm is to be expected for a product resolution in the order of hundreds of meters. This may be a sufficient product performance for a variety of applications. For a Harmony-like scenario, with acquisition S1 (zero squint) generated by Sentinel-1 in a monostatic manner and acquisition S2 generated by one of the Harmony satellites in a bistatic manner with a squint angle of roughly 22°, the standard deviation increases by a factor of 2 due to the bistatic acquisition. For the specific case of Harmony with two receiver satellites, the inversion can be performed twice followed by an averaging step, improving the standard deviation by a factor of approximately $\sqrt{2}$. Note that this is also valid for the subsequent approaches presented in Sections III-B and III-C.

B. Absolute Phase and ΔSWE Estimation for Moderate- to High-Coherence Scenarios

In moderate- to high-coherence scenarios, one can assume that a robust phase unwrapping is feasible. Still, the unwrapped interferograms may have an unknown bulk phase offset that needs to be resolved if no reference point is present in the scene. The bulk phase offset is an integer multiple of 2π. Similar to delta-k approaches for absolute phase estimation [29], the phase offset can be estimated from the difference phase.

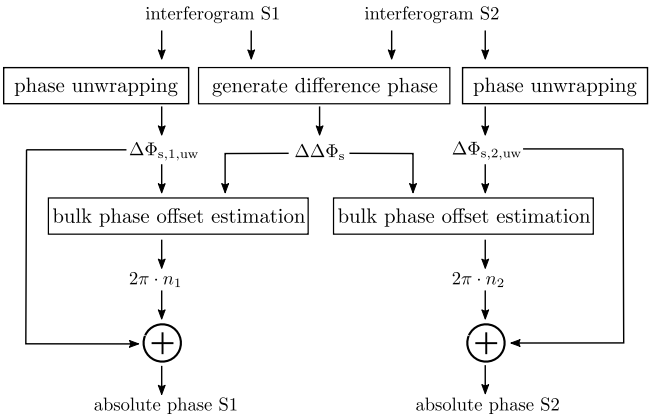

Fig. 11. Flow graph illustrating the absolute phase estimation approach.

From (10) follows that noisy versions of the absolute phase from acquisition S1 and S2 can be obtained as:

$$\Delta\tilde{\Phi}_{s,1} = \Delta\Delta\Phi_s \cdot \frac{\beta_1}{\beta_2 - \beta_1}$$
$$\Delta\tilde{\Phi}_{s,2} = \Delta\Delta\Phi_s \cdot \frac{\beta_2}{\beta_2 - \beta_1} \tag{15}$$

where the factor $(\beta_i/(\beta_2 - \beta_1))$ amplifies the phase noise on the difference phase. We can use the unwrapped phase $\Delta\Phi_{s,i,uw}$, which is equal to $\Delta\Phi_{s,i}$ except for the bulk phase offset, to estimate the integer multiple of the 2π phase offset according to

$$n_i = \left(\Delta\Delta\Phi_s \cdot \frac{\beta_i}{\beta_2 - \beta_1} - \Delta\Phi_{s,i,uw}\right) \cdot \frac{1}{2 \cdot \pi} \tag{16}$$

where the index i indicates the respective acquisition, S1 or S2. This integer estimate can be averaged over the whole scene, i.e., over scene blocks in which a high confidence level in the phase unwrapping is ensured, to mitigate the high phase noise. An estimate of the single absolute phases with an accuracy and resolution like the interferograms is obtained as

$$\Delta\Phi_{s,i} = \Delta\Phi_{s,i,uw} + 2 \cdot \pi \cdot n_i. \tag{17}$$

The process of the absolute phase estimation is illustrated in Fig. 11.

It is important to note that since the phase offset estimate has to be accurate within 2π, the difference phase has to be accurate within $2\pi \cdot ((\beta_2 - \beta_1)/\beta_i)$. Therefore, we can derive a minimum number of samples, N, to be used in the averaging of the integer estimate in (16) as (assuming an equivalent phase noise variance of the interferograms S1 and S2)

$$N_i > \frac{1 - \gamma^2}{\gamma^2} \cdot \left(\frac{\beta_i}{\beta_2 - \beta_1}\right)^2 \cdot \frac{1}{4 \cdot \pi^2}. \tag{18}$$

Fig. 12 shows the minimum N_1 for an incident angle of S1 of 45° and a squint angle of S2 of 22° for different values of coherence and normalized snow density. Note that for coherence values above 0.3 only several tens of samples are required. Note also that for the Sentinel-1/Harmony scenario with one monostatic and one bistatic acquisition, the required number of samples increases by a factor of 4. For the Sentinel-1 IW mode, e.g., 100 samples correspond to blocks

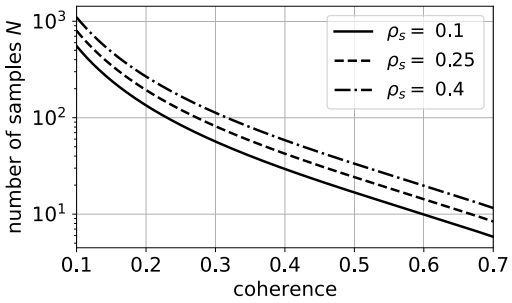

Fig. 12. Required number of samples, N, for estimating the bulk phase offset. Shown for different coherence and snow density values.

of 100 × 100 m. Such moderate block sizes may even allow to perform the absolute phase estimation, as illustrated in Fig. 11, on small blocks over the scene without the spatial phase unwrapping steps. Under the assumption that the spatial variation of ΔSWE does not produce phase wraps over the extent of one block, the absolute phase can be estimated at the resolution and accuracy of the single interferograms without the need for phase unwrapping. For small block sizes, i.e., moderate coherence values, this assumption may hold for a variety of snow accumulation scenarios.

C. Permittivity and Density Estimation

In contrast to delta-k approaches, the ratio of the absolute phases can be used to estimate the permittivity, hence, the density of the accumulated snow. The ratio can be written as

$$\frac{\Delta\Phi_{s,1}}{\Delta\Phi_{s,2}} = \alpha = \frac{\sqrt{\varepsilon_s - \sin^2\theta_1} - \cos\theta_1}{\sqrt{\varepsilon_s - \sin^2\theta_2} - \cos\theta_2} \tag{19}$$

where α is used from here on as a short hand notation for the phase ratio. Solving (19) for the permittivity results in two roots. One root is equal to 1 and the other, the physical one, can be written as

$$\varepsilon_s = \frac{1}{(\alpha^2 - 1)^2} \cdot \left[-4 \cdot \alpha \cdot \cos\theta_1 \cdot \cos\theta_2 \cdot (\alpha^2 + 1) + 2 \cdot \alpha^2 \cdot (\cos 2\theta_1 + \cos 2\theta_2) + \alpha^4 + 2 \cdot \alpha^2 + 1\right]. \tag{20}$$

Note that α is independent of the snow height. Hence, only information on the acquisition geometry is required for estimating the permittivity. Using the relation in (3), the density can be estimated from ε_s. A derivation of the standard deviation of the permittivity estimate is given in Appendix, resulting in

$$\sigma_{\varepsilon_s} = \frac{\lambda \cdot \rho_s}{\Delta\text{SWE} \cdot 4 \cdot \pi} \cdot \left[\sigma^2_{\Delta\Phi_{s,1}} + \sigma^2_{\Delta\Phi_{s,2}} \cdot \frac{\left(\sqrt{\varepsilon_s - \sin^2\theta_1} - \cos\theta_1\right)^2}{\left(\sqrt{\varepsilon_s - \sin^2\theta_2} - \cos\theta_2\right)^2}\right]^{\frac{1}{2}} \cdot \frac{2 \cdot \sqrt{\varepsilon_s - \sin^2\theta_1} \cdot \sqrt{\varepsilon_s - \sin^2\theta_2} \cdot \left(\sqrt{\varepsilon_s - \sin^2\theta_2} - \cos\theta_2\right)^2}{\cos\theta_1 \cdot \sqrt{\varepsilon_s - \sin^2\theta_1} + \sin^2\theta_1 - \cos\theta_2 \cdot \sqrt{\varepsilon_s - \sin^2\theta_2} - \sin^2\theta_2}. \tag{21}$$

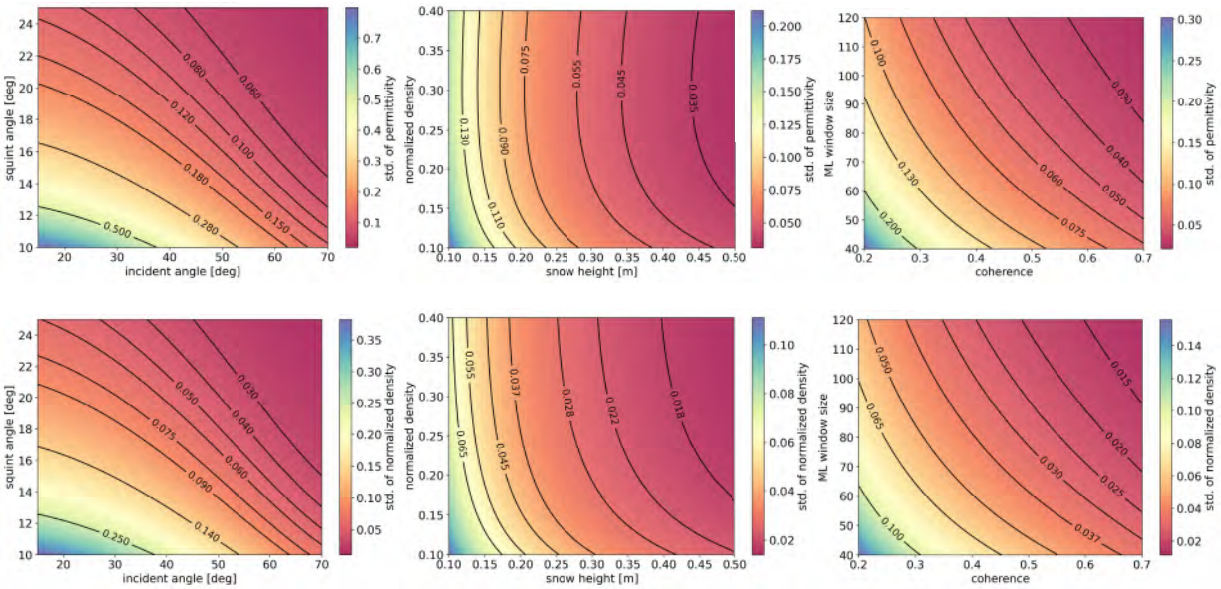

Fig. 13. Standard deviation of the (top) permittivity and (bottom) density estimation for (left) different incident angles of acquisition S1 and squint angles of S2, (center) different snow heights and snow densities, and (right) different coherence values and window sizes used for ML (assumed quadratic). Further description is given in the text of Section III-C.

It is important to note that the standard deviation depends on the ΔSWE and the used frequency, resulting in a higher accuracy for larger ΔSWE values or higher frequencies. Note, however, that the apparent benefit of a higher frequency is likely to be equalized by a commonly reduced coherence with increasing frequency, i.e., larger standard deviations $\sigma_{\Delta\Phi_{s,1}}$ and $\sigma_{\Delta\Phi_{s,2}}$. Fig. 13 shows plots of the standard deviation of the permittivity estimate (top panels) and derived standard deviations of estimates of the normalized snow density (bottom panels). The left panels show the dependence on the squint angle of interferogram S2 and the incident angle of S1 assuming a snow height change of 30 cm, a normalized snow density of 0.1, a coherence of 0.4 for both interferograms, and a ML window size of 80 × 80 samples which can be assumed equivalent to a 800 × 800 m window of a Sentinel-1 IW acquisition. For the same coherence and ML values, in the center panels, the dependence on the snow height change and the snow density is shown for a squint angle of S2 of 22° and an incident angle of S1 of 45°. Note the strong dependence to the snow height change and the relatively weak dependence to the snow density. The right panels show the influence of the coherence and the ML window size (assumed quadratic) for the same values of snow height, density, squint angle, and incident angle as described for the left and center panels. Note that substantial averaging (hundreds of meters for the Sentinel-1 IW resolution) is necessary to reach an accuracy for the density estimate of, e.g., <0.1. Still, the proposed measurement may provide a valuable proxy for the snow permittivity and density in scenarios of a low-frequency spatial variability of the snow density.

IV. Simulation Results

Until the launch of the Harmony satellites, no spaceborne sensor configuration exists that provides a sufficient squint diversity (i.e., greater than few degrees) to test the proposed approaches. A high-resolution airborne SAR sensor at a relatively low frequency (i.e., L band) could be used to synthesize almost simultaneous acquisitions with large squint diversity from different portions of the Doppler spectrum. A dedicated airborne campaign with accompanying ground measurements may be conducted in the future.

To test the potential of the developed approaches and the functionality of the proposed algorithms in the absence of real data, we use simulated Sentinel-1/Harmony acquisitions at a single-look complex (SLC) level. These simulations are derived from a real Sentinel-1 D-InSAR acquisition over Alaska, which indicates a snow accumulation event based on measurements from two snow depth measurement stations within the scene. The Sentinel-1 D-InSAR acquisition is used to provide the acquisition geometry and to model a ΔSWE map and coherence map which are then used to simulate the simultaneous Sentinel-1 and Harmony acquisitions. This method allows us to analyze the functionality of the algorithms in a controlled environment, while preserving realistic assumptions in terms of the correct geometry as well as a realistic spatial variability of phase and coherence signatures.

A. Derivation of Simulation Inputs From a Sentinel-1 Acquisition

Two Sentinel-1 IW images, acquired at January 28, 2020 and February 9, 2020 over Alaska, are used to form the D-InSAR acquisition. The geocoded amplitude image and the location of the snow measurement sites are shown in the top panel of Fig. 14. The *Galena* measurement site is located at 64°41′48″ N and 156°42′54″ W and the *Hozatka Lake* site at 65°11′53″ N and 156°38′6″ W. We selected the acquisition because of the moderate topography paired with constantly low temperatures within the acquisition interval, a variety of

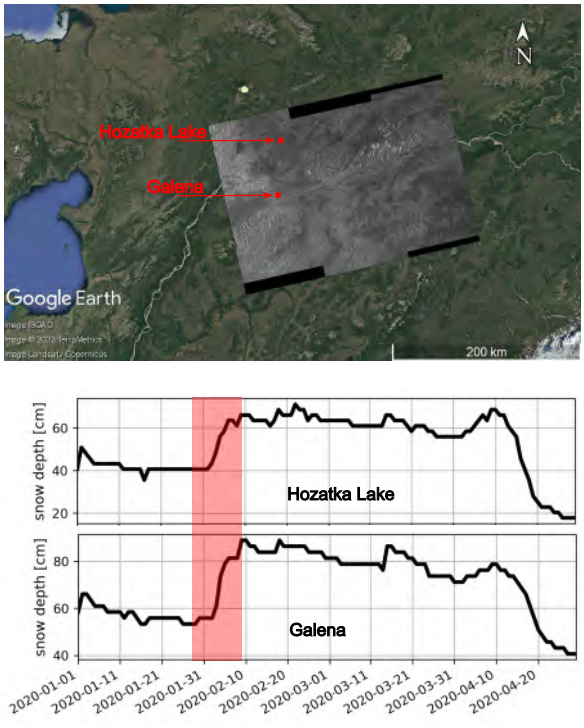

Fig. 14. (Top) location of the Sentinel-1 scene and the snow measurement sites in Alaska, which are used as basis for the simulation. The location is indicated by the geocoded amplitude image. (Bottom) snow depth at the measurement sites in the beginning of 2020. The red bar indicates the temporal baseline of the Sentinel-1 D-InSAR acquisition.

coherence values over the extent of the scene, and the presence of the snow measurement sites within the scene. The snow depth at the two sites is shown in the bottom panel of Fig. 14. It is measured using snow telemetry sensors (SNOTEL) and is provided by the *Natural Resources Conservation Service* of the *U.S. Department of Agriculture* (USDA). The red bar indicates the 12-day temporal baseline between the acquisitions.

The SAR processing chain TAXI (experimental TanDEM-X Interferometric Processor) [30] of the Microwaves and Radar Institute at the German Aerospace Center (DLR) is used for performing the InSAR processing. The TanDEM-X 30 m digital elevation model (DEM) is used to remove the residual topographic fringes. In the following, we only consider a portion (90 $\times$ 45 km) of the left sub-swath that contains the snow measurement sites. Fig. 15 shows the wrapped D-InSAR phase, coherence, DEM, and local incident angles of the scene in radar coordinates. The location of the measurement sites is indicated by red stars in the coherence map. A variety of coherence areas are present within the scene ranging from 0 to 0.85. Both the DEM and the local incident angles indicate that only moderate topography is present within most areas of the scene. Considering also the small interferometric baselines of Sentinel-1, we can assume that topographic phase residuals have been effectively removed using the TanDEM-X 30 m DEM. The D-InSAR phase shows a moderate variability. We do not want to exclude that in addition to ΔSWE signatures also atmospheric contributions are visible in the phase signature. However, due to the dry conditions caused by the low temperatures ($\ll$0 °C), the water vapor content and, hence, the atmospheric phase delay, is expected to be rather low [5]. We want to highlight that with the outlined simulation approach, we do not aim on providing a validated ΔSWE measurement of the analyzed area, but to perform a simulation based on realistic phase and coherence signatures to analyze the functionality of the proposed multiple squint approaches. Therefore, we do not attempt to remove potential residual atmosphere signatures from the data.

The formulation in (6) is used to retrieve an estimate of the ΔSWE variation from the interferogram. This retrieval requires the unwrapped phase, the local incident angles, and the density (i.e., the permittivity). The local incident angles result from the geocoding process in the InSAR processing and are shown in Fig. 15(d). We use *SNAPHU* [31] to perform the phase unwrapping. We assume a synthetically generated density distribution which scales with the unwrapped phase (assuming that a stronger SWE change results in a higher density through compression) and has some random low-frequency variations over the scene (potentially representing wind-induced snow compression). The density distribution is shown in Fig. 16(a) ranging from $\rho_s = 0.1$ to $\rho_s = 0.3$, representing a variety of dry snow density values (the real density values for the Alaska scene are expected to be at the lower end of this interval). The resulting synthetic ΔSWE map is shown in Fig. 16(b). Note that we used the data from the snow measurement stations to offset the ΔSWE map. The synthesized ΔSWE map ranges from roughly 1 to 6.5 cm. Low coherence areas were masked out for the phase unwrapping and inversion and filled with interpolated ΔSWE values. Note again that the generated density map and, hence, also the ΔSWE map is of synthetic nature, likely not accurately capturing the real ΔSWE of the analyzed area, but representing realistic signatures in terms spatial variability and geometry effects.

B. Data Simulation for the Sentinel-1/Harmony Geometry

The data simulation is performed on a co-registered SLC level. To generate the SLCs, for both the Sentinel-1 and Harmony acquisitions, we use the amplitude images of the real Sentinel-1 scene as a reflectivity map, multiplied by independent realizations of high-resolution speckle. The coherence and phase are injected in the form of a complex coherence in both of the D-InSAR pairs by means of a two-image Cholesky decomposition. The magnitude of the complex coherence is assumed to be equivalent for both interferograms and corresponds to the real Sentinel-1 coherence map [see Fig. 15(b)]. The phase of the coherence represents the ΔSWE phase and is computed according to (6), assuming the synthetic ΔSWE and density maps shown in Fig. 16 and the respective local incident angle maps for the Sentinel-1 and Harmony acquisition. For the Sentinel-1 acquisition, the local incident angles correspond to the real acquisition [see Fig. 15(d)]. The Harmony satellite is assumed to be flying on the same orbit but 350 km behind the Sentinel-1 satellite, receiving the scattered echoes from Sentinel-1 in a receive-only configuration, as foreseen for the Harmony constellation [23]. The incident angles are mapped accordingly to this squinted acquisition. Due to the bistatic nature of the Harmony acquisition, the ΔSWE phase

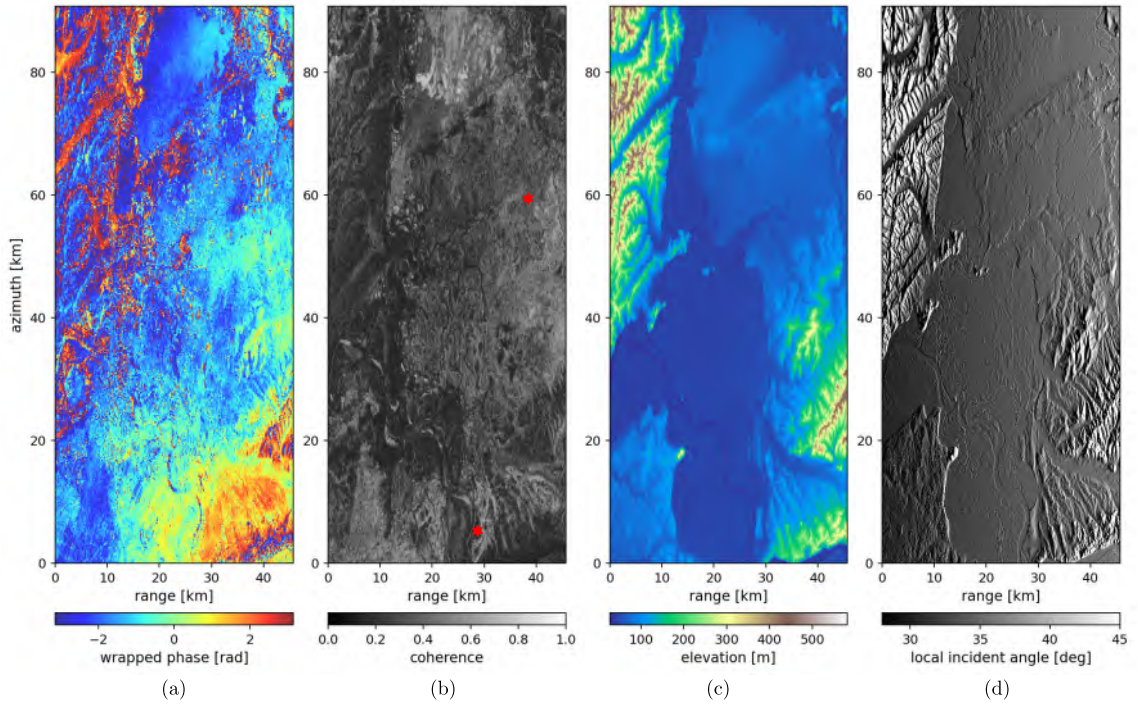

Fig. 15. Products from the InSAR processing of the Sentinel-1 D-InSAR pair showing in radar coordinates. (a) Topography-corrected wrapped phase. (b) Interferometric coherence. (c) Elevation of the TanDEM-X 30 m DEM. (d) Local incident angles retrieved from the geocoding process.

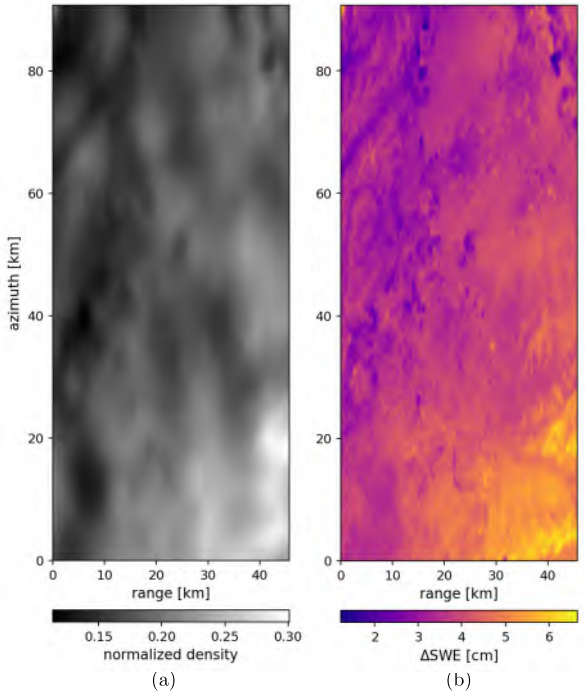

Fig. 16. (a) Synthetically generated density map. (b) ΔSWE map resulting from the inversion of the interferometric phase, the density map, and the local incident angles. Both the density and ΔSWE maps are used as input to the simulation of the Sentinel-1/Harmony acquisitions.

formulation from (6) changes to

$$\Delta\Phi_{s,S2} = \Delta\mathrm{SWE} \cdot \frac{2 \cdot \pi}{\lambda \cdot \rho_s} \cdot \left(\sqrt{\varepsilon_s(\rho_s) - \sin^2\theta_{S1}} - \cos\theta_{S1} + \sqrt{\varepsilon_s(\rho_s) - \sin^2\theta_{S2}} - \cos\theta_{S2} \right) \quad (22)$$

where the labels S1 and S2 indicate the Sentinel-1 and Harmony geometry, respectively. Fig. 17 shows the resulting interferograms for Sentinel-1 and Harmony in panels (a) and (b), respectively. A ML window of 50 × 50 m was used. As expected, the interferograms show similar patterns but have systematic differences due to the difference of the local incident angles. The two interferograms are used in the following to test the proposed retrieval approaches.

C. Low-Resolution ΔSWE Estimation

We use the procedure described in Section III-A to obtain a low-resolution estimate of the ΔSWE distribution. Note that no phase unwrapping is required if the difference phase is computed as

$$\Delta\Delta\Phi_s = \arg\left[\left(i_{S1,m} \cdot i^*_{S1,s} \right) \cdot \left(i_{S2,m} \cdot i^*_{S2,s} \right)^* \right] \quad (23)$$

where i indicates the single SLCs, * indicates complex conjugation, and the indices m and s represent the primary and secondary acquisitions, respectively. We assume at this point that the density (i.e., permittivity) distribution is known. The density inversion is outlined in Section IV-D. Fig. 18 shows the result of the inversion according to formula (11), adapted to the bistatic propagation geometry of the Harmony acquisition [cf. (22)]. The retrieved ΔSWE map is shown in Fig. 18(a). A ML window of 400 × 400 m was used. The retrieved ΔSWE distribution resembles the one used as an input to the simulation [see Fig. 16(b)] but is very noisy in low-coherence areas. The error of the ΔSWE measurement is shown in Fig. 18(b). Note the different scale of the error map compared to the ΔSWE map. Error statistics are given in Fig. 18(c) and (d) in form of a 2-D histogram, as well as the

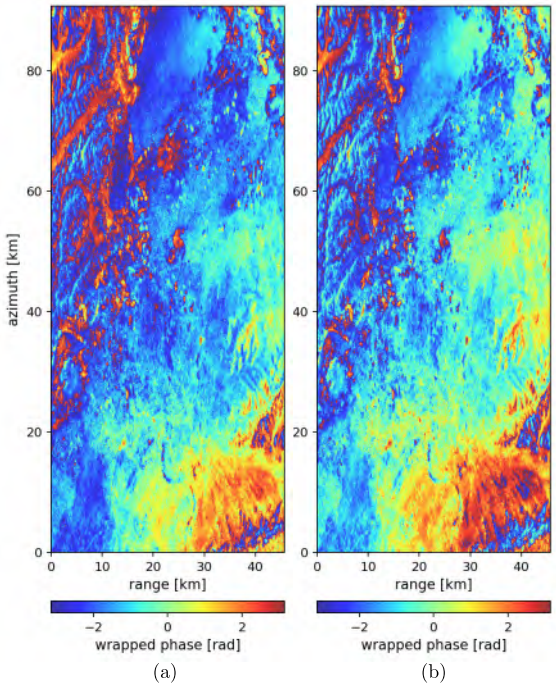

Fig. 17. Interferograms of the simulated (a) Sentinel-1 and (b) Harmony acquisitions. Note the systematic phase differences between (a) and (b) resulting from the difference of the squint angle.

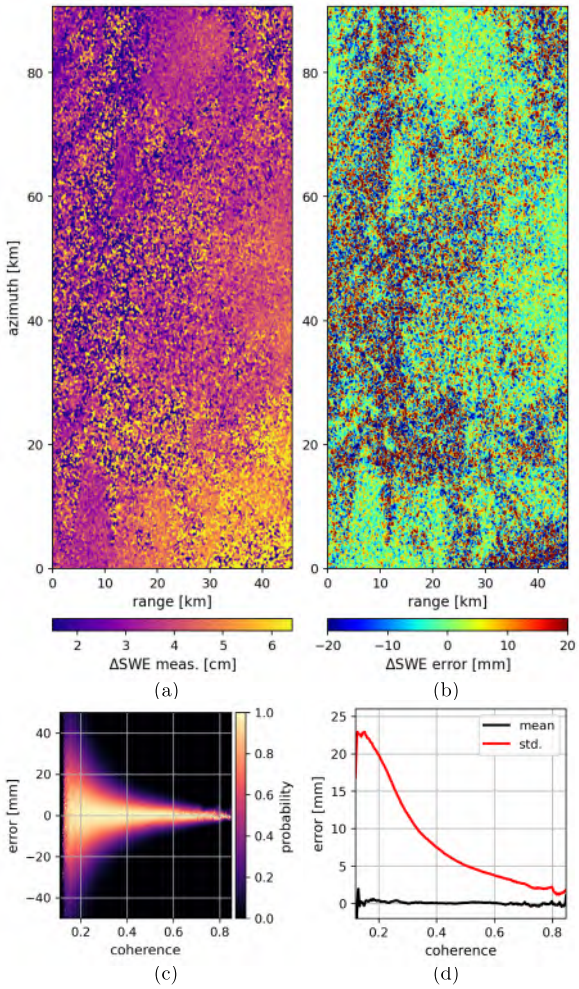

Fig. 18. Results of the low-resolution ΔSWE inversion, showing (a) retrieved ΔSWE map, (b) estimation error, and (c) and (d) error statistics in form of a 2-D histogram as well as mean and standard deviation values for different coherence values.

mean and standard deviation values of the error for different coherence levels over the scene. Note that the histogram is normalized for each coherence bin. Note also that pixels with coherence values <0.1 were masked for the inversion. The statistics in Fig. 18(d) show that the inversion is unbiased and for the used ML window, sub-centimeter accuracy is reached for coherence values >0.33. The accuracy may be increased by using larger windows at the cost of a reduced spatial resolution.

D. Absolute Phase, ΔSWE, and Density Estimation

Here, we are presenting a joint inversion of the ΔSWE and the density by means of the absolute phase estimation and permittivity estimation strategies outlined in Sections III-B and III-C, respectively, adapted to the bistatic propagation geometry of the Harmony acquisition [cf. (22)]. As an initial guess, a constant normalized density of $\rho_s = 0.1$ is assumed over the scene. *SNAPHU* [31] is used to perform the phase unwrapping on both interferograms with a common reference point and the bulk phase offset is estimated as described in Section III-B. A single bulk offset is computed for the whole scene, assuming that a consistent unwrapping was possible over the whole extent of the scene. Note that the rough initial density estimate is sufficient, because the bulk phase offset needs to be accurate only within 2π. The estimated bulk phase offset results in $1 \cdot 2\pi$ for both the Sentinel-1 and Harmony interferogram. The absolute phase is obtained as the unwrapped phase plus the bulk offset. Fig. 19(a) shows the ΔSWE retrieved from the estimated absolute phase. The distribution is well resolved and resembles the original one in Fig. 16. The estimation error is shown in Fig. 19(b), where a systematically varying bias is present, caused by the inaccurate initial density estimate. We use the approach from Section III-C to estimate the permittivity from the absolute phase and the formulation in (3) to retrieve the density, shown in Fig. 19(c). A large ML window of 500 × 500 m is used in the permittivity estimation to mitigate the strong noise on the ratio of the interferograms that is used for the inversion. The ΔSWE inversion is then performed again with the estimated permittivity and density. Fig. 19(d) shows the error of the finally retrieved ΔSWE. Note that we performed the ΔSWE inversion from the estimated absolute phases of both the Sentinel-1 and Harmony interferogram and averaged the resulting products to further improve the accuracy. The error statistics for the density estimate and the final ΔSWE estimate are shown in Fig. 19(e)–(h) for different coherence values. When comparing the accuracy of the ΔSWE estimate see [Fig. 19(h)] to the one resulting from the low-resolution procedure based on the difference phase [see Fig. 18(d)], it is obvious that including the absolute phase estimation is superior since the ΔSWE can be estimated at the resolution and accuracy of the single interferograms. This results in an accuracy around 1 mm for the present example using a

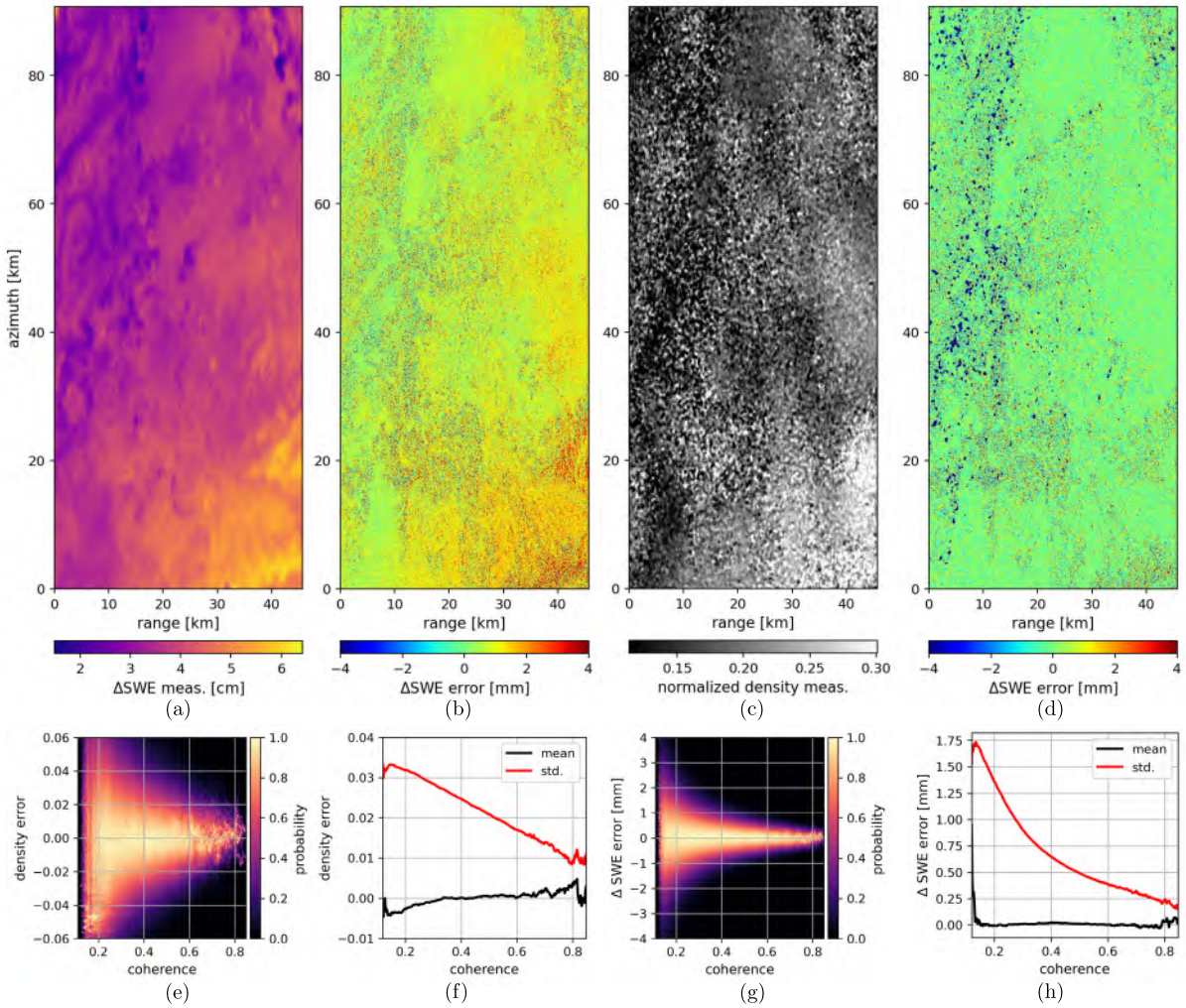

Fig. 19. Results from the absolute phase and density estimation, showing (a) retrieved ΔSWE from the absolute phase using an initial density estimate of 0.1, (b) ΔSWE measurement error that shows systematic biases resulting from the inaccurate initial density estimate, (c) measured density, (d) resulting ΔSWE error when using the measured density in the inversion, (e) and (f) error statistics of the density estimate, and (g) and (h) error statistics of the final ΔSWE estimate.

ML window of 50 × 50 m. Note that a consistent phase unwrapping is required in order to apply the absolute phase estimation.

V. Potential Limitations

The proposed methodologies are limited to dry snow conditions that allow penetration of the radar signals through the snow cover. Note that this limitation is intrinsic to standard D-InSAR approaches for snow parameter retrieval [4], [5], [6], [7]. Especially in the early and late winter periods, at higher temperatures and solar illumination, consistent dry snow conditions are not present and commonly prevent robust D-InSAR snow parameter retrieval. Under dry snow conditions, systematic biases and a deterioration of the accuracy may arise from atmospheric effects, ground deformation, co-registration errors between the two acquisition geometries, as well as orbit, baseline and attitude knowledge errors. These error sources have not been treated in the scope of this article and a detailed study is left for future research.

Tropospheric effects are expected to partially cancel out when forming the difference phase between the interferograms due to the simultaneous acquisition [32]. Still, because of the significantly different acquisition geometries, residual troposphere phase terms are to be expected [22]. Note that tropospheric effects may be rather small, due to the dry snow conditions under which ΔSWE D-InSAR measurements have to be conducted, which are expected to commonly correlate with a rather low water vapor content in the atmosphere and hence, small phase delays [5]. Signatures from the ionosphere are likely to not be correlated among the different geometries since they occur at high altitudes. The split-spectrum technique has been proven successful for removing ionospheric signatures [33]. By additionally avoiding acquisitions at dusk (showing high ionosphere activity), systematic errors caused by the ionosphere are expected to be controllable. Additional calibrations based on atmospheric weather models (as, e.g., proposed in [18]) or on snow-free areas within the scene extent can be applied to mitigate atmospheric effects.

The most common sources of ground deformation in areas with consistent dry snow conditions are expected to happen over time scales that are significantly larger than the D-InSAR temporal baselines (e.g., seasonal ground ice or seasonal active

layer displacements). More rapid deformations caused by, e.g., glacier flow, frost heave, or landslides may introduce significant errors. A differentiation between rapid deformations and ΔSWE may be in some cases possible based on their distinct spatial patterns.

Co-registration, orbit, baseline, and attitude errors are expected to be controllable, based on the heritage of state-of-the-art SAR missions. However, the large squint diversity and the bistatic nature of, e.g., the Harmony mission may complicate those aspects.

Note that the listed bias and error sources are common also to standard D-InSAR SWE retrieval.

VI. Conclusion

In this article, we have analyzed the potential of multiple simultaneous D-InSAR acquisitions with different squints for the estimation of snow parameters, in particular the SWE and the snow density. The line-of-sight diversity between two interferograms acquired with different squint angles results in a systematic difference of the interferometric phase caused by the propagation through the snow. The phase difference can be exploited to directly obtain an unbiased ΔSWE estimate without the need for phase unwrapping and without a reference point within the scene. Furthermore, the ratio of the two interferograms is a measure of the dielectric permittivity of the snow and, hence, can be inverted to the density of the snow. The developed ΔSWE estimation concepts follow a similar rationale as previously proposed delta-k approaches. In contrast to delta-k approaches, the multiple squints provide a direct measure for the density (i.e., the permittivity) which is not only an important input for the D-InSAR ΔSWE mapping, but also for other sensor concepts and modeling approaches.

We showed that a sufficient squint diversity (e.g., more than a few degrees) is required to provide adequate sensitivity for the proposed inversion techniques. The planned Earth Explorer 10 mission, Harmony, may be a suitable candidate to implement these techniques. By means of simulated D-InSAR acquisitions of Sentinel-1 and Harmony, we demonstrated that with the large squint diversity of the Harmony constellation, convincing inversion results of both ΔSWE and density may be obtained. Systematic biases and a deterioration of the accuracy may arise from atmospheric effects, ground deformation, co-registration errors between the two acquisition geometries, as well as orbit, baseline, and attitude knowledge errors. A detailed study of the potential error sources is left for future research.

Beyond sensor constellations like Harmony (acquiring with different squints), in general, systems which acquire D-InSAR simultaneously with significant incident angle differences beyond few degrees could apply the proposed approaches in a similar manner. For across-track interferometers like TanDEM-X, with baselines of few hundreds of meters, no relevant sensitivity is expected. Two D-InSAR acquisitions from different orbits (potentially resulting in significantly different incident angles), could be used for the proposed approaches if they were to be acquired simultaneously or quasi-simultaneously (e.g., by a constellation deployed on different orbits). Simultaneity is expected to be a key requirement for: 1) sensing at the same snow conditions and 2) minimizing atmospheric effects.

Appendix
Derivation of the Standard Deviation of the Permittivity Estimate

The permittivity estimate, ε_s, in (20) is a function of the variable α that describes the ratio of the two random variables $\Delta\Phi_{s,1}$ and $\Delta\Phi_{s,2}$, i.e., the two interferometric phases. For the sake of simple readability, $\Delta\Phi_{s,1}$ and $\Delta\Phi_{s,2}$ are in the following substituted by the variables a and b, respectively. The standard deviation of the permittivity can be expressed in terms of the standard deviation of α, i.e., σ_α, as

$$\sigma_{\varepsilon_s} = \sigma_\alpha \cdot \frac{d\varepsilon_s}{d\alpha}. \tag{24}$$

From (19), the reciprocal of the derivative in (24) is obtained as

$$\frac{d\alpha}{d\varepsilon_s} = \frac{\begin{array}{c}\cos\theta_1 \cdot \sqrt{\varepsilon_s - \sin^2\theta_1} + \sin^2\theta_1 \\ -\cos\theta_2 \cdot \sqrt{\varepsilon_s - \sin^2\theta_2} - \sin^2\theta_2\end{array}}{\begin{array}{c}2 \cdot \sqrt{\varepsilon_s - \sin^2\theta_1} \cdot \sqrt{\varepsilon_s - \sin^2\theta_2} \\ \cdot \left(\sqrt{\varepsilon_s - \sin^2\theta_2} - \cos\theta_2\right)^2\end{array}}. \tag{25}$$

Since α is the ratio of two random variables, the standard deviation σ_α needs to be approximated using a Taylor expansion around the expected values of the two variables, a and b, resulting in

$$\sigma_\alpha^2 = \mathrm{Var}\left(\frac{a}{b}\right) \approx \frac{\mu_a^2}{\mu_b^2} \cdot \left[\frac{\sigma_a^2}{\mu_a^2} - \frac{2 \cdot \mathrm{Cov}(a,b)}{\mu_a \cdot \mu_b} + \frac{\sigma_b^2}{\mu_b^2}\right] \tag{26}$$

where $\mathrm{Var}(\cdot)$ indicates the variance, $\mathrm{Cov}(a,b)$ the covariance between a and b, and μ_x and σ_x the expected value and the standard deviation of a variable x, respectively. If the squint angle difference between the two interferometric acquisition results in non-overlapping Doppler spectra (considered as a standard scenario in the frame of this article), the covariance between a and b vanishes and σ_α can be written as

$$\sigma_\alpha \approx \sqrt{\frac{\sigma_a^2}{\mu_b^2} + \frac{\mu_a^2 \cdot \sigma_b^2}{\mu_b^4}}. \tag{27}$$

Using (24), (25), and (27), the standard deviation of the permittivity estimate results in

$$\sigma_{\varepsilon_s} = \sqrt{\frac{\sigma_a^2}{\mu_b^2} + \frac{\mu_a^2 \cdot \sigma_b^2}{\mu_b^4}} \cdot \frac{\begin{array}{c}2 \cdot \sqrt{\varepsilon_s - \sin^2\theta_1} \cdot \sqrt{\varepsilon_s - \sin^2\theta_2} \\ \cdot \left(\sqrt{\varepsilon_s - \sin^2\theta_2} - \cos\theta_2\right)^2\end{array}}{\begin{array}{c}\cos\theta_1 \cdot \sqrt{\varepsilon_s - \sin^2\theta_1} + \sin^2\theta_1 \\ -\cos\theta_2 \cdot \sqrt{\varepsilon_s - \sin^2\theta_2} - \sin^2\theta_2\end{array}}. \tag{28}$$

By substituting the expected values, μ_a and μ_b, by the expressions in (8) and (9), respectively, we obtain the final relation (21).

Acknowledgment

The authors would like to thank the three reviewers for their efforts and insightful comments that helped improving the article.

REFERENCES

[1] M. Takala et al., "Estimating Northern Hemisphere snow water equivalent for climate research through assimilation of space-borne radiometer data and ground-based measurements," *Remote Sens. Environ.*, vol. 115, no. 12, pp. 3517–3529, Dec. 2011.

[2] C. Derksen, A. Walker, and B. Goodison, "A comparison of 18 winter seasons of in situ and passive microwave-derived snow water equivalent estimates in western Canada," *Remote Sens. Environ.*, vol. 88, no. 3, pp. 271–282, Dec. 2003.

[3] R. L. Grasty, "Direct snow-water equivalent measurement by air-borne gamma-ray spectrometry," *J. Hydrol.*, vol. 55, nos. 1–4, pp. 213–235, Feb. 1982.

[4] T. Guneriussen, K. A. Hogda, H. Johnsen, and I. Lauknes, "InSAR for estimation of changes in snow water equivalent of dry snow," *IEEE Trans. Geosci. Remote Sens.*, vol. 39, no. 10, pp. 2101–2108, Oct. 2001.

[5] H. Rott, T. Nagler, and R. Scheiber, "Snow mass retrieval by means of SAR interferometry," in *Proc. 3rd Fringe Workshop Eur. Space Agency Earth Observ.*, 2004, pp. 1–6.

[6] G. Engen, T. Guneriussen, and Y. Overrein, "Delta-K interferometric SAR technique for snow water equivalent (SWE) retrieval," *IEEE Geosci. Remote Sens. Lett.*, vol. 1, no. 2, pp. 57–61, Apr. 2004.

[7] S. Leinss, A. Wiesmann, J. Lemmetyinen, and I. Hajnsek, "Snow water equivalent of dry snow measured by differential interferometry," *IEEE J. Sel. Topics Appl. Earth Observ. Remote Sens.*, vol. 8, no. 8, pp. 3773–3790, Aug. 2015.

[8] H. Li, P. Xiao, X. Feng, G. He, and Z. Wang, "Monitoring snow depth and its change using repeat-pass interferometric SAR in Manas river basin," in *Proc. IEEE Int. Geosci. Remote Sens. Symp. (IGARSS)*, Jul. 2016, pp. 4936–4939.

[9] Y. Liu, L. Li, J. Yang, X. Chen, and J. Hao, "Estimating snow depth using multi-source data fusion based on the D-InSAR method and 3DVAR fusion algorithm," *Remote Sens.*, vol. 9, no. 11, p. 1195, Nov. 2017.

[10] V. Conde, G. Nico, P. Mateus, J. Catalão, A. Kontu, and M. Gritsevich, "On the estimation of temporal changes of snow water equivalent by spaceborne SAR interferometry: A new application for the Sentinel-1 mission," *J. Hydrol. Hydromech.*, vol. 67, no. 1, pp. 93–100, Mar. 2019.

[11] P. N. Dagurov, T. N. Chimitdorzhiev, A. V. Dmitriev, and S. I. Dobrynin, "Estimation of snow water equivalent from L-band radar interferometry: Simulation and experiment," *Int. J. Remote Sens.*, vol. 41, no. 24, pp. 9328–9359, Dec. 2020.

[12] D. Varade, A. K. Maurya, O. Dikshit, G. Singh, and S. Manickam, "Snow depth in dhundi: An estimate based on weighted bias corrected differential phase observations of dual polarimetric bi-temporal Sentinel-1 data," *Int. J. Remote Sens.*, vol. 41, no. 8, pp. 3031–3053, Apr. 2020.

[13] J. Eppler, B. Rabus, and P. Morse, "Snow water equivalent change mapping from slope-correlated synthetic aperture radar interferometry (InSAR) phase variations," *Cryosphere*, vol. 16, no. 4, pp. 1497–1521, Apr. 2022.

[14] H. P. Marshall et al., "L-band InSAR depth retrieval during the NASA SnowEx 2020 campaign: Grand mesa, Colorado," in *Proc. IEEE Int. Geosci. Remote Sens. Symp. (IGARSS)*, Jul. 2021, pp. 625–627.

[15] T. Nagler et al., "Airborne experiment on InSAR snow mass retrieval in Alpine environment," in *Proc. IEEE Int. Geosci. Remote Sens. Symp.*, Jul. 2022, pp. 4549–4552.

[16] K. Belinska, G. Fischer, T. Nagler, and I. Hajnsek, "Snow water equivalent estimation using differential SAR interferometry and co-polar phase differences from airborne SAR data," in *Proc. IEEE Int. Geosci. Remote Sens. Symp.*, Jul. 2022, pp. 4545–4548.

[17] K. Belinska, G. Fischer, and I. Hajnsek, "Differential SAR interferometry and co-polar phase differences for snow water equivalent estimation," in *Proc. 14th Eur. Conf. Synth. Aperture Radar*, Jul. 2022, pp. 1–4.

[18] S. Oveisgharan, R. Zinke, Z. Hoppinen, and H. P. Marshall, "Snow water equivalent retrieval over Idaho—Part 1: Using Sentinel-1 repeat-pass interferometry," *Cryosphere*, vol. 18, no. 2, pp. 559–574, Feb. 2024.

[19] A. B. Mahmoodzada et al., "Capability assessment of Sentinel-1 data for estimation of snow hydrological potential in the Khanabad watershed in the Hindu Kush Himalayas of Afghanistan," *Remote Sens. Applications: Soc. Environ.*, vol. 26, Apr. 2022, Art. no. 100758.

[20] R. T. Palomaki and E. A. Sproles, "Assessment of L-band InSAR snow estimation techniques over a shallow, heterogeneous Prairie snowpack," *Remote Sens. Environ.*, vol. 296, Oct. 2023, Art. no. 113744.

[21] J. Tarricone, R. W. Webb, H.-P. Marshall, A. W. Nolin, and F. J. Meyer, "Estimating snow accumulation and ablation with L-band interferometric synthetic aperture radar (InSAR)," *Cryosphere*, vol. 17, no. 5, pp. 1997–2019, May 2023.

[22] Y. Li, P. L. Dekker, G. Mulder, L. Iannini, and P. Prats-Iraola, "Differential tropospheric delay estimation by simultaneous multi-angle repeat-pass InSAR," *IEEE Trans. Geosci. Remote Sens.*, vol. 60, 2022, Art. no. 5213118.

[23] "Earth explorer 10 candidate mission Harmony," Eur. Space Agency, Noordwijk, The Netherlands, Tech. Rep. ESA-EOPSM-HARM-RP-4129, 2022, p. 369.

[24] A. Benedikter, M. Rodriguez-Cassola, P. Prats-Iraola, K. Belinska, and G. Krieger, "On the decorrelation effect of dry snow in differential SAR interferometry," in *Proc. IEEE Int. Geosci. Remote Sens. Symp.*, Jul. 2023, pp. 8323–8326.

[25] J. Kellndorfer et al., "Global seasonal Sentinel-1 interferometric coherence and backscatter data set," *Sci. Data*, vol. 9, no. 1, p. 73, Mar. 2022, doi: 10.1038/s41597-022-01189-6.

[26] R. Touzi, A. Lopes, J. Bruniquel, and P. W. Vachon, "Coherence estimation for SAR imagery," *IEEE Trans. Geosci. Remote Sens.*, vol. 37, no. 1, pp. 135–149, Jan. 1999.

[27] P. López-Dekker et al., "The harmony mission: End of phase-0 science overview," in *Proc. IEEE Int. Geosci. Remote Sens. Symp. (IGARSS)*, Jul. 2021, pp. 7752–7755.

[28] M. S. Seymour and I. G. Cumming, "Maximum likelihood estimation for SAR interferometry," in *Proc. IEEE Int. Geosci. Remote Sens. Symp.*, vol. 4, Aug. 1994, pp. 2272–2275.

[29] S. N. Madsen, H. A. Zebker, and J. Martin, "Topographic mapping using radar interferometry: Processing techniques," *IEEE Trans. Geosci. Remote Sens.*, vol. 31, no. 1, pp. 246–256, Jan. 1993.

[30] P. Prats et al., "Taxi: A versatile processing chain for experimental TanDEM-X product evaluation," in *Proc. IEEE Int. Geosci. Remote Sens. Symp.*, Jul. 2010, pp. 4059–4062.

[31] C. W. Chen and H. A. Zebker, "Two-dimensional phase unwrapping with use of statistical models for cost functions in nonlinear optimization," *J. Opt. Soc. Amer. A, Opt. Image Sci.*, vol. 18, no. 2, p. 338, Feb. 2001.

[32] P. Prats-Iraola, P. Lopez-Dekker, F. De Zan, N. Yagüe-Martínez, M. Zonno, and M. Rodriguez-Cassola, "Performance of 3-D surface deformation estimation for simultaneous squinted SAR acquisitions," *IEEE Trans. Geosci. Remote Sens.*, vol. 56, no. 4, pp. 2147–2158, Apr. 2018.

[33] G. Gomba, A. Parizzi, F. D. Zan, M. Eineder, and R. Bamler, "Toward operational compensation of ionospheric effects in SAR interferograms: The split-spectrum method," *IEEE Trans. Geosci. Remote Sens.*, vol. 54, no. 3, pp. 1446–1461, Mar. 2016.

Andreas Benedikter (Member, IEEE) was born in Munich, Germany, in 1994. He received the B.Sc. degree in medical engineering and the M.Sc. degree (Hons.) in electrical engineering and information technology from the Friedrich-Alexander University Erlangen-Nürnberg, Erlangen, Germany, in 2017 and 2019, respectively. In 2017, he spent one semester at the University of Bristol, Bristol, U.K. He is currently pursuing the Ph.D. degree with the Friedrich-Alexander University Erlangen-Nürnberg.

Since 2019, he has been with the Microwaves and Radar Institute of the German Aerospace Center (DLR), Oberpfaffenhofen, Germany, as a Research Scientist. His current research interests include radar signal processing, SAR interferometry, radar signal propagation, and scattering mechanisms, and the study of future radar concepts, especially in the context of cryospheric applications, and planetary exploration missions.

Mr. Benedikter was a recipient of the first prize of the Student Paper Competition of the IEEE International Geoscience and Remote Sensing Symposium 2023 Conference held in Pasadena, CA, USA.

Kristina Belinska received the B.Sc. and M.Sc. degrees in physics from the University of Bremen, Bremen, Germany, in 2017 and 2019, respectively. She is currently pursuing the Ph.D. degree with the Swiss Federal Institute of Technology (ETH) Zurich, Zurich, Switzerland.

In 2019, she joined the Polarimetric SAR Interferometry (Pol-InSAR) Group, the Microwaves and Radar Institute, German Aerospace Space Center (DLR), Wessling, Germany. Her main research interests include the retrieval of snow parameters from repeat pass interferometric, multifrequency, and polarimetric SAR data.

Marc Rodriguez-Cassola was born in Barcelona, Spain, in 1977. He received the Ingeniero degree in telecommunication engineering from the Universidad Pública de Navarra, Pamplona, Spain, in 2000, the Licenciado (M.Sc.) degree in economics from the Universidad Nacional de Educación a Distancia, Madrid, Spain, in 2012, and the Ph.D. degree in electrical engineering from Karlsruhe Institute of Technology, Karlsruhe, Germany, in 2012.

From 2000 to 2001, he was a Radar Hardware Engineer with the Study Center of Terrestrial and Planetary Environments (CETP)/French National Centre for Scientific Research (CNRS), Saint Maur des Fosses, France. From 2001 to 2003, he was a Software Engineer with Altran Consulting, Munich, Germany. Since 2003, he has been with German Aerospace Center, Microwaves and Radar Institute, Weßling, Germany, where he is leading the SAR Missions Group. His research interests include radar signal processing, SAR end-to-end simulation, SAR processing and calibration algorithms, crisis theory, and radar mission analysis and applications.

Pau Prats-Iraola (Fellow, IEEE) was born in Madrid, Spain, in 1977. He received the Ingeniero and Ph.D. degrees in telecommunications engineering from the Universitat Politècnica de Catalunya (UPC), Barcelona, Spain, in 2001 and 2006, respectively.

In 2001, he was a Research Assistant at the Institute of Geomatics, Barcelona. In 2002, he was at the Department of Signal Theory and Communications, UPC, where he worked in the field of airborne repeat-pass interferometry and airborne differential SAR interferometry. From December 2002 to August 2006, he was an Assistant Professor at the Department of Telecommunications and Systems Engineering, Universitat Autònoma de Barcelona, Barcelona. In 2006, he joined the Microwaves and Radar Institute, German Aerospace Center (DLR), Wessling, Germany, where, since 2009, he has been the Head of the Multimodal Algorithms Group. He is the responsible and main developer of the TanDEM-X Interferometric (TAXI) Processor, an end-to-end processing chain for data acquired by the TerraSAR-X and TanDEM-X Satellites, which has been used to demonstrate novel SAR acquisition modes and techniques. He is currently involved in the design and implementation of the ground processor prototypes and end-to-end simulators of ESA's BIOMASS, ROSE-L and Harmony missions. His research interests include high-resolution airborne/spaceborne monostatic/bistatic SAR processing, SAR interferometry, advanced interferometric acquisition modes, Persistent Scatterer Interferometry (PSI), SAR tomography, and end-to-end SAR simulation. He has co-authored more than 70 peer-reviewed journal articles in these field.

Georg Fischer received the M.Sc. degree in geography from the Ludwig Maximilians University of Munich, Munich, Germany, in 2012, and the Ph.D. degree in environmental engineering from the ETH Zurich, Zurich, Switzerland, in 2019.

From 2012 to 2013, he conducted a traineeship at the Mission Science Division, Directorate of Earth Observation Programs, ESA, Noordwijk, The Netherlands. In 2013, he joined the Polarimetric Synthetic Aperture Radar Interferometry Research Group, Radar Concepts Department, Microwaves and Radar Institute, German Aerospace Center (DLR), Wessling, Germany. His research interests include the characterization and modeling of polarimetric, interferometric, and tomographic synthetic aperture radar (SAR) measurements from snow and ice and the development of methods for the estimation of geophysical properties of glaciers and ice sheets from polarimetric and interferometric SAR data.

Gerhard Krieger (Fellow, IEEE) received the Dipl.-Ing. (M.S.) and Dr.-Ing. (Ph.D.) (Hons.) degrees in electrical and communication engineering from the Technical University of Munich, Munich, Germany, in 1992 and 1999, respectively.

From 1992 to 1999, he was with the Ludwig Maximilians University, Munich, where he conducted multidisciplinary research on neuronal modeling and nonlinear information processing in biological and technical vision systems. Since 1999, he has been with the Microwaves and Radar Institute of the German Aerospace Center (DLR), Oberpfaffenhofen, Germany, where he started as a research associate developing signal processing algorithms for a novel forward-looking radar system employing digital beamforming on receive. From 2001 to 2007, he led the New SAR Missions Group which pioneered the development of advanced bistatic and multistatic radar systems, such as TanDEM-X, as well as innovative multichannel SAR techniques and algorithms for high-resolution wide-swath SAR imaging. Since 2008, he has been the Head of the Radar Concepts Department which currently hosts about 60 scientists focusing on new SAR techniques, missions and applications. He has been serving as Mission Engineer for TanDEM-X and he made also major contributions to the development of the Tandem-L mission concept, where he led the Phase-0 and Phase-A studies. Since 2019, he holds also a professorship at the Friedrich-Alexander-University Erlangen, Germany, and he is author or co-author of more than 100 peer-reviewed journal articles, nine invited book chapters, about 500 conference papers, and more than 30 patents.

Prof. Krieger received several national and international awards, including two Best Paper Awards at the European Conference on Synthetic Aperture Radar, two Transactions Prize Paper Awards of the IEEE Geoscience and Remote Sensing Society, and the W.R.G. Baker Prize Paper Award from the IEEE Board of Directors. In 2014 and 2024, he served as the Technical Program Chair for European Conference on Synthetic Aperture Radar and in 2014 also as a Guest Editor for the IEEE JOURNAL OF SELECTED TOPICS IN APPLIED EARTH OBSERVATIONS AND REMOTE SENSING. He has been an Associate Editor of IEEE TRANSACTIONS ON GEOSCIENCE AND REMOTE SENSING, since 2012.

Irena Hajnsek (Fellow, IEEE) received the Dipl. degree (Hons.) in fluvial river systems from the Free University of Berlin, Berlin, Germany, in 1996, and the Dr. rer. nat. degree (Hons.) in model-based estimation of soil moisture from fully polarimetric synthetic aperture radar from the Friedrich Schiller University of Jena, Jena, Germany, in 2001.

Since November 2009, she has been a Professor of Earth Observation at the Swiss Federal Institute of Technology (ETH) Zürich Institute of Environmental Engineering, Zürich, Switzerland, and at the same time the Head of the Polarimetric SAR Interferometry Research Group, German Aerospace Center Microwaves and Radar Institute. Since 2010, she has been with the Science Coordinator of German Satellite Mission TanDEM-X. Her main research interests include electromagnetic propagation and scattering theory, radar polarimetry, SAR and interferometric SAR data processing techniques, and environmental parameter modeling and estimation.

Dr. Hajnsek was a member of the IEEE GRSS AdCom, from 2013 to 2021. She is a member of European Space Agency Mission Advisory Group for the ROSE-L Mission. She has been awarded with the Doctor degree honoris causa from the University of Oslo, Norway for her outstanding contributions to science, including the development of algorithms using innovative radar techniques for environmental parameter estimation and setting requirements for the design of future radar missions in application areas as permafrost, glaciers, disaster management, agriculture, and climate change impacts, in 2024. She was Technical Program Co-Chair of the IEEE IGARSS 2012 in Munich, Germany, and 2019 in Yokohama, Japan. She was the Vice President of the IEEE GRSS Technical Committees, from 2016 to 2020. She has been the Founder of the New Technical Committee Remote Sensing Environment, Analysis and Climate Technologies (REACT) that exists, since November 2021.